Two-dimensional electron layers in perovskite oxides

Cover

Stairstep twinning in lanthanum aluminate ($LaAlO_3$), one of the main constituents of the perovskite heterostructures discussed in this thesis. Image was taken by Michael W. Davidson of the Florida State University and is used with permission.

Ph.D. committee

Chairman and secretary
   Prof. dr. G. van der Steenhoven (University of Twente)

Supervisor
   Prof. dr. ing. D.H.A. Blank (University of Twente)

Assistant supervisor
   Dr. ing. A.J.H.M. Rijnders (University of Twente)

Members
   Prof. dr. Ir. H. Hilgenkamp (University of Twente)
   Prof. dr. P.J. Kelly (University of Twente)
   Prof. H.Y. Hwang (University of Tokyo, Japan)
   Prof. J.-M. Triscone (University of Geneva, Switzerland)
   Prof. dr. J. Aarts (Leiden University)
   Prof. dr. M.S. Golden (University of Amsterdam)

G.W.J. Hassink
Two-dimensional electron layers in perovskite oxides
Ph.D. thesis University of Twente, Enschede, the Netherlands.

TWO-DIMENSIONAL ELECTRON LAYERS IN PEROVSKITE OXIDES

PROEFSCHRIFT

ter verkrijging van
de graad van doctor aan de Universiteit Twente,
op gezag van de rector magnificus,
Prof. dr. H. Brinksma,
volgens besluit van het College voor Promoties
in het openbaar te verdedigen
op vrijdag 20 november 2009 om 15:00

door

Gerrit Willem Johannes Hassink

geboren op 2 maart 1980
te Ede

Dit proefschrift is goedgekeurd door de promotor
    Prof. dr. ing. D.H.A. Blank

en de assistent-promotor
    Dr. ing. A.J.H.M. Rijnders

Contents

Chapter 1

Attractive repulsion

1.1 Introduction

From the earliest days of the natural sciences, humanity has tried to understand and classify the world around us. The 'classical' Elements in Greek, Chinese and Japanese philosophy are examples of this. Even electric charge had a place in this picture; in fact, the very word 'electron' is derived from the Greek word for amber, 'elektron', as they knew that when you rub a piece of amber with a fur skin, a static electric charge will develop[1].

Later on, the alchemists of the Middle Ages would take this philosophical basis and, combined with continuing technological development, slowly start to turn these natural philosophies into the natural sciences we know today. Driven by the same wish to understand the world around them as the ancient Greeks and modern scientists, they strove to understand matter and energy. Indeed, their very goal was the ability to control matter to such a point that one could turn common materials into gold.

Since the first half of the last century we actually have the knowledge how to achieve that goal (though it is tremendously inefficient, costing much more than the possible gains)[2]. This was the result of a huge increase in the understanding of matter following the development of quantum mechanics at roughly the same time. Slowly, metals, semiconductors and simple insulators became understood as the field of solid state science was developed.

This understanding of these simple materials, though, is based on a simple assumption: that the outer electrons of the atoms making up these materials are independent from each other[3, 4]. This simplification to only include electron-ion and ion-ion interaction greatly simplifies the calculations and allows for a surprisingly comprehensive theory of metals, most semiconductors and simple insulators. Indeed, its success greatly contributed to the technological advances that occurred during the last century. The fast development of IC technology described by

Moore's law[5] was possible only because of the almost equally fast increase in materials knowledge.

However, there are many materials and properties that cannot be described using this independent electron approximation. For these materials the electron-electron interaction has to be explicitly included. These correlated electron materials have always been of interest (for example, lodestone, Fe_2O_3, was already known and used as a compass in the 4th century in China[6]), but more recently these materials and their applications have become of more and more technological importance because of their diverse and often desirable properties. It is often thought that the only way to continue Moore's law is to switch to new, correlated, materials as the end of the semiconductor parameter space is coming closer and closer.

Most of the correlated electron materials research focuses on the transition metal oxides[7], of which the previously mentioned lodestone is one. Superconductors[8, 9], transparent conductors[10], high dielectric constant insulators[11], colossal magnetoresistance sensors[12]; all these, and more, can be found within this group of materials. And all these attractive properties are due to the Coulomb interactions within the compounds.

The ultimate example of this correlated nature is the Mott insulator. From independent-electron band theory we know that a partially filled band should conduct. In transition metal oxides, the situation can be different. Where in a normal metal the electrons are 'spread out' over the entire space occupied by the metal, in a transition metal oxides the narrow orbitals force the electrons to move by hopping from ion to ion. If, however, there is already an electron present on the target site, there will be a Coulomb repulsion between the stationary and moving electron. If this energy becomes too large to overcome, hopping will not occur and thus the material will become insulating.

These Mott insulators are the 'parent' compounds from which most oxide superconductors are derived through doping, either with electrons or with holes. At the same time, they provide very interesting systems to study electron correlation itself as well. The Coulomb force balance can easily be disturbed by pressure[13] or doping[14]. This also makes these materials very interesting for the fabrication of transistors, especially in thin films, because of the high electron sheet density (of the order of 10^{14} cm^{-2} compared to GaAs which has 10^{11} cm^{-2}) and the possibility for a density-driven metal-to-insulator transition[15]. On the other hand, the electron mobilities in transition metal oxides are lower compared to those in semiconductors; at room temperature about 6 cm^2/Vs compared to 6000 cm^2/Vs for GaAs. Still an on/off ratio exceeding 2000 can theoretically be achieved in these materials.

So, two-dimensional layers of transition metal oxides are of interest both from a scientific and a technological viewpoint. The high electron densities make them excellent choices for transistor devices, while the simplified two-dimensional structure would facilitate the study of electron correlations. A lot of work has been done on two-dimensional Mott theory[16–18], so a physical two-dimensional Mott insulator would be a model system to compare with such theories.

As a part of the Nanoelectronic Materials flagship of the Dutch NanoNed initiative such thin layers have been studied. Using pulsed laser deposition[19] (PLD) and reflective high-energy electron diffraction[20] (RHEED) it is possible to grow well-defined oxide heterostructures with sharp interfaces (for example, Lee[21] or Huijben[22]). The actual fabrication of the layers was studied, trying to control and optimize the growth and to understand the influence of important parameters on the heterostructure properties. Confined, quasi-two-dimensional (q2D) electron layers were fabricated. Some of these q2D heterostructures have a strong perpendicular confinement so that the layers themselves become Mott insulating. Other heterostructures focused more on conducting properties where a unique combination of insulating materials yield a conducting interface. Such interfaces could provide interconnects between difference electron-correlated devices, especially as these interfaces can be patterned[23]. All together, this thesis studies these electron layers, with the goal to both understand the physics and study their applicability in new devices.

1.2 Outline

The first part of my thesis, chapters two and three, are an introduction to the rest of this booklet. Chapter two provides an overview of correlated-electron physics, covering both basic idea's as well as a literature review of relevant work. This covers a little semiconductor and transition metal physics followed by a more detailed look at the precursors to the structures studied in this thesis: lanthanum titanate/strontium titanate, or $LaTiO_3/SrTiO_3$ (LTO/STO), superlattices and lanthanum aluminate//strontium titanate, or $LaAlO_3//SrTiO_3$ (LAO//STO), interfaces. Chapter three discusses the various techniques to fabricate and analyse these structures. This covers sample preparation and fabrication, as well as *in situ* and *ex situ* analysis methods.

The second part, chapters four to six, collects together information and data from all the work done during my Ph.D. It discusses the growth of LTO/LAO superlattices and LAO//STO interfaces on STO substrates. The properties of these structures as a function of growth parameters such as the gas pressure during deposition, deposition duration or heterostructure design are discussed.

Breaking down the second part in more detail, chapter four discusses the LTO/LAO superlattices. Here a LTO layer is sandwiched between LAO layers, leading to a perpendicular confinement of the electrons in the LTO layer that is different from in-plane. Only for thin LTO layers is the perpendicular confinement strong enough to become a Mott insulator. Further ellipsometry and X-ray spectroscopy (XPS) measurements provide collaborating results. Chapter five focusses on the LAO//STO single interfaces. The influence of the deposition gas is investigated, as well as the sequence of deposition itself. LAO//STO interfaces deposited within a single perovskite LTO block are found to have different properties compared to interfaces created between LAO and STO blocks. Chapter six deals with LAO//STO double-interface heterostructures. The properties of these heterostructures have

been studied as a function of the interface separation and deposition pressure. Transport and optical reflectivity measurements help to elucidate the physics inherent to these conducting interfaces.

My thesis closes with a brief epilogue & outlook, a summary and a 'thank-you' to all the people who have been involved in the process that was my Ph.D. and eventually resulted in this booklet.

1.3 References

[1] "Electron." http://en.wikipedia.org/wiki/Electron#History (04-17-2008).

[2] "Synthesis of noble metals." http://en.wikipedia.org/wiki/Synthesis_of_noble_metals (22-06-2009).

[3] N. W. Ashcroft and N. D. Mermin, *Solid state physics*. Philadelphia: Saunders College Publishing, 1976.

[4] C. Kittel, *Introduction to solid state physics*. Hoboken, NJ: Wiley, 8th ed., 2005.

[5] "Moore's law." http://en.wikipedia.org/wiki/Moore's_law (04-16-2008).

[6] "Compass." http://en.wikipedia.org/wiki/Compass#China (16-04-2008).

[7] E. Dagotto and Y. Tokura, "Strongly correlated electronic materials: present and future," *MRS Bulletin*, vol. 33, pp. 1037–1045, 2008.

[8] M. K. Wu, J. R. Ashburn, C. J. Torng, P. H. Hor, R. L. Meng, L. Gao, Z. J. Huang, Y. Q. Wang, and C. W. Chu, "Superconductivity at 93 K in a new mixed-phase Y-Ba-Cu-O compound system at ambient pressure," *Physical Review Letters*, vol. 58, pp. 908–910, 1987.

[9] M. Jourdan and H. Adrian, "Possibility of unconventional superconductivity of $SrTiO_{3-d}$," *Physica C*, vol. 388-389, pp. 509–510, 2003.

[10] M. Dekkers, G. Rijnders, and D. H. A. Blank, "$ZnIr_2O_4$, a p-type transparent oxide semiconductor in the class of spinel zinc-d^6-transition metal oxide," *Applied Physics Letters*, vol. 90, p. 021903, 2007.

[11] M. Suzuki, T. Yamaguchi, N. Fukushima, and M. Koyama, "$LaAlO_3$ gate dielectric with ultrathin equivalent oxide thickness and ultralow leakage current directly deposited on Si substrate," *Journal of Applied Physics*, vol. 103, p. 034118, 2008.

[12] Y. Tokura and N. Nagaosa, "Orbital physics in transition-metal oxides," *Science*, vol. 288, pp. 462–468, 2000.

[13] Y. Okada, T. Arima, Y. Tokura, C. Murayama, and N. Mori, "Doping- and pressure-induced change of electrical and magnetic properties in the Mott-Hubbard insulator $LaTiO_3$," *Physical Review B*, vol. 48, pp. 9677–9883, 1993.

[14] Y. Tokura, Y. Taguchi, Y. Okada, Y. Fujishima, and T. Arima, "Filling dependence of electronic properties on the verge of metal-Mott-insulator transitions in $Sr_{1-x}La_xTiO_3$," *Physical Review Letters*, vol. 70, pp. 2126–2129, 1993.

[15] D. M. Newns, J. A. Misewich, C. C. Tsuei, A. Gupta, B. A. Scott, and A. Schrott, "Mott transition field effect transistor," *Applied Physics Letters*, vol. 73, pp. 780–782, 1998.

[16] M. Imada, A. Fujimori, and Y. Tokura, "Metal-insulator transitions," *Reviews of Modern Physics*, vol. 70, pp. 1039–1263, 1998.

[17] A. Rüegg, S. Pilgram, and M. Sigrist, "Strongly renormalized quasi-two-dimensional electron gas in a heterostructure with correlation effects," *Physical Review B*, vol. 75, p. 195117, 2007.

[18] R. Pentcheva and W. E. Pickett, "Correlation-driven charge order at the interface between a Mott and a band insulator," *Physical Review Letters*, vol. 99, p. 016802, 2007.

[19] R. Eason, ed., *Pulsed laser deposition of thin films*. Wiley, 2006.

[20] A. J. H. M. Rijnders, G. Koster, D. H. A. Blank, and H. Rogalla, "In situ monitoring during pulsed laser deposition of complex oxides using reflection high energy electron diffraction under high oxygen pressure," *Applied Physics Letters*, vol. 70, pp. 1888–1890, 1997.

[21] H. N. Lee, H. M. Christen, M. F. Chisholm, C. M. Rouleau, and D. H. Lowndes, "Strong polarization enhancement in asymmetric three-component ferroelectric superlattices," *Nature*, vol. 433, pp. 395–399, 2005.

[22] M. Huijben, G. Rijnders, D. H. A. Blank, S. Bals, S. van Aert, J. Verbeeck, G. van Tendeloo, A. Brinkman, and H. Hilgenkamp, "Electronically coupled complementary interfaces between perovskite band insulators," *Nature Materials*, vol. 5, pp. 556–560, 2006.

[23] C. W. Schneider, S. Thiel, G. Hammerl, C. Richter, and J. Mannhart, "Microlithography of electron gases formed at interfaces in oxide heterostructures," *Applied Physics Letters*, vol. 89, p. 122101, 2006.

Chapter 2

Two-dimensional electron layers in correlated-electron oxides

Abstract

Two-dimensional electron layers in semiconductor materials are easily understood within the free-electron model and can show clear quantum signatures. The appropriate length scale for quantum structures is the Bohr radius. However, as the electron densities increase and the electron separation length reaches this same Bohr radius scale, electron correlations become important. These give rise to material properties such as magnetism and superconductivity. Two-dimensional electron layers in correlated-electron materials exhibit many of the features found in bulk materials, but the anisotropy of the electron layer gives rise to additional ordering and properties, such as planar magnetic order.

2.1   Introduction

One of the fastest and most pervasive technologies of the last century was that of semiconductor physics. In a fascinating interplay between theoretical understanding, experimental acumen and technological applications the field developed rapidly and extensively. Moore's law[1] would not have been possible without this development.

Two-dimensional electron gases (2DEG) probably are one of the prime examples of this process. Based on fundamental and easy to understand principles from quan-

tum mechanics (see introductory quantum mechanics books like Gasiorowicz[2] or Griffiths[3]), their realisation was only made possible once the experimental fabrication techniques were developed thoroughly; a gap of about 50 years between concept and device. Once available, though, these 2DEG's provided a wealth of new opportunities for research, such as the quantum Hall effect[4], but also led to the development of new applications such as the quantum cascade laser[5] and the high electron mobility transistor. In recent years the growth of transition metal oxides, especially by PLD, has risen to similar levels of control and *in situ* monitoring[6, 7] resulting in the fabrication of high-quality films and heterostructures of these oxides[8–11].

This chapter gives an overview of theory about quantum wells and correlated electron materials as well as previous work on the systems under investigation here: LTO/LAO heterostructures and LAO//STO interfaces. This lays the foundation for the physics in the later chapters.

2.2 Two-dimensional electron gases

Every physics student is familiar with the particle-in-a-box example from quantum dynamics. In it, a single particle is confined to a certain area by an external potential. Schrödinger's equation for this (one-dimensional) situation is

$$-\frac{\hbar^2}{2m}\frac{\mathrm{d}^2\Psi}{\mathrm{d}x^2} + V\Psi = E\Psi \tag{2.1}$$

where $\hbar$ is the reduced Planck's constant, m is the particle mass, Ψ is the electron wave function, x the position, V the (in)finite external potential and E the (eigen) energy of the system. For an infinite external potential, the particle is truly confined, with specific energy levels:

$$E_n = \frac{n^2 h^2}{8mL^2} \tag{2.2}$$

where n is the quantum number and L is the size of the potential well. Or written in a slightly different way:

$$E_n = \frac{\hbar^2 k^2}{2m} \tag{2.3}$$

where k is the wave number. In a more realistic case, the potential is finite and the wave function is not completely contained within the potential well. This is shown schematically in Figure 2.1.

This simple one-dimensional picture can be extended to three dimensions quite easily, but in this thesis the focus is on two-dimensional layers which are confined in only one direction. In such layers the particles are confined perpendicular to the layer, but are free to move within the layer. In that case, any additional quantum properties are well described by the one-dimensional case.
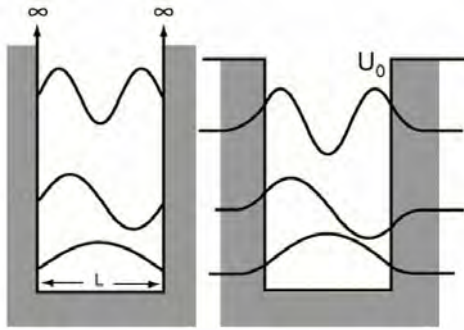
Figure 2.1: The energy levels in an infinite (left) and a finite (right) quantum well, taken from Ref. [12].

2.2.1 Potential wells in semiconductors

So far quantum theory has shown that a single particle in a potential well has distinct, numbered energy levels. To realize such a 2DEG system in an experimental device, three conditions need to be met:

1. There has to be a potential well;

2. There have to be particles, here electrons, within the potential well;

3. The electrons within the well should not interact significantly.

Again, the interplay between theory and experiments forged the way to such devices. The application of quantum mechanics to solid state science gave rise to band structure theory. There, the (electrical) properties of materials are defined by the appearance of collections of electron levels named bands. If the Fermi level, the maximum energy level electrons can reach if the system is in its ground state, is within such a band, it is a conductor. See Figure 2.2(c).
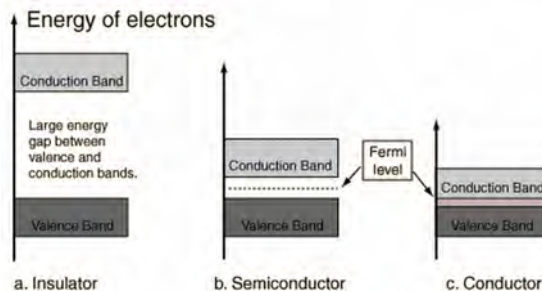
Figure 2.2: The simple band picture of insulators (a), semiconductors (b) and conductors (c). Figure taken from Ref. [13].

9

If the Fermi level is within a gap between two bands and thermal fluctuations do not excite some electrons to the upper, conducting band, the material is an insulator (See Figure 2.2)(a). However, if some electrons *are* excited to the conduction band, it is a semiconductor (Figure 2.2(b)).

The band gap is unique for each semiconductor material. Table 2.1 shows some band gaps for representative semiconductors and oxides.

material	band gap E_{g} (eV)	effective mass m^* (-)	electron mobility μ (cm^2/Vs)	electron density n (cm^{-3})
Si	1.12	1.08	1300	$2.0{\cdot}10^{16}$
GaAs	1.42	0.067	6000	$3.0{\cdot}10^{15}$
AlAs	2.168	0.146	200	$2{\cdot}10^{17}$
Nb:SrTiO$_3$	1.8	6	3.2	$1.4{\cdot}10^{17}$
LaAlO$_3$	5.6	-	-	-

Table 2.1: Important parameters for some representative semiconductors and oxides at room temperature[14–18].

From Table 2.1 it can be seen that the band gap varies substantially. By layering different semiconductors a potential well can be created. An example of such a potential well is shown in Figure 2.3.
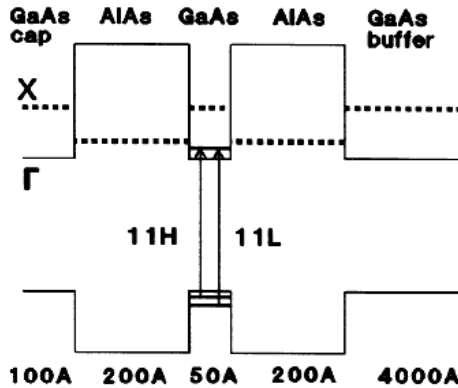
Figure 2.3: Band diagram of a simple semiconductor potential well.

The next question is how to get electrons into the potential well. The standard technique is to dope the semiconductor with atoms of an element that is more valent. Silicium is four-valent. Doping with phosphorus, which is five-valent would result in an excess of electrons after covalent bonding. These 'excess' electrons are now doped into the conduction band and can freely move throughout the potential well.

Such doped atoms, however, also form scattering centers which inhibit the electron mobility. As the electrons should be disturbed as little as possible within the

potential well, the active layer (the central GaAs layer in Figure 2.3) should not be doped. Here an additional bonus of the potential well appears. If the layers to the side of the actual well are doped, the free electrons will search out the energy minimum within the well as their ground state. This way the number of electrons within the well can be controlled, without disturbing the crystal perfection of the well itself.

This control also gives the opportunity to make sure the electrons are independent from one another. As long as the mean free path is much smaller than the average distance between electrons, the electron-electron interaction will be negligible. Thus, by controlling the density of electrons within the potential well the independent electron regime can be maintained.

2.2.2 Confinement of electrons

The most basic effect of such confinement would be the splitting of the energy bands into distinct states with energies as approximated by Equation 2.3. However, if the potential well is so large that the energy levels are very close together, thermal fluctuations blend the transitions and the energy levels are not distinct. If all levels are to be resolved, it can be stated that:

$$E_2 - E_1 > k_\mathrm{B}T \tag{2.4}$$

where k_B is the Boltzmann constant and T the absolute temperature. After inserting Equation 2.2 this gives an upper limit to the potential well size:

$$L_\mathrm{thermal} < \sqrt{\frac{3h^2}{8mk_\mathrm{B}T}} \tag{2.5}$$

This is an upper limit to the size of the potential well to have distinct energy levels, or, to be a quantum well. Another important criterium is whether the electronic state of the electron is larger than the potential well. Only in that case the external potential well forms the 'true' potential well controlling the electron properties instead of the atomic potential well. This length scale is conveniently described by the Bohr radius:

$$a_\mathrm{Bohr} = \frac{4\pi\epsilon\hbar^2}{me^2} \tag{2.6}$$

If, however, these conditions are met and a quantum well is created, the density of states splits up. The lower the dimensions of the quantum well, the sharper the density of states is (see Figure 2.4). Note that even though for a 2D quantum well the density of states is a step function, Figure 2.4 only gives the ground states. The transitions between levels is still well defined.

Even if the electrons are confined within a potential well, but not to the quantum limit, the two-dimensional nature of the electron layer can influence its properties. Under both an applied magnetic and electric field, the Lorentz force will force the
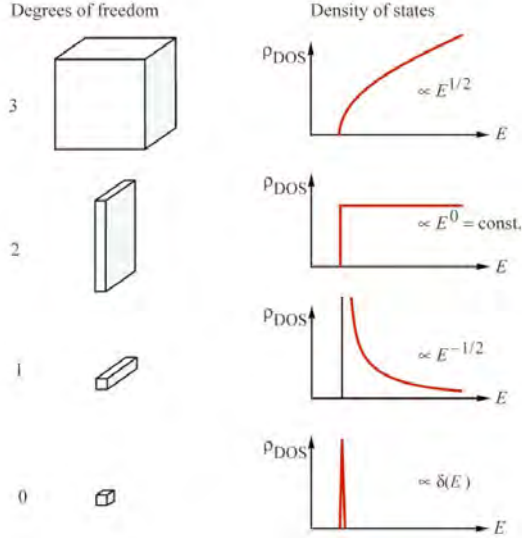
Figure 2.4: Density of states for different dimensionalities of quantum wells, taken from Ref. [19].

electrons in a material to undergo a cyclotron oscillation[20, 21] with a fundamental frequency of:

$$\omega_c = \frac{eB}{m^*} \tag{2.7}$$

where B is the applied magnetic field. ω_c can be written as $\omega_c = v_F/r_c$ where v_F is the Fermi velocity of the electron and r_c the radius of the cyclotron oscillation. Basic solid state physics gives then for the cyclotron radius:

$$r_c = \frac{m^* v_F}{eB} = \frac{\hbar k_F}{eB} \tag{2.8}$$

where k_F is the Fermi wave vector. This is a basic quantity in solid state physics and can, in approximation, easily be derived from the electron density. Depending on whether the system is two- or three-dimensional either $k_{F,3D} = \sqrt[3]{2\pi^2 n_{3D}}$ or $k_{F,2D} = \sqrt{2\pi n_{2D}}$ is used respectively. For interface and thin layer samples it is often the electron sheet density n_{2D} that can be measured instead of the full electron volume density n_{3D}. Under the assumption that $n_{3D} = n_{2D}/L$ where L is the average thickness of the electron layer two criteria for a two-dimensional electron layer can be derived.

The first is whether the Fermi wavelength is larger than the electron layer thickness. This indicates that no Bloch waves can develop perpendicular to the layer, so the properties of the electron gas are two-dimensional. Combining the equations for the 3D Fermi wave vector $k_{F,3D}$ and the 3D electron density n_{3D} yields:

$$\lambda_F = \sqrt[3]{\frac{8\pi L}{3n_{2D}}} \tag{2.9}$$

From Equation 2.9 it follows that $\lambda_F > L$ if $L < \sqrt{8\pi/3n_{2D}}$. For an electron sheet density of $n_{2D} = 2 \cdot 10^{13}$ cm^{-2} this criterion can be evaluated to be $L < 6.5$ nm.

The second is whether the cyclotron radius is larger than the electron layer thickness. If the electron layer has a thickness less than the cyclotron radius no full cyclotron movement can be carried out by the electrons in that direction. As the cyclotron movement is always perpendicular to the magnetic field, this would be most pronounced if the magnetic field is parallel to the electron layer. Related electrical properties such as the Hall effect and magnetoresistance would disappear for such magnetic field orientations. Indeed, this has been observed in STO field-effect transistor (FET) structures[22]. In a magnetic field of 3 T and with the same electron sheet density as above $r_c > L$ would be fulfilled for $L < 89$ nm.

For such systems the Fermi wavelength respectively the cyclotron radius form an upper bound to the electron layer thickness. These systems are not quantum confined, but do still exhibit a clear two-dimensional nature.

2.2.3 Properties and applications of confined electron gases

Probably the most common application of a confined electron gas is as the active layer in semiconductor transistors. Because of the confined nature in (at least) one direction, the absolute number of electrons that have to be manipulated at similar electron densities is small compared to bulk channels. In addition, because the electron donors are outside the actual conduction layer, very high mobilities can be achieved. Together this leads to high speed devices[23].

When the potential well is small enough to achieve quantum confinement, the distinct energy levels lead to interesting new possibilities. One of the most obvious properties is the appearance of new optical features due to transitions between these levels. A familiar example is shown in Figure 2.5. These flasks all contain cadmium selenide quantum dots, the zero-dimensional variety of a quantum well. The only difference between them is their respective size. But the light they give off by fluorescence is markedly different.

Figure 2.5: Cadmium selenide quantum dots fluorescence at different wavelengths, taken from Ref. [24].

Such dots (0D quantum wells) have a very distinctive spectrum, making them excellent choices for tracers in biological systems, their brightness and chemical

stability making them superior to organic dies[25, 26]. This same sensitivity to light also makes them interesting for applications in photovoltaic cells. At the right (tunable) wavelength, the transition of electrons to higher states is easily facilitated. Again the reverse is also interesting: because the light emission of the quantum dots can be tuned, better blue, or even white, light emitting diodes may be created.

Aside from active channels in semiconductors transistors, 2D quantum wells are commonly used as the active layer in diode lasers. Either the quantum well is the lasing medium itself or, as in a cascade quantum well laser, the lasing transitions are between levels in different quantum wells[5]. In the first case, the advantage is that the step in the density of states (see Figure 2.4) concentrates the electrons at that energy. This concentration of electrons at a specific energy increases the efficiency of the whole structure, but the transition energies themselves are still mostly determined by the material. The advantage of the second type of quantum well laser is that the lasing transition are between the different levels in different quantum wells. Because these levels can be determined during the growth of the laser structure, the transition and thus the wavelength of the cascade laser can be tuned from device to device.

One final, possible application of quantum wells that has to be mentioned is their use in quantum computing. Because quantum wells, especially quantum dots, are host to well-defined artificial (as in, non-atomic) electron levels they can be used to store quantum information. Coupled quantum dots, together with a method to read and manipulate those states, could form the basis for a quantum computer[27].

2.3   Correlated-electron oxides

In all of the previous discussion the assumption was made that electrons, apart from Pauli's exclusion principle, did not interact with one-another. This is a fundamental assumption, and a large approximation. The success of this independent electron approximation[20, 21] stems from the fact that both metals and semiconductors are well-described by this approximation. In many of these materials the electron-electron distance is larger than the Bohr radius, the traditional electron interaction length scale.

Already from Table 2.2 it can be seen that for many oxide examples the electron separation length is of the order of, or smaller than, the interaction length as determined by the Bohr radius. For these materials the electron-electron interaction or electron correlation will not be negligible. This also means that quantum wells in these materials are going to behave very different from those in semiconductors. In correlated-electron materials the 'free-particle-in-a-box' approximation is untrue and thus a lot of the simple quantum physics becomes a lot more complicated, and, as will be seen later, interesting[34].

This also indicates that correlated-electron materials cannot be thought of as either purely ionic (salts) or purely covalent (i.e. organics). Both of these bindings are

material	electron density[1] n (cm^{-3})	electron separation L (Å)	Bohr radius a_{Bohr} (Å)
Si	$2{\cdot}10^{16}$	368	6
GaAs	$3{\cdot}10^{15}$	693	110
CaMnO$_3$	$6{\cdot}10^{18}$	55	7
LaTiO$_3$	-	4	1
YBa$_2$Cu$_3$O$_{7-x}$	$3.6{\cdot}10^{21}$	7	67

Table 2.2: Electron interaction lengths in some semiconductors and oxides at room temperature[14, 15, 28–33].

in essence closed-shell configurations; salts with all their valence electrons on their own ion, organics with all their valence electrons shared with the other ion. In correlated-electron materials the valence electrons are mostly located on their own ion, but interact with the valence electrons of other ions in a slightly covalent way.

All this, both the electron correlation itself and the limiting of the effective quantum well length to the size of single atoms, indicates that semiconductor quantum well phenomena cannot occur in correlated electron materials. Artificial (i.e. non-atomic) electron energy levels like in Equation 2.2 do not occur; either because their free movement is impeded by correlations or because the confining potential is of the same scale as the atomic potential.

2.3.1 Independent vs. correlated electrons

To appreciate the difference between the independent electron approximation and the inclusion of electron correlation a look at the Schrödinger equation can already reveal much.

$$-\sum_i \frac{\hbar^2}{2m}\nabla_i^2 \Psi + \sum_{<i,j>} \frac{1}{2}\frac{e^2}{\epsilon K \left|\vec{r}_i - \vec{r}_j\right|}\Psi - \sum_{i,j} \frac{e^2}{\epsilon K \left|\vec{r}_i - \vec{R}_j\right|}\Psi = E\Psi \qquad (2.10)$$

Here, the first term is the standard kinetic term. The other terms described the background potential formed by the other electrons and ions in the system. The second term of the Schrödinger equation describes the electron-electron interaction, while the third describes the electron-ion interaction.

In the independent electron approximation the electron correlation is thought to be negligible. Also, the ions are much more massive than the electrons, so their movement is also negligible on the time scale on which the electrons move. These two assumption greatly simplify Equation 2.10 and it is this that lead to the success of much of the solid state theory in the beginning of the last century. It made the

---

[1]The electron density noted here is the density obtained from Hall measurements. However, this density of mobile electrons may very well be different from the density of interacting electrons. That is why though CaMnO$_3$ seems to have a large electron spacing compared to the Bohr radius, it still is a correlated-electron material.

complex Schrödinger equations tractable before the advance of complex numerical calculations like density functional theory that are nowadays able to work with the full, correlated Schrödinger equations.

However, the independent electron approximation is not able to explain several important physical properties such as (anti)ferromagnetism, the Mott insulating state and superconductivity. The single-band Hubbard model is often used as a starting point in the discussion of correlated materials. It simplifies the treatment of the background ions, but explicitly includes the electron-electron interaction. The Hamiltonian of the model takes the form of:

$$H = -\sum_{<i,j>\sigma} t_{ij} c_{i\sigma}^{\dagger} c_{j\sigma} + U \sum_i n_{i\uparrow} n_{i\downarrow} \tag{2.11}$$

where t_{ij} is the hopping parameter between nearest-neighbor sites i and j, $c_{i\sigma}^{\dagger}(c_{i\sigma})$ is the creation (annihilation) operator for an electron on site i with spin σ ($\uparrow$ or $\downarrow$), U is the on-site Coulomb repulsion energy and $n_{i\sigma} \equiv c_{i\sigma}^{\dagger} c_{i\sigma}$ is the electron occupation of site i. The transfer integral captures the physics where delocalizing an electron lowers its energy, similar to Bloch waves and thus represents the kinetic term from Equation 2.10. The Coulomb energy denotes the energy it costs to bring two electrons in close proximity, i.e. on the same site. By varying the total number of electrons and the relative energies of t and U a large phase space of properties opens upo. It is the recent and current interest in these properties that drove the work described in this thesis.

2.3.2 Transition metal oxides

Transition metal oxides are a class of materials that contains a wide variety of physical properties, be they electrical, magnetic, structural or optical. Most of this is due to the electron correlation nature of these materials.

There are several reasons for the strongly correlated nature of the transition metal oxides. Probably the most important factor is the high directionality of the outer electron orbitals, either 3d or 4d for the 4th and 5th row transition metals[35] (See Figure 2.6). This directionality corresponds to narrow bands in reciprocal space, and broadens for lower row transition metals. The directionality increases the probability of electron-electron interaction. It also means that small changes to the crystal structure will have immediate consequences for the physical properties.

Another factor of note is that many of the transition metal ions can be multivalent. This means that they can easily accommodate electrons without changing the core states of the ions in the system. These electrons do not become part of the changed ion core, but remain in the outer shells where the electron correlation takes place.

One of the most commonly investigated transition metal oxide crystal structures is that of the perovskite oxides (See Figure 2.7). This crystal group with the basic chemical formula ABO_3 has attracted much attention because many of the correlated electron properties mentioned above are present within this group:
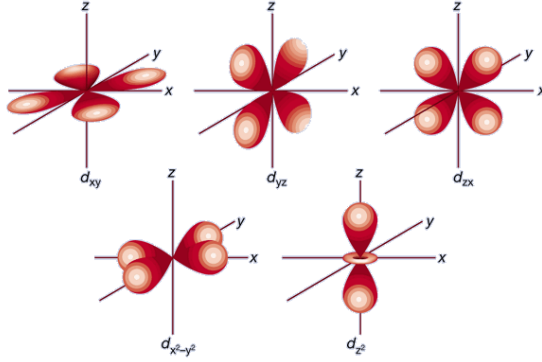
Figure 2.6: A graphical representation of 3d orbitals. Despite appearances, all orbitals are degenerate and add up to a spherical distribution.

$YBa_2Cu_3O_{7-\delta}$ is superconducting[36] (though officially only a 'derivative' of the perovskite crystal structure, it is still close enough to be included here), $LaTiO_3$ is a Mott insulator[37] and $La_{1-x}Sr_xMnO_3$ can be ferromagnetic[38].
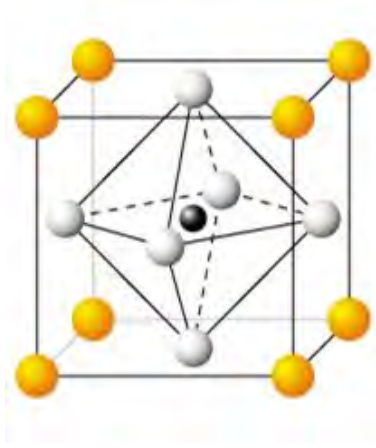
Figure 2.7: A perovskite unit cell. The A ions are on the corners of the cube and the B ion is at the center. The oxygen ions are in the middle of the sides.

There are several reasons to choose the perovskite materials as subject for research. Most importantly, chemical substitution of A- and B-ions leads to different physical properties, but the crystal structures are still compatible for thin film growth. Roughly, cell parameters, the cube side length, range from 3.7 to 4.2 Å. With care, materials with intrinsically different physical properties can be combined with only small strains. Even combinations with silicon are possible, though this has extra demands in terms of intermixing, oxidation and strain[39]. An additional advantage is that in a perovskite unit cell the complex electron-electron interactions can

be easier to visualize. Other crystal structures, such as spinel or corundum, have a more complex crystal structure, making this more difficult.

The perovskite crystal structure already captures a lot of the underlying structural physics that makes correlated electron materials so interesting. Small external strains can drive materials to new behaviour, such as ferroelectricity[11]. In fact, the strain induced by substitution with cations with different ionic radii can already change the system properties[40]. The oxygen configuration itself is also of importance, as the oxygen octrahedra drives a crystal field splitting[41] that is of great importance to especially multivalent B-site ions (see Figure 2.8). Again, strain can influence this splitting even further.
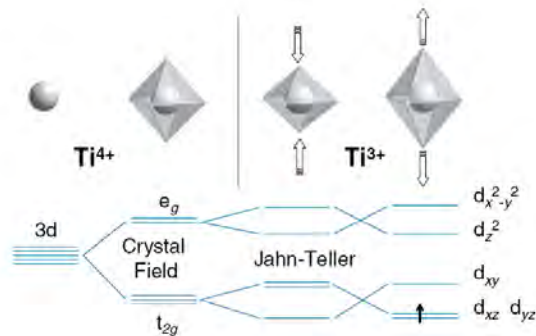
Figure 2.8: Crystal field splitting in a perovskite oxygen octahedra. Both octahedra on the right side are further modified by the Jahn-Teller effect.

All this shows that transition metal oxides are candidate systems to study correlated electron physics.

2.3.3 Electron correlation effects

Describing all possible electron correlations effects is both impossible and goes beyond the scope of this thesis, so the focus will be on the three already mentioned: (anti)ferromagnetism, Mott insulating state and superconductivity.

In and of itself, each electron has a magnetic moment. However, in many materials, these electron spins are randomly aligned, yielding a material with no net magnetization. Only through interactions between the different electrons, either directly or through Hund's coupling to the host ions, can any magnetic order arise. In perovskite materials, the two most common mechanisms for such interaction are superexchange and double exchange, giving rise to respectively an anti-ferromagnetic and a ferromagnetic alignment.

Figure 2.9 shows the superexchange interaction for Fe^{3+}-O^{2-}-Fe^{3+}. Both cations are equally filled and interact through the oxygen anion. Because of the anti-parallel alignment of the electron spins between neighbouring bands and because of the Pauli exclusion principle within bands the electrons show an anti-parallel spin arrangement from left to right. Finally the Hund's coupling aligns all the spins on a single cation, resulting in an anti-ferromagnetic alignment between the two cations.
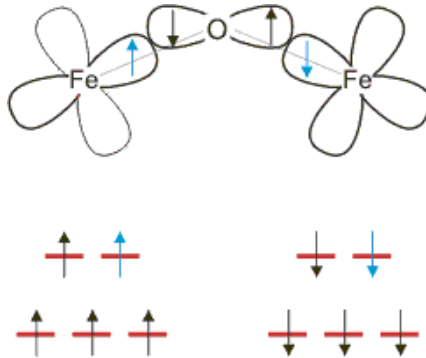
Figure 2.9: Superexchange mechanism in an iron oxide. Figure taken from Ref. [42].

In double exchange, the neighbouring cations are not equally filled, allowing for electrons to hop from one cation to another. Because of Hund's coupling, the energy of the mobile electron is lower if the bound electrons on each cation are aligned parallel. Thus, because delocalizing the electron leads to an energy gain, all the cations are aligned parallel, resulting in a ferromagnetic alignment. In both cases the electron-electron interaction, or correlation, is directly responsible for the magnetic properties.

The Mott insulating state is easily conceptualized (though more difficult in actual calculations) and forms the basis for a lot of different physical systems, such as the superexchange mentioned above and the superconducting states below. Again, the starting point is a lattice of equally filled cations, like in Figure 2.10. Now, any electron that wants to move to another site has to move to the next unoccupied band, which costs a certain amount of energy. If this Coulomb energy is larger than the energy gained from the delocalization no movement occurs and a system that can nominally have a half-filled band does not conduct. Here, the fundamental Coulomb repulsion between electrons causes macroscopic correlated behaviour.

This can be written as:

$$\frac{U}{W} > 1 \tag{2.12}$$

where U is the Coulomb energy between two electrons on a single site and W is the bandwidth of the system, corresponding to the energy gained by delocalizing electrons. Within the single-band Hubbard model of Equation 2.11 the correspondence between the bandwidth and the hopping parameter is $W \approx 4 \langle t \rangle$. If the
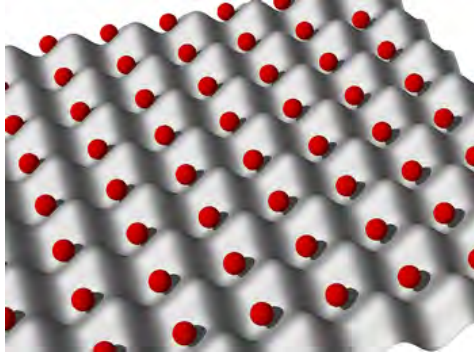
Figure 2.10: Cartoon picture of a Mott insulator with a single electron per site. Figure taken from Ref. [43].

Coulomb repulsion is larger than the bandwidth, a Mott insulating state occurs. Mott[44] was the first to rewrite this in terms of the Bohr radius and the electron separation length, followed later by generalizations[45] that lead to the Mott criterion:

$$a_{\text{Bohr}} \sqrt[3]{n} < 0.26 \pm 0.05 \tag{2.13}$$

This is an example that shows the importance of the Bohr radius in the discussion of correlated-electron effects.

If such a Mott insulator is hole-doped, i.e. some electrons are removed, a superconductor may be created. Classical BCS theory interprets the superconducting state as a condensate of bosonic Cooper pairs of electrons. Though a fundamental theory for high-T_c superconductivity is not yet found, electron interactions are thought to be of importance; the fact that the superconductivity can be tuned by changing the carrier density points to this fact[46, 47].

These examples show some of the variety of properties that can occur in correlated oxides. From here on the focus will be on the material systems under research in this thesis, where some of these properties will be encountered again.

2.4 Mott insulator/band insulator heterostructures

In a Mott insulator each electron is surrounded by neighbouring electrons and the Coulomb repulsion localizes each and every one of them. If, however, such a material would be combined with a band insulator, this symmetry can be broken.

2.4.1 LaTiO$_3$/SrTiO$_3$ heterostructures

Scanning transmission electron microscopy (STEM) showed sharply defined layers in superlattices of LTO and STO[48]. The electron distribution in this system is

of particular interest, because the B-site lattice consists entirely of titanium ions, respectively Ti^{3+} (electron configuration $3d^1$) for LTO and Ti^{4+} ($3d^0$) for STO. Using electron energy-loss spectroscopy (EELS) the Ti^{3+} fraction across such a superlattice was determined. Figure 2.11 shows these results for a single monolayer of LTO embedded in STO.
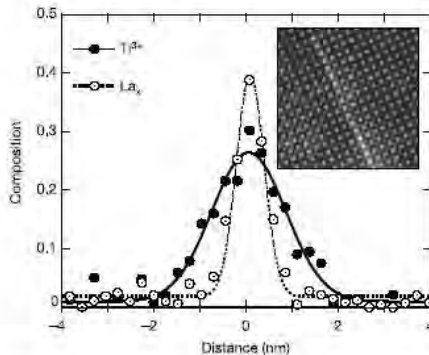
Figure 2.11: EELS profiles for La and Ti recorded across a LTO monolayer. Inset, the STEM image for the monolayer. The La signal is recorded simultaneously with the Ti, yet the Ti signal is considerably wider than that of the La. Graph taken from Ref. [48].

These superlattices were found to be conducting, with a resistivity (ρ) ≈ 300 $\mu\Omega$ cm, electron density (n_{3D}) $\approx 8\cdot10^{21}$ cm^{-3} ($n_{3D} \approx 0.48$ electron per unit cell volume) and Hall mobility (μ) ≈ 3 cm^2/Vs at room temperature[48, 49]. The absence of a Mott insulating state can already be seen from Figure 2.11: the peak Ti^{3+} fraction is about 0.4, meaning the cation lattice is only partially filled. Without the complete filling and the corresponding completely balanced Coulomb repulsion, the insulating state will not occur. Ultraviolet photoemission spectroscopy (UPS) showed a Fermi edge, indicating conducting states[50]. Infra-red spectroscopic ellipsometry was used to obtain a sheet carrier density (n_{2D}) per interface of about $2\cdot10^{14}$ cm^{-2} ($n_{2D} \approx 0.34$ electron per unit cell area), with a mobility of 6 cm^2/Vs at room temperature[51]. However, other superlattices were found to be insulating[52]. A weak antiferromagnetic coupling was observed below 85 K (J_{AF} = 7 meV), lower than the $T_{\text{Néel}}$ of 135 K in bulk LTO.

A similar system was recently investigated in the $LaVO_3$/$SrVO_3$ system. $LaVO_3$ (LVO) is a Mott insulator with a V^{3+} $3d^2$ configuration. $SrVO_3$ (SVO) is a paramagnetic metal with a V^{4+} $3d^1$ configuration. This is different from the LTO/STO system where both parent compounds are insulators, but both the spill-over of electrons from the lanthanum into the strontium compound and the absence of the Mott insulating state in thin layers of the lanthanum compound are reproduced[53]. This shows that the doping mechanism is generally applicable.

Theoretical correlated electron physics requires complex approximations and calculations and a simplification to a two-dimensional case would facilitate the un-

derstanding of the fundamental physics behind these systems, where spin-, charge- and orbital-ordering plus crystal deformations all act together to form the various interesting ground states. For the LTO/STO system, calculations were able to confirm that the conducting states were located at the interfaces[54]. In a phase diagram for different electron filling and interaction strength a variety of phases, orbital-ordered, magnetic and not, were found. Density functional theory (DFT) confirmed a sharp potential well around a single LTO monolayer about 2 nm wide, similar to that observed with EELS (Figure 2.11)[55, 56]. Further calculations showed the importance of lattice relaxations, with a ferroelectric like distortion perpendicular to the LTO layer, which is in a close agreement with the experimental data[57, 58]. At the same time such a distortion leads to a d_{xy} orbital order at the interface between LTO and STO. This is something that will be encountered in the next section on LAO//STO interfaces as well. In partially filled systems, this d_{xy} ordering results in an overall antiferromagnetic checkerboard charge ordering[59].

Such a two-dimensional conduction channel looks very similar to a quantum well. However, for a true quantum well the dimensions of the electron gas have to be on the order of, or smaller than, the Bohr length (see Table 2.2). For oxide materials this equates to about 1 to 5 unit cells. This is a big challenge, as already a single monolayer of LTO results in an electron layer extending over 6 unit cells.

2.4.2 LaVO$_3$/LaAlO$_3$ heterostructures

One way to increase the confinement of the electrons is by using a different buffer material. Okamota and Millis showed that for materials with a lower dielectric constant, the spread of the electrons out from the Mott layer is reduced[54]. STO has a dielectric constant of about 300 at room temperature, one of the highest known. LAO has a much lower dielectric constant of about 24. In addition, for LAO the dielectric constant is nearly independent of temperature as opposed to STO whose dielectric constant increases to about 10000[60] for low temperatures.

By embedding LVO in LAO there is no cation lattice on which the extra electrons can redistribute themselves, leading to a better confinement of the electrons. Indeed, XPS shows the presence of mostly V^{3+}, with only a small amount of V^{4+}, which is also located only at the top of the LVO layer based on the angle-dependence of the signal[61, 62]. This V^{3+} fraction is found to depend on the thickness of the capping layer, as seen from Figure 2.12, and results from a balance between reconstruction at the air//LAO surface and the dipole formed when electrons are transferred from the LVO layer to the surface to compensate the charge discontinuity[63, 64]. For a thin capping layer, it is energetically cheaper to let a dipole develop across the capping layer and use electrons from the LVO layer to compensate the polar discontinuity at the air//LAO surface. The surface requires half an electron per unit cell area, so the minimum V^{3+} fraction is $1 - 1/2 = 1/2$. As the capping layer gets thicker, the dipole energy increases as well. Above roughly 12 unit cells of LAO, a surface reconstruction is less costly and no electrons are transferred from the LVO layer to the surface.
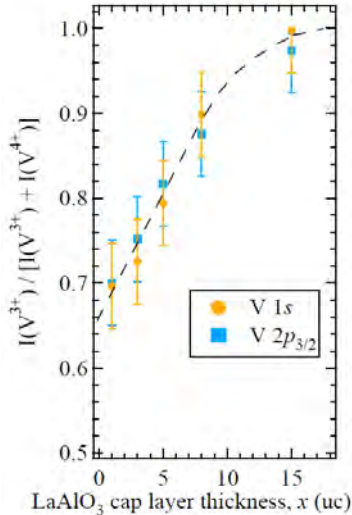
Figure 2.12: V^{3+} fraction as a function of the LAO capping layer thickness, as obtained from both the V 1s and $2p_{3/2}$ core-level spectra. The dashed curve is a guide to the eye. Graph taken from Ref. [63].

Transport measurements on similar samples showed a similar behaviour, where the sheet resistance reached a constant value above a capping layer thickness of about 15 unit cells[65]. In effect, the hole-doping of the LVO layer is changed by varying the LAO capping layer thickness.

2.5 Polar/non-polar interfaces

In the previous section an example of a polar interface was described: the LAO(001) surface. There is a charge discontinuity between the LaO//AlO$_2$ stacking and the 'vacuum'. The LAO consists in this orientation of alternating layer of $(La^{3+}O^{2-})^+$ and $(Al^{3+}O_2^{2-})^-$ while the vacuum has an effective charge of zero. Such discontinuities are often resolved by a surface reconstruction in bulk materials[66, 67]. However, such polar discontinuities can also occur inside heterostructures; a fact well known from semiconductor physics, where it results in an ionic reconstruction at the interface between different semiconductors[68][2]. In correlated-electron materials, however, an electronic reconstruction, similar to the redistribution of electrons in the LTO/STO system, is also possible. Examples are the electronic reconstruction at domain walls in BiFeO$_3$[70], where the polarization discontinuity gives rise to a conducting interface and the destruction of half-metallicity in Fe$_3$O$_4$/BaTiO$_3$ due to the electron transfer across the interface[71].

---

[2]Though recently a 2DEG resulting from an *electronic* reconstruction at the interface between two polytypes of silicon carbide was observed[69].

2.5.1 LaAlO$_3$//SrTiO$_3$ interfaces

In 2004 Ohtomo and Hwang showed that the interface between LAO and STO in the (001) direction can be conducting, depending on the actual chemical composition of the interface. Such an interface exhibits a polar discontinuity, as LAO has alternating planes ± 1 while the (Sr^{2+}O^{2-}) and (Ti^{4+}O$_2^{2-}$) planes of STO are neutral[72]. In a purely ionic picture, this discontinuity transfers either half an electron per unit cell area from LAO into STO for a LaO//TiO$_2$ interface or half a hole per unit cell area for a AlO$_2$//SrO interface. Figure 2.13 shows how the electrons and holes are distributed in this model. The former interface is found to be conducting, while the latter, though nominally hole-doped, is insulating. Hole-doping of closed shell ions is very difficult and the compensation of holes by oxygen-vacancy induced electrons results in no net free carriers[73, 74].

(a) *n*-type interface   (b) *p*-type interface
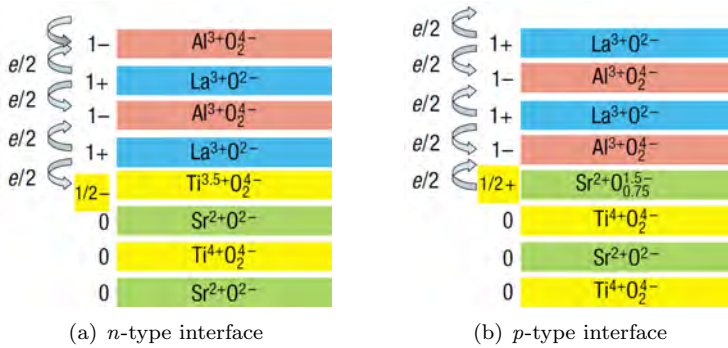
Figure 2.13:   Electron transfer at polar discontinuous interfaces in LAO/STO systems. Diagrams taken from Ref. [73].

Though easy to understand, the purely ionic picture is never complete for a correlated-electron material. Another, more physical way to interpret these results is by looking at the internal dipole that develops across the charged LAO layers. In the electronically unreconstructed case, the abrupt transition of neutral to charged layers results in a potential build-up due to the electric fields between the oppositely charged layers in LAO (see Figure 2.14). This 'polar catastrophe' grows with the LAO thickness and has to be compensated when the energy can no longer be accommodated by internal deformations[75–77]. In a band picture, this happens when the potential build-up becomes larger in energy than the band gap of STO[77–80]. The valence band of LAO rises above the Fermi level, allowing for transfer of electrons from the top surface to the interface. This reduces the potential build-up, as seen on the right in Figure 2.14. Recently, an argument has been made for the existence of in-gap states to which electrons can tunnel[81][3].

---

[3]Note however, that this article shows one of the subtle details of density-functional calculations. By choosing an odd number of LaO and AlO$_2$ layers, the authors need to introduce an extra electron to make the entire stack neutral. This way, free electrons are introduce artificially. See for example the discussion by Lee and Demkov[82]

However, their calculations show a constant electron density independent of the LAO layer thickness, contrary to experimental results [83, 84].
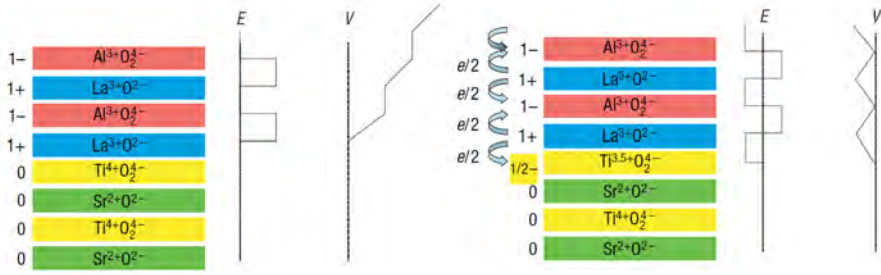
Figure 2.14: Polar catastrophe in a unreconstructed case (left) and a reconstructed case (right), where half an electron is transferred into the TiO_2 layer. Diagrams taken from Ref. [73].

The crossing of the potential build-up and the band gap implies that up to a certain thickness of the LAO layer, this dipole can be accommodated by the strain within the LAO and no electronic reconstruction (i.e. electron-doping into the TiO_2 layer) occurs. It was observed that up to a thickness of 4 monolayers of LAO the interface was still insulating, followed by an abrupt change in conductivity[85]. Optical second-harmonic measurements confirm this and find an indication that the electrons already rearrange for 3 monolayers, though the interface does not become conducting until a thickness of 4 monolayers[86]. Thicker LAO layers show a decreasing mobility, though the mechanism behind that behaviour is one of the many unsolved mysteries in this system[84]. Theoretical calculations actually show a larger critical thickness, but this can have several explanations. One is that the supercell used in the calculations is too small, so not all possible reconstructions are included[76, 87]. Another explanation is that in real samples there are surface defects that form in-gap states, so the LAO band needs to shift less before electrons are doped[77, 88]. Finally, DFT always has a problem calculating the band gap of materials, which may make these calculations only qualitative, not quantitative. This thickness effect can be used to pattern structures into the conducting layer by selectively depositing thick LAO[89]. Only those areas where the LAO layer is thicker than 4 monolayers the dipole energy is large enough to trigger the electronic reconstruction and create a conducting interface. Or, by letting the dipole develop to just below the threshold value for electronic reconstruction, the conducting state can then be induced by applying an electric field and thus altering the dipole across the LAO layer. This can be done either by a back-gate field-effect transistor configuration[85, 90] or by writing with a conducting AFM tip[91, 92].

Interestingly, this minimum LAO thickness requirement for a conducting interface does not seem to apply when the LAO layer itself is again capped with STO. The created double-interface (one n-type, one p-type) structures are conducting down to a single monolayer of LAO embedded in STO[83, 93, 94]. There is, however, a clear interaction between the two interfaces. Below a LAO thickness of about 6 monolayers, the sheet resistance increases. Hall measurements show that

this is due to a decrease of the electron density, while the electron mobility is constant (as opposed to single interfaces, where the mobility decreases with increasing thickness[84]). Interestingly enough, about half a year earlier a jump in the optical absorption spectrum of superlattices of LAO and STO as observed which does not appear in alloyed films of the same chemical composition[95]. This jump occurred at the same LAO thickness of 6 monolayers where the transport properties started to diverge in double-interface structures. The $LaNiO_3/SrMnO_3$ system also undergoes an insulator-to-metal transition upon increasing the $LaNiO_3$ layer thickness[96]. Ionically, the system does have a polarization discontinuity ($La^{3+}Ni^{3+}O_3/Sr^{2+}Mn^{4+}O_3$), so electron reconstruction may play a role here. The analysis of the transport behaviour points to a more complex conduction mechanism for this system compared to the LAO/STO system.

In general, the electron gas acts as a Fermi liquid with a $1/T^2$ behaviour of the electron mobility[72, 83, 97–99], ranging from $\sim$6 cm^2/Vs at room temperature to $\sim$1000 cm^2/Vs at 5 K. This correlated electron liquid model was confirmed by scanning tunneling spectroscopy[100]. Though in general the electron-electron interactions are weaker than electron-phonon interactions at room temperature[21], in STO they are typically weak (as seen from the poor heat conduction) and would give rise to a different temperature dependence[83]. The electron density varies widely with fabrication parameters such as substrate termination[97], oxygen pressure during deposition[72, 99, 101, 102] and, for PLD[4], laser fluency[107]. There is some argument for intermixing[73, 105, 108], but transmission electron microscopy images do not give conclusive evidence. Also, if intermixing would occur, the complimentary p-type interface should also become conducting[97]. A thermally-activated behaviour of the electron density, similar to that in semiconductors, with an activation energy of about 6 meV was observed[83]. This points to weakly-bound donors as the source of the electrons[92]. In general, electron densities on the order of 10^{14} cm^{-2} at room temperature are achieved. Remarkably, at low temperatures almost all data converge to a value around $2 \cdot 10^{13}$ cm^{-2}[83, 85, 102, 109–111]. These values for the electron density would translate to, respectively, about 0.15 and 0.03 electron per unit cell area at room temperature and 5 K. This is far below the nominal half electron per unit cell area transferred in the purely ionic model above. One explanation might be that the electrons are distributed over different sub-bands, of which only some contribute to the (Hall) free electron density[112](see also footnote on page 3). However, XPS detects both free and bound electrons and the densities observed with this technique are close to those obtained from Hall measurements[113].

Table 2.3 compares the transport properties of semiconductor (Si and GaAs) and correlated-electron (LTO/STO and LAO//STO) systems. The electron mobilities in semiconductors are always higher than those in correlated-electron materials. This is not surprising, as the mobility is limited by the scattering of electrons, either from ions or with other electrons. Thus correlated-electron materials, with

---

[4]Which is the majority of the experiments. LAO films grown by molecular beam epitaxy[103], sol-gel[104] or sputter deposition[105] have not yet been electrically characterized, though Ti^{3+} has been observed using XPS[106].

their higher electron densities, will almost always display lower mobilities than semiconductors.

system	m^*	μ	n_{3D}	n_{2D}
	(-)	(cm^2/Vs)	(cm^{-3})	(cm^{-2})
Si	1.08	1300	$2.0 \cdot 10^{16}$	
GaAs	0.067	6000	$3.0 \cdot 10^{15}$	
ZnO/Mg$_x$Zn$_{1-x}$O	0.32	160		$2.5 \cdot 10^{13}$
Nb:STO	1.8	6	$1.4 \cdot 10^{17}$	
LTO/STO	1.8	3	$8 \cdot 10^{21}$	
LAO//STO	1.5	6		$1.2 \cdot 10^{14}$

Table 2.3: Comparison of the transport properties at room temperature of semiconductor and correlated-electron systems[14–16, 48, 49, 51, 83, 114].

To study the possibility of quantum effects in these electron gases, the requirements for Shubnikov-de Haas oscillations can be studied. The occurrence of these oscillations is a clear sign of the quantum nature of the electron gas, i.e. the width of the electron gas is smaller than the Bohr radius (see Table 2.2 and discussion). The requirements are[115]:

$$\frac{\hbar \omega_c}{k_B T} > 1 \tag{2.14}$$

and:

$$\omega_c \tau > 1 \tag{2.15}$$

where ω_c is the cyclotron frequency and τ is the mean time between scattering events. The first requirement states that the energy difference between Landau levels must be larger than the thermal energy, while the second states that the electrons must be mobile enough to travel at least a single orbit before scattering.

Examples in semiconductor physics are readily found, with some examples given below. But in correlated oxides, the high effective electron mass and high scattering rate reduce the likelihood of these requirements being met. Table 2.4 shows these requirements at 5 K and 9 T for several semiconductors, a few transition metal oxides where Shubnikov-de Haas oscillations have been reported and the two systems discussed in this chapter. Assuming the standard form for the cyclotron frequency (Equation 2.7) and electron mobility $\mu = \frac{e}{m^*} \tau$ Equations 2.14 and 2.15 transform into:

$$\frac{\hbar e B}{k_B T} \frac{1}{m^*} > 1 \tag{2.16}$$

and:

$$\mu B > 1 \tag{2.17}$$

system	m^* (-)	μ (cm^2/Vs)	$\hbar\omega_c/k_BT > 1$	$\omega_c\tau > 1$
Si	1.08	13000	2.2	12
GaAs	0.067	5000	36.1	4.5
ZnO/Mg$_x$Zn$_{1-x}$O	0.32	5000	7.6	4.5
Nb:STO	1.8	22000	1.3	19.8
LTO/STO	1.8	50	1.3	0.05
LAO//STO	1.5	800	1.6	0.72

Table 2.4: Comparison of the Shubnikov-de Haas requirements at 5 K and 9 T for semiconductors, transition metal oxides & discussed systems[14–16, 48, 49, 51, 83, 114].

As can be seen, the high electron mass en low mobility yield low values for the two requirements, meaning they are only barely met, if at all.

So far the discussion focussed primarily on macroscopic properties. On a more microscopic level, the crystal structure at the LAO//STO interface has been studied both experimentally and theoretically. The ionic model described above is not perfectly applicable to correlated-electron materials and often more complex first-principle calculations - explicitly including the Coulomb energy U - are needed.

One of the first observations, both experimental[105, 116, 117] and theoretical[75, 88, 118, 119], was that at the interface the local crystal structure deforms. A similar effect was already known for the LTO/STO system[57] and has some similarities to the Jahn-Teller distortion observed in manganites[41]. Indeed, where in the case of the Jahn-Teller effect the electron is the driving force behind the crystal distortion, at the LAO//STO interface it is possible that the distortion induces a local energy minimum for an electron. Calculations on a LTO/STO/SrRuO$_3$ stack shows that charge transfer only occurs for structures where the ionic positions are relaxed[120]. Though the exact mechanism is not clear, in the resulting crystal structure the cation separation has increased, while the top of the oxygen octahedra contracts and moves closer to the interface. This elongation is accompanied by a GdFeO$_3$-like rotation of the octahedra[121].

These changes are about 4 % of the lattice parameter and greatly influence the orbital order at the interface. Again there is a similarity to the Jahn-Teller effect where certain orbitals are favorably occupied because of the lower overlap energy with the oxygen ions in the surrounding octahedra. At the LAO//STO interface the contraction of the oxygen octahedra favors the occupation of the d$_{xy}$ orbital of the titanium ion[82, 122, 123]. X-ray absorption spectroscopy indeed finds that these orbitals are the first to be occupied on the formation of the conducting state[124]. More careful calculations actually show a orbital-ordered situation where the partially-filled d$_{xy}$ orbital shows a checkerboard pattern[121].

These energy differences between the different 3d orbitals of titanium also gives a clue as to why an electron density much lower than half an electron per unit cell

area is observed. It can be argued that the lowest-lying bands are two-dimensional in nature due to their d_{xy} origin and are Anderson localized due to disorder. Higher-lying orbitals, though not as densely populated, may not be localized and thus contribute to the conduction[112]. It is this electron population that is measured in Hall measurements. This is still considered an interface effect, as all electrons are still confined within 4 monolayers of STO from the interface. Indeed, the actual crystal distortions extend to a similar length[93, 125].

Aside from the LAO/STO system, there are only two other polar/non-polar systems that have been investigated: $KTaO_3$//STO[126] and LVO//STO[127]. Both show remarkably similar behaviour to the LAO/STO system. $KTaO_3$ (KTO) is very similar having an thermally-activated electron density with a low-temperature value of $2 \cdot 10^{13}$ cm^{-2} identical to that in LAO/STO. The mobility follows that of LAO/STO with a low-temperature value of about 3000 cm^2/Vs. This is especially intriguing, as the formal charge of the ion layers in $KTaO_3$ is reversed compared to LAO: $(KO)^-$ and $(TaO_2)^+$ vs. $(LaO)^+$ and $(AlO_2)^-$. Thus one would assume hole doping at the KO/TiO_2 interface, while electron doping is observed from Hall measurements. In addition, theoretical calculations predict that superlattices of $KTaO_3$ and STO are insulating at least up to 30 monolayers of $KNbO_3$ and STO[128]. However, the difficulty of growing a potassium-containing film is well known[129], so off-stoichiometry may play an important role here. LVO is slightly different as now both materials can be multivalent ($Ti^{3+/4+}$ and $V^{4+/3+}$), but it exhibits a critical thickness of about 5 monolayers similar to 4 monolayers in LAO/STO.

An interesting variation of materials is the inclusion of a doped STO interlayer between the STO substrate and the LAO film[130]. The inclusion of any such a layer lowers the electron density, even an undoped high-pressure grown film of STO. The effect of the dopants on the electron mobility varies, however. While no doping leaves the mobility constant, doping with cobalt lower the mobility, while doping with manganese increases the mobility for a few layers. The difference may well be the ion configuration of the two transition metals, Mn^{4+} ($3d^3$) and Co^{3+} ($3d^6$) respectively, compared to that of the host Ti^{4+} ($3d^0$). The less positive cobalt ion is probably a larger scatterer than the conformal manganese ion. In the manganese doped system, the extra electrons in the 3d band may be able to screen nearby scatterers, thus slightly increasing the mobility. This effect, however, will be smaller than the full -1 charge difference that leads to extra scattering with the Co^{3+}. In either case, the sensitivity of the transport properties to the $\sim$5 monolayer thick interlayers shows that the electron layer is confined to that thin layer as well.

2.5.2   Oxygen vacancy dependence

A prominent part of the scientific discussion on the LAO//STO interface was - and is - the influence of oxygen vacancies on the conductivity. At the typical growth temperatures for LAO of about 800 °C the time needed for an oxygen

vacancy to diffuse through a STO crystal a millimeter thick is about 5 minutes[131]. An experiment on STO shows how the migration of oxygen vacancies changes the surface Ti valency purely by an applied external electric field[132]. Fields of $10 \cdot 10^6$ V/m may be easily obtained at the LAO//STO interface, which are larger than the $1 \cdot 10^6$ V/m fields used in field-effect structures. This indicates that the vacancy concentration and the conduction electron density are closely linked. Already in the original paper it was noted that the electron density derived from Hall measurements varied greatly as a function of the oxygen pressure during the deposition of the LAO film[72]. At low pressures electron density values of about 200 electrons per unit cell area were obtained, far from the half an electron from the ionic model. Given the ease with which oxygen vacancies are introduced in STO care must be taken to distinguish between a 3D vacancy-driven state and the much more interesting 2D interface state.
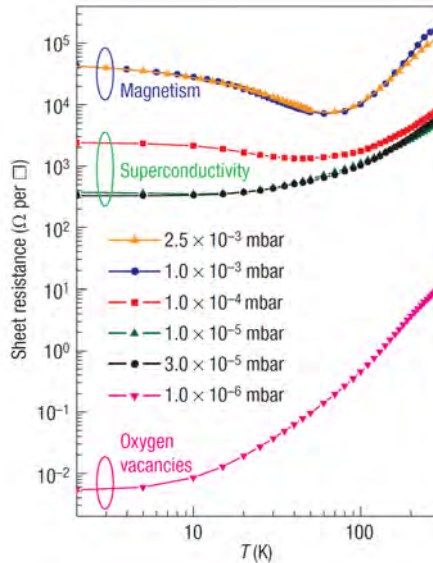
Figure 2.15: Sheet resistance as a function of temperature for LAO//STO interfaces grown in different pressures. Graph taken from Ref. [133].

Perhaps a good starting point to discuss the various effects of oxygen vacancies on the system is Figure 2.15[133]. It can clearly be seen that with increasing the oxygen pressure during the deposition of the LAO layer the sheet resistance increases. There is a large jump on going from $1 \cdot 10^{-6}$ mbar O_2 to $3 \cdot 10^{-5}$ mbar O_2. Then upon further increasing the pressure the system reaches a state where a 'normal' interface conducting state, a superconducting state or a magnetically-active state can be present due to factors other than oxygen contents.

When all transport data at room temperature and low temperature (300 K resp. $\sim$5 K) from literature is compared, a similar trend shows[5]. Below $1 \cdot 10^{-5}$ mbar

---
[5]See for example Brinkman[99] and Kalabukhov[107].

the electron density varies wildly, while above that pressure the electron density is about $21\pm7\cdot10^{13}$ cm^{-2} at room temperature and $4.9\pm2.5\cdot10^{13}$ cm^{-2} at 5 K. Or equivalently about 0.32 and 0.07 electron per unit cell area. The electron mobility also evolves with the deposition pressure, but more slowly. A power law dependence $\mu \propto n^{-x}$ like in doped STO[134] fits the data quite well, though with an exponent of $x = 1.0\pm0.1$ compared to $x = 0.75\pm0.03$ for doped STO. But this difference may be due to the difference between 3D conduction in the bulk STO compared to 2D conduction in the LAO/STO system.

Grown at low pressure ($\sim1\cdot10^{-6}$ mbar O$_2$) the main contribution to the conduction is due to oxygen vacancies. Samples grown at this pressure exhibit Shubnikov-de Haas oscillations[98] and blue light luminescence[109] similar to doped STO[115, 135]. Distinguishing between the vacancy-dominated regime and the interface-related regime is very difficult: EELS measurements clearly show the presence of Ti^{3+} for samples at both $1\cdot10^{-6}$ and $1\cdot10^{-3}$ mbar O$_2$[123, 136], but it is difficult to explain the 4 orders of magnitude difference in the sheet resistance from the observed Ti^{3+} signal. EELS, though, has a low sensitivity and contributions from oxygen vacancy levels below 1 % are still significant[137]. Transport properties for low-pressure grown samples are also very similar to doped STO; the electron mobility dependence on temperature for interfaces, doped and reduced STO are nearly the same[98] and the interfaces show no dependence on LAO thickness[102]. The oxygen vacancies are thought to diffuse throughout the entire STO substrate during deposition[98], though post-annealing with atomic oxygen greatly reduces the vacancy concentration and thus the electron density to a value of about $1.3\cdot10^{13}$ cm^{-2}[101]. This change from conduction throughout the crystal to conduction at the interface was also observed with conducting-tip AFM where the resistance as a function of position was mapped across a LAO//STO interface grown at $1\cdot10^{-6}$ mbar both as-grown and post-annealed[110]. Figure 2.16 shows the resistance along a line perpendicular to the interface for both cases.
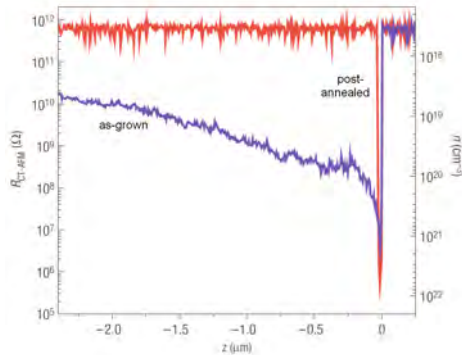

Figure 2.16: Resistance and equivalent carrier density profiles for the as-grown (blue) and post-annealed (red) interfaces. Graph taken from Ref. [110].

It can clearly be seen how the as-grown low-pressure interface has a wide area with lower resistance. In fact, the entire STO substrate has a reduced resistance, even 500 μm away from the interface; which is about the bottom of the substrate. For the post-annealed interface, the resistance quickly returns to its maximum value. So, for post-annealed or high-pressure grown interfaces the conducting electrons are confined to an area about 10 nm from the interface[110, 113, 138, 139]. Interestingly enough, the confinement holds at low temperatures, despite huge increase in the dielectric constant of STO[140]. The electric field close to the interface reduces the dielectric constant so much that at 5 K the electrons are still confined within an area about 20 nm thick. This is close to the Fermi wavelength of 16 nm[138] and smaller than the cyclotron radius (Equation 2.8), indicating quasi-2D behaviour.

Comparing the mobilities for samples grown at different pressures, the mobility decreases with increasing deposition pressure[99]. This is an interesting observation, as in general the assumption would be that for increasing pressure, there are less oxygen vacancies that can scatter the mobile electrons. A similar trend was observed for the film-thickness-dependence where the mobility decreases with increasing thickness[84]. In this last case the electron density also decreases with thicker layers, again suggesting that the mobility is lower for a system with less vacancies. No explanation for either trend has been given, though it may be related to the spatial distribution of the electrons. It was shown that an external field can drastically change the Hall mobility by almost an order of magnitude[141]. For high negative gate voltages the electrons are pulled close to the interface, where they are scattered by interface defects. In addition, their closer proximity increases the local internal electric field and lowers the dielectric constant[138]. This decreases the screening of defects and compounds the reduction of the mobility.

For samples grown at higher pressures several different ground states have been observed. Figure 2.15 already shows a superconducting and a magnetic state. Above 70 K most of the behaviour described in the previous section applies: the Fermi-liquid description, the critical LAO thickness, the coupling between interfaces, etcetera. Below that 70 K there are systems that develop towards a superconducting state with a critical temperature of $\sim$200 mK and a critical current of $\sim$95 μA/cm[142]. The two-dimensional nature of the superconducting electron gas gives a close upper limit on the electron distribution of about 10 nm, which was confirmed by measuring the critical magnetic field in different directions[143]. Combining this work with earlier work on a back-gate field-effect transistor it was possible to obtain an electronic phase diagram of the superconducting state, yielding the onset of superconductivity starting from an electron density of about $2.9 \cdot 10^{13}$ cm^{-2} to a maximum critical temperature of 300 mK at an electron density of $5.7 \cdot 10^{13}$ cm^{-2}[90, 139, 141]. This two-dimensional superconducting transition has been described in the Beresinkii-Kosterlitz-Thouless framework[90, 142]. The broadening of the superconducting transition below T_c has been attributed to finite-size effects[139] or inhomogeneities[144]. On the other hand, a magnetic signature, possibly from Kondo scattering, was found at interfaces grown at a slightly higher pressure compared to the superconducting samples[99]. The effective crossover temperature from electron-electron scattering to Kondo scattering

is around 70 K; the sheet resistance starts to visually deviate at 50 K. The susceptibility as obtained from the magnetoresistance curve follows the Curie-Weiss law, from which an antiferromagnetic coupling energy of 40 μeV was obtained.

Now this seems to be a dichotomy, as superconductivity and magnetism are almost mutually exclusive. A simple way of looking at it, is that the electrons of the basic Cooper pairs in superconductivity have opposite spin. Any magnetic material will have a preferred spin direction, thus breaking the Cooper pairs and preventing superconductivity. Reconciling these two states in a single system is something that is still a topic of research. One possible explanation is that the electron doping of the interface is actually a compound process. It includes contributions from oxygen vacancies, doping through an external field effect and interface reconstruction[145]. Together, these three can create a phase diagram that spans all the observed properties. Separating out the different contributions is going to be one of the challenges in understanding the LAO/STO system. This is further convoluted by the fact that oxygen vacancies not only influence the electron density, but also the dielectric constant[146]. This greatly influences the spread of the electrons into the STO, so that for samples with similar 2D electron *sheet* densities the local 3D electron density at the interface can be different. As a result, the 3D electron density can cross the critical density for superconductivity[147] in one sample but not in another, despite their apparent similar 2D electron sheet densities.

Not only internal processes play a role. The surface preparation is just as important. Every interface will have steps in it due to the miscut from the perfect crystal plane of the perovskite block. It was observed that depending on the orientation of the current path with respect to these step edges, the sheet resistance changes for some samples[148, 149]. Parallel to the step edges, so over the terraces, the sheet resistance is lowest, while perpendicular the steps - across them - the sheet resistance is highest. These step edges form 'defects' in the conducting state, most likely due to the residual SrO at these edges[97]. Magnetoresistance measurements further corroborate this, as the rough periodicity between the step edges gives rise to an oscillating signal in the resistance as a function of the magnetic field[150]. Inducing artificial dislocations by using STO bicrystals as substrates shows clearly how these defects affect the conducting state[149]. An area of about 5 nm across is depleted of conduction electrons for each dislocation. This all shows how careful fabrication, both in the preparation of the materials and during the growth itself, is necessary to distinguish between all the different factors involved.

2.6   Concluding remarks

Creating two-dimensional electron layers - or even quantum wells - in correlated-electron materials is a challenging and exciting undertaking. Starting from simple concepts and examples in semiconductor physics, the definitions and possible confinement strategies are easy to discuss. The free-electron approximation makes it easy to discuss the 'particle-in-a-box' scheme, as well as the band picture. Extend-

ing the simple Schrödinger equation to electron-electron interaction leads the way to the discussion of correlated-electron materials with as their primary example the perovskite transition metal oxides. The inclusion of electron correlation opens up a wide variety of properties, which at the same time are highly useful and deviously complex.

Extending the semiconductor picture of electron layers to correlated-electron materials is not easily done, but advances in the last decade in both control of the growth (through substrate preparation and deposition manipulation) and *in situ* monitoring are now allowing the fabrication of well-defined interfaces, heterostructures and multilayers. The material systems that attract the most attention are the LTO/STO and LAO/STO systems. The common ground for using STO is the extensive knowledge base for this material. Indeed, as it turns out, a lot of the knowledge obtained for doped STO is almost directly applicable to these systems. But the differences are very exciting.

The confinement of the electron layer close to the dopant film (either the Mott insulator LTO or the band insulator LAO) leads to specific crystal and electronic reconstructions not present in bulk doped STO. Two-dimensional orbital ordering may lead to magnetic order as well, a new feature. Further confinement might lead to more strongly correlated electrons which would be of great interest to theorists as a model system for simpler, two-dimensional models. More application-oriented, field-effect tuning of this interface electron layer has been demonstrated. Changing the electron density of such interfaces by bringing another interface or surface close by allows for a wider variety of possible applications and perhaps even a surface-sensitive detection technique.

The research so far has yielded much information on many interesting properties, but there is still more interesting things to discover. The further confinement of the electrons within these materials, the interaction perpendicular to the interface, the anisotropy of the conducting state and the oxygen-dependence are some examples that make the research of these systems such a lively field.

2.7   References

[1] "Moore's law." http://en.wikipedia.org/wiki/Moore's_law (04-16-2008).

[2] S. Gasiorowicz, *Quantum physics*. Wiley (New York), 2nd ed., 1996.

[3] D. J. Griffiths, *Introduction to quantum mechanics*. Upper Saddle River, NJ: Pearson Prentice Hall, 2nd ed., 2005.

[4] T. Ando, Y. Matsumoto, and Y. Uemura, "Theory of Hall effect in a two-dimensional electron system," *Journal of the Physical Society of Japan*, vol. 39, pp. 279–288, 1975.

[5] J. Faist, F. Capasso, D. L. Sivco, C. Sirtori, A. L. Hutchinson, and A. Y. Cho, "Quantum cascade laser," *Science*, vol. 264, pp. 553—-556, 1994.

[6] G. Koster, B. L. Kropman, A. J. H. M. Rijnders, D. H. A. Blank, and H. Rogalla, "Quasi-ideal strontium titanate crystal surfaces through formation of strontium hydroxide," *Applied Physics Letters*, vol. 73, pp. 2920–2922, 1998.

[7] A. J. H. M. Rijnders, G. Koster, D. H. A. Blank, and H. Rogalla, "In-situ growth monitoring during PLD of oxides using RHEED at high oxygen pressure," *Materials Science and Engineering: B*, vol. 56, pp. 223–227, 1998.

[8] H. Koinuma, N. Kanda, J. Nishino, A. Ohtomo, H. Kubota, M. Kawasaki, and M. Yoshimoto, "Laser MBE of ceramic thin films for future electronics," *Applied Surface Science*, vol. 109-110, pp. 514–519, 1997.

[9] H. N. Lee, H. M. Christen, M. F. Chisholm, C. M. Rouleau, and D. H. Lowndes, "Strong polarization enhancement in asymmetric three-component ferroelectric superlattices," *Nature*, vol. 433, pp. 395–399, 2005.

[10] D. A. Muller, N. Nakagawa, A. Ohtomo, J. L. Grazul, and H. Y. Hwang, "Atomic-scale imaging of nanoengineered oxygen vacancy profiles in $SrTiO_3$," *Nature*, vol. 430, pp. 657–661, 2004.

[11] J. H. Haeni, P. Irvin, W. Chang, R. Uecker, P. Reiche, Y. L. Li, S. Choudhury, W. Tian, M. E. Hawley, B. Craigo, A. K. Tagantsev, X. Q. Pan, S. K. Streiffer, L. Q. Chen, S. W. Kirchoefer, J. Levy, and D. G. Schlom, "Room-temperature ferroelectricity in strained $SrTiO_3$," *Nature*, vol. 430, pp. 758–761, 2004.

[12] "Particle in a box." http://hyperphysics.phy-astr.gsu.edu/hbase/quantum/pbox.html (05-13-2008).

[13] "Band theory of solids." http://hyperphysics.phy-astr.gsu.edu/hbase/solids/band.html (05-13-2008).

[14] F. J. Morin and J. P. Maita, "Electrical properties of silicon containing arsenic and boron," *Physical Review*, vol. 96, pp. 28–35, 1954.

[15] G. E. Stillman, C. M. Wolfe, and J. O. Dimmock, "Hall coefficient factor for polar mode scattering in n-type GaAs," *Journal of Physics and Chemistry of Solids*, vol. 31, pp. 1199–1204, 1970.

[16] O. N. Tufte and P. W. Chapman, "Electron mobility in semiconducting strontium titanate," *Physical Review*, vol. 155, pp. 796–802, 1967.

[17] E. F. Schubert, "Room temperature properties of semiconductors: IIIV arsenides." http://www.rpi.edu/s̃chubert/Educational-resources/Materials-Semiconductors-III-V-arsenides.pdf (22−06-2009).

[18] U. R. O. Madelung and M. Schulz, eds., *Group IV Elements, IV-IV and III-V Compounds. Part b - Electronic, Transport, Optical and Other Properties*, vol. 41A1b of *Landolt-Brnstein - Group III Condensed Matter*, ch. Aluminum arsenide (AlAs), electrical and thermal conductivity, carrier concentration, pp. 1–2. Springer-Verlag, 2002.

[19] E. F. Schubert, "Quantum mechanics applied to semiconductor devices - Ch 16 High doping effects." http://www.ecse.rpi.edu/ schubert/Course-ECSE-6968 Quantum mechanics/Ch16 High doping effects.pdf (23-04-2008), 2004.

[20] N. W. Ashcroft and N. D. Mermin, *Solid state physics.* Philadelphia: Saunders College Publishing, 1976.

[21] C. Kittel, *Introduction to solid state physics.* Hoboken, NJ: Wiley, 8th ed., 2005.

[22] H. Nakamura, H. Tomita, H. Akimoto, R. Matsumura, I. H. Inoue, T. Hasegawa, K. Kono, Y. Tokura, and H. Takagi, "Tuning of metal-insulator transition of quasi-two-dimensional electrons at parylene/$SrTiO_3$ interface by electric field," *Journal of the Physical Society of Japan*, vol. 78, p. 083713, 2009.

[23] "High electron mobility transistor." http://en.wikipedia.org/wiki/HEMT (07-07-2008).

[24] P. Hadley, "The nanoscale and quantum mechanics." http://lamp.tu-graz.ac.at/ hadley/nanoscience/week2/2.html (05-14-2008).

[25] M. Dahan, S. Levi, C. Luccardini, P. Rostaing, B. Riveau, and A. Triller, "Diffusion dynamics of glycine receptors revealed by single-quantum dot tracking," *Science*, vol. 302, pp. 442–445, 2003.

[26] B. Ballou, C. Lagerholm, L. A. Ernst, M. P. Bruchez, and A. S. Waggoner, "Noninvasive imaging of quantum dots in mice," *Bioconjugate Chemistry*, vol. 15, pp. 79–86, 2004.

[27] "Quantum dot." http://en.wikipedia.org/wiki/Quantum_dot (07-07-2008).

[28] J. L. Cohn, C. Chiorescu, and J. J. Neumeier, "Polaron transport in the paramagnetic phase of electron-doped manganites," *Physical Review B*, vol. 72, p. 024422, 2005.

[29] J. L. Cohn, M. Peterca, and J. J. Neumeier, "Low-temperature permittivity of insulating perovskite manganites," *Physical Review B*, vol. 70, p. 214433, 2004.

[30] P. Lunkenheimer, T. Rudolf, J. Hemberger, A. Pimenov, S. Tachos, F. Lichtenberg, and A. Loidl, "Dielectric properties and dynamical conductivity of $LaTiO_3$: from DC to optical frequencies," *Physical Review B*, vol. 68, p. 245108, 2003.

[31] Y. Fujishima, Y. Tokura, T. Arima, and S. Uchida, "Optical-conductivity spectra of $Sr_{1-x}La_xTiO_3$: filling-dependent effect of the electron correlation," *Physical Review B*, vol. 46, pp. 11167–11170, 1992.

[32] A. T. Fiory, A. F. Hebard, R. H. Eick, P. M. Mankiewich, R. E. Howard, and M. L. Oḿalley, "Metallic and superconducting surfaces of $YBa_2Cu_3O_7$ probed by electrostatic charge modulation of epitaxial-films," *Physical Review Letters*, vol. 65, pp. 3441–3444, 1990.

[33] L. R. Testardi, W. G. Moulton, H. Mathias, H. K. Ng, and C. M. Rey, "Large static dielectric constant in the high-temperature phase of polycrystalline $YBa_2Cu_3O_x$," *Physical Review B*, vol. 37, pp. 2324–2325, 1988.

[34] E. Dagotto, "Complexity in strongly correlated electronic systems," *Science*, vol. 309, pp. 257–262, 2005.

[35] Y. Tokura and N. Nagaosa, "Orbital physics in transition-metal oxides," *Science*, vol. 288, pp. 462–468, 2000.

[36] M. K. Wu, J. R. Ashburn, C. J. Torng, P. H. Hor, R. L. Meng, L. Gao, Z. J. Huang, Y. Q. Wang, and C. W. Chu, "Superconductivity at 93 K in a new mixed-phase Y-Ba-Cu-O compound system at ambient pressure," *Physical Review Letters*, vol. 58, pp. 908–910, 1987.

[37] Y. Okada, T. Arima, Y. Tokura, C. Murayama, and N. Mori, "Doping- and pressure-induced change of electrical and magnetic properties in the Mott-Hubbard insulator $LaTiO_3$," *Physical Review B*, vol. 48, pp. 9677–9883, 1993.

[38] Y. Tokura, Y. Tomioka, H. Kuwahara, A. Asamitsu, Y. Moritomo, and M. Kasai, "Origins of colossal magnetoresistance in perovskite-type manganese oxides," *Journal of Applied Physics*, vol. 79, pp. 5288–5291, 1996.

[39] M. P. Warusawithana, C. Cen, C. R. Sleasman, J. C. Woicik, Y. Li, L. F. Kourkoutis, J. A. Klug, H. Li, P. Ryan, L.-P. Wang, M. Bedzyk, D. A. Muller, L.-Q. Chen, J. Levy, and D. G. Schlom, "A ferroelectric oxide made directly on silicon," *Science*, vol. 324, pp. 367–370, 2009.

[40] S. Zemni, J. Dhahri, K. Cherif, J. Dhahri, M. Oummezzine, M. Ghedira, and H. Vincent, "The effect of a cation radii on structural, magnetic and electrical properties of doped manganites $La_{0.6-x}Pr_xSr_{0.4}MnO_3$," *Journal of Solid State Chemistry*, vol. 177, pp. 2387–2393, 2004.

[41] M. Karplus and R. N. Porter, *Atoms & molecules: An introduction for students of physical chemistry*. Menlo Park, CA: Benjamin/Cummings, 1970.

[42] "Superaustausch im oxygenierten Hr-Zentrum im Orbitalschema." http://www.cup.uni-muenchen.de/ac/kluefers/homepage/L/BAC/L_bac_Hr_superexchange.html (14-01-2009).

[43] D. Dickerscheid, "Welcome to the Quantum Fluids and Solids Group." http://www.phys.uu.nl/ stoof/new_page_1.htm (14-01-2009).

[44] N. F. Mott, *Metal-insulator transitions*. London: Taylor and Francis, 1974.

[45] P. P. Edwards and M. J. Sienko, "Universality aspects of the metal-nonmetal transition in condensed media," *Physical Review B*, vol. 17, pp. 2575–2581, 1978.

[46] C. H. Ahn, J. M. Triscone, and J. Mannhart, "Electric field effect in correlated oxide systems," *Nature*, vol. 424, pp. 1015–1018, 2003.

[47] A. Cho, "High T_c: The mystery that defies solution," *Science*, vol. 314, pp. 1072–1075, 2006.

[48] A. Ohtomo, D. A. Muller, J. L. Grazul, and H. Y. Hwang, "Artificial charge-modulation in atomic-scale perovskite titanate superlattices," *Nature*, vol. 419, pp. 378–380, 2002.

[49] K. Shibuya, T. Ohnishi, M. Kawasaki, H. Koinuma, and M. Lippmaa, "Metallic $LaTiO_3/SrTiO_3$ superlattice films on the $SrTiO_3(100)$ surface," *Japanese Journal of Applied Physics*, vol. 43, pp. L1178–L1180, 2004.

[50] M. Takizawa, H. Wadati, K. Tanaka, M. Hashimoto, T. Yoshida, A. Fujimori, A. Chikamatsu, H. Kumigashira, M. Oshima, K. Shibuya, T. Mihara, T. Ohnishi, M. Lippmaa, M. Kawasaki, H. Koinuma, S. Okamoto, and A. J. Millis, "Photoemission from buried interface in $SrTiO_3/LaTiO_3$ superlattices," *Physical Review Letters*, vol. 97, p. 057601, 2006.

[51] S. S. A. Seo, W. S. Choi, H. N. Lee, L. Yu, K. W. Kim, C. Bernhard, and T. W. Noh, "Optical study of the free-carrier response of LaTiO$_3$/SrTiO$_3$ superlattices," *Physical Review Letters*, vol. 99, p. 266801, 2007.

[52] W. Siemons, *Nanoscale properties of complex oxide films*. PhD thesis, University of Twente, 2008.

[53] W. C. Sheets, Ph. Boullay, U. Lders, B. Mercey, and W. Prellier, "Artificial charge modulation in perovskite vanadate superlattices," *Thin Solid Films*, vol. 517, pp. 5130–5133, 2009.

[54] S. Okamoto and A. J. Millis, "Theory of Mott insulator-band insulator heterostructures," *Physical Review B*, vol. 70, p. 075101, 2004.

[55] S. Thulasi and S. Satpathy, "Jellium model of the two-dimensional Airy electron gas at the perovskite titanate interface," *Physical Review B*, vol. 73, p. 125307, 2006.

[56] Z. S. Popović and S. Satpathy, "Wedge-shaped potential and Airy-function electron localization in oxide superlattices," *Physical Review Letters*, vol. 94, p. 176805, 2005.

[57] S. Okamoto, A. J. Millis, and N. A. Spaldin, "Lattice relaxation in oxide heterostructures: LaTiO$_3$/SrTiO$_3$ superlattices," *Physical Review Letters*, vol. 97, p. 056802, 2006.

[58] P. Larson, Z. S. Popović, and S. Satpathy, "Lattice relaxation effects on the interface electron states in the perovskite oxide heterostructures: LaTiO$_3$ monolayer embedded in SrTiO$_3$," *Physical Review B*, vol. 77, p. 245122, 2008.

[59] R. Pentcheva and W. E. Pickett, "Correlation-driven charge order at the interface between a Mott and a band insulator," *Physical Review Letters*, vol. 99, p. 016802, 2007.

[60] H. M. Christen, J. Mannhart, E. J. Williams, and C. Gerber, "Dielectric properties of sputtered SrTiO$_3$ films," *Physical Review B*, vol. 49, p. 012095, 1994.

[61] Y. Hotta, H. Wadati, A. Fujimori, T. Susaki, and H. Y. Hwang, "Electronic structure of the Mott insulator LaVO$_3$ in a quantum well geometry," *Applied Physics Letters*, vol. 89, p. 251916, 2006.

[62] H. Wadati, Y. Hotta, A. Fujimori, T. Susaki, H. Y. Hwang, Y. Takata, K. Horiba, M. Matsunami, S. Shin, M. Yabashi, K. Tamasaku, Y. Nishino, and T. Ishikawa, "Hard x-ray photoemission study of LaAlO$_3$/LaVO$_3$ multilayers," *Physical Review B*, vol. 77, p. 045122, 2008.

[63] M. Takizawa, Y. Hotta, T. Susaki, Y. Ishida, H. Wadati, Y. Takata, K. Horiba, M. Matsunami, S. Shin, M. Yabashi, K. Tamasaku, N. Nishino, T. Ishikawa, A. Fujimori, and H. Y. Hwang, "Spectroscopic evidence for competing reconstructions in polar multilayers LaAlO$_3$/LaVO$_3$/LaAlO$_3$," *Physical Review Letters*, vol. 102, p. 236401, 2009.

[64] H. Wadati, D. G. Hawthorn, J. Geck, T. Z. Regier, R. I. R. Blyth, T. Higuchi, Y. Hotta, Y. Hikita, H. Y. Hwang, and G. A. Sawatzky, "Interface reconstruction in V-oxide heterostructures determined by X-ray absorption spectroscopy," *Applied Physics Letters*, vol. 95, p. 023115, 2009.

[65] T. Higuchi, Y. Hotta, T. Susaki, A. Fujimori, and H. Y. Hwang, "Modulation doping of a Mott quantum well by a proximate polar discontinuity," *Physical Review B*, vol. 79, p. 075415, 2009.

[66] B. C. Russell and M. R. Castell, "Reconstructions on the polar SrTiO$_3$(110) surface: Analysis using STM, LEED, and AES," *Physical Review B*, vol. 77, p. 245414, 2008.

[67] R. J. Francis, S. C. Moss, and A. J. Jacobson, "X-ray truncation rod analysis of the reversible temperature-dependent [001] surface structure of LaAlO$_3$," *Physical Review B*, vol. 64, p. 235425, 2001.

[68] W. A. Harrison, E. A. Kraut, J. R. Waldrop, and R. W. Grant, "Polar heterojunction interfaces," *Physical Review B*, vol. 18, pp. 4402–4410, 1978.

[69] J. Lu, M. V. S. Chandrashekhar, J. J. Parks, D. C. Ralph, and M. G. Spencer, "Quantum confinement and coherence in a two-dimensional electron gas in a carbon-face 3C-SiC/6H-SiC polytype heterostructure," *Applied Physics Letters*, vol. 94, p. 162115, 2009.

[70] J. Seidel, L. W. Martin, Q. He, Q. Zhan, Y. H. Chu, A. Rother, M. E. Hawkridge, P. Maksymovych, P. Yu, M. Gajek, N. Balke, S. V. Kalinin, S. Gemming, F. Wang, G. Catalan, J. F. Scott, N. A. Spaldin, J. Orenstein, and R. Ramesh, "Conduction at domain walls in oxide multiferroics," *Nature Materials*, vol. 8, pp. 229–234, 2009.

[71] M. S. Park, J.-H. Song, and A. J. Freeman, "Charge imbalance and magnetic properties at the Fe_3O_4/$BaTiO_3$ interface," *Physical Review B*, vol. 79, p. 024420, 2009.

[72] A. Ohtomo and H. Y. Hwang, "A high-mobility electron gas at the $LaAlO_3$/$SrTiO_3$ heterointerface," *Nature*, vol. 427, pp. 423–426, 2004.

[73] N. Nakagawa, H. Y. Hwang, and D. A. Muller, "Why some interfaces cannot be sharp," *Nature Materials*, vol. 5, pp. 204–209, 2006.

[74] M. S. Park, S. H. Rhim, and A. J. Freeman, "Charge compensation and mixed valency in $LaAlO_3$/$SrTiO_3$ heterointerfaces studied by the FLAPW method," *Physical Review B*, vol. 74, p. 205416, 2006.

[75] R. Pentcheva and W. E. Pickett, "Ionic relaxation contribution to the electronic reconstruction at the n-type $LaAlO_3$/$SrTiO_3$ interface," *Physical Review B*, vol. 78, p. 205106, 2008.

[76] N. Pavlenko and T. Kopp, "Structural relaxation and metal-insulator transition at the interface between $SrTiO_3$ and $LaAlO_3$." cond-mat/0901.4610, 2009.

[77] H. Chen, A. M. Kolpak, and S. Ismail Beigi, "Fundamental asymmetry in interfacial electronic reconstruction between insulating oxides: An ab initio study," *Physical Review B*, vol. 79, p. 161402, 2009.

[78] Y. Li and J. Yu, "Polarization screening and induced carrier density at the interface of $LaAlO_3$ overlayer on $SrTiO_3(001)$." cond-mat/0904.1636, 2009.

[79] W.-J. Son, E. Cho, B. Lee, J. Lee, and S. Han, "Density and spatial distribution of charge carriers in the intrinsic n-type $LaAlO_3$-$SrTiO_3$ interface," *Physical Review B*, vol. 79, p. 245411, 2009.

[80] N. C. Bristowe, E. Artacho, and P. B. Littlewood, "Oxide superlattices with alternating p and n interfaces," *Physical Review B*, vol. 80, p. 045425, 2009.

[81] K. Janicka, J. P. Velev, and E. Y. Tsymbal, "Quantum nature of two-dimensional electron gas confinement at $LaAlO_3$/$SrTiO_3$ interfaces," *Physical Review Letters*, vol. 102, p. 106803, 2009.

[82] J. Lee and A. A. Demkov, "Charge origin and localization at the n-type $SrTiO_3$/$LaAlO_3$ interface," *Physical Review B*, vol. 78, p. 193104, 2008.

[83] M. Huijben, G. Rijnders, D. H. A. Blank, S. Bals, S. van Aert, J. Verbeeck, G. van Tendeloo, A. Brinkman, and H. Hilgenkamp, "Electronically coupled complementary interfaces between perovskite band insulators," *Nature Materials*, vol. 5, pp. 556–560, 2006.

[84] C. Bell, S. Harashima, Y. Hikita, and H. Y. Hwang, "Thickness dependence of the mobility at the $LaAlO_3$/$SrTiO_3$ interface," *Applied Physics Letters*, vol. 94, p. 222111, 2009.

[85] S. Thiel, G. Hammerl, A. Schmehl, C. W. Schneider, and J. Mannhart, "Tunable quasi-two-dimensional electron gases in oxide heterostructures," *Science*, vol. 313, pp. 1942–1945, 2006.

[86] A. Savoia, D. Paparo, P. Perna, Z. Ristic, M. Salluzzo, F. Miletto Granozio, U. Scotti di Uccio, C. Richter, S. Thiel, J. Mannhart, and L. Marrucci, "Polar catastrophe and electronic reconstructions at the $LaAlO_3/SrTiO_3$ interface: evidence from optical second harmonic generation," *Physical Review B*, vol. 80, p. 075110, 2009.

[87] U. Schwingenschlögl and C. Schuster, "Interface relaxation and electrostatic charge depletion in the oxide heterostructure $LaAlO_3/SrTiO_3$," *Europhysics Letters*, vol. 86, p. 27005, 2009.

[88] R. Pentcheva and W. E. Pickett, "Avoiding the polarization catastrophe in $LaAlO_3$ overlayers on $SrTiO_3(001)$ through a polar distortion," *Physical Review Letters*, vol. 102, p. 107602, 2009.

[89] C. W. Schneider, S. Thiel, G. Hammerl, C. Richter, and J. Mannhart, "Microlithography of electron gases formed at interfaces in oxide heterostructures," *Applied Physics Letters*, vol. 89, p. 122101, 2006.

[90] A. D. Caviglia, S. Gariglio, N. Reyren, D. Jaccard, T. Schneider, M. Gabay, S. Thiel, G. Hammerl, J. Mannhart, and J. M. Triscone, "Electric field control of the $LaAlO_3/SrTiO_3$ interface ground state," *Nature*, vol. 456, pp. 624–627, 2008.

[91] C. Cen, S. Thiel, G. Hammerl, C. W. Schneider, K. E. Andersen, C. S. Hellberg, J. Mannhart, and J. Levy, "Nanoscale control of an interfacial metal-insulator transition at room temperature," *Nature Materials*, vol. 7, pp. 298–302, 2008.

[92] C. Cen, S. Thiel, J. Mannhart, and J. Levy, "Oxide nanoelectronics on demand," *Science*, vol. 323, pp. 1026–1030, 2009.

[93] N. Ogawa, K. Miyano, M. Hosoda, T. Higuchi, C. Bell, Y. Hikita, and H. Y. Hwang, "Enhanced lattice polarization in $SrTiO_3/LaAlO_3$ superlattices measured using optical second-harmonic generation," *Physical Review B*, vol. 80, p. 081106, 2009.

[94] R. Pentcheva, M. Huijben, K. Otte, W. E. Pickett, J. E. Kleibeuker, J. Huijben, H. Boschker, D. Kockmann, W. Siemons, G. Koster, H. J. W. Zandvliet, G. Rijnders, D. H. A. Blank, H. Hilgenkamp, and A. Brinkman, "Parallel electron-hole bilayer conductivity from electronic interface reconstruction," *Nature Physics*, p. *submitted*, 2009.

[95] A. Ohkubo, A. Ohtomo, J. Nishimura, T. Makino, Y. Segawa, and M. Kawasaki, "Combinatorial synthesis and optical characterization of alloy and superlattice films based on $SrTiO_3$ and $LaAlO_3$," *Applied Surface Science*, vol. 252, pp. 2488–2492, 2006.

[96] S. J. May, T. S. Santos, and A. Bhattacharya, "Onset of metallic behavior in strained $(LaNiO_3)_n/(SrMnO_3)_2$ superlattices," *Physical Review B*, vol. 79, p. 115127, 2009.

[97] J. Nishimura, A. Ohtomo, A. Ohkubo, Y. Murakami, and M. Kawasaki, "Controlled carrier generation at a polarity-discontinued perovskite heterointerface," *Japanese Journal of Applied Physics*, vol. 43, pp. L1032–L1034, 2004.

[98] G. Herranz, M. Basletić, M. Bibes, C. Carrétéro, E. Tafra, E. Jacquet, K. Bouzehouane, C. Deranlot, A. Hamzić, J. M. Broto, A. Barthélémy, and A. Fert, "High mobility in $LaAlO_3/SrTiO_3$ heterostructures: Origin, dimensionality, and perspectives," *Physical Review Letters*, vol. 98, p. 216803, 2007.

[99] A. Brinkman, M. Huijben, M. van Zalk, J. Huijben, U. Zeitler, J. C. Maan, W. G. van der Wiel, G. Rijnders, D. H. A. Blank, and H. Hilgenkamp, "Magnetic effects at the interface between nonmagnetic oxides," *Nature Materials*, vol. 6, pp. 493–496, 2007.

[100] M. Breitschaft, V. Tinkl, N. Pavlenko, S. Thiel, C. Richter, J. R. Kirtley, Y. C. Liao, G. Hammerl, V. Eyert, T. Kopp, and J. Mannhart, "Two-dimensional electron liquid state at $LaAlO_3$-$SrTiO_3$ interfaces." cond-mat/0907.1176, 2009.

[101] W. Siemons, G. Koster, H. Yamamoto, W. A. Harrison, G. Lucovsky, T. H. Geballe, D. H. A. Blank, and M. R. Beasley, "Origin of charge density at $LaAlO_3$ on $SrTiO_3$ heterointerfaces: possibility of intrinsic doping," *Physical Review Letters*, vol. 98, p. 196802, 2007.

[102] W. Siemons, G. Koster, H. Yamamoto, T. H. Geballe, D. H. A. Blank, and M. R. Beasley, "Experimental investigation of electronic properties of buried heterointerfaces of $LaAlO_3$ on $SrTiO_3$," *Physical Review B*, vol. 76, p. 155111, 2007.

[103] C. Merckling, M. El Kazzi, G. Delhaye, V. Favre Nicolin, Y. Robach, M. Gendry, G. Grenet, G. Saint Girons, and G. Hollinger, "Strain relaxation and critical thickness for epitaxial $LaAlO_3$ thin films grown on $SrTiO_3$(001) substrates by molecular beam epitaxy," *Journal of Crystal Growth*, vol. 306, pp. 47–51, 2007.

[104] A. Sheth, V. Lasrado, M. White, and M. P. Paranthaman, "Bench scale evaluation of batch mode dip-coating of sol-gel $LaAlO_3$ buffer material," *IEEE Transactions on Applied Superconductivity*, vol. 9, pp. 1514–1518, 1999.

[105] C. L. Jia, S. B. Mi, M. Faley, U. Poppe, J. Schubert, and K. Urban, "Oxygen octahedron reconstruction in the $SrTiO_3$/$LaAlO_3$ heterointerfaces investigated using aberration-corrected ultrahigh-resolution transmission electron microscopy," *Physical Review B*, vol. 79, p. 081405, 2009.

[106] M. El Kazzi, C. Merckling, G. Delhaye, L. Arzel, G. Grenet, E. Bergignat, and G. Hollinger, "Photoemission (XPS and XPD) study of epitaxial $LaAlO_3$ fiim grown on $SrTiO_3$(001)," *Materials Science in Semiconductor Processing*, vol. 9, pp. 954–958, 2006.

[107] A. Kalabukhov, R. Gunnarsson, J. Börjesson, E. Olsson, D. Winkler, and T. Claeson, "Effect of various deposition conditions on the electrical properties of LAO/STO hetero interfaces," *Journal of Physics: Conference Series*, vol. 100, p. 082039, 2008.

[108] P. R. Willmott, S. A. Pauli, R. Herger, C. M. Schlepütz, D. Martoccia, B. D. Patterson, B. Delley, R. Clarke, D. Kumah, C. Cionca, and Y. Yacoby, "Structural basis for the conducting interface between $LaAlO_3$ and $SrTiO_3$," *Physical Review Letters*, vol. 99, p. 155502, 2007.

[109] A. Kalabukhov, R. Gunnarsson, J. Börjesson, E. Olsson, T. Claeson, and D. Winkler, "Effect of oxygen vacancies in the $SrTiO_3$ substrate on the electrical properties of the $LaAlO_3$/$SrTiO_3$ interface," *Physical Review B*, vol. 75, p. 121404, 2007.

[110] M. Basletic, J. L. Maurice, C. Carrétéro, G. Herranz, O. Copie, M. Bibes, E. Jacquet, K. Bouzehouane, S. Fusil, and A. Barthélémy, "Mapping the spatial distribution of charge carriers in $LaAlO_3$/$SrTiO_3$ heterostructures," *Nature Materials*, vol. 7, pp. 621–625, 2008.

[111] F. J. Wong, M. Chi, R. V. Chopdekar, B. B. Nelson Cheeseman, N. D. Browning, and Y. Suzuki, "Potential barrier lowering and electrical transport at the $LaAlO_3$/$SrTiO_3$ heterointerface." cond-mat/0809.0926, 2008.

[112] Z. S. Popović, S. Satpathy, and R. M. Martin, "Origin of the two-dimensional electron gas carrier density at the $LaAlO_3$ on $SrTiO_3$ interface," *Physical Review Letters*, vol. 101, p. 256801, 2008.

[113] M. Sing, G. Berner, K. Goß, A. Müller, A. Ruff, A. Wetscherek, S. Thiel, J. Mannhart, S. A. Pauli, C. W. Schneider, P. R. Willmott, M. Gorgoi, F. Schäfers, and R. Claessen, "Profiling the interface electron gas of $LaAlO_3$/$SrTiO_3$ heterostructures with hard X-ray photoelectron spectroscopy," *Physical Review Letters*, vol. 102, p. 176805, 2009.

[114] A. Tsukazaki, A. Ohtomo, T. Kita, Y. Ohno, H. Ohno, and M. Kawasaki, "Quantum Hall effect in polar oxide heterostructures," *Science*, vol. 315, pp. 1388–1391, 2007.

[115] H. P. R. Frederikse, W. R. Hosler, W. R. Thruber, J. Babiskin, and P. G. Siebenmann, "Shubnikov-de Haas effect in $SrTiO_3$," *Physical Review*, vol. 158, pp. 775–778, 1967.

[116] J. L. Maurice, C. Carrétéro, M. J. Casanove, K. Bouzahouane, S. Guyard, E. Larquet, and J. P. Contour, "Electronic conductivity and structural distortion at the interface between insulators $SrTiO_3$ and $LaAlO_3$," *Physica Status Solidi A*, vol. 203, pp. 2209–2214, 2006.

[117] V. Vonk, M. Huijben, K. J. I. Driessen, P. Tinnemans, A. Brinkman, S. Harkema, and H. Graafsma, "Interface structure of $SrTiO_3/LaAlO_3$ at elevated temperatures studied in situ by synchrotron X-rays," *Physical Review B*, vol. 75, p. 235417, 2007.

[118] S. Gemming and G. Seifert, "$SrTiO_3(001)|LaAlO_3(001)$ multilayers: a density-functional investigation," *Acta Materialia*, vol. 54, pp. 4299–4306, 2006.

[119] U. Schwingenschlögl and C. Schuster, "Surface effects on oxide heterostructures," *Europhysics Letters*, vol. 81, p. 17007, 2008.

[120] J. D. Burton, J. P. Velev, and E. Y. Tsymbal, "Oxide tunnel junctions supporting a two-dimensional electron gas," *Physical Review B*, vol. 80, p. 115408, 2009.

[121] Z. Zhong and P. J. Kelly, "Electronic-structure-induced reconstruction and magnetic ordering at the $LaAlO_3|SrTiO_3$ interface," *Europhysics Letters*, vol. 84, p. 27001, 2008.

[122] R. Pentcheva and W. E. Pickett, "Charge localization or itineracy at $LaAlO_3/SrTiO_3$ interfaces: hole polarons, oxygen vacancies, and movile electrons," *Physical Review B*, vol. 74, p. 035112, 2006.

[123] J. L. Maurice, I. Devos, M. J. Casanove, C. Carrétéro, G. Gachet, G. Herranz, D. G. Crété, D. Imhoff, A. Barthélémy, M. Bibes, K. Bouzehouane, C. Deranlot, S. Fusil, E. Jacquet, B. Domengès, and D. Ballutaud, "Charge imbalance at oxide interfaces: How nature deals with it," *Materials Science and Engineering: B*, vol. 144, pp. 1–6, 2007.

[124] M. Salluzzo, G. Chiringhelli, J. C. Cezar, N. B. Brookes, V. Bisogni, G. M. d. Luca, C. Richter, S. Thiel, J. Mannhart, M. Huijben, A. Brinkman, and G. Rijnders, "Orbital reconstruction and the two-dimensional electron gas at the $LaAlO_3/SrTiO_3$ interface," *Physical Review Letters*, vol. 102, p. 166804, 2009.

[125] U. Schwingenschlögl and C. Schuster, "Exponential decay of relaxation effects at $LaAlO_3/SrTiO_3$ heterointerfaces," *Chemical Physics Letters*, vol. 467, pp. 354–357, 2009.

[126] A. Kalabukhov, R. Gunnarsson, T. Claeson, and D. Winkler, "Electrical transport properties of polar heterointerface between $KTaO_3$ and $SrTiO_3$." cond-mat/0704.1050, 2007.

[127] Y. Hotta, T. Susaki, and H. Y. Hwang, "Polar discontinuity doping of the $LaVO_3/SrTiO_3$ interface," *Physical Review Letters*, vol. 99, p. 236805, 2007.

[128] E. D. Murray and D. Vanderbilt, "Theoretical investigation of polarization-compensated II-IV/I-V perovskite superlattices," *Physical Review B*, vol. 79, p. 100102, 2009.

[129] H. M. Christen, L. A. Boatner, J. D. Budai, M. F. Chisholm, L. A. Géa, P. J. Marrero, and D. P. Norton, "The growth and properties of epitaxial $KNbO_3$ thin films and $KNbO_3/KTaO_3$ superlattices," *Applied Physics Letters*, vol. 68, pp. 1488–1490, 1996.

[130] T. Fix, J. L. MacManus Driscoll, and M. G. Blamire, "Delta-doped $LaAlO_3/SrTiO_3$ interfaces," *Applied Physics Letters*, vol. 94, p. 172101, 2009.

[131] P. Pasierb, S. Komornicki, and M. Rekas, "Comparison of the chemical diffusion of undoped and Nb-doped $SrTiO_3$," *Journal of Physics and Chemistry of Solids*, vol. 60, pp. 1835–1844, 1999.

[132] T. Leisegang, H. Stoecker, A. A. Levin, T. Weissach, M. Zschornak, E. Gutmann, K. Rickers, S. Gemming, and D. C. Meyer, "Switching Ti valence in $SrTiO_3$ by a dc electric field," *Physical Review Letters*, vol. 102, p. 087601, 2009.

[133] G. Rijnders and D. H. A. Blank, "An atomic force pencil and eraser," *Nature Materials*, vol. 7, pp. 270–271, 2008.

[134] H. P. R. Frederikse and W. R. Hosler, "Hall mobility in $SrTiO_3$," *Physical Review*, vol. 161, pp. 822–827, 1967.

[135] D. Kan, T. Terashima, R. Kanda, A. Masuno, K. Tanaka, S. Chu, H. Kan, A. Ishizumi, Y. Kanemitsu, Y. Shimakawa, and M. Takano, "Blue-light emission at room temperature from Ar^+-irradiated $SrTiO_3$," *Nature Materials*, vol. 4, pp. 816–819, 2005.

[136] J. L. Maurice, G. Herranz, C. Colliex, I. Devos, C. Carrétéro, A. Barthélémy, K. Bouzehouane, S. Fusil, D. Imhoff, E. Jacquet, F. Jomard, D. Ballutaud, and M. Basletic, "Electron energy loss spectroscopy determination of Ti oxidation state at the (001) $LaAlO_3/SrTiO_3$ interface as a function of $LaAlO_3$ growth conditions," *Europhysics Letters*, vol. 82, p. 17003, 2008.

[137] H. P. R. Frederikse, W. R. Thurber, and W. R. Hosler, "Electronic transport in strontium titanate," *Physical Review*, vol. 134, pp. A442–A445, 1964.

[138] O. Copie, V. Garcia, C. Bödefeld, C. Carrétéro, M. Bibes, G. Herranz, E. Jacquet, J. L. Maurice, B. Vinter, S. Fusil, K. Bouzehouane, H. Jaffrès, and A. Barthélémy, "Towards two-dimensional metallic behavior at $LaAlO_3/SrTiO_3$ interfaces," *Physical Review Letters*, vol. 102, p. 216804, 2009.

[139] T. Schneider, A. D. Caviglia, S. Gariglio, N. Reyren, and J. M. Triscone, "Electrostatically-tuned superconductor-metal-insulator quantum transition at the $LaAlO_3/SrTiO_3$ interface," *Physical Review B*, vol. 79, p. 184502, 2009.

[140] R. C. Neville, B. Hoeneisen, and C. A. Mead, "Permittivity of strontium titanate," *Journal of Applied Physics*, vol. 43, pp. 2124–2131, 1972.

[141] C. Bell, S. Harashima, Y. Kozuka, M. Kim, B. G. Kim, Y. Hikita, and H. Y. Hwang, "Dominant mobility modulation by the electric field effect at the $LaAlO_3/SrTiO_3$ interface." cond-mat/0906.5310, 2009.

[142] N. Reyren, S. Thiel, A. D. Caviglia, L. Fitting Kourkoutis, G. Hammerl, C. Richter, C. W. Schneider, T. Kopp, A. S. Rüetschim, D. Jaccard, M. Gabay, D. A. Muller, J. M. Triscone, and J. Mannhart, "Superconducting interfaces between insulating oxides," *Science*, vol. 317, pp. 1196–1199, 2007.

[143] N. Reyren, S. Gariglio, A. D. Caviglia, D. Jaccard, T. Schneider, and J. M. Triscone, "Anisotropy of the superconducting transport properties of the $LaAlO_3/SrTiO_3$ interface," *Applied Physics Letters*, vol. 94, p. 112506, 2009.

[144] L. Benfatto, C. Castellani, and T. Giamarchi, "Broadening of the Beresinkii-Kosterlitz-Thouless superconducting transition by inhomogeneity and finite-size effects." cond-mat/0909.0479, 2009.

[145] M. Huijben, A. Brinkman, G. Koster, G. Rijnders, H. Hilgenkamp, and D. H. A. Blank, "Structure-property relation of $SrTiO_3$-$LaAlO_3$ interfaces," *Advanced Materials*, vol. 21, pp. 1665–1677, 2009.

[146] X. Z. Liu, B. W. Tao, and Y. R. Li, "Effect of oxygen vacancies on nonlinear dielectric properties of $SrTiO_3$ thin films," *Journal of Materials Science*, vol. 42, pp. 389–392, 2007.

[147] C. S. Koonce, M. L. Cohen, J. F. Schooley, W. R. Hosler, and E. R. Pfeiffer, "Superconducting transition temperatures of semiconducting SrTiO$_3$," *Physical Review*, vol. 163, pp. 380–390, 1967.

[148] M. Huijben, *Interface engineering for oxide electronics*. PhD thesis, University of Twente, 2006.

[149] S. Thiel, C. W. Schneider, L. Fitting Kourkoutis, D. A. Muller, N. Reyren, A. D. Caviglia, S. Gariglio, J. M. Triscone, and J. Mannhart, "Electron scattering at dislocations in LaAlO$_3$/SrTiO$_3$ interfaces," *Physical Review Letters*, vol. 102, p. 046809, 2009.

[150] M. van Zalk, J. Huijben, A. J. M. Giesbers, M. Huijben, U. Zeitler, J. C. Maan, W. G. van der Wiel, Rijnders G., D. H. A. Blank, H. Hilgenkamp, and A. Brinkman, "Magnetoresistance oscillations and relaxation effects at the SrTiO$_3$-LaAlO$_3$ interface." cond-mat/0806.4450, 2008.

Chapter 3

Fabrication & characterization of perovskite thin films

Abstract

Besides purity and quality of the bulk complex oxides, purity and quality of the interfaces becomes important in the search for two-dimensional electron layers. Careful material preparation, *in situ* monitoring during the fabrication and optimal growth conditions are all required obtain the desired perfection, be it crystallographic, chemical, or morphological. Different techniques to probe these structural factors are needed, so they can be linked to the functional properties of the final sample.

3.1   Introduction

The technological boom in the second half of the previous century is in no small part due to the corresponding increase in understanding of the physics of solid state materials. In an iterative process our better understanding led to improved and new devices which in turn lead to new measurements and thus deeper understanding. Thus our knowledge of materials, both basic and applied, grew almost exponentially. Nowhere is this better exemplified than in Moore's law[1], which state that the number of transistors per area doubles every two years.

This 'law' is a tribute to the precision technologies that allow the fabrication of nanometer-sized features of semiconductors. Various technologies, starting from

the fabrication of pure single crystals, through the deposition of atomic layers using techniques such as molecular beam epitaxy or metalorganic vapour phase epitaxy, to the etching and structuring of integrated circuits using chemical or ion etching, make it possible to grow the plethora of devices in current-day technology.

In the perovskite transition metal oxides such precise fabrication has only more recently become possible with the rise of pulsed laser deposition since the discovery of high-T_c superconductors in 1986[2]. Especially the control of the surface termination of the STO substrate[3–8] and the *in situ* monitoring of the crystal growth using high-pressure reflective high-energy electron diffraction (RHEED)[9, 10] have allowed the fabrication of a variety of high-quality perovskite oxide heterostructures, including the LTO/STO and LAO/STO systems mentioned in the previous chapter[11–14].

This chapter discusses the various techniques used to fabricate and characterize the transition metal oxide samples. First the fabrication of the thin films is discussed, followed by the structural and chemical characterization. These two aspects determine the electronic and optical properties of the samples, which have been measured using several techniques discussed in the last section.

3.2 Thin film fabrication

Similar to semiconductor devices, the fabrication of transition metal oxide thin films start with the careful preparation of both substrate and source material, followed by a controlled deposition. Each of these steps requires considerable care.

3.2.1 Substrates & targets

As Figure 2.7 on page 17 shows the perovskite unit cell can be considered as a stacking of AO and BO_2 layers. Cleaving such crystals will in general result in a terraced surface with step heights of about half a unit cell. The crystal then has a mixed termination with both AO and BO_2 on the surface. For a precise control of both stacking sequence and interface chemistry, it is necessary to control the surface termination to obtain single-terminated surfaces.

STO is often used as a substrate in the research of transition metal oxides because of its cubic crystal structure, chemical and thermal stability and availability. Another reason to use STO substrates for the growth of heterostructures containing LTO and LAO is that the lattice constant of STO lies somewhere between those of LTO and LAO. The lattice mismatch is -1.6 % for LTO (compressive) and 3.1 % for LAO (tensile). Several recipes for obtaining TiO_2-terminated STO substrates have been published[3–8]. In fact, this precise control of the termination is another reason for the success of STO as the substrate of choice. Here the following recipe, based on the one by Koster et al.[4], was used:

1. Cleaning of the as-received substrates with acetone and ethanol;

2. Hydroxylation of SrO by immersion in demiwater for half an hour;

3. Etching of the hydrolized SrO away by immersion in a buffered NH_4-HF solution for 30 seconds;

4. After etching, the substrates are pre-annealed. Two different procedures were used:

   (a) Before deposition, the substrates were pre-annealed *in situ* at 900 °C and $7 \cdot 10^{-6}$ mbar for 60 minutes.
   These substrates were used for the LTO/LAO material system.

   (b) The substrates were pre-annealed ex-site in a tube oven at 930-950 °C in 150 l/hr flowing O_2 for 60-120 minutes depending on the substrate miscut.
   These substrates were used for the LAO/STO material system.

Substrates obtained from Shinkosha Co. Ltd., Japan, SurfaceNet GmbH., Germany and CrysTec GmbH., Germany were prepared following these procedures. They show a terraced surface with roughly parallel step edges. Step height was ~4 Å or about a unit cell. Friction force microscopy showed a single termination across a 5×5 μm^2 area. Prepared substrates treated at the temperature, oxygen pressure and time conditions for a deposition were all insulating.

In a few cases other substrates, such as LAO and $GdScO_3$, were used. The LAO substrates were cleaned with acetone and ethanol and then etched with carbonic acid by placing it in demi-water just below its boiling temperature for 30 minutes followed by a three-hour annealing in flowing oxygen at 950 °C. Straight step edges were observed with a height of about 3.5 Å and a RMS value of ~2 Å. Friction force microscopy showed no differences in sticking force on the surface. The $GdScO_3$ substrates were also cleaned with acetone and ethanol before pre-annealing *in situ* at 786 °C in $7 \cdot 10^{-6}$ mbar of oxygen for one hour. The surface showed clear terraces with step heights of about 4 Å, but the edges were very rough with many islands. Still, the RMS value over the 5×5 μm area was ~2 Å.

As source targets for the deposition process single crystals of STO and LAO and polycrystalline pellets of $La_2Ti_2O_7$ and $SrRuO_3$ (SRO) were used. The synthesis of stoichiometric $LaTiO_3$ is very difficult due to the strongly oxidizing nature of titanium, but thin films of the 113 composition can readily be grown from a 227 target[15]. Before use, the target surfaces are ground to clean the surface, followed by an *in situ* laser cleaning step before the actual deposition.

3.2.2 Principles & advantages of pulsed laser deposition

Pulsed laser deposition (PLD) is a physical vapour deposition technique where the transferred material is evaporated from the source target by heating with an

intense laser pulse. Most commonly pulsed excimer lasers (XrF, XeCl) with a wavelength between 240-310 Å are used. The laser pulses are focussed onto the target material using a lens external to the vacuum chamber to achieve the required energy density. The heated material quickly evaporates and further laser heating of the evaporated species creates a plasma that expands away from the target towards the substrate. There the evaporated material adsorps at the substrate, where it undergoes a thermally-activated diffusion process before forming a thin layer[10].

Figure 3.1 shows this process. In this schematic the laser beam enters diagonally from the top and hits one of the targets on the carousel in the center. The evaporated material is further heated and the plasma then expands towards the substrate, mounted on a heater block, above.
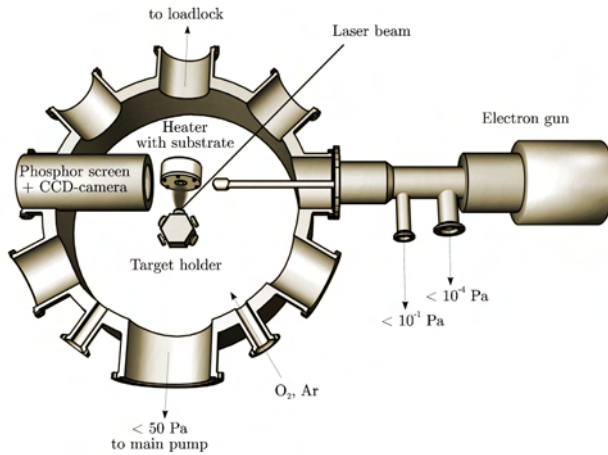
Figure 3.1: Schematic topview of the core PLD device.

Important parameters for the PLD process are the laser fluency (energy per pulse per unit area), laser spot size, target-to-substrate distance, background gas pressure & composition and the substrate temperature. These parameters influence the real advantages of PLD: the supersaturation during the deposition pulse & subsequent relaxation on the substrate and the tuneable kinetics of the species arriving on the substrate.

Due to the pulsed nature of the laser, the plasma is also pulsed. During a single pulse about $3 \cdot 10^{13}$ ion species arrive on the substrate. At a typical laser pulse frequency of 2 Hz this translates to a growth rate of 0.02 nm/s. This is not unlike growth rates achieved with molecular-beam epitaxy. However, the material is only transferred during the plasma pulse instead of continuously. Given the fact that the plasma pulse duration is very short ($\sim$500 μs[16]) the species density during the plasma pulse is much higher than at any time during a continuous deposition technique.

This supersaturation causes a high nucleation density. Then, because the plasma pulse is mostly much shorter than the mean diffusion time of adatoms on the substrate, the adatoms diffuse across the surface and relax into their optimal positions[17]. This relaxation can be seen in the RHEED signal, where the intensity relaxes exponentially after each plasma pulse. The high nucleation density promotes the interlayer transport during the following plasma pulses, thus promoting layer-by-layer growth. In the extreme limit, all material for a single monolayer can be deposited nearly instantaneous by giving a burst of laser pulses. This promotes layer-by-layer growth of materials that are otherwise difficult to grow as monolayers[18].

Furthermore, to optimize this process of supersaturation and relaxation, the kinetics of the arriving species in the plasma can be tuned by varying the parameters mentioned above. The laser fluency and substrate temperature directly influence the energy of the adatoms on the substrate. Oppositely, interactions with the background gas during the crossing from target to substrate cause the forefront of the plasma to thermalize and reach an equilibrium state. It has been argued that this thermalized front is the optimal condition for the arriving species[19]. So, using these parameters the growth kinetics of the thin films can be optimized.

Though not a unique advantages of PLD, the ease with which stoichiometric transfer of the target compound is achieved is a great plus. MBE can also achieve this stoichiometry through careful calibration of each independent source, but lacks the high oxygen pressure required for the growth of oxides. In fact, control of the background gas pressure and composition actually makes it possible to experiment with the oxygen stoichometry[20]. PLD combines this compositional advantage with the supersaturated growth, making it an ideal process to fabricate transition metal oxide thin films.

3.2.3 High-pressure reflective high-energy electron diffraction

For the fabrication of well-defined stacks of thin films, or even single films of a precise thickness, with PLD it is necessary to monitor the growth *in situ* for example with RHEED. Though it was already used to monitor thin film growth in molecular-beam epitaxy, the high pressure during deposition made it difficult to apply this monitoring technique due to scattering of the electron beam. The invention of high-pressure RHEED, where the electrons travel only a short distance through the high-pressure region, allowed this technique to be applied to PLD[9]. And with great success, as all systems discussed so far would have been impossible to make without this tool.

Figure 3.1 shows the central experimental part of the RHEED set-up. An electron gun provides a beam of electrons with a typical energy of 35 keV. This beam travels through a small tube which is pumped down to a low pressure; lower than that in the deposition chamber. This way the electron beam can come close to the monitored substrate without losing coherence through scattering. In Figure 3.1

this tube enters from the right. The electron beam then travels a short distance to the substrate, or film, and diffracts from the surface. The shallow incident angle causes the beam to interact with only the top few layers. The diffracted beam then falls on a phosphor screen shown to the left of the sample heater, giving rise to the characteristic RHEED pattern which is observed using a digital camera.

This RHEED pattern originates from the reciprocal lattice of the sample surface. Figure 3.2 shows this schematically. The two-dimensional nature of the samples surface gives rise to reciprocal rods instead of points. The intersection of these rods with the Ewald sphere results in spots which will appear in the RHEED pattern on the phosphor screen. The spherical nature of the Ewald sphere can be recognized in the fact that the diffraction spots also lie on a Laue circle. Optimalization of both the incident angle and the in-plane azimuth is often necessary to obtain sharp spots and symmetric patterns.
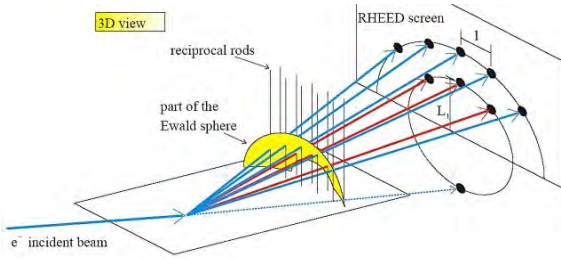
Figure 3.2: Ewald construction for RHEED, showing Laue circles and diffraction spots. Image taken from Ref. [21].

Monitoring the RHEED pattern with time yields a variety of information. Measuring the intensity of a central spot gives information about the film growth. Starting from a well-prepared substrate, partial coverage by deposited material will reduce the intensity due to the change in step density. As the layer is filled and the complete surface is restored, the intensity will recover. Depending on the growth mode, the behaviour of these oscillations differs. Perfect layer-by-layer growth (2D) would yield perfect oscillations that come back to the same maximum intensity every time. Island growth (3D) would show a decreasing intensity without oscillations until an average roughness of the sample surface is reached. Step flow growth, where all the material immediately diffuses towards the step edges of the substrate, would show no change at all as the overall morphology of the sample does not change. Finally, mixed growth would give oscillations that slowly lose intensity over time until again an average roughness is reached[17].

Aside from information about the growth process, the diffracted patterns can also yield other information. The side spots of the RHEED pattern are the result of a simple diffraction process described by:

$$d\sin(\theta) = n\lambda \tag{3.1}$$

The right-hand side of this equation is constant, so by observing the lateral position of the side spots it is possible to derive the in-plane lattice parameter during

growth. It is observed to oscillate with the same period as the intensity oscillations of the central spot.

Also similar to the X-ray diffraction, the width of the central spot yields information about the coherence of the surface crystal structure. For a bare substrate or completed film, the coherence is maximum. This relation between coherence and peak width is similar to Scherrer's equation:

$$\xi = \frac{K\lambda}{FWHM\cos(\theta)} \tag{3.2}$$

For the shallow incident angles of RHEED $\cos(\theta)$ is almost 1, so the coherence, or the length scale over which the crystal structure is perfect, is inversely proportional to the full-width half-maximum of the central spot. Again, this oscillates with the same period as the intensity of the central spot. However, numerical values for the coherence are difficult to obtain, because the necessary calibration of the RHEED system is difficult to do and unstable during deposition.

3.2.4 Experimental set-up

For this work two different PLD set-ups were used. Both were equipped with a KrF excimer laser (Coherent, wavelength $\lambda = 248$ nm). A rectangular mask was used to select the homogeneous part of the laser beam. This mask was then projected onto the target inside the vacuum chamber using a lens, resulting in a spot size of about $2\,\text{mm}^2$. The energy of the laser pulse was measured outside the deposition chamber and the fluency was then calculated from the spotsize area, taking into account the losses at the lens and the deposition chamber window. A load-lock system allows the loading of samples and multiple targets without breaking the vacuum inside the main deposition chamber. Moving the target prevented 'burn in' of the surface which can result in droplet formation or non-stiochiometric transfer. The deposition pressure varied from 10^{-6} to 10^{-1} mbar of either O_2, Ar or a mixture of the two.

The work on the LTO/LAO system was carried out at Hwang Lab, University of Tokyo, Japan. A schematic of that system is given in Figure 3.3. All the work on LAO//STO interfaces was carried out at the MESA+ Institute for Nanotechnology, University of Twente, the Netherlands[17]. A schematic of the core of that system was shown in Figure 3.1.

Though not of great influence on the PLD process itself, the different design results in some differences in practice. A short list of some characteristic differences is given in Table 3.1.

3.3 Structural & compositional characterization

After its fabrication it is necessary to characterize the sample. Because every one of its properties, be they electrical, mechanical or optical, are due to its structure

Figure 3.3: Schematic sideview of the PLD set-up at Hwang lab, University of Tokyo, Japan.

feature	Hwang Lab Japan	MESA+ Institute The Netherlands
base pressure	10^{-8} mbar	10^{-7} mbar
laser	Coherent Compex	Coherent LPX200
target movement	rotation	translation
deposition direction	vertical	horizontal
target-substrate distance	50 mm	55 mm
sample heater	lamp	resistive
Thermal contact glue	Pt-based	Ag-based
temperature measurement	pyrometer	*in situ* thermocouple

Table 3.1: Differences in PLD set-up between Hwang lab, Japan and MESA+ Institute for Nanotechnology, the Netherlands.

and composition, these need to be identified first. Atomic force microscopy yields information on the surface morphology, while X-ray diffraction and transmission electron microscopy give information on the (local) crystal structure. Electron energy loss spectroscopy, combined with scanning TEM can identify chemical (and some electronic) information of the crystal structure.

3.3.1 Atomic force microscopy

AFM measurements were used to determine the surface morphology of the samples, specifically the topography and friction profile. Contact mode AFM measurements were carried out with either a Dimension V or a MultiMode scanning probe microscope from Veeco, UK. Typically, silicon tips from Nanosensors, Switzerland with a force constant k = 0.02-0.77 N/m were used. All measurements were carried out *ex situ*, either directly after etching & annealing for substrates or after fabrication for deposited films to minimize surface contamination. In general 5×5 μm^2 areas at 512×512 points were scanned.

3.3.2 X-ray diffraction

The crystallographic structure of the substrates and samples were determined by XRD on either a thin-film diffractometer or a four-circle diffractometer (CAD4, Enraf-Nonius, the Netherlands; D8discover, Bruker, Germany; X'pert MRD, Philips, the Netherlands[1]) using Cu Kα radiation. The samples and substrates were analysed using θ-2θ scans, ω rocking curves, ϕ scans, Matthieson scans and reciprocal space mapping to determine crystal structure, roughness, orientation, phase information and superlattice periodicity. The instrumental broadening of the CAD4 system is estimated at about $0.2°$ because of the lack of a monochromator. This also gives rise to additional peaks corresponding to $\lambda/2$ and $\lambda/3$. Both the D8discover and X'pert MRD system have a lower broadening due to the incorporation of a monochromator, allowing only the Cu Kα1 line into the diffractometer.

3.3.3 (Scanning) Transmission electron microscopy

(Scanning) Transmission electron microscopy images were taken to investigate the local crystal structure and epitaxial quality of the deposited thin films. Different instruments were used over the course of the studies. First, for the study of the LTO/LAO system samples were investigated with a Tecnai F20-ST from FEI Company, USA[2]. The core of the instrument is the electron monochromator that reduces the energy spread from the 200 kV field emission gun, resulting in an ultra-high energy resolution. The SuperTwin objective lens with a spherical aberration of 1.2 mm makes for a spatial resolution of ∼1.6 Å. Together this allows for the determination of electronic properties with atomic resolution[20, 22].

Both annular dark field images and high-angle annular dark field (HAADF) images were obtained. The latter resulted in high-resolution Z-contrast images using a Fischione Model 3000 detector. This detector only detects electrons scattered over

---

[1]XRD measurements on the X'pert MRD were carried out at the Hwang lab, University of Tokyo, Japan

[2]STEM & EELS measurements on the Tecnai F20-ST were carried out at the Muller group, Cornell University, USA.

large angels, thus avoiding the direct beam. The intensity of these incoherently scattered electrons is directly proportional to the atomic weight Z of the atoms in the image atomic columns. This facilitates qualitative interpretation of the HAADF images, as heavier chemical elements appear as brighter spots in the image.

TEM images of the LAO/STO system were obtained using a Philips CM30 Twin/ STEM[3]. The maximum operating voltage is 300 kV with a resolution of ∼2.3 Å, which is limited by instrumental parameters.

3.3.4   Electron energy loss spectroscopy

Local chemical information can be obtained with EELS in combination with the first STEM set-up described above. The high spatial and energy resolution makes it possible to measure precise EELS spectra at atomic resolution. In STEM mode, the electrons scatter incoherently on the ions in the sample and loose part of their energy. These transmitted electrons in the direct beam are then captured on a 865-ER Gatan imaging filter and their energy spectrum is measured with a resolution of about 0.6 eV[23]. From this spectrum the chemical, and often electronical, properties can be determined. For oxygen vacancies, the detection limit is about 1 % ($\delta \approx 0.05$)[20].

3.4   Electronic & optical characterization

With the structure of the sample known, it is necessary to determine its electronic and optical properties. It is these properties that are often of most interest, either because they are useful for applications or because they give information about what physics is going on inside the sample. Linking these functional properties to the sample structure makes it possible to determine and understand the physics inherent to the structures.

3.4.1   X-ray photoelectron spectroscopy

Similar to EELS, XPS yields both chemical and electronical information about the sample. XPS measurements on the LTO/LAO system were carried out on a Quantera SXM, Physical Electronics, USA or on a custom-build spectrometer equipped with a SES-100 electron-energy analyzer, VG Scienta, Sweden[4]. Samples were transferred *ex situ* from the deposition chamber to the spectrometer. All measurements were carried out at room temperature. X-rays are generated from an Al Kα ($h\nu$ = 1486.6 eV) X-ray source, with a correction for the Al K$\alpha_{3,4}$

---

[3]TEM measurements on the Philips CM30 Twin/STEM were carried out at the Central Materials Analysis Laboratory, MESA+, University of Twente, the Netherlands.

[4]XPS measurements on the second machine were carried out at the Fujimori group, University of Tokyo, Japan.

satellites. The total energy resolution was set to about 0.8 eV for the Quantera SXM and 0.9 eV for the SES-100. Either the C 1s core level (E_B = 285 eV) or the Au $4f_{7/2}$ core level (E_B = 84.0 eV) was used for the calibration.

Hard X-ray photoelectron spectroscopy measurements were performed at the undulator beamline BL29XU of SPring-8, using a R4000-10 keV hemispherical electron energy analyzer, VG Scienta, Sweden[5]. Details of the apparatus including X-ray optics are described elsewhere[24–26]. Samples were transferred from the PLD chamber to the spectrometer chamber *ex situ* and no surface treatment was performed prior to XPS measurements. All the measurements were carried out at room temperature, and the total energy resolution was set to about 200 meV. The position of the Fermi level was determined using gold spectra.

XPS measurements on the LAO/STO system were performed with an XPS/UPS system designed by Omicron Nanotechnology GmbH, Germany. The system is equipped with an EA 125 electron energy analyser. Several X-ray sources are present; a non-monochromatic Al Kα (1486.3 eV) and Mg Kα (1253.6 eV) source (DAR 400) and a monochromatic Al Kα source (XM 1000). The UV light source is a He plasma lamp (HIS 13) which can be operated at either the He I (21.22 eV) and He II (40.8 eV) excitation edges. The base pressure of the system is below $1 \cdot 10^{-10}$ mbar. The analyser is calibrated with the use of an *in situ* sputter cleaned Au sample. The escape angle of the electrons can be varied by rotation of the sample between 10 and 80 degrees of the sample surface normal for surface sensitive measurements.

3.4.2 Electronic transport analysis

Electrical measurements as a function of temperature and magnetic field allow for a variety of transport properties such as Hall electron density and electron mobility to be determined. From these it is often possible to draw other conclusions about the electron scattering and capture processes inside the samples.

The basic measurement is a resistivity measurement as function of temperature and/or magnetic field (Hall effect). However, for two-dimensional samples it is difficult to determine or even assign a thickness to the conducting layer. The sheet resistance is analogous to the resistivity but for two dimensions.

$$R_s = \frac{R\,w}{l} \tag{3.3}$$

Here R_s is the sheet resistance (unit is $\Omega/\square$ or Ohm-per-square, to distinguish from resistance which has the same basic unit but a different meaning), R the measured resistance and w & l the width and length respectively of the current path. Such measurements allow for the extraction of the (mobile) carrier density,

---

[5]XPS measurements at SPring-8 were carried out by a collaboration between the Fujimori group, Univeristy of Tokyo, Japan and the Coherent X-ray Optics Laboratory, RIKEN/SPring-8, Japan.

electron mobility and type of the carriers through the relation:

$$R_\text{s} = \frac{1}{n_\text{2D}\, e\, \mu} \tag{3.4}$$

where n_2D is the two-dimensional carrier density, e the electric charge of an electron and μ the electron mobility.

All transport measurements were done using a PPMS, Quantum Design, USA with a DC measurement. For the Hall effect and magnetoresistance measurements magnetic fields up to $2.5{\cdot}10^4$ Oe were used. Measurements currents were kept as low as possible to prevent resistive heating, but still large enough to limit the noise. In general, this resulted in a current of the order 1-10 μA. Two different measurement geometries, Hall-bar and Van-der-Pauw, were used.

Low-temperature transport measurements between 0.254 and 8 K were performed in a Heliox VL ^{3}He cryostat, Oxford Instruments, United Kingdom[6]. The system has a base temperature of $\sim$250 mK and can achieve magnetic fields of up to 10 T at 2 K. Four-point Van-der-Pauw measurements were carried out using purpose-build modules fabricated by the Delft University of Technology, the Netherlands. Typical operating currents were in the range 1-100 nA with resulting voltages of the order of μV. After amplification, the voltage was measured using a Keithley 2000 multimeter.

Hall-bar geometry

In the Hall-bar geometry the sample is cut into a bar about 3 mm wide and 5 mm long. Four electrodes are placed across the current path, with the inner two forming the voltage contacts. Two smaller side-contacts allow for the measurement of the Hall voltage. The electrodes are formed by first cracking the surface of the sample by laser heating through a mask, thus defining where the electrodes are placed and leaving the rest of the sample in tact. This is followed by the evaporation of aluminium onto the cracked area to contact the deeper-laying layers. Contact leads are then glued to the electrodes using silver epoxy. The sheet resistance can then be extracted using Equation 3.3.

Van-der-Pauw geometry

In the Van-der-Pauw geometry[27] the contact leads are directly wirebonded to the sample. The wirebonding process itself cracks the surface and makes contact to the deeper layers. The resistance is then measured amongst these four electrodes in different combinations. Figure 3.4 shows the typical location and labelling in the Van-der-Pauw geometry.

The sheet resistance is numerically extracted from Equation 3.5. The advantage of this geometry is that the shape and size of the sample can be arbitrary, as long

---

[6]Low-temperatyre transport measurements were done in co-operation with the NanoElectronics group, MESA+ Institute for Nanotechnology, University of Twente, the Netherlands.
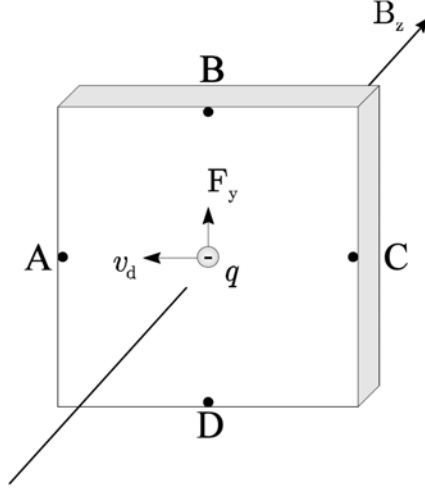
Figure 3.4: Typical Van-der-Pauw geometry on a sample. Labels A to D indicated current and voltage contacts.

as it is homogeneous, both structurally and electronically. The Hall resistance is obtained at the same time by measuring $\frac{V_{BD}}{I_{AC}}$.

$$1 = \exp\left(-\frac{\pi}{R_s}\frac{V_{AB}}{I_{DC}}\right) + \exp\left(-\frac{\pi}{R_s}\frac{V_{AD}}{I_{BC}}\right) \tag{3.5}$$

3.4.3 UV-vis photoreflectance spectroscopy

Photoreflectance measurements were carried out using a Cary 50 UV-vis spectrophotometer from Varian, USA. The photoreflectance was obtained using a 30° fixed angle specular reflectance accessory. The spectrometer uses a Czerny-Turner 0.28 m monochromator to select the desired frequency from the xenon flashlight. The dual beam operation mode allows to correct for intensity fluctuations in either source or surroundings. Scan range, resolution and speed can be adjusted but typical settings are 400 to 190 nm (3.1 to 6.5 eV)[7] with a step size of 0.5 nm at 5 nm/s. No baseline or zero was subtracted, as without calibration the absolute value of the reflectance has no quantitative value. However, tests with a silver mirror show that the qualitative structure of the reflectance spectra is still physically correct. The RefFIT program[28] was used to fit the reflectance data with Lorentz oscillators to unambiguously determine the transition energies.

---

[7]For longer wavelengths (lower energy) systematic artefacts appear. Also, that energy range would fall within the bandgap op STO and LAO, so no structure is present.

3.4.4   UV-vis absorption & ellipsometry

Optical measurements make it possible to probe material properties such as the complex dielectric constant or similarly the complex optical conductivity. Absorption measurements are an easy way to probe this, but the extraction of quantitative information is difficult except for the simplest samples. Ellipsometry is able to extract the complex optical conductivity without Kramer-Kronig analysis or phenomenological fitting with Lorentz oscillators. This allows for an unambiguous determination of the optical properties. Both types of measurements were carried out on a VASE ellipsometer from J.A. Woollam, USA[8]. The maximum energy range is 0.75 to 6.5 eV with a resolution of 0.05 eV for a typical measurement. Δ/Ψ spectra are taken at angles between 55° and 85°. Analysis of the spectra is done with the accompanying V.A.S.E. software.

3.5   Concluding remarks

Understanding the properties of a material system requires knowledge of the structure of the material, which is determined during the fabrication. All three parts, fabrication, characterization and functionality, require careful attention and sophisticated techniques. It is this sequence - fabrication determines structure which in turn determines properties - that forms the basis of the research in this thesis.

Pulsed laser deposition in combination with RHEED monitoring has become a mainstay of oxide thin film fabrication because of the tuneable growth kinetics and the ease of stoichiometric transfer. The use of single-terminated substrates allows for the growth of well-defined structures of complex oxides. Several techniques to characterize these structures, either available in-house or through collaborations with groups world-wide, have been discussed. Finally, techniques to measure the electrical and optical properties are necessary to be able to discuss the relation between these functional properties and the structural features.

---

[8]Ellipsometry and absorption measurements with the VASE ellispometer were carried out at the Group Solid State, Université Fribourg, Switzerland.

3.6   References

[1] "Moore's law." http://en.wikipedia.org/wiki/Moore's_law (04-16-2008).

[2] J. Bednorz and K. Müller, "Possible high T_c superconductivity in the Ba-La-Cu-O system," *Zeitschrift für Physik B*, vol. 64, pp. 189–193, 1986.

[3] M. Kawasaki, A. Ohtomo, T. Arakane, K. Takahashi, M. Yoshimoto, and H. Koinuma, "Atomic control of $SrTiO_3$ surface for perfect epitaxy of perovskite oxides," *Applied Surface Science*, vol. 107, pp. 102 – 106, 1996.

[4] G. Koster, B. L. Kropman, A. J. H. M. Rijnders, D. H. A. Blank, and H. Rogalla, "Quasi-ideal strontium titanate crystal surfaces through formation of strontium hydroxide," *Applied Physics Letters*, vol. 73, pp. 2920–2922, 1998.

[5] T. Ohnishi, K. Shibuya, M. Lippmaa, D. Kobayashi, H. Kumigashira, M. Oshima, and H. Koinuma, "Preparation of thermally stable TiO_2-terminated $SrTiO_3(100)$ substrate surfaces," *Applied Physics Letters*, vol. 85, pp. 272–274, 2004.

[6] D. Kobayashi, R. Hashimoto, A. Chikamatsu, H. Kumigashira, M. Oshima, T. Ohnishi, M. Lippmaa, K. Ono, M. Kawasaki, and H. Koinuma, "Sr surface segregation and water cleaning for atomically controlled SrTiO3(001) substrates studied by photoemission spectroscopy," *Journal of Electron Spectroscopy and Related Phenomena*, vol. 144, pp. 443–446, 2005.

[7] M. Kareev, S. Prosandeev, J. Liu, C. Gan, A. Kareev, J. W. Freeland, M. Xiao, and J. Chakhalian, "Atomic control and characterization of surface defect states of TiO_2 terminated $SrTiO_3$ single crystals," *Applied Physics Letters*, vol. 93, p. 061909, 2008.

[8] J. Zhang, D. Doutt, T. Merz, J. Chakhalian, M. Kareev, J. Liu, and J. Brillson, "Depth-resolved subsurface defects in chemically etched $SrTiO_3$," *Applied Physics Letters*, vol. 94, p. 092904, 2009.

[9] A. J. H. M. Rijnders, G. Koster, D. H. A. Blank, and H. Rogalla, "In-situ growth monitoring during PLD of oxides using RHEED at high oxygen pressure," *Materials Science and Engineering: B*, vol. 56, pp. 223–227, 1998.

[10] R. Eason, ed., *Pulsed laser deposition of thin films*. Wiley, 2006.

[11] H. Koinuma, N. Kanda, J. Nishino, A. Ohtomo, H. Kubota, M. Kawasaki, and M. Yoshimoto, "Laser MBE of ceramic thin films for future electronics," *Applied Surface Science*, vol. 109-110, pp. 514–519, 1997.

[12] A. Ohtomo, D. A. Muller, J. L. Grazul, and H. Y. Hwang, "Artificial charge-modulation in atomic-scale perovskite titanate superlattices," *Nature*, vol. 419, pp. 378–380, 2002.

[13] H. N. Lee, H. M. Christen, M. F. Chisholm, C. M. Rouleau, and D. H. Lowndes, "Strong polarization enhancement in asymmetric three-component ferroelectric superlattices," *Nature*, vol. 433, pp. 395–399, 2005.

[14] Y. S. Kim, D. H. Kim, J. D. Kim, Y. J. Chang, T. W. Noh, J. H. Kong, K. Char, Y. D. Park, S. D. Bu, J. G. Yoon, and J. S. Chung, "Critical thickness of ultrathin ferroelectric $BaTiO_3$ films," *Applied Physics Letters*, vol. 86, p. 102907, 2005.

[15] A. Ohtomo, D. A. Muller, J. L. Grazul, and H. Y. Hwang, "Epitaxial growth and electronic structure of LaTiO$_x$ films," *Applied Physics Letters*, vol. 80, pp. 3922–3924, 2002.

[16] Tatsuo Okada, Yoshiki Nakata, Mitsuo Maeda, and W. K. A. Kumuduni, "Ultraviolet laser light scattering diagnostics of the plume in pulsed-laser deposition process," *Journal of Applied Physics*, vol. 82, pp. 3543–3547, 1997.

[17] A. J. H. M. Rijnders, *The initial growth of complex oxides: study and manipulation*. PhD thesis, University of Twente, 2001.

[18] G. Koster, A. J. H. M. Rijnders, D. H. A. Blank, and H. Rogalla, "Imposed layer-by-layer growth by pulsed laser interval deposition," *Applied Physics Letters*, vol. 74, pp. 3729–3731, 1999.

[19] M. Strikovski and J. H. Miller Jr., "Pulsed laser deposition of oxides: why the optimum rate is about 1 Å per pulse," *Applied Physics Letters*, vol. 73, pp. 1733–1735, 1998.

[20] D. A. Muller, N. Nakagawa, A. Ohtomo, J. L. Grazul, and H. Y. Hwang, "Atomic-scale imaging of nanoengineered oxygen vacancy profiles in SrTiO$_3$," *Nature*, vol. 430, pp. 657–661, 2004.

[21] J. Klein, "LEED/RHEED." http://www.wmi.badw-muenchen.de/methods/leed_rheed.htm (10-02-2009).

[22] D. A. Muller, A. Ohtomo, J. L. Grazul, and H. Y. Hwang, "Artificial charge modulations in La-doped SrTiO$_3$ superlattices," *Microscopy and Microanalysis*, vol. 8, pp. 576–577, 2002.

[23] L. Fitting Kourkoutis, Y. Hotta, T. Susaki, H. Y. Hwang, and D. A. Muller, "Nanometer scale electronic reconstruction at the interface between LaVO$_3$ and LaVO$_4$," *Physical Review Letters*, vol. 97, p. 256803, 2006.

[24] K. Tamasaku, Y. Tanaka, M. Yabashi, H. Yamazaki, N. Kawamura, M. Suzuki, and T. Ishikawa, "SPring-8 RIKEN beamline III for coherent X-ray optics," *Nuclear Instruments & Methods in Physics Research Section A*, vol. 467, pp. 686–689, 2001.

[25] T. Ishikawa, K. Tamasaku, and M. Yabashi, "High-resolution X-ray monochromators," *Nuclear Instruments & Methods in Physics Research Section A*, vol. 547, pp. 42–49, 2005.

[26] Y. Takata, M. Yabashi, K. Tamasaku, Y. Nishino, D. Miwa, T. Ishikawa, E. Ikenaga, K. Horiba, S. Shin, M. Arita, K. Shimada, H. Narnatame, M. Taniguchi, H. Nohira, T. Hattori, S. Södergren, B. Wannberg, and K. Kobayashi, "Development of hard X-ray photoelectron spectroscopy at BL29XU in SPring-8," *Nuclear Instruments & Methods in Physics Research Section A*, vol. 547, pp. 50–55, 2005.

[27] L. J. van der Pauw, "A method of measuring specific resistivity and Hall effect of discs of arbitrary shape," *Philips Research Reports*, vol. 13, pp. 1–9, 1958.

[28] A. Kuzmenko, "RefFIT." http://optics.unige.ch/alexey/reffit.html (13-05-2009), 2009.

Chapter 4

Electron localization in LaTiO$_3$/LaAlO$_3$ heterostructures

Abstract

Embedding LaTiO$_3$ in LaAlO$_3$ allows for a better confinement of the Ti 3d^1 electrons. Compared to the LaTiO$_3$/SrTiO$_3$ system the new system is a Mott insulator for single monolayers of LaTiO$_3$. Ellipsometry measurements confirm the presence of a narrow Ti^{3+} state and the orbitals are xz/yz ordered, different from bulk LaTiO$_3$ which shows no orbital order. External doping of the electron layer is possible and depends on the separations of the donor and receiver layers. It is found that a balance between surface oxidation and electron transfer between the electron layer and the surface drives this doping. A small part of this electronic stress is relieved within the LaAlO$_3$ layer itself, leading to a small band bending effect as observed from a change in the optical transition energies of the system.

4.1 Introduction

Two-dimensional layers of electrons are of great use in both research and applications. In combination with correlated-electron materials, their behaviour could be even more peculiar, as discussed in Chapter 2. But to obtain properties truly different from those in semiconductors a higher density system has to be found, since only when the electron-electron separation is small, the correlation effects become dominant.

Figure 2.11 already shows that electrons can be confined to about 20 nm thick layer in heterostructures of STO and LTO. However, the effective electron density is about 0.25 e/u.c. as obtained from the EELS measurements. But for a Mott insulating state a theoretical density of 1 e/u.c. is required. So, ways to increase the confinement of electrons should lead to more interesting physical systems.

There are several methods to increase the confinement of electrons within a potential well. First, increasing the depth of the well is a simple example, often discussed in basic quantum mechanics texts as well[1, 2]. Band gap engineering in semiconductors readily uses combinations of different materials with different band gaps to achieve such potential wells. Second is reducing the penetration of electrons into the buffer material. Decreasing the dielectric constant of the buffer material, for example, decreases the Debye length which governs the electron distribution at a potential step. More precise calculations show that indeed decreasing the dielectric constant of the buffer material decreases the 'spill over' of electrons[3]. Figure 4.1 shows this decrease clearly.
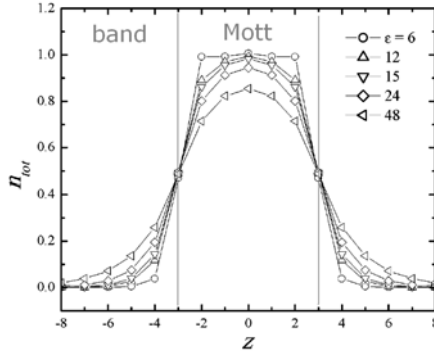

Figure 4.1: Theoretical charge density across a six-monolayer Mott/band insulator heterostructure for different values of the dielectric constant of the band insulator. Graph adapted from Ref. [3].

Finally, avoiding a polarization discontinuity at the interface between both materials should also reduce the amount of charge outside of the central layer. LAO remarkably fulfils all three requirements, as shown in Table 4.1. It is an $A^{3+}B^{3+}O_3$ material with a band gap larger than that LTO and a dielectric constant lower than that of STO.

parameter	STO	LTO	LAO
$A^x B^y O_3$	$Sr^{2+}Ti^{4+}O_3$	$La^{3+}Ti^{3+}O_3$	$La^{3+}Al^{3+}O_3$
E_g (eV)	3.2	3.4	5.6
K (-)	300	20	24

Table 4.1: Material parameters of the perovskite oxides STO, LTO and LAO at room temperature.

Thus using LAO as the buffer material instead of STO the electron density on the embedded LTO layer is expected to be closer to the bulk value of 1 electron per unit cell. This would make the system a Mott insulator in two dimensions, offering a model system for comparison with high-temperature superconductors or for field effect systems where the electron density can be tuned by adding or subtracting electrons from the active layer.

In this chapter the LTO/LAO system is investigated to determine whether the confinement of the electrons in the LTO layer does indeed increase compared to the LTO/STO system. To prevent any surface contributions, EELS is used to study buried layers of LTO embedded in LAO. The ability of EELS to distinguish between Ti^{3+} and Ti^{4+} makes it an ideal tool to determine the electron occupation of such buried layers[4]. Superlattices are used as they offer several measurement opportunities within a single sample, which is efficient as extensive sample preparation is required. But the ground state of the system cannot be derived from the electronic state of the titanium alone. Transport measurements were used to directly probe whether the system is insulating or not, indicating whether a Mott state is present or not. Such a state would be a sure sign of confinement, as it is closely related to the local electron density. Studies of the optical conductivity obtained from ellipsometry on superlattices of LTO and LAO, and comparison with the density-of-states obtained from calculations, are used to prove the existence of occupied Ti $3d^1$ levels, proving the Mott state does exist in these superlattices.

The interaction between such electron layers is known to affect the doping of either interface[5]. As the top surface of LAO is electronically reconstructed, probing thin layers of LTO with a thin LAO cap can give information on this interaction. XPS is a useful tool here, as it can also distinguish between Ti^{3+} and Ti^{4+}, but does not require the extensive sample preparation for EELS. However, only the region close to the surface can be probed, so samples with a single LTO layer and a thin LAO capping layer are required. A model where there is a balance between surface reconstruction and electron-transfer from the LTO layer to the surface was used to describe the observations. Optically probing these single-layer LTO films shows that the LAO capping layer relaxes slightly, but well within the materials capability to accommodate. This helps bridge the (chemical) potential difference between the LTO layer and the air, but the energy scale of this deformation is small compared to that of the competition between surface relaxation and electron transfer.

4.2   Sample fabrication

Both types of LTO/LAO heterostructures, superlattices and single-layer films, were grown by PLD using the set-up at Hwang Lab, University of Tokyo, Japan. STO(001) substrates 5×5×0.5 mm in size were used as substrates. These substrates were pre-etched using buffered HF acid by the supplier and cleaned with acetone and ethanol before loading into the PLD system. An *in situ* pre-anneal at 900 °C and $7\cdot10^{-6}$ mbar for 60 minutes results in a clear step-and-terrace structure observed with AFM with step edges of about 4 Å and a RMS roughness value of

about 2 Å over a 5×5 μm area. STO substrates treated at deposition conditions (700 °C and $1.7\cdot10^{-6}$ mbar for 30 minutes) were found to be non-conducting. This confirms that any conduction in the fabricated samples finds its cause in the deposition; either in the deposited film itself or through the interaction between the PLD plasma, the deposition pressure and the substrate.

Special care has to be taken with the growth of LTO, as it easily forms a $La_2Ti_2O_7$ (227 phase) layered-perovskite structure. A phase diagram for the growth of LTO as a function of temperature and deposition pressure was obtained previously[6]. This phase diagram is reproduced in Figure 4.2 and clearly shows that a low pressure growth regime is necessary to obtain the desired phase.
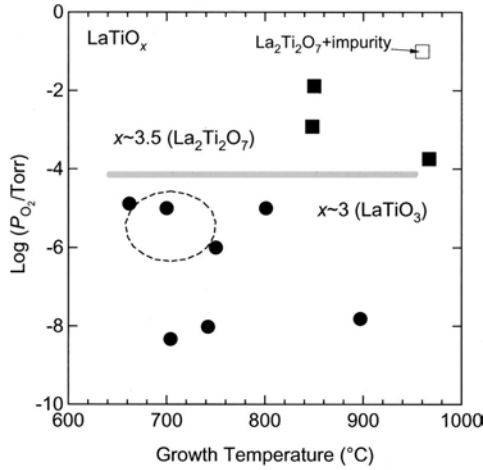

Figure 4.2: Experimental phase diagram with temperature and deposition pressure for the growth of LTO. Graph taken from Ref. [6].

An example of the RHEED signal for the growth of LTO at the optimum conditions is shown in Figure 4.3. Up to about 15 2D growth oscillations can clearly be seen, after which a steady growth with small oscillations extends to at least 40 oscillations. This shows that the 2D growth occurs to thicker layers than previously reported[6], so the few monolayers required for the structures considered in this thesis can be readily grown. Total thickness of the thick LTO film was $\sim$42 nm, or a hundred monolayers. XRD θ-2θ scans for thicker LTO films give a c-axis parameter of 3.98 Å, comparable to the bulk value of 3.97 Å. The presence of higher order peaks indicates that the grown film is indeed the cubic 113 phase[1] AFM measurements again give a clear step-and-terrace structure with step heights of about $\sim$4 Å. Together these observations show that thin layers of the 113 phase of LTO can be grown in a 2D regime, as expected from the temperature-pressure phase diagram.

---

[1]The monoclinic unit cell of the 227 phase is miss-aligned about 4.5° with respect to the cubic unit cell of the STO substrate. As such, only the (001) peak appears when the XRD θ-2θ measurement is aligned to the substrate unit cell. If the sample is given a 4.5° offset, the higher-order peaks for the 227 phase are all visible again[6].
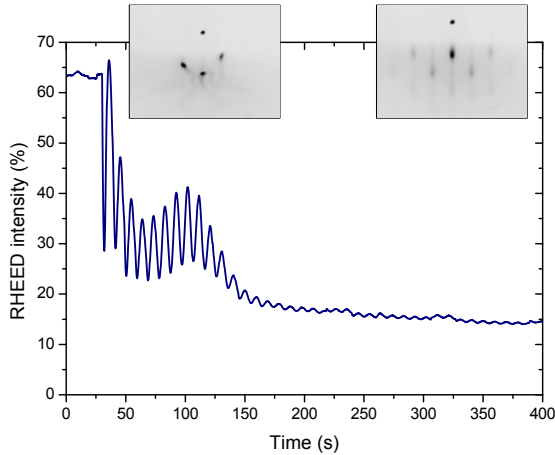
Figure 4.3: RHEED oscillations for the growth of thick LTO films at Hwang lab, University of Tokyo, Japan. The insets show the RHEED pattern at the begining (left) and end (right) of the LTO growth.

As STO(001) crystals are used as substrates, the growth of SrO monolayers was investigated to eliminate the electron gas at that interface[7]. SrO in bulk form has a rock-salt structure where each unit cell consists of two layers of SrO. Figure 4.4(a) shows the RHEED oscillations for the growth of SrO on STO(001). The period of the first oscillation is much shorter than the periods of the later oscillations by a factor of two. As already shown in literature[8], during the growth of SrO on TiO_2-terminated STO, the first layer of SrO adopts the STO perovskite structure and completes one oscillation. Later oscillations follow the SrO rock-salt structure which requires twice the amount of deposited SrO to finish one unit cell compared to the first oscillation. The vertical lines in Figure 4.4(a) show this clearly.

Figure 4.4(b) shows the in-plane lattice spacing as obtained during the growth from the RHEED side spots. The oscillations in the intensity are clearly reproduced. The film can be seen relaxing towards the value for bulk SrO as the growth proceeds. Although the relaxation is large (about 6 %) this behaviour has been observed before for SrO[8].

Two types of samples were fabricated. Superlattice samples of LTO and LAO were grown for EELS & ellipsometry measurements, while single layers of LTO embedded in LAO were grown for XPS & photoreflectance investigations. Both types of samples were grown at the same deposition parameters: fluency 2.5 J/cm^2, pulse frequency 2 and 4 Hz for LTO and LAO, respectively, spot size 2 mm^2, deposition pressure $1.7 \cdot 10^{-6}$ mbar O_2, target-to-substrate distance 50 mm and deposition temperature 700 °C. The sample was cooled down in deposition pressure. The low oxygen pressure is necessary for the growth of LTO, but also influences the properties of the other materials, especially STO[4, 9].
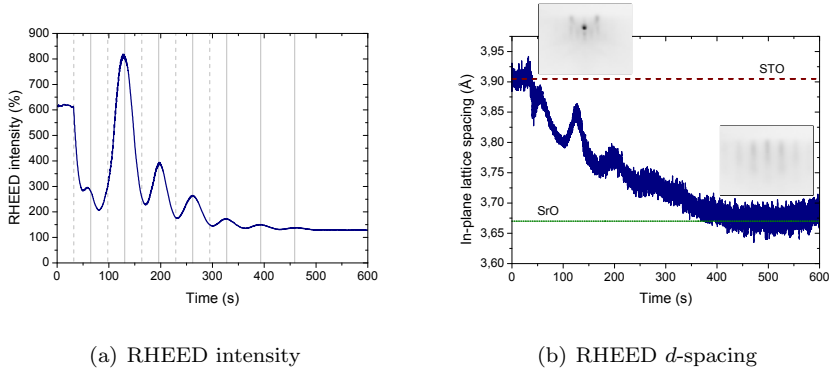
(a) RHEED intensity

(b) RHEED d-spacing

Figure 4.4: RHEED data for the growth of SrO on TiO$_2$-terminated STO(001).

The default structures for either are as follows. A superlattice is made of n repetitions of a supercell consisting of m monolayers of LAO and p monolayers of LTO. The LAO layer was chosen because its lower dielectric constant and higher band gap should lead to better confinement of the electrons in the LTO layer, as discussed in the introduction. The first layer on the TiO$_2$-terminated STO(001) substrate is a LAO layer, while the entire stack is capped with another m monolayers of LAO. Shorthand notation for the superlattice structure is 'SL(p-m)$_n$'. A single-layer sample consists of a 30 monolayer LAO buffer on a TiO$_2$-terminated STO(001) substrate. p monolayers of LTO are deposited on top of the LAO buffer layer and the structure is capped with m layers of LAO. Shorthand notation for the single-layer structure is 'PS(m-p)'. Both structure are shown in Figure 4.5 for clarity.

(a) superlattice SL(p-m)$_n$
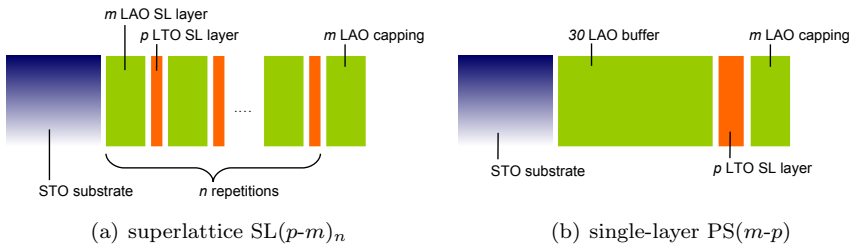
(b) single-layer PS(m-p)

Figure 4.5: Designed LTO/LAO structures.

RHEED oscillations are visible for all samples, superlattices and single-layers, up to the end of the deposition. The LTO deposition is always more difficult compared to the LAO deposition because the RHEED signal drops rapidly during deposition. However, by combining the intensity oscillations with the oscillations in the in-plane d-spacing and FWHM of the main peak the growth can still be controlled sufficiently. Deposition rates were on the order of 45 pulses per monolayer.

4.3 Two-dimensional Mott insulator

The super-periodicity inherent in superlattices makes these structures ideal for optical investigations, either with light or with electrons. EELS was used to determine the level of confinement of the electrons within the LTO layers, while transport and ellipsometry measurements helped investigate the ground state of the LTO layers.

4.3.1 Structural characterization

AFM scans of the top surface of such superlattices show again a clear step-and-terrace structure similar to the pre-annealed substrates. Figure 4.6 shows a 5×5 μm scan for a substrate and a SL(2-5)$_{20}$ superlattice for comparison. RMS values are of the order of 2 Å over the same area.
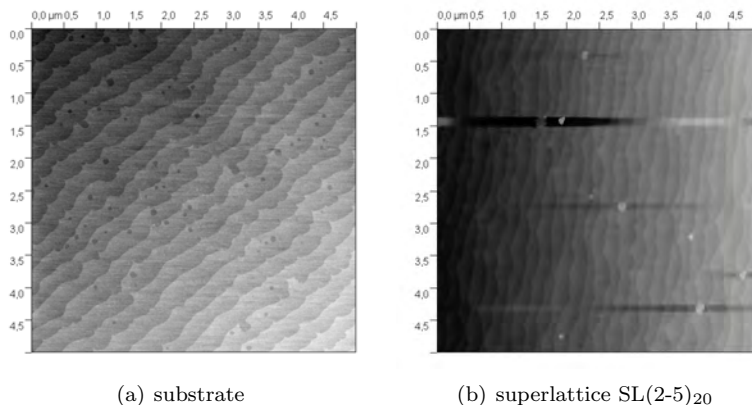

(a) substrate   (b) superlattice SL(2-5)$_{20}$

Figure 4.6: Comparison of top surface AFM scans for (a) substrate and (b) SL(2-5)$_{20}$ superlattice.

XRD θ-2θ scans give an average c-axis parameter of 3.77 Å, which is close to the weighted-average of the c-axis parameters of the thick films of LTO and LAO. Figure 4.7(a) shows that thickness fringes are observed, confirming the quality of the superlattice. For the SL(2-5)$_{20}$ the fringes confirm the superlattice period of 7 monolayers. Reciprocal space mapping shows that the films are coherently grown on the substrate. For the SL(1-5)$_{20}$ the reciprocal space map shows $a = 3.902$ Å, $c_{STO} = 3.906$ Å and $c_{film} = 3.77$ Å which is very close to bulk STO and the value obtained from θ-2θ scans, respectively.

To check the crystal structure in more detail, STEM was performed by Dr. L. Fitting-Kourkoutis[2] on a special superlattice with different LTO thicknesses and a protective STO capping layer. HAADF images such as those in the inset in Figure

---

[2]Muller group, Cornell University, Ithaca, USA.

(a) θ-2θ scan of SL(2-5)$_{20}$

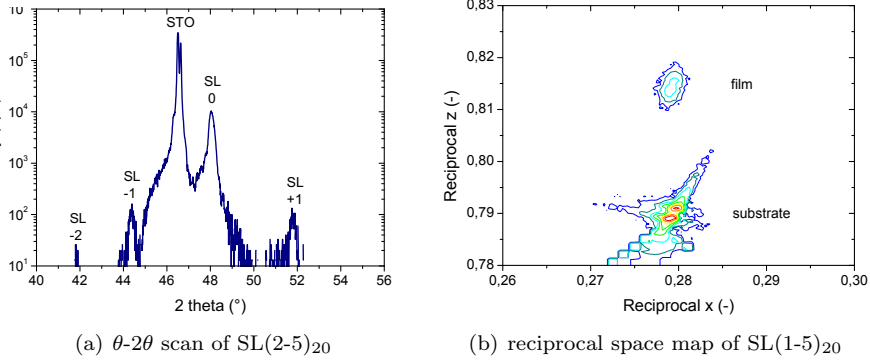(b) reciprocal space map of SL(1-5)$_{20}$

Figure 4.7: XRD scans of LTO/LAO superlattices.

4.8 show that the heterostructure is coherently grown. Both the STO substrate and STO capping layer for this special sample are easily distinguished because of the difference in atomic weight of the constituent ions. The difference between the LTO and LAO layers is more difficult to see, especially for the thinnest LTO layers.
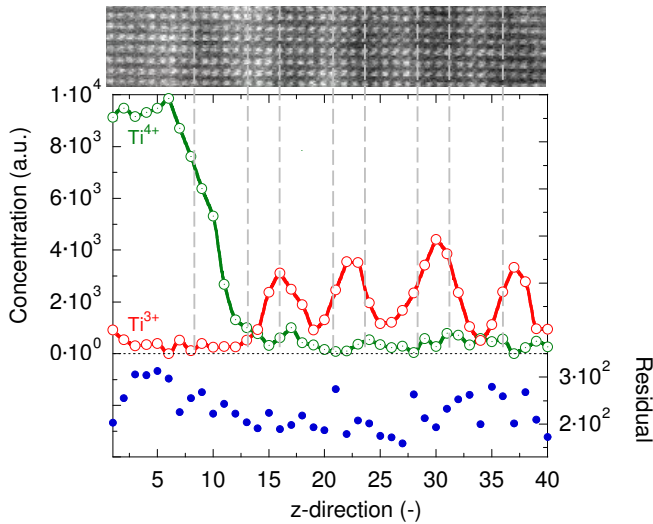
Figure 4.8: HAADF image (top) and STEM/EELS scan (bottom) of a LTO/LAO superlattice.

The different EELS fingerprints for Ti^{3+} and Ti^{4+} allow to deconvolve the Ti^{3+}/Ti^{4+} content of the different layers. In Figure 4.8 the z-scan starts from the STO capping layer and then moves into the LAO/LTO superlattice. The Ti^{4+} signal disappears as the superlattice is entered and the Ti^{3+} signal shows a peak every time a LTO

68

layer is encountered. Because both superlattice layers contain lanthanum which has a large atomic mass, there is little contrast between the layers. Still, the atomic mass difference between titanium and aluminium is large enough for the LTO layers to show up as brighter layers in the HAADF image. These brighter bands coincide with the Ti^{3+} peaks in the EELS trace.

4.3.2 Comparing LaTiO$_3$/SrTiO$_3$ and LaTiO$_3$/LaAlO$_3$

A more extensive EELS study on similar LTO/LAO superlattices fabricated by Dr. N. Nakagawa[3] shows that the confinement of the electrons has increased. Figure 2.11 shows the EELS profile across a single LTO layer. Assuming that the integrated electron density under the curve is the same for all samples, the peak fraction is directly proportional to the degree of confinement. The closer to one electron per unit cell the peak fraction is, the closer the system is to a Mott state. First because a higher fraction implies a higher local electron density and second because the smaller distribution out-of-plane confines the current path to the Mott-active LTO layer.

Figure 4.9 plots the peak fraction as a function of the number of LTO layers and shows that for thicker LTO layers the peak fraction increases and comes closer to 1. Which is unsurprising, as for thicker layers the bulk behaviour is recovered[10]. Furthermore, the peak height for the LTO/LAO system is significantly higher than that for the LTO/STO system: 0.85 vs. 0.25 for 1 monolayer of LTO. This shows that the electron confinement is much higher in the LTO/LAO system.
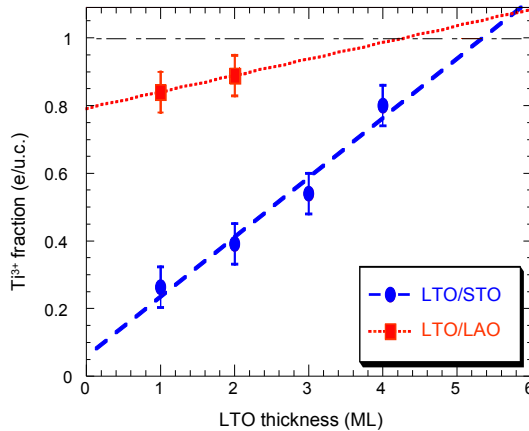
Figure 4.9: EELS Ti^{3+} fraction vs. LTO layer thickness. The data for the LTO/STO system is from Ohtomo[10], the data for the LTO/LAO system from private communications. The lines are guides to the eye.

Such a change in local electron density should be reflected in, for example, transport measurements. Figure 4.10 shows a comparison of the transport behaviour

[3]Hwang lab, University of Tokyo, Tokyo, Japan. Currently at Toshiba Research, Japan.

of two representative superlattices: one a LTO/LAO superlattice, the other a LTO/STO superlattice. The as-grown samples behave metallic, aside from a small upturn below 40 K for the LTO/LAO superlattice. Upon post-annealing at 400-600 °C in flowing oxygen for 2 hours, the behaviour changes completely. The LTO/LAO superlattices (and the single-layer LTO/LAO samples from the next Section as well) become insulating, while for the LTO/STO superlattices the conductivity decreases but stays metallic.

The transport properties of more recently grown samples were dominated by the large substrate contribution, but they turn insulating upon post-annealing as well. This is exemplified by the observation that LAO//STO interfaces fabricated with both terminations were found to be conducting, opposed to what was found in literature[7]. Later investigation showed that the STO substrates themselves, in combination with the low deposition pressure[11], are the most likely cause for this behaviour. Infrared spectroscopy showed a larger Drude behaviour in these substrates compared to later substrates from different suppliers. This behaviour is further discussed in the next chapter on single LAO//STO interfaces. The importance here, however, is that though transport measurements on these samples are dominated by the substrate contribution, the metal-to-insulator transition upon post-annealing still shows that the superlattice itself also turns insulating.
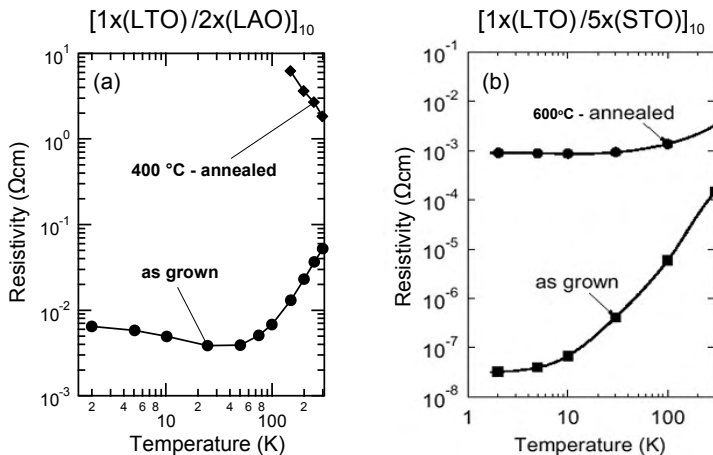
Figure 4.10: Resistivity as a function of temperature for two superlattices:
(a) LTO/LAO and (b) LTO/STO.

The increase in resistivity upon post-annealing is a familiar feature of STO. Post-annealing in general reduces the number of oxygen vacancies that can contribute to the mobile electron density[12, 13]. In LTO post-annealing could turn the LTO layers from the 113 phase into the 227 phase[6, 14]. However, reciprocal space mapping before and after post-annealing showed no change in the crystal structure. The striking difference in the transport properties of the post-annealed samples cannot be explained by this mechanism. Assuming that the LTO layer is

the conduction channel, a Mott metal-to-insulator transition driven by the electron density might be involved here, since the local electron density is very different between the two samples.

To investigate whether this transition fits with Mott theory, the Mott criterion (Equation 2.13) can be evaluated for both systems. Equation 2.6 readily gives the Bohr radius, taking into account the effective mass and dielectric constant of the system. Both these parameters are dependent on the electron density[15–17], as shown in Figure 4.11(a) for the effective mass. The local electron density takes more consideration. Figure 4.11(b) shows that for the LTO/STO system the local electron density drops off exponentially away from the central LTO layer.

(a) effective mass in $Sr_{1-x}La_xTiO_3$ (b) Ti^{3+} trace in LTO/STO, log-scale
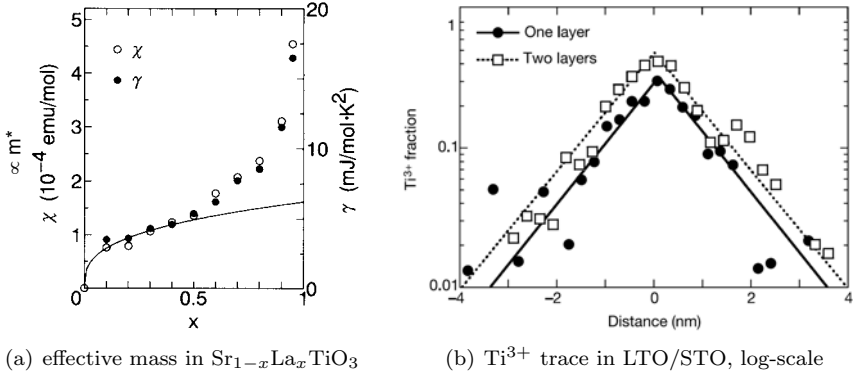
Figure 4.11: Important parameters for the calculation of the Mott criterion.
Graphs taken from respectively (a) Ref. [15] and (b) Ref. [10].

From this Figure it is clear that the Ti^{3+} fraction drops by a factor of 100 3 nm away from the interface, which is three times the decay length L of the exponential decay. The area enclosed by this boundary includes about 95 % of the electron density and is taken as the size of the electron layer. For the average local electron fraction we find:

$$\langle f \rangle = \frac{2 \int_0^\infty f_{\max} e^{-z/L} dz}{2\,3L} = \frac{2 f_{\max} L}{6L} = \frac{f_{\max}}{3} \tag{4.1}$$

where $f_{\max}$ is the maximum Ti^{3+} peak fraction observed from EELS. The local electron density is then calculated by dividing by the volume $a^2 6L$. Table 4.2 shows all parameters and the outcome for the Bohr radius, local electron density and Mott criterion. The value for L for the LTO/LAO system is based on the fact that the total number of electrons doped by the LTO layers $2 f_{\max} L$ should be the same for both systems.

Referring back to Equation 2.13 the LTO/LAO system fulfils the criterion and can be thought to be a Mott insulator. The LTO/STO system, however, far exceeds the criterion and thus stays metallic; the distance between the electrons is too large compared to the Bohr radius for the electrons to correlate so strongly that an insulating phase is formed.

parameter	LTO/STO	LTO/LAO
m^* (-)	1.8	6[15, 16]
K (-)	120[17]	20
$f_{\max}$ (-)	0.25	0.85
L (Å)	10[10]	3
a_{Bohr} (Å)	35	1.8
$\langle n \rangle$ (cm^{-3})	$9.1 \cdot 10^{19}$	$1.0 \cdot 10^{21}$
$a_{\mathrm{Bohr}} \sqrt[3]{\langle n \rangle}$ (-)	1.59	0.18

Table 4.2: Parameters and calculated results for the determination of the Mott criterion.

4.3.3 Origin & stability of the 2D Mott insulating state

While the previous discussion is suggestive, transport measurements cannot provide complete proof for a Mott transition as they cannot probe the insulating state. In addition, the contribution from oxygen vacancies in the STO substrate induced during the low-pressure growth make it difficult to draw conclusions based purely on the transport data. Optical measurements, however, can probe the insulating phase and any substrate contribution can be subtracted using an appropriate reference sample, in this case a thin LAO film on STO. In collaboration with the Research Center for Oxide Electronics, Seoul National University, South Korea such measurements were performed by Dr. S.S.A. Seo[4]. For absorption measurements the light travels through the entire substrate, so any contributions from the substrate will show up strongly compared to the signal from the small probed volume of the superlattice. GdScO$_3$ is then a better choice as a substrate compared to STO, which is very sensitive to oxygen vacancies, or LAO, which has a twinned crystal structure. Figure 4.12 shows the absorption spectrum of a SL(1-5)$_{20}$ superlattice grown on GdScO$_3$. Two distinct energy gaps can be observed, one close to the Mott-Hubbard gap for LTO of 0.4 eV and one close to the charge-transfer gap in LTO as observed from a LTO reference sample. This Mott-Hubbard gap again points to a Mott insulating state being present in the LTO/LAO system.

The single-band Hubbard model from Equation 2.11 is useful in introducing basic concepts in correlated electrons. Since perovskites will have a multi-band structure a multi-band model is required. In the case of the Ti 3d^1 ion the lowest occupied orbitals are d$_{xz/yz}$ orbitals due to crystal field splitting. In this t$_{2g}^1$ system there are three possible transition energies, though five orbital/spin configurations[18]. Table 4.3 lists all five configurations and their corresponding transition energies. The transition energies are shown in terms of the Coulomb repulsion energy U and the inter-orbital Hund coupling energy J_{H}.

In the absorption spectra in Figure 4.12 the higher energy transitions seem to be very weak, with only the $U - 3J_{\mathrm{H}}$ transition clearly visible. The strength of this

---

[4]ReCOE, Seoul National University, Seoul, Korea. Currently at Oak Ridge National Laboratory, USA.
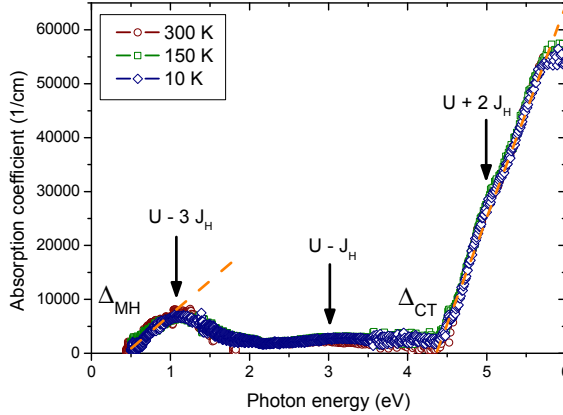
Figure 4.12: Absorption spectrum for a SL(1-5)$_{20}$ superlattice on GdScO$_3$.

$U - 3J_{\mathrm{H}}$	$U - J_{\mathrm{H}}$	$U + 2J_{\mathrm{H}}$
AFO/FM	FO/AFM	FO/AFM
AFO/AFM	AFO/AFM	

Table 4.3: Orbital/spin configurations in a multi-band Hubbard model for a t$_{2g}^1$ electron system[18]. (A)FO (anti)ferro-orbital order, (A)FM (anti)ferromagnetic order.

feature suggests that the occupied Ti 3d orbitals are antiferro-orbital ordered xz/yz orbitals. This configuration lowers the overlap of occupied orbitals, as in the z-direction the neighboring AlO$_2$ layers do not contain electrons. Using the spectral features indicated in Figure 4.12, we can estimate the values for the Coulomb repulsion $U = 3.6 \pm 0.1$ eV and the Hund coupling $J_{\mathrm{H}} = 0.78 \pm 0.05$ eV. The former is lower than the value of 4.5 eV commonly assumed for early 3d transition metals, while the latter is close to the common value of 0.7 eV[18]. This possible reduction of the Coulomb repulsion U could push the system out of the Mott insulating state. But the antiferro-orbital ordering will also reduce the hopping energy and thus the bandwidth. So the U/W ratio (see Equation 2.12) stays about the same and the system can still be Mott insulating though having a lower Coulomb energy.

Though indicative, internal reflections make it very difficult top deconvolve an absorption measurement of a superlattice into fundamental material properties such as the optical conductivity. Ellipsometry allows the determination of such properties directly from the observed reflectance intensity and phase. With measurements at different incident angles it is even possible to determine in-plane and out-of-plane contributions. Figure 4.13 shows the real part of the optical conductivity for the in-plane (a) and out-of-plane (b) direction[19].
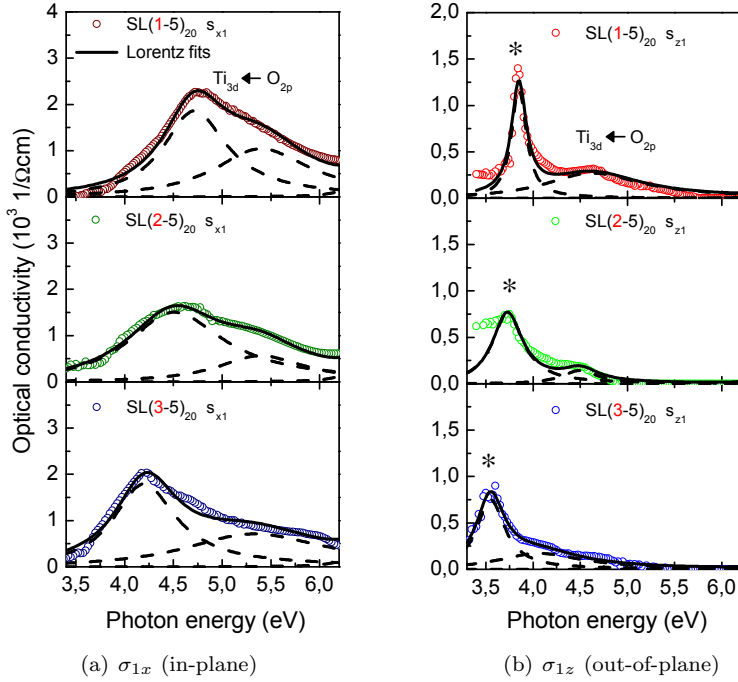
Figure 4.13: Real part of the optical conductivity (a) in-plane and (b) out-of-plane for LTO/STO superlattices as obtained from ellipsometry. The fitted Lorentz peaks for (a) are the t_{2g} and e_g at low and high energy, respectively. The * marks a new transition in (b).

The Lorentz fits shown in Figure 4.13 represent the transitions between two electron bands. The actual shape of the peaks is actually a convolution of the shape of both bands, as the transitions can take place from anywhere in one band to anywhere in the other band. Both transitions at 4.5 and 5.5 eV can be contributed to $O_{2p} \rightarrow Ti_{3d}$ transitions. The sharp peak in the out-of-plane optical conductivity around 3.7 eV (marked with an *), however, has been observed in neither bulk LAO nor bulk LTO. Near the surface of LTO some similarities to the optical conductivity in Figure 4.13(b) seem to appear. This means the peak is unique to a LTO interface, though the exact link between the two is unclear. One possibility is that the induced orbital order at the interface gives rise to special bands. The sharpness of the peak indicates that both of the electron bands involved in this transition are narrow.

Local density approximation DFT calculations were done by Dr. M.J. Han[5] using LDA+U with a Coulomb energy U of 6 eV[20, 21]. The supercells for the calcula-

---

[5]Department of Physics and Astronomy and Center for Theoretical Physics, Seoul National University, South Korea.

tion have a $\sqrt{2} \times \sqrt{2}$ basis and a similar stacking as the superlattices investigated with ellipsometry. Figure 4.14 shows the partial density of states (PDOS) for the TiO$_2$ slabs for each of the superlattice configurations with 1, 2 or 3 monolayers of LTO.
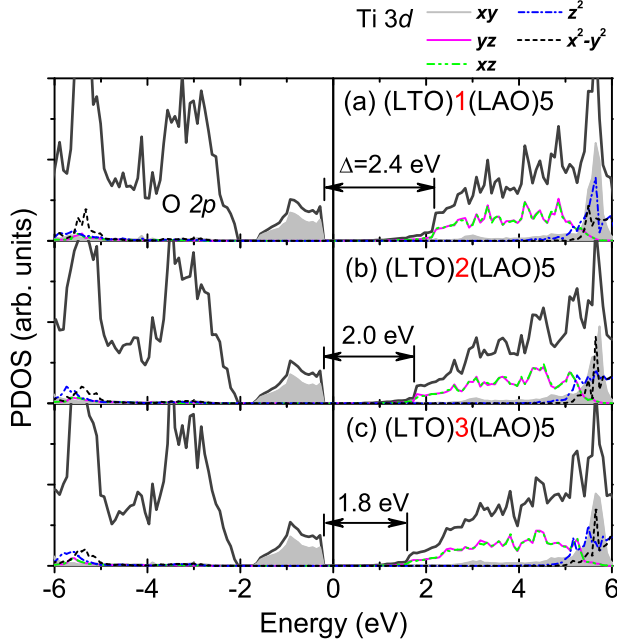

Figure 4.14: Partial density of state plots for the TiO$_2$ layers in a SL$(p$-5$)_n$ superlattice from DFT calculations.

It is immediately clear that the d$_{xy}$ state is much lower in energy compared to the other t$_{2g}$ d$_{xz/yz}$ states. This is notably different from bulk LTO where the near cubic unit cell leads to an absence of orbital order[22]. The spins order in a checkerboard antiferromagnetic (AFM) pattern. This AFM ordering is of a lower energy scale compared to the xy - xz/yz separation, as a forced ferromagnetic ordering still yields the d$_{xy}$ state as the ground state. Such an in-plane ordering can be expected, because the hybridization out-of-plane is much weaker due to the Al states which are much higher in energy.

The occupation of the Ti 3d$_{xy}$ orbital increases the in-plane interaction, enhancing a Mott insulating state. Indeed, this xy orientation is present for all LTO thicknesses, which agrees with the observation that all samples turn insulating upon post-annealing (See Figure 4.10(a)). The calculations also show that the crystal field splitting between the t$_{2g}$ xz/yz and e$_g$ z^2 & x^2-y^2 levels shifts with increasing LTO thickness. This behaviour can also be observed in the in-plane optical conductivity in Figure 4.13(a) from the difference between the two peak positions. Figure 4.15 shows how this energy difference increases with increasing LTO layer thickness, similar to the DFT calculations. The differences in magnitude may be

due to the fact that DFT calculations always underestimate energy differences, especially for empty states. This correspondence shows that only the Ti $3d_{xy}$ is occupied.

This configuration, Ti $3d_{xy}$ occupation and AFM ordering, is strikingly similar to that of the cuperate mother compounds which are also Mott insulators. The electrons are confined to the LTO layer, which agrees with the confinement obtained from the EELS data. This confinement is the driving factor behind the Mott state of the 2D electron layer in the LTO.
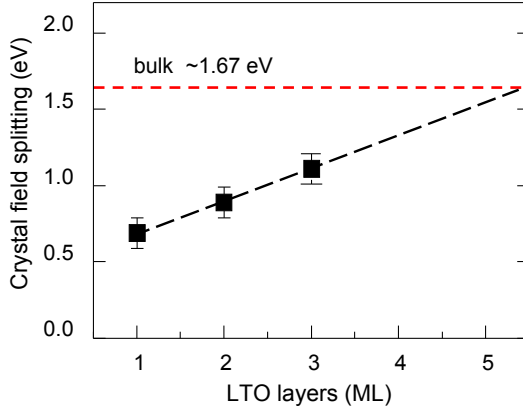

Figure 4.15: Observed crystal field splitting from in-plane optical conductivity in Figure 4.13(a).

From the calculations there is no clear candidate for the sharp transition at 3.7 eV. However, the sharpness of these peaks still indicates that both initial and final states for this transition are narrow. The d_{xy} level is still a likely candidate for the initial state because it, like the new transition, is a new feature of these superlattices. Experimentally, such a narrow band can be expected because of the high degree of directionality (compared to bulk LTO) of the Ti $3d_{xy}$ orbital.

4.4 Single layers of LaTiO$_3$ in LaAlO$_3$

Probing the dependence of the properties of LTO layers on another interface or surface nearby is very interesting due to the possibilities provided by doping from one interface to the other[23]. The embedded layers of LTO in the superlattices are all deeply buried within the structure and difficult to probe as a function of the layer separation. XPS allows for the probing of layers close to the sample surface where interaction between layer and surface is possible. Just like EELS, XPS is also capable of probing both the chemical and electronic state of a sample. Given the limited measurement depth of XPS, samples with only a few layers of LTO beneath a LAO capping layer of varying thickness are required.

4.4.1 Structural characterization

AFM scans of the top surface of single-layer samples show similar results to the superlattices. Figure 4.16 shows a 5×5 μm scan for a substrate (a) and a single-layer sample (b) for comparison. RMS values are of the order of 2 Å over the same area and roughly the RMS value seems to decrease for thicker LAO capping layers. Measuring the friction force on the AFM tip gives an indication for the chemical composition of the surface; though identification of the surface is not possible, it is possible distinguish whether the surface has a single termination or not. Figure 4.16(c) shows that indeed the surface of a PS(10-2) sample is single-terminated. As the stacking is preserved in layer-by-layer growth the top surface is expected to be AlO_2.

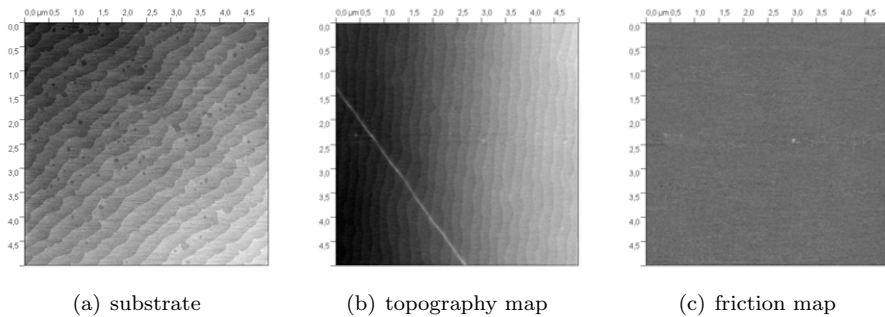(a) substrate   (b) topography map   (c) friction map

Figure 4.16: Comparison of top surface AFM scans for (a) substrate topography and a PS(10-2) single-layer sample (b) topography and (c) friction map.

XRD θ-2θ scans give an average c-axis parameter of 3.747 Å, which is smaller than the average c-axis parameter for superlattices. This might be due to a larger relative fraction of LAO in the sample compare to the superlattices. ϕ-scans around (112) shows a four-fold symmetry in the same crystal directions for both substrate and film. Reciprocal space mapping, in this case over the (h1l) plane around (012), shows that the films are coherently grown on the substrate. For the PS(5-2) single-layer film shown in Figure 4.17 $c_{\text{film}} = 3.76$ Å, close to the value for thick LAO films and the value obtained from θ-2θ scans.

4.4.2 Electronic configuration as a function of surface separation

XPS can distinguish between Ti^{3+} and Ti^{4+}, thus giving a clear probe for the electronic state of the titanium in the LTO layer. In the single-layer samples the thickness of both the LTO layer (1-3 monolayers) and the LAO capping (1-15 monolayers) was varied. The 30 monolayer LAO buffer was thick enough, given the estimated penetration depth of about 20 Å, to prevent observation of any
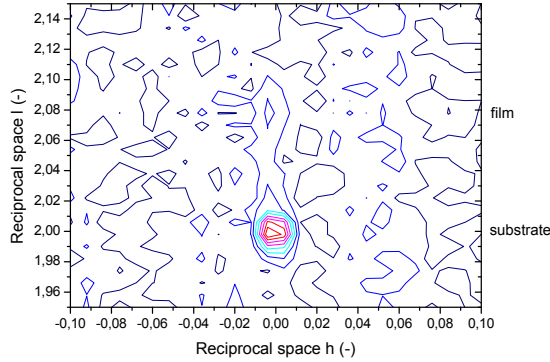
Figure 4.17: Reciprocal space mapping over the (h1l) plane around (012) of a PS(5-2) single-layer sample.

signal from the STO substrate, so any titanium observed is from the LTO layer. In addition, this 30 monolayer is enough to electronically separate the LAO//STO interface at the substrate from the LTO layer. Figure 4.18 shows the XPS spectra around the Ti 2p peak that were measured by Dr. Takizawa[6]. The smaller peak at 457 eV is the signature for Ti^{3+}. It can clearly be seen that the fraction of Ti^{3+} increases with the LAO capping layer thickness.

Figure 4.18: XPS spectra of the PS(m-2) samples series around the Ti 2p peak.

---

[6]Fujimori group, Department of Physics and Department of Complexity Science and Engineering, University of Tokyo, Japan. Currently at the SR Center, Ritsumeikan University, Japan.

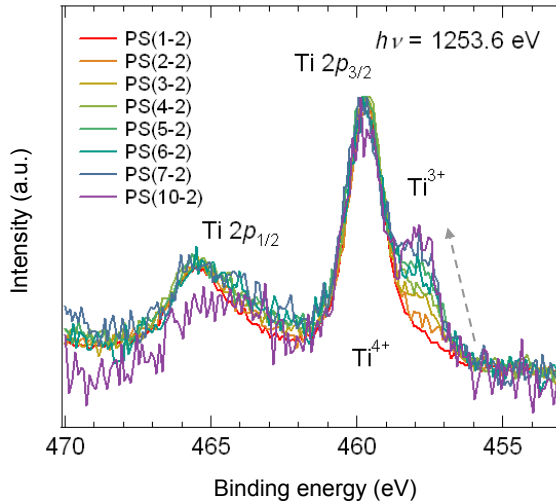Using reference spectra for Ti^{3+} and Ti^{4+} the measured spectra from Figure 4.18 can be deconvolved and the relative Ti^{3+} fraction ($[Ti^{3+}]/[Ti^{4+}]+[Ti^{3+}]$) can be determined. Figure 4.19 shows the Ti^{3+} fraction vs. the LAO capping thickness for all three LTO layer thicknesses and compares it with the similar LAO/LVO system[23]. Both LTO and LVO are Mott insulators, but Ti^{3+} has a $3d^1$ electron configuration while V^{3+} has a $3d^2$ configuration.

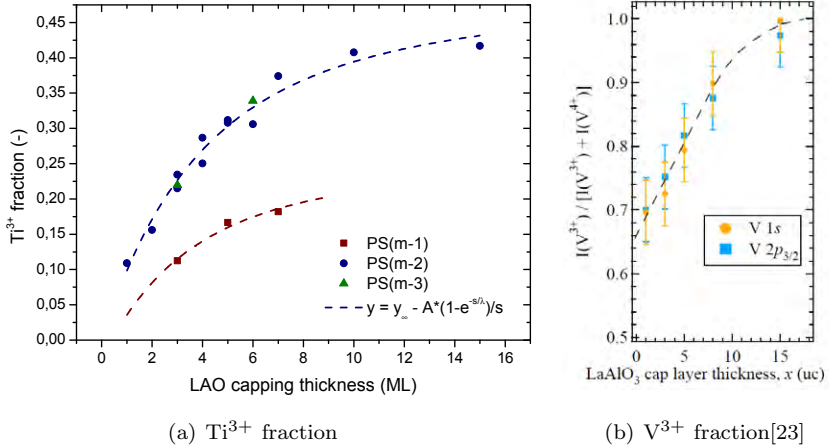(a) Ti^{3+} fraction

(b) V^{3+} fraction[23]

Figure 4.19: Comparison of the Ti^{3+} (a) resp. V^{3+} (b) fraction as a function of the LAO layer thickness. The lines in (a) are fits to Equation 4.8. LVO thickness is 3 ML. The graph in (b) is taken from Ref. [23].

The trend shown in both the LTO/LAO and the LVO/LAO system is that for thicker LAO capping the B^{3+} fraction increases. This is due to a balance between two processes. One is oxygen vacancy creation at the air//LAO surface. To fully oxidize the AlO_2 termination requires extra electrons. For PS(m-n) samples with thick LAO layers these extra electrons generally come from oxygen vacancies, which cost energy to create. These oxygen vacancies form V^* donor states at the interface and cause band bending in the LAO conduction band. The doped electrons are trapped on the remaining oxygen ions so no surface conducting state exists. As the LAO capping becomes thinner, the second process of electron transfer from the Ti $3d^1$ bands to the surface can provide some of the required electrons, reducing the cost of vacancy creation but keeping the band bending. In addition the transferred electrons create a dipole that lowers the energy across the entire LAO capping layer. As these electrons are transferred, the vacancy creation costs is further reduced. This process ends when the potential due to the electron transfer lowers the LAO conduction band to the energy level of the LTO conduction band. This process is schematically shown in Figure 4.20. Unlike the LAO//STO interface, there is no inherent polar discontinuity here, as both LTO and LAO are $A^{3+}B^{3+}O_3$ perovskites. In addition, the LAO buffer layer breaks the polar discontinuity necessary for a conducting interface.
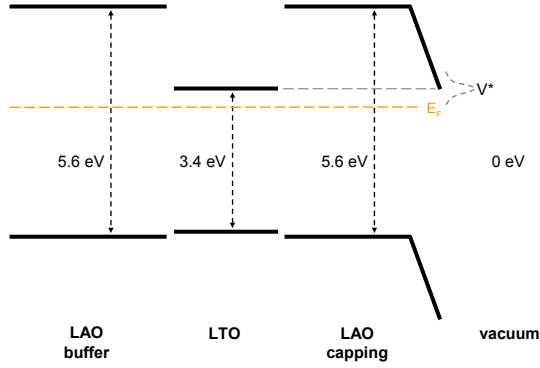
(a) with surface vacancies
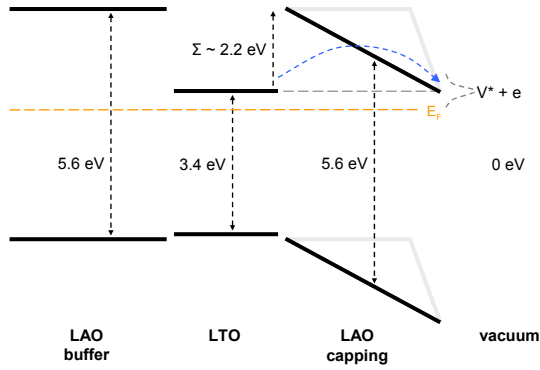
(b) after electron transfer

Figure 4.20: Band schematics for the doping mechanism of LTO/LAO single layers. (a) the initial schematic with surface vacancies, (b) the schematic with electron transfer.

As Figure 4.20(a) shows even thin LAO capping layers need to overcome an energy difference of about 2.2 eV. In the ultimate case of a single monolayer of LAO this seems not possible. For such strong depletion layers it is possible to calculate the extent of the band bending using the Schottky depletion width from the equation[24]:

$$|\Phi| = \left| \frac{e n_{\mathrm{donor}} d^2}{K \epsilon_0} \right| \tag{4.2}$$

Here Φ is the potential shift, n_{donor} is the 3D donor density, K is the dielectric constant of the material and d is the depletion width. For the case of a single monolayer of LAO, the dielectric constant is very small, as there is little to no

material to screen the electric field, so $K = 2$. The potential difference is $\Phi = 2.2$ eV and the donor density is derived from the vacancy density at the surface where $(AlO_{15/8})^0$ so $n_{donor} = \frac{1/8}{a^2 d}$ where $a = 3.905$ Å is the in-plane lattice parameter[7]. The Schottky depletion width calculated with these values is 3 Å, or 0.8 monolayer. This shows that a single monolayer of LAO can induce such a large band shift, primarily due to the large donor density of $3 \cdot 10^{21}$ cm^{-3}.

To model this electron transfer a dipole model can be used. In the initial state, the entire LAO/LTO/LAO stack is $A^{3+}B^{3+}O_3$. The AlO_2 surface needs electrons to reconstruct. Normally, these are due to oxygen vacancies. However, in the LTO/LAO system electrons can be transferred from the LTO layer to the surface because titanium is multivalent. These transferred electrons give rise to a dipole:

$$D_{et} = q\Delta z = (1 - x)esc \tag{4.3}$$

where x is the observed Ti^{3+} fraction per unit cell, c is the LAO c-axis lattice parameter and s is the number of LAO capping monolayers. The factor $(1 - x)$ is included because the amount of transferred electrons is one minus the amount of remaining electrons.

A dipole gives rise to a polarization:

$$P = \frac{D}{V} \tag{4.4}$$

where $V = a^2 sc$ is the supercell volume with a the in-plane STO lattice parameter. The resulting electric field is related to the polarization by $P = \epsilon_0 \chi E$, where χ is the susceptibility. The potential resulting from a dipole is:

$$\Phi = Esc = \frac{Psc}{\epsilon_0 \chi} = \frac{D}{\epsilon_0 \chi a^2} \tag{4.5}$$

Electrons will be transferred until the donor state, the LTO conduction band, is level with the receiver state, the LAO conduction band at the surface. Thus electrons are transferred until the dipole energy reaches Σ, which for two semiconductors would be equal to the difference in the band gaps. If more electrons are required for full oxidation of the surface, vacancies are formed to provide the additional electrons. However, the transferred electrons stay because that is energetically favourable compared to complete surface reduction. The LTO layer is now partially reduced to Ti^{4+}, which could be interpreted to induce a polar catastrophe. However, only a few monolayers of LTO embedded in LAO are not enough to force the potential in LAO to diverge very much. A small amount of band bending does occur, as discussed in the next Section.

Equating Σ to Equation 4.5, substituting Equation 4.3 for the dipole and solving for the Ti^{3+} fraction x yields:

$$x = 1 - \frac{\epsilon_0 \chi a^2 \Sigma}{esc} \tag{4.6}$$

[7]Per unit cell area $2x$ electrons are necessary. 3 electrons are available from the Al ion with another 1/2 electron from the LaO layer below the surface layer. The other electrons are supplied by vacancies: $2(2 - x)$. Equating supply and demand results in an oxygen fraction of 15/8.

A similar equation was arrived at from discussing the balance between electron transfer processes across the entire stack (surface to substrate) and across the buffer layer (LTO layer to substrate)[25]. However, surface-interface interaction is mostly limited to LAO films thinner than 10 monolayers[5], so for this system the LAO buffer layer of 30 monolayers is enough to decouple the LTO layer from the substrate/film interface.

Now the susceptibility can also depend on the thickness of the LAO capping layer. For very thin layers the crystal structure of the LAO layer can deform and susceptibility is reduced. Here a simple exponential decay is assumed, given the fact that the crystal structure was found to relax exponentially away from an interface as well[26].

$$\chi = \chi_0 \left(1 - e^{-s/\lambda}\right) \tag{4.7}$$

where $\chi_0 = K - 1$ is the bulk susceptibility. Substitution into Equation 4.6 gives a corrected equation:

$$x = 1 - \frac{\epsilon_0 \chi_0 a^2 \Sigma}{ec} \frac{\left(1 - e^{-s/\lambda}\right)}{s} \tag{4.8}$$

An equation of this form has been fit to the data from Figure 4.19. As the PS(m-2) series has the most data points, a function of the form $x = x_\infty - A(1 - e^{-s/\lambda})/s$ has been fit to this series. As material parameters were taken $a = 3.905$ Å, $c = 3.747$ Å from the XRD measurements and $K = 24$. The resulting fit is shown in Figure 4.19(a). The data for the PS(m-3) series seem to coincide with that of the PS(m-2) series. The PS(m-1) series has too few points to reliably fit the function. However, assuming that the susceptibility evolves the same in all cases (i.e. $\lambda = 2$ ML), values for x_∞ and Σ can be obtained. All these parameters, as well as quality-of-fit values are shown in Table 4.4.

parameter	PS(m-1)	PS(m-2)
x_∞ (-)	0.27 ± 0.02	0.51 ± 0.03
Σ (eV)	1.1 ± 0.2	2.2 ± 0.5
λ (ML)	2 (fixed)	2.3 ± 0.5
R^2 (-)	0.973	0.972
X^2 (-)	$7 \cdot 10^{-5}$	$31 \cdot 10^{-5}$

Table 4.4: Fit parameters for fitting Equation 4.8 to the electron density data from Figure 4.19.

For the series with the thicker LTO layer the expected energy shift of 2.2 eV is indeed recovered. The lower energy barrier for the 1 monolayer LTO series can be explained from the fact that for a single monolayer of LTO the electron interactions are purely two-dimensional. This Coulomb interaction raises the energy of the electrons in the LTO layer, so that delocalization of those electrons lowers the energy of the system. This energy bonus ΔU reduces the effective energy shift from the pure band gap difference Σ to $\Sigma - \Delta U$.

The most striking observation is that the Ti^{3+} fraction does not go up to 1 for very thick capping layers where no electron transfer is expected. The fitted parameter $x_\infty = 0.27$ resp. 0.51 shows this clearly. This is in contrast to the LVO/LAO system, which does go to 1 for thick layers as seen from Figure 4.19(b). From the EELS measurement on the superlattices, which were grown under the same conditions, the Ti^{3+} fraction of the embedded LTO should also be close to 1, as seen from Figure 4.8.

This low Ti^{3+} fraction is especially pronounced for the PS(m-1) series. Whatever is the mechanism for lowering the amount of detected Ti^{3+}, it is different between the 1 and the 2 & 3 monolayer LTO series. It cannot be a thickness effect, because then the 2 and the 3 monolayer LTO series should be different as well. A similar step change when going from 1 to more monolayers of LTO was found in the DFT calculations for the superlattices. There the abrupt change in orbital order from 1 to 2 monolayers of LTO was the likely cause. Though the optical conductivity data points to a more gradual change in orbital order still the change from pure xz/yz orbital order to mixed $xy/xz/yz$ order may be related to this change in the XPS signal.

A mixed phase LTO layer with both 113 and 227 could explain the lower Ti^{3+} content, but no sign of the 227 phase was observed with XRD. Also, it is known that LTO only adopts the 227 phase for layers thicker than 3 monolayers[14]. Post-annealing did not change the crystal phase as far as observed from reciprocal space mapping and ϕ-scans. The transport measurements do change upon post-annealing, changing from conducting to insulating. This may indicate a filling of oxygen vacancies, either in the film or in the substrate. Given the oxygen affinity of both LTO and LAO it is more likely that it is the substrate that is re-oxidized. An oxygen-deficient substrate would also explain the observation that both substrate terminations yield a conducting LAO//STO interface.

Another possibility is that for the thicker LTO layers the Ti^{3+} electrons are distributed differently over the different monolayers, as observed in LVO[27]. Angle-dependent measurements such as shown in Figure 4.21(a), however, show no difference for an incident angle of 0 or 60°. This indicates that the Ti^{3+} density is nearly the same throughout the entire LTO layer. Also, as the effective penetration depth is halved for the measurement at 60°, again any contribution from the STO substrate is excluded. What the XPS did observe was an apparent off-stoichiometric La/Al ratio of 0.8. Figure 4.21(b) shows how the La 4d peaks are lower for the grown films compared to a single-crystal substrate when the spectra are normalized to the Al 2p peaks. However, quantitative chemical characterization by XPS is difficult. For example, the Sr/Ti ratio for TiO_2 terminated STO single-crystal substrates was about 1.2 as obtained with XPS.

In the ionic limit, such a cation off-stoichiometry could explain the lower Ti^{3+} fraction. Assuming the lanthanum concentration is constant throughout the heterostructure and the heterostructure is fully oxidized, the chemical formula for the LTO layer could be written as:

$$La_{0.8}^{3+}Ti_x^{3+}Ti_{1-x}^{4+}O_3^{2-}$$
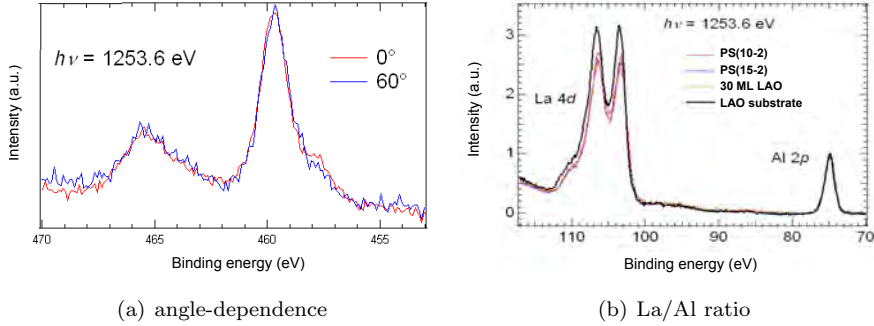
(a) angle-dependence

(b) La/Al ratio
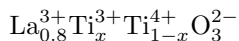
Figure 4.21: (a) Angle-dependent measurement of the Ti 2p of a PS(3-2) sample. (b) XPS spectra for core peaks of lanthanum and aluminium normalized to the aluminium peak, showing the apparent deficiency of lanthanum.

which yields $x = 0.4$, close to the observed value. However, with a penetration depth of about 20 monolayers, this would indicate that the La/Al ratio is off by 20 % for that entire stack. Such a large density of faults was not observed by TEM or XRD. All other non-113 La-Al-O compounds have a drastically different crystal structure that would show up in any XRD measurement.

As XPS is a very surface-sensitive technique, it might be important what the termination of the LAO reference substrate is. With a LaO layer on top, the La contribution to the XPS signal might be higher than the Al contribution from the subsequent AlO_2 layer. For the single-layer samples the termination of the top surface is AlO_2 as the substrate termination is preserved, so the La/Al ratio may be lower than one. However, XPS measurements on LAO layers grown on either TiO_2- or SrO-terminated STO show that that La/Al ratio is nearly identical for the LAO substrate and these two films. In addition, for the TiO_2-terminated STO substrates a Sr/Ti ratio of 1.2 was observed, which is the opposite of what would be expected based on the surface termination.

So neither oxygen nor cation off-stoichiometry seems to be the origin of this low Ti^{3+} fraction. Another possibility is an electron configuration that is not centered on the titanium ion and thus would have less influence on the observed core levels. However, such a configuration would induce changes in the XPS spectra of the other ions, something which is not observed in the XPS spectra reported here. Thus the origin of the reduced electron fraction is still unresolved.

4.4.3 Band bending as a function of surface separation

The changes in electron occupation with capping layer thickness should be reflected by changes in the band structure of the system. To probe this structure, photoreflectance measurements in the UV-visible range were performed on the

single-layer samples. Figure 4.22 show the photoreflectance spectra for the PS(m-2) series over the photon energy range 3.1-6.5 eV (400-190 nm). A systematic change of the minimum at 5.3 eV in both position and depth is clearly visible.
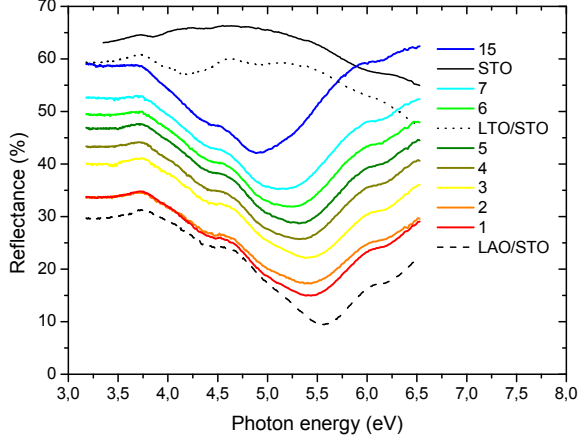

Figure 4.22: Photoreflectance spectra of the PS(m-2) series. The graphs are offset with respect to one-another for clarity.

From the graphs for STO and LAO//STO it can clearly be seen that the signal from the strained LAO dominates in the reflectance measurement. This is unsurprising as this is a relatively surface-sensitive measurement. However, interpretation of these measurements has to be done with great care, as the lack of a proper calibration makes comparing the magnitudes impossible. Still, comparison between reflectance measurements of a sputtered Ag film and literature data shows that though the magnitudes of the spectra are different, the energy positions of feature is not.

To unambiguously define the energy position of all transitions, the RefFIT[28] program was used. This program allows for the fitting of spectroscopic data to a variety of models for the optical properties. Here the reflectance was used, which is related to the dielectric function:

$$R = \left| \frac{1 - \sqrt{\epsilon(\omega)}}{1 + \sqrt{\epsilon(\omega)}} \right|^2$$

where R is the reflectance and $\epsilon(\omega)$ is the dielectric function describing the system. A combination of Lorentz oscillators was used to model the dielectric function. These oscillators describe the optical transitions seen in the reflectance data.

$$\epsilon(\omega) = \epsilon_\infty + \sum_i \frac{\omega_{p,i}^2}{\omega_{0,i}^2 - \omega^2 - \mathrm{i}\,\Gamma_i \omega}$$

Given the fact that the wavelength of the light is ten times the thickness of the single-layer structure any reflectance measurement probes the averaged dielectric function of the entire stack, so no interference effects are considered. ϵ_∞ is the high-frequency dielectric constant, which represents the constant dielectric constant far above the transition frequencies represented by the Lorentz oscillators. $\omega_{p,i}$ is the plasma frequency, $\omega_{0,i}$ is the eigenfrequency and Γ_i the damping factor for the ith oscillator. Of these, the plasma frequency and the damping factor control the shape of the Lorentz peak in the optical conductivity, which is derived from the dielectric function:

$$\sigma(\omega) = \frac{(1 - \epsilon(\omega))\,\omega}{4\pi}\mathrm{i}$$

The eigenfrequency determines the position of the Lorentz peak and is thus the one quantity that can be determined from the fitting of the reflectance data to the Lorentz oscillators. To fit the reflectance data 5 to 6 oscillators are needed. The two oscillators with the highest and lowest energies are influenced by the cut-off of the measurement range, so only the eigenfrequencies inbetween were considered.

Figure 4.23 shows the fitting results for a PS(7-2) sample. Figure 4.23(a) shows the reflectance data and the Lorentz fit. The quality-of-fit R^2 value was 0.9997. Outside the data range, the fit rapidly drops down to zero. This is the reason the outermost oscillators are not considered in the further discussion. Figure 4.23(b) shows the real part of the optical conductivity, both the total signal and its components. The contribution of each oscillator can clearly be seen.

Similar fits were obtained for all PS(m-n) samples, as well as bare STO and LAO substrates and LAO, LTO and STO films grown on STO substrates. Most of the eigenfrequencies are constant between samples, very close to those observed in the LAO and LTO films on STO substrates. Table 4.5 shows the typical eigenenergies for the PS(m-n) samples and for the references samples.

transition	PS(m-n)	LAO/STO	LTO/STO	bare STO	lit. STO[29]
E_2 (eV)	3.63	3.65	3.68	3.81	4.00
E_3 (eV)	4.53	4.53	4.57	4.53	4.86
E_4 (eV)	5.09	5.11	5.01	5.20	5.5
E_5 (eV)	5.5-5.9	5.89			

Table 4.5: Eigenenergies obtained from Lorentz fitting to the reflectance data for the PS(m-n) series and reference samples.

It is clear from Table 4.5 that there are large similarities between the PS(m-n) samples and the LTO and LAO films. The STO data, both experimental and from literature, is less compatible. This is because the strongest features of the spectra are due to the LAO film, not the STO substrate. The eigenenergies E_2, E_3 and E_4 are the averaged results for all PS(m-n) samples. The standard deviation of about 0.03 eV shows that they vary very little across the series.
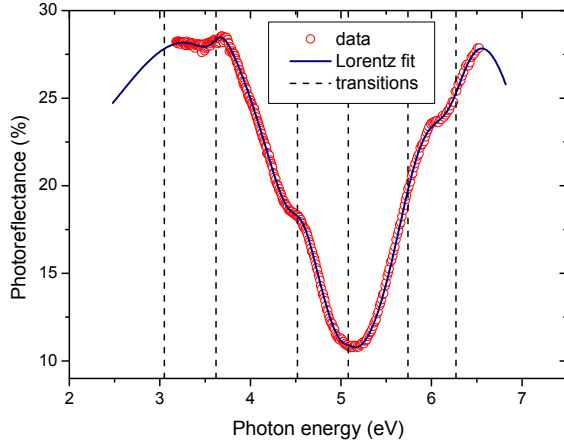
(a) reflectance fit
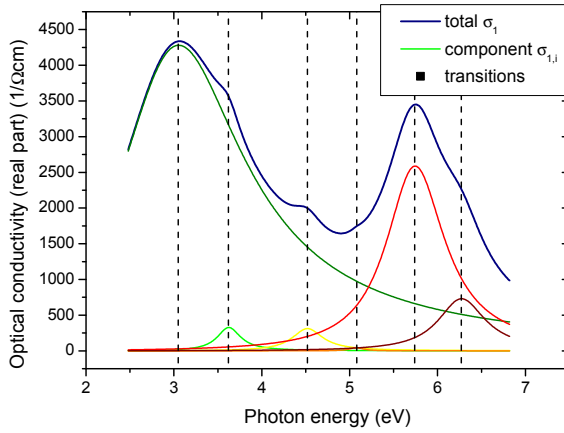
(b) optical conductivity

Figure 4.23: An example for a reflectance Lorentz fit for a PS(7-2) sample. (a) the reflectance fit and (b) the corresponding real part of the optical conductivity. Note that the magnitude of the optical conductivity is arbitrary, as the photoreflectance measurements were not properly calibrated.

The E_5 transition, however, does systematically depend on the LAO capping layer thickness. Figure 4.24 shows the eigenenergies for the E_4 and E_5 transitions for all PS(m-n) samples. Also included is the position of the minimum around 5.3 eV shown in Figure 4.22. The latter shows that the change in energies is not just

an artefact of the fitting process, but an actual feature of the spectrum. Figure 4.23(b) shows that the E_5 transition has a large spectral weight compared to the other transitions, indicating that it is a prominent feature of the spectrum.
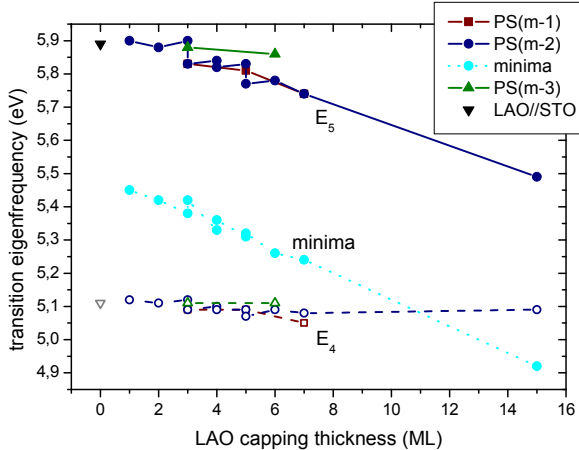

Figure 4.24: E_4 (open) and E_5 (filled) eigenenergies as a function of LAO capping thickness. The position of the minimum around 5.3 eV is shown for comparison.

From Figure 4.24 it can be seen that the E_5 transition energies decreases with increasing LAO capping layer thickness. Each unit cell lowers the transition energy with 0.03 eV, independent of the number of LTO layers involved. This is unsurprising, as Figure 4.22 shows that the PS(m-n) samples show a greater similarity to the LAO film than the LTO film or STO substrate.

It is of note that this band bending is not influenced by the electron density inside the LTO layer. Figure 4.24 includes all data for all three LTO layer thicknesses and they collapse onto a single line. In addition, post-annealing of these samples does not change the eigenenergies obtained from the reflectance fitting. Both of these findings point to the fact that this band bending is independent of the Ti^{3+} occupation and solely due to the LAO capping layer. This is unsurprising, as the dipole mechanism involves the LTO conduction band and the LAO conduction band minimum at the air//LAO interface, which are both pinned. Thus the LAO band bending is independent of the dipole mechanism discussed in the previous section.

Compared to the other energies in the system, this change is relatively small. The band shift energy $\Phi_{et} = \Sigma = 2.2$ eV is almost two orders of magnitude larger. Another energy scale associated with LAO/ATiO$_3$ systems is the dipole energy of the LAO film due to the charge difference between the $(LaO)^+$ and $(AlO_2)^-$ layers. As the ionic layer in LAO are charged, a dipole develops between them. In

the ionic limit, the dipole moment associated with a single LAO plane is given by:

$$D_{\text{uc}} = q\Delta z = e\frac{c}{2} \approx 1.9 \ \text{eÅ}$$

Using Equation 4.5 a value of $\Phi_{\text{uc}} = 1$ eV is obtained, again almost two orders of magnitude larger. This is an upper limit, as covalent effects can reduce the ionic character of the ions in correlated-electron materials. This also shows that the LAO capping layer does not have a polar discontinuity, as any potential shift on the order of one eV should be visible in XPS or optical measurements[30].

Going the other way, an energy difference per unit cell of 0.03 eV would require a dipole moment of 0.06 eÅ. Similar values were obtained for the LAO/STO system where the LAO distorts to (partially) compensate the polar catastrophe[31]. There, this mechanism is limited by the occurrence of electron transfer due to the polar discontinuity which lowers the energy of the dipole that builds across the LAO slab due to its interface with STO. In the LTO/LAO there is no such polarization discontinuity and the only driving force for the band bending is the lowering of the interface distortion between LTO and LAO. Compared to the 5.6 eV band gap of LAO the little amount of band bending required for the change in eigenenergies can easily be accommodated.
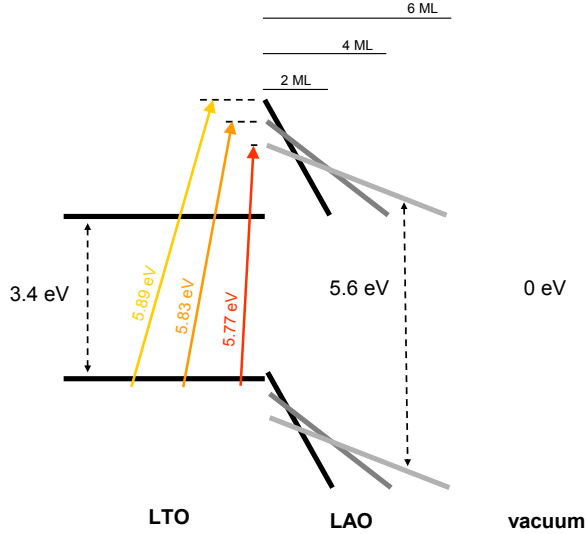
Figure 4.25: Schematic picture of the band bending in LAO/LTO single-layer heterostructures due to relaxation in the LAO capping layer.

Under the assumption that the LaO and/or AlO$_2$ ionic layers distort to form these moments they would separate by about $\Delta z = 0.06$ Å. This is a relative shift of 1.5 %, comparable to the lattice mismatch in the c-direction of 1.1 %. So the band bending is caused by the strain on the LAO capping layer. This helps the LAO 'bridge' the potential difference between LTO and the air. Actually, any material

has to perform some kind of bridging from the bulk-like states to the vacuum. LAO itself is no exception[32]. So, each LAO monolayer allows for part of the electronic strain to be relaxed. With the LAO bands pinned at the air//LAO interface, the relaxation through the LAO allows the LAO conduction band to lower at the LAO//LTO interface. As the capping layer increases in thickness, the conduction band becomes lower in energy and the transition energy from the LTO valence band to the LAO conduction band lowers as well. Figure 4.25 shows this schematically. This diagram is only roughly correct, as the band model of electronic states is only qualitatively correct for correlated-electron materials.

4.5   Conclusions

Monolayers of LTO embedded in LAO behave like two-dimensional Mott insulators. Analysis of the transport data and EELS measurements shows that the higher concentration of electrons in the LTO/LAO system compared to the LTO/STO system drives the LTO electrons into the Mott insulating state. When evaluating the Mott criterion, it becomes clear that the high local electron density drives up the electron effective mass. This combination finally yields a value of $a_{\mathrm{Bohr}} \sqrt[3]{\langle n \rangle}$ = 0.18 which is below the Mott criterion (Equation 2.13), indicating the system is in a Mott insulating state. The optical conductivity of such superlattices obtained by ellipsometry shows a sharp peak attributed to the transition from Ti^{3+} $3d^1$ to La $5d^0$. The sharpness of the peak indicates that the density of states of both the originating and receiving bands are narrow. Confirmed by theoretical calculations the Ti^{3+} $3d^1$ state is indeed populated for single monolayers of LAO and its sharp density-of-state is reminiscent of Hubbard bands. Such a 2D $3d^1$ system could form a reference system for the evaluation of the two-dimensional Hubbard model. Similar structures with separated 2D planes could be formed using Ruddlesden-Popper phases ($A_{n+1}M_nO_{3n+1}$), but not with a valence of 3+.

Probing with XPS shows that the LTO layer can be externally doped by bringing it in close proximity to another suitable interface, here an air/LAO surface, similar to the LVO/LAO system. This doping might tune the system through an insulator-to-metal transition as well as allow for fine-tuning of the conduction channel for FET applications. The low electron mobility compared to semiconductor FET's could be a concern, but the high electron density and the abruptness of the Mott transition can offset that short-coming[33]. A model is developed to describe the change in electron occupancy with the capping layer thickness. Balancing the energy costs of surface vacancies and of electrons transferred between the LTO layer and the surface can describe the observed electron fraction-capping thickness relation. The expected band shift energy is recovered; interestingly for the Mott insulating state on a single monolayer of LTO the band shift is reduced due to the Coulomb interaction that raises the energy of the electrons in the LTO layer.

Despite the similarities between the LTO/LAO and LVO/LAO systems, the Ti^{3+} fraction in the LTO layer is far below the expected value of one for thick capping layers. About half that value is found for the LTO/LAO system, contrary to the

LVO/LAO system that does recover the full one electron per unit cell. So far the origin of this discrepancy is unclear, especially since EELS measurements on the superlattices grown with the same settings show only Ti^{3+} in the LTO layers.

On a smaller energy scale, LAO can accommodate part of the electronic strain that results from joining different materials together. In semiconductors such interface band bending is readily understood. But in the more electronically complex transition metal oxides the band model cannot be rigidly applied. Still, it points to a strained structure of LAO that induces a slight polarization which lowers the conduction band minimum at the LAO//LTO interface. As the amount of electronic stress that can be relieved is dependent on the thickness of the LAO capping layer, the conduction band minimum varies as well. This band bending effect of about 0.4 eV over 15 monolayers might be useful again in FET applications in fine-tuning the gate voltage dependence.

4.6 References

[1] S. Gasiorowicz, *Quantum physics*. Wiley (New York), 2nd ed., 1996.

[2] D. J. Griffiths, *Introduction to quantum mechanics*. Upper Saddle River, NJ: Pearson Prentice Hall, 2nd ed., 2005.

[3] S. Okamoto and A. J. Millis, "Theory of Mott insulator-band insulator heterostructures," *Physical Review B*, vol. 70, p. 075101, 2004.

[4] D. A. Muller, N. Nakagawa, A. Ohtomo, J. L. Grazul, and H. Y. Hwang, "Atomic-scale imaging of nanoengineered oxygen vacancy profiles in $SrTiO_3$," *Nature*, vol. 430, pp. 657–661, 2004.

[5] M. Huijben, G. Rijnders, D. H. A. Blank, S. Bals, S. van Aert, J. Verbeeck, G. van Tendeloo, A. Brinkman, and H. Hilgenkamp, "Electronically coupled complementary interfaces between perovskite band insulators," *Nature Materials*, vol. 5, pp. 556–560, 2006.

[6] A. Ohtomo, D. A. Muller, J. L. Grazul, and H. Y. Hwang, "Epitaxial growth and electronic structure of $LaTiO_x$ films," *Applied Physics Letters*, vol. 80, pp. 3922–3924, 2002.

[7] A. Ohtomo and H. Y. Hwang, "A high-mobility electron gas at the $LaAlO_3/SrTiO_3$ heterointerface," *Nature*, vol. 427, pp. 423–426, 2004.

[8] R. Takahashi, Y. Matsumoto, T. Ohsawa, M. Lippmaa, M. Kawasaki, and H. Koinuma, "Growth dynamics of the epitaxial SrO films on $SrTiO_3(001)$," *Journal of Crystal Growth*, vol. 234, pp. 505–508, 2002.

[9] A. Brinkman, M. Huijben, M. van Zalk, J. Huijben, U. Zeitler, J. C. Maan, W. G. van der Wiel, G. Rijnders, D. H. A. Blank, and H. Hilgenkamp, "Magnetic effects at the interface between nonmagnetic oxides," *Nature Materials*, vol. 6, pp. 493–496, 2007.

[10] A. Ohtomo, D. A. Muller, J. L. Grazul, and H. Y. Hwang, "Artificial charge-modulation in atomic-scale perovskite titanate superlattices," *Nature*, vol. 419, pp. 378–380, 2002.

[11] S. H. Paek, J. H. Won, J. E. Jang, Y. S. Hwang, J. P. Mah, J. S. Choi, S. T. Ahn, J. G. Lee, and C. S. Park, "Characteristics of $SrTiO_3$ thin films deposited under various oxygen partial pressures," *Journal of Materials Science*, vol. 31, pp. 4357–4362, 1996.

[12] R. Moos, W. Menesklou, and K. H. Härdtl, "Hall mobility of undoped n-type conducting strontium titanate single crystals between 19 K and 1373 K," *Applied Physics A: Materials Science & Processing*, vol. 61, pp. 389–395, 1995.

[13] H. Yamada and G. R. Miller, "Point defects in reduced strontium titanate," *Journal of Solid State Chemistry*, vol. 6, pp. 169 – 177, 1973.

[14] J. Fompeyrine, J. W. Seo, and J. P. Locquet, "Growth and characterization of ferroelectric $LaTiO_{3.5}$ thin films," *Journal of the European Ceramic Society*, vol. 19, pp. 1493–1496, 1999.

[15] Y. Tokura, Y. Taguchi, Y. Okada, Y. Fujishima, and T. Arima, "Filling dependence of electronic properties on the verge of metal-Mott-insulator transitions in $Sr_{1-x}La_xTiO_3$," *Physical Review Letters*, vol. 70, pp. 2126–2129, 1993.

[16] Y. Fujishima, Y. Tokura, T. Arima, and S. Uchida, "Optical-conductivity spectra of $Sr_{1-x}La_xTiO_3$: filling-dependent effect of the electron correlation," *Physical Review B*, vol. 46, pp. 11167–11170, 1992.

[17] Z. Yu and C. Ang, "Dielectric and conduction behavior of La-doped $SrTiO_3$ with suppressed quantum-paraelectric background," *Applied Physics Letters*, vol. 80, pp. 643–645, 2002.

[18] J. S. Lee, M. W. Kim, and T. W. Noh, "Optical excitations of transition-metal oxides under the orbital multiplicity effects," *New Journal of Physics*, vol. 7, p. 147, 2005.

[19] S. S. A. Seo, *Optical spectroscopic investigations on oxide superlattices*. PhD thesis, Seoul National University, 2007.

[20] M. J. Han, T. Ozaki, and J. Yu, "O(N) LDA+U electronic structure calculation method based on the nonorthogonal pseudoatomic orbital basis," *Physical Review B*, vol. 73, p. 045110, 2006.

[21] M. J. Han and J. Yu, "Electronic structure and insulating nature of the $(LaTiO_3)_2/(LaAlO_3)_2$ superlattice," *Journal of the Korean Physical Society*, vol. 53, pp. 1074–1078, 2008.

[22] B. Keimer, D. Casa, A. Ivanov, J. W. Lynn, M. v. Zimmermann, J. P. Hill, D. Gibbs, Y. Taguchi, and Y. Tokura, "Spin Dynamics and Orbital State in $LaTiO_3$," *Physical Review Letters*, vol. 85, pp. 3946–3949, 2000.

[23] M. Takizawa, Y. Hotta, T. Susaki, Y. Ishida, H. Wadati, Y. Takata, K. Horiba, M. Matsunami, S. Shin, M. Yabashi, K. Tamasaku, N. Nishino, T. Ishikawa, A. Fujimori, and H. Y. Hwang, "Spectroscopic evidence for competing reconstructions in polar multilayers $LaAlO_3/LaVO_3/LaAlO_3$," *Physical Review Letters*, vol. 102, p. 236401, 2009.

[24] H. Lüth, *Solid surfaces, interfaces and thin films*. Berlin: Springer-Verlag, 4th ed., 2001.

[25] M. Takizawa, *Photoemission study of perovskite-type transition-metal oxide thin films and multilayers*. PhD thesis, University of Tokyo, 2007.

[26] U. Schwingenschlögl and C. Schuster, "Exponential decay of relaxation effects at $LaAlO_3/SrTiO_3$ heterointerfaces," *Chemical Physics Letters*, vol. 467, pp. 354–357, 2009.

[27] H. Wadati, Y. Hotta, A. Fujimori, T. Susaki, H. Y. Hwang, Y. Takata, K. Horiba, M. Matsunami, S. Shin, M. Yabashi, K. Tamasaku, Y. Nishino, and T. Ishikawa, "Hard x-ray photoemission study of $LaAlO_3/LaVO_3$ multilayers," *Physical Review B*, vol. 77, p. 045122, 2008.

[28] A. Kuzmenko, "RefFIT." http://optics.unige.ch/alexey/reffit.html (13-05-2009), 2009.

[29] M. Cardona, "Optical properties and band structure of $SrTiO_3$ and $BaTiO_3$," *Physical Review*, vol. 140, pp. A651–A655, 1965.

[30] M. Minohara, Y. Furukawa, R. Yasuhara, H. Kumigashira, and M. Oshima, "Orientation dependence of the Schottky barrier height for $La_{0.6}Sr_{0.4}MnO_3/SrTiO_3$ heterojunctions," *Applied Physics Letters*, vol. 94, p. 242106, 2009.

[31] R. Pentcheva and W. E. Pickett, "Avoiding the polarization catastrophe in $LaAlO_3$ overlayers on $SrTiO_3(001)$ through a polar distortion," *Physical Review Letters*, vol. 102, p. 107602, 2009.

[32] R. J. Francis, S. C. Moss, and A. J. Jacobson, "X-ray truncation rod analysis of the reversible temperature-dependent [001] surface structure of $LaAlO_3$," *Physical Review B*, vol. 64, p. 235425, 2001.

[33] D. M. Newns, J. A. Misewich, C. C. Tsuei, A. Gupta, B. A. Scott, and A. Schrott, "Mott transition field effect transistor," *Applied Physics Letters*, vol. 73, pp. 780–782, 1998.

Chapter 5

Fabrication & analysis of single LaAlO$_3$//SrTiO$_3$ interfaces

Abstract

In LaAlO$_3$//SrTiO$_3$ interfaces the electron density and mobility evolve differently with pressure. Below a critical pressure of $1\cdot10^{-5}$ mbar O$_2$ the re-oxidation during the cool-down governs the electron density, while above this critical pressure the electron density is independent of the pressure. The electron mobility decreases with increasing pressure as the dielectric constant of the SrTiO$_3$ decreases and the electrons are confined closer to the interface, where interface defects increase the scattering rate. The interface polarization due to structural strain forms the basis for an alternative model describing the origin of the interface conduction. The polarization results in a potential well at the interface which can be modified by mismatch strain and is doped by electrons from defect states in the SrTiO$_3$. Testing the model, the LaO//TiO$_2$ interface in LaTiO$_3$ is investigated and is found to be insulating. Similarities between the LaAlO$_2$//SrTiO$_3$ and LaTiO$_3$ interfaces suggests that the binding sites at both interfaces are the same.

5.1   Introduction

To create a 2D electron layer, it is necessary to confine the electrons within a material. In the previous chapter this was done in a manner similar to band gap engineering, a very familiar procedure from semiconductor physics. But ionic

materials such as the complex oxides also offer the opportunity of what could be called 'Coulomb confinement': the confinement of negative electrons close to a positively-charged layer due to electrostatic forces. The LTO/STO system from which the LTO/LAO band gap confined structures were derived is a prime example of this[1]. Here the electrons are placed on a continuous titanium lattice, but are confined close to the lanthanum ions, as shown in Figure 2.11.

The LAO//STO interface is another system where the conducting electrons are confined to the interface due to the positive charge of the LaO layer[2]. Since the discovery of conduction at this interface[3], much work has been done investigating this system[4, 5]. The influence of the deposition gas pressure has been highlighted right from the beginning[6, 7], but the persistence of the conduction to higher pressures indicates that it is not the sole origin of mobile electrons[8]. From theoretical calculations a different model for the origin of the mobile electrons appears. As an effect of the polar discontinuity at the interface, there is a shift in the LAO valence band up to the Fermi level at the surface. The subsequent surface-to-interface electron transfer can explain observations such as the minimum LAO thickness required before the onset of conduction[9–12].

All this gathered knowledge makes it possible to study more subtle details of these interfaces. The extensive investigation of the superconducting state is one example[13–15]. The study of the effect of defects on the conducting state shows the quality of the fabricated samples, as well as the ability to manipulate their properties[16, 17]. The knowledge and study of the PLD growth process is essential, as so far almost all interface samples have been fabricated with this technique.

This chapter explores how the PLD growth process influences the structure of the LAO//STO interfaces and through that their properties. The first part discusses the observations from literature in more detail. The role of the deposition pressure *sic* is already well-known, but a closer look at the trends show more intriguing physics than is obvious at first glance: the electron density and electron mobility evolve differently with changing deposition pressure and often contrary to bulk STO. The doping of electrons to the interface is also reviewed and an alternative model is proposed.

The second part of this chapter discusses further investigations into the pressure dependencies. Varying the deposition time shows how the oxygen equilibrium density changes with oxygen pressure both during deposition and during the cooldown afterwards. Changing the gas composition explores how the plasma kinetics and oxygen chemical equilibrium steer the transport properties.

The last part of this chapter discusses how a LaO//TiO_2 interface can be fabricated not only by growing LAO on TiO_2-terminated STO but also by sandwiching a single monolayer of LTO between SrO-terminated STO and AlO_2-terminated LAO. By comparing this interface with the LAO//TiO_2-STO interface the origin of the interface electrons is investigated. Striking similarities between the electron host sites in both LAO//STO inter-block and LTO intra-block interfaces are observed, just as there are striking differences between the transport behaviours.

5.2   Pressure dependence from literature data

Right from the first paper by Ohtomo and Hwang[3] it was noted that the deposition pressure had a great influence on the transport properties. Since then it has been used to partially explain the observed effects through the formation of oxygen vacancies. Indeed, this has been fingered as the sole cause of the interface conduction[7, 18]. But it has been shown in a systematic pressure-dependent series of samples that the interface conduction persists to higher pressure where the influence of oxygen vacancies can be thought to be negligible compared to any interface contribution[8]. Figure 5.1 shows the the sheet resistances, electron sheet densities and electron mobilities as they have been published in literature vs. the deposition pressure. The transition from vacancy-dominated to interface-dominated seems to be rather sharp, as can be seen from the electron density data in Figure 5.1(b). Judging from this data, the critical pressure above which the interface contribution is dominant is about $1 \cdot 10^{-5}$ mbar. The change in electron density is about three orders of magnitude. It should be noted that for the entire range of pressures the substrate is still within the plasma range[19].

Another difference is that some samples grown at $1 \cdot 10^{-6}$ mbar, so below the critical pressure, turn completely insulating upon post-annealing (400 °C in flowing oxygen for two hours). Figure 4.10(a) shows this for a SL(1-2)$_{10}$ LTO/LAO superlattice. Similarly, thinner PS(7-2) single-layer LTO/LAO samples turn insulating as well. In contrast, other samples that have been fabricated at 10^{-6} mbar do not turn completely insulating[3, 26]. This shows that below the critical pressure there are two situations. In one case the entire sample is reduced and the electron density is increased everywhere, as evidenced by the sample turning gray[7, 30]. In the other case the doping is still due to oxygen vacancies, but the doped electrons are bound to the interface[26]. The origin of this difference is unclear, as no systematic investigation has been made. Samples grown at pressures above this critical pressure have a slight increase in sheet resistance upon post-annealing, but do not turn completely insulating as will be shown in the next chapter in Section 6.4.5.

Such a large and sudden change in the electron density upon increasing the pressure seems to point towards a thermodynamic threshold being crossed. It was calculated using DFT that for different chemical potential of the free oxygen different vacancy densities in the top LAO layer are most energetically favourable[31, supplementary information]. However, the oxygen chemical potential only depends on the pressure through $k_{\mathrm{B}}T \ln(p/p_0)$[32], which over this pressure range and a p_0 referenced at atmospheric pressure only changes about 0.5 eV. Such a small change is unlikely to affect the electronic state this drastically - and reproducibly.

Plotting the literature data in the form of an Ellingham diagram as shown in Figure 5.2 again clearly shows the critical influence of the pressure. All samples with an electron fraction above half an electron per unit cell area are grown at $1 \cdot 10^{-6}$ mbar, while all samples grown at higher pressures have an electron fraction below half an electron.
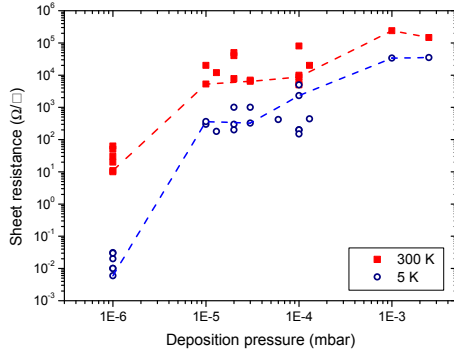
(a) sheet resistance
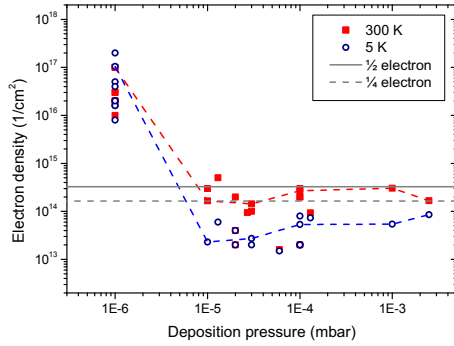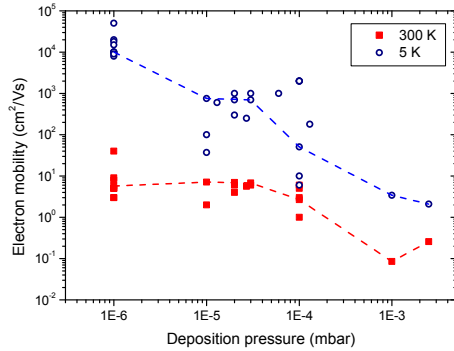
(b) electron density

(c) electron mobility

Figure 5.1: Transport parameters from literature[3, 6–8, 13, 18, 20–29]. The dashed lines connect the values from the pressure series from Brinkman[8]. (a) sheet resistance, (b) electron density and (c) electron mobility.
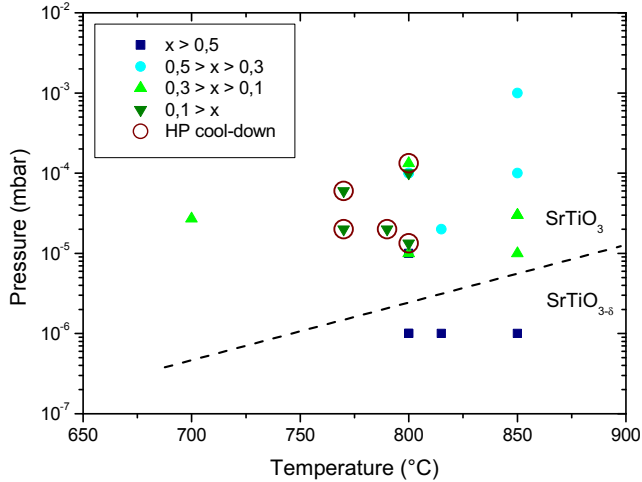
Figure 5.2: Pressure-temperature phase diagram for the same literature data as Figure 5.1. Points are coloured according to the electron fraction calculated from the electron density at 300 K: $x = a^2 n_{2D}$. The red circles indicate the samples cooled down at high pressure (4 mbar). The black dashed line is a proposed boundary between the vacancy-dominated and interface-dominated samples.

A possible explanation for the observed behaviour is that for low pressures the LAO layer strongly getters oxygen from the STO substrate. As such, it creates an abundance of oxygen vacancies in the STO. At these low pressures, the chemical equilibrium is such that the desorption of oxygen is larger than the diffusion of oxygen from the interior of the STO and there is a net loss of oxygen[33].

The electron mobility develops more gradually with deposition pressure, as can be seen from Figure 5.1(c). But the relation is opposite to what would be expected: the mobility decreases with increasing oxygen pressure. For bulk STO it is known that the mobility decreases with increasing electron density[34, 35], which is equivalent to an increasing vacancy density[36, 37]. So for higher pressures a lower vacancy density would be expected and a higher mobility.

There have been some arguments that for samples grown above the critical pressure the spatial extent of the electron density in the z-direction is important[10, 38–40]. At the interface electrons can have a lower mobility due to interface defects[17] or localized bands[10, 41]. So high mobilities are reached if the electrons are distributed far into the STO layer. But for LAO//STO samples fabricated at higher pressures, the higher oxygen content reduces the dielectric constant[42–44]. This decrease of the dielectric constant lowers the screening of the interface charge, confining the electrons closer to the interface. In semiconductor physics the extent of the electron density at an interface is given by the Debye length $\lambda_D \propto \sqrt{K}$, describing this behaviour[45]. This local concentration of electrons again enhances

the local electric field, which further reduces the dielectric constant, enhancing the confinement of electrons[39]. Above a critical electron density of about $5 \cdot 10^{13}$ cm^{-2} this confinement rapidly increases and thus reduces the electron mobility. This density is close to the typical values observed for LAO//STO interfaces.

A similar mechanism is at work in LAO//STO field-effect structures where the external electric field pulls the electrons closer to the interface[40]. Whether it is also applicable to the mobility vs. film thickness dependence for LAO//STO interfaces is unclear. There the mobility decreases with increasing LAO film thickness[29]. The theoretical increase of the electron density at the interface with increasing thickness[9–12] may be enough to trigger the interfacial confinement and mobility reduction. The reduction of the electron density with film thickness as observed from Hall measurements fits well into this picture, as the interfacial confinement will cause more electrons to become localized.

This closer look at the physics of single-interface LAO//STO structures shows how the oxygen pressure plays an important role in determining the electron densities and mobilities, though the mechanisms are different. This dual mechanism complicates the analysis of LAO/STO heterostructures. In conclusion this analysis of literature results can be summarized as follows:

- There is a critical deposition pressure below which oxygen diffusion from the STO becomes dominant. As a consequence the electron density below the critical pressure is dominated by oxygen vacancies, above it by the interface doping.

- The electron mobility monotonously decreases with increasing pressure. This dependence is due to the decreasing dielectric constant, which causes the 3D electron density to collapse closer to the interface. The increased scattering near the interface then reduces the mobility.

This dependence of the transport properties on the local dielectric constant and the spatial distribution of the 3D electron density can also explain the different properties observed at LAO//STO interfaces. For example, it is known that oxygen-deficient STO becomes superconducting if the 3D electron density exceeds $3 \cdot 10^{19}$ cm^{-3}[46]. Depending on the spatial distribution of the carriers, this critical value may or may not be exceeded[38]. This shows the importance of knowing the spatial distribution of the electrons, which cannot be derived from the measurement of the 2D electron sheet density in itself. Calculations show that the spatial distribution depends in a nontrivial way on both dielectric properties[40] and 3D electron density[39]. Phase diagrams such as the one in Ref. [5] should be extended to include this third dimension.

From these conclusions several questions arise. First, if changes in the substrate vacancy density or dielectric constant have such a profound effect on the conduction, how does the structural quality of the substrates themselves affect the transport properties? Second, why is there a sharp transition in the electron density from the vacancy-dominated to the interface-dominated regime? What process 'activates' the oxygen diffusion? Finally, what is the main role of the pressure during

deposition? Is it a moderator of the thermodynamic energy of the arriving species or is it a chemical reservoir for oxygen in contact with the sample? The first part of this chapter will focus on these questions.

5.3 Alternative model for LaAlO$_3$//SrTiO$_3$ interfaces

In the discussion in the previous section all the activity was in the STO substrate. As long as there are electrons present at the interface, regardless of their origin, the physics remains the same. Therefore it is interesting to study what mechanisms for the interfacial doping exist.

For the LAO//STO interface a model emerges based on the polar discontinuity at the interface[9–12]. This discontinuity, if uncompensated, would give rise to an internal field in the LAO layer that would bend the LAO bands. As the thickness of the LAO layer increases, the LAO valence band rises above the Fermi level. At this point electrons can be transferred from the LAO surface to the LAO//STO interface. This creates an electric field opposite to the internal field of the LAO, thus lowering the band shift in LAO. Further increasing the LAO thickness increases the electron doping and reduces the internal field. Simply put, the LAO band shift must be enough to cross the STO band gap of 3.2 eV regards less of the LAO thickness. So the internal field must be equal to $E_{int} = V_g/ed$. Figure 5.3 shows this schematically for the critical thickness of 4 monolayer LAO[25] (a) and a thicker LAO layer where more electrons are transferred and the LAO band shift is reduced back to the Fermi level (b)[10].

There is some discussion, however, whether this model holds. For example, the LAO band shift should induce a corresponding shift in the LAO core peaks observed with XPS. This expected broadening of the La peaks has not been observed, even though photospectroscopy techniques do have the resolution to resolve shifts of this order[47]. Alternatively, oxygen vacancies at the LAO surface[31, supplementary information] can flatten the LAO band shift. Without this band shift, there is no Fermi level crossing and no doping.

Here a different model is suggested that focusses on the structural polarization in STO at the LAO//STO interface. It has been proven through both calculations [48–51] and observations[52–54] that the STO unit cells closest to the interface undergo a ferroelectric-like structural deformation. Whether this is due to electron doping of the interface or due to mechanical strain and electrostatic interactions with the neighbouring LaO layer is uncertain at the moment. It is known that STO at the LAO//STO interface undergoes compressive strain which can drive the STO ferroelectric with the polarization direction perpendicular to the interface[55].

The interesting thing is that such a *polarization* discontinuity can form conduction channels, even in nominally undoped and neutral materials. Ferroelectric domain walls in BiFeO$_3$ have been found to be conducting[56]. Calculations showed that
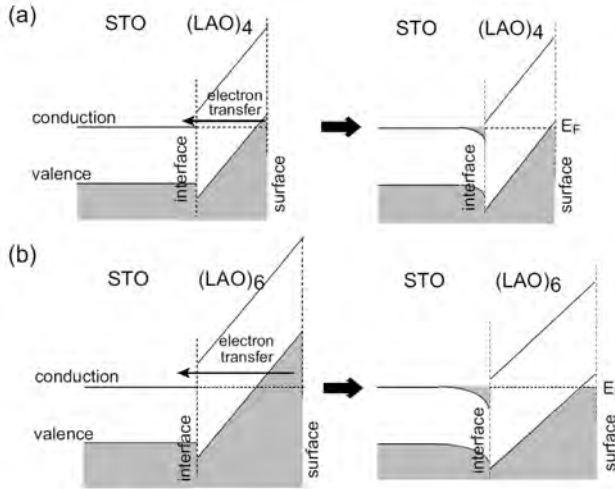
Figure 5.3: Band schematics to illustrate the electron-transfer model. At the critical thickness, electrons are transferred from the surface to the interface (a). For thicker layers, more electrons are transferred and the LAO band shift is reduced (b). Image is taken from Ref. [10].

the change in local polarization resulted in a reduction of the band gap, and thus a lowering of the conduction band to the Fermi level. Similarly, polarization switching in $Pb(Zr_{0.2}Ti_{0.8})O_3$ reduced the tunneling barrier for STM when the polarization surface charge and the tip charge were opposite[57], similar to electron-doped TiO_2 and LaO layers. Calculations on $KNbO_3/STO$ superlattices also showed that the polarization of the $KNbO_3$ influenced the density of states at the interfaces[58]. Similar polarization-driven interface doping processes have been observed in ZnO[59] and SiC[60].

The structural-polarization model for the LAO//STO interface would then be that the structural reconstruction in STO at the interface, due to both strain and electrostatic forces, results in a local polarization that lowers the STO conduction band to the Fermi level. Electrons from defect states in the STO[61] can then migrate to the interface where their presence will increase the band bending and magnify the effect until an equilibrium is reached[39]. This may explain why LAO//STO interfaces where the STO is a deposited layer have a lower electron density[62]. Deposited STO often has less defects than bulk-grown STO. The LAO bands need not shift, and all the physics regarding the oxygen pressure discussed in the previous section do still apply.

When evaluating the two models it is useful to look at experimental features unique to LAO/STO interfaces. These same features show why an explanation of the interface conduction purely from oxygen vacancies cannot hold. Any model must be able to explain these features. The three most important are listed below.

- Termination dependence
  LAO//SrO-STO is non-conducting, while LAO//TiO$_2$-STO is[20].

- Critical thickness
  Below a critical thickness of 4 monolayers of LAO a LAO//TiO$_2$-STO interface is non-conducting[25].

- Coupled interfaces
  Two interfaces, a n- and a p-type, interact below a minimum separation of 6 monolayers of LAO[22].

The termination dependence in the electron-transfer model would make the LAO bands shift downwards instead of upwards to the Fermi level. So no electron transfer can be expected and the interface stays insulating. In the structural-polarization model the structural reconstruction at the interface would be completely different, because it is mainly the SrO layer that reconstructs. The interface remains insulating because the STO conduction band which is mostly comprised of Ti 3d bands is not lowered, similar to the high-resistance polarization in PZT for the STM measurement[57].

The critical thickness in the electron-transfer model is due to the fact that a single monolayer of LAO can only accommodate about 1 eV (see discussion on page 89). To bridge the complete STO band gap of 3.2 eV about 3.3 monolayers of LAO are needed. Thus the critical thickness of 4 monolayers. For the structural-polarization model it has been calculated that for thin LAO layers the LAO layers deform instead of the STO[51, 63]. So for thin layers, the STO is not structurally reconstructed and no band bending occurs.

The coupled interfaces are a direct consequence of the electron transfer from the top interface to the bottom one. For the double-interface structure the top interface is a p-type interface. Such interfaces require extra electrons to be charge compensated. Generally these electron come from oxygen vacancies[2]. Transferring electrons would then cost energy as oxygen vacancies have to be created. For thin LAO layers the LAO band shift is not large enough to overcome this energy and most electrons remain at the top interface. As the LAO layer becomes thicker, the band shift increases and more and more electrons are transferred until the two interfaces are no longer coupled. The mechanism for the structural-polarization model is nearly the same, and very reminiscent of the interface-surface interaction in the LTO/LAO and LVO/LAO systems discussed in Section 4.4.2. Assuming that electrons are already present at the bottom n-type interface there is a competition between electron transfer from bottom to top and vacancy creation. Here this transfer is reduced for thicker layers until both layers are decoupled.

With both models seemingly describing the same behaviour, what arguments are there for adopting the structural-polarization model? As already mentioned, the possible lack of a LAO band shift is an important argument to investigate the new model. Also the reduction of the electron density for LAO//STO interfaces on a deposited STO layer cannot be explained by the electron-transfer model[62]. As

the LAO layer has the same thickness for samples with and without STO interlayer the electron density should not be different.

What may be an additional argument is an explanation for the interface conduction observed in the $KTaO_3$/STO system[64], though tantalum interdiffusion can play a role. Compared to the LAO/STO system the KTO/STO system has its polarities reversed: the interface is now $(KO)^-//(TiO_2)^0$ instead of $(LaO)^+//(TiO_2)^0$. According to the electron-transfer model no interface conduction is expected as the LAO band shift is downwards. From the structural-polarization model however an enhanced polarization is expected, though with the polarization opposite to that at the LAO//STO interface. Indeed, an enhanced polarization has recently been calculated at the $KO//TiO_2$ interface in the $KNbO_3$/STO system[65]. What is especially interesting is that the calculations show that the KNO/STO superlattice is not metallic, even with its interface polarization. So the observation of conduction at the KTO//STO interface may show that the origin of the conducting interfaces is not electron transfer from the surface to the interface, but band bending due to structural forces at the interface.

To further prove the structural-polarization model, LAO//STO interfaces can be fabricated on other substrates with different lattice parameters. In such heterostructures the electrostatic driving force behind the structural polarization would be the same, but the strain on STO would be different. Interfaces fabricated on substrates with a larger lattice parameter compared to STO should exhibit more insulating behaviour, as the compressive strain at the interface is compensated by tensile strain from the substrate. Additionally, tensile strain would induce a polarization parallel to the interface, which would not induce a potential well[55]. Interfaces fabricated on substrates with smaller lattice parameters would be more difficult to analyse. On one hand the compressive strain at the interface is not compensated, on the other hand the entire STO film is compressively strained thus reducing the polarization discontinuity at the interface.

So far the $LaO//TiO_2$ interfaces that have been studied most in literature were fabricated by depositing LAO on TiO_2-terminated STO. This interface can be called an <u>inter</u>-block interface, as it is constructed between deposited perovskite blocks[1]. A second way to construct a $LaO//TiO_2$ interface is by depositing a monolayer of LTO in between STO and LAO. Such a LAO//STO interface can be called an <u>intra</u>-block interface. Comparing inter- and intra-block interfaces which have a different method of strain release can give information about these models. From the electron-transfer model it is expected that, if the LAO layer has the same thickness, both interfaces are nearly the same. The structural-polarization model however shows that the two interfaces will be dissimilar, as the structural strain has been resolved differently.

---

[1]Though during the PLD process all elements and complexes thereof arrive at the substrate without any crystalline order, it is energetically favourable for the adsorbants to form into complete perovskite unit cells of the grown material. Thus the PLD deposition is often thought of as the deposition of complete unit cell blocks instead of partial structures.

5.4 Sample fabrication

To study the questions raised in the previous two sections, both LAO//STO inter-block and LTO intra-block interfaces have been fabricated. Figure 5.4 shows how these two types of interfaces can be fabricated. The LAO//STO inter-block interface can simply be fabricated by depositing a LAO layer on chemically-etched TiO_2-terminated STO (Figure 5.4(a)). A LTO intra-block interface can be fabricated by depositing a monolayer of LTO on a SrO-terminated STO layer (Figure 5.4(b)). The SrO-termination is obtained by depositing one-and-a-half monolayer of strontium ruthenate (SRO).
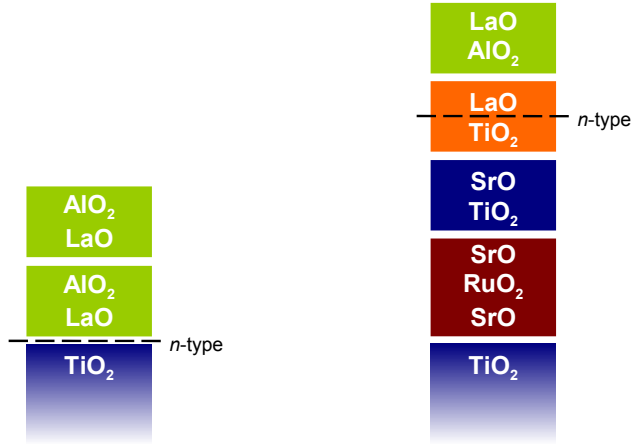
Figure 5.4: Inter- and intra-block $LaO//TiO_2$ interfaces. (a) LAO//STO inter-block and (b) LTO intra-block on SrO-terminated STO.

Samples discussed in this chapter were fabricated both at Hwang Laboratory, University of Tokyo, Japan and MESA+ Institute for Nanotechnology, University of Twente, the Netherlands. As such, Table 5.1 shows multiple growth conditions for some of the deposited materials. Both LAO and STO are relatively easy to grow throughout the entire pressure range from 10^{-6} to 10^{-1} mbar O_2. SRO and LTO require more precise settings to obtain optimal growth. Though good deposition settings for LTO were obtained in the research on LTO/LAO superlattices at Hwang lab, the different PLD set-up at the MESA+ Institute made it necessary to re-optimize the deposition settings. Primary differences were the laser itself and the optical path, so the corresponding settings were changed the most. The conditions for the growth of SRO resulted in clear layer-by-layer RHEED patterns. The high volatility of RuO_2 causes a termination switch from BO_2 to AO[66]. This was used to obtain SrO-terminated STO films to study the LTO intra-block interfaces.

material	LAO (H)	LAO (M)	LTO (M)	STO (M)	SRO (M)
F (J/cm^2)	2.0	1.3	1.6	1.3	2.0
A (mm^2)	2.0–2.6	0.9–1.7	1.3	1.3	1.3
f (Hz)	4	1 / 2	1	1	1
p (mbar)	10^{-6}–10^{-5}	10^{-5}–10^{-3}	10^{-3}	10^{-3}–10^{-1}	10^{-1}
d (mm)	50	55	55	55	55
T (°C)	700	850	850	700 / 850	700
r (pulses/ML)	$\sim$30–50	$\sim$20–26	$\sim$20–40	$\sim$20–40	$\sim$100

Table 5.1: PLD conditions for the layer-by-layer growth of LAO, LTO, STO and SRO. Shown here are the fluency F, laser spot size A, laser pulse frequency f, deposition pressure p, target-to-substrate distance d, substrate temperature T and growth rate r. The indicators 'H' and 'M' show whether the conditions were for the PLD set-up at Hwang Lab, Japan or the MESA+ Institute, the Netherlands.

Figure 5.5 shows the RHEED intensity oscillations for three samples. Two are LAO//STO structures, one grown at Hwang lab and one at the MESA+ Institute. The third is an intra-block interface fabricated on AlO$_2$-terminated LAO. For all materials and conditions in Table 5.1 RHEED oscillations were observed throughout the growth. This, and the side spots seen during and after growth, show that the deposition of all materials occurs in layer-by-layer mode when deposited on STO. The oscillations in the intensity were also reproduced in the d-spacing of the side spots and the FWHM of the main spot.
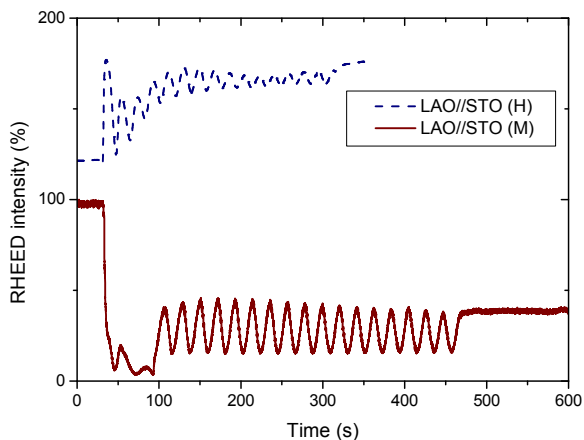

Figure 5.5: RHEED intensity oscillations for the growth of LAO/STO heterostructures. The indicators 'H' and 'M' refer to Hwang lab and MESA+ Institute, respectively.

5.5 Structural characterization

AFM scans of the top surfaces of heterostructures fabricated on STO substrates show step-and-terrace similar to that of the corresponding substrates. Figures 5.6(a) and (b) compare the top surfaces of two LAO//STO films, one fabricated at Hwang lab and one at the MESA+ Institute. Both show the same structure and their RMS roughness values are around 2 Å.

(a) LAO//STO, Hwang lab   (b) LAO//STO, MESA+ Institute
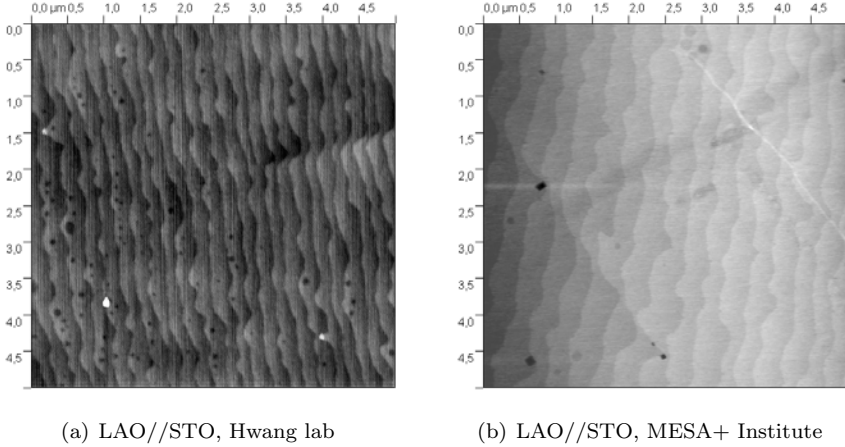
Figure 5.6: Comparison of top surface AFM scans for several LAO/STO heterostructures. (a) inter-block interfaces grown at Hwang lab and (b) inter-block interface grown at the MESA+ Institute.

XRD θ-2θ scans show unsurprising results for all samples. The obtained c-axis lattice parameters are summarized in Table 5.2. Reciprocal space mapping shows that the films are grown coherently. Rocking curves of the LAO//STO inter-block samples around (002) have a FWHM of 0.02 or 0.05° for the Hwang or MESA+ samples, respectively.

structure	c_{film} (H) (Å)	c_{film} (M) (Å)	a_{bulk} (Å)	c_{calc} (Å)
LAO//STO	3.75 ± 0.01	3.73 ± 0.01	3.789	3.71
SRO//STO	-	4.01 ± 0.06	3.923	3.94

Table 5.2: XRD θ-2θ c-axis lattice parameters for different structures. The bulk values are for the top layer. The last column is calculated using a Poisson's ratio of 0.25[67, 68]. The indicator 'H' or 'M' shows whether the conditions were for the PLD set-up at Hwang lab, Japan or the MESA+ Institute, the Netherlands.

5.6 Subtle details of the substrate

Aside from the quality of the grown films, the substrate quality also plays an important role in determining the transport properties of LAO//STO interfaces. Figure 5.7(a) shows the sheet resistance vs. temperature plots of three LAO//STO inter-block interface samples. The LAO layer was 5 monolayer thick, above the minimum thickness for interface conduction[25]. Two are grown on Shinkosha substrates following *in situ* pre-annealing for one hour while the third is grown on a SurfaceNet substrate following *ex situ* etching and annealing for one to two hours. A monolayer of SrO was included in one of the samples grown at Hwang lab to make a termination switch. From Figure 5.7(a), and the normalized sheet resistance in Figure 5.7(b), it is clear that all three show similar behaviour. The similarity to oxygen-deficient STO has been observed before[18] and can be attributed to the similar conduction channel, i.e. the titanium lattice, despite the different doping mechanisms. These samples were grown at a deposition pressure of 1.3–$3\cdot10^{-5}$ mbar, so the interface contribution should be dominant. Substrates treated at deposition conditions, but without any deposition occurring, remain insulating. A sample grown at the MESA+ Institute with SrO-termination was insulating.

(a) sheet resistance   (b) normalized sheet resistance
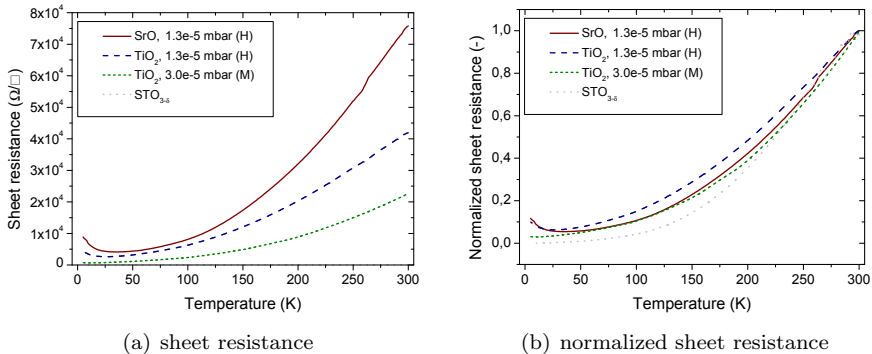
Figure 5.7: Sheet resistance vs. temperature for LAO//STO inter-block interfaces on STO substrates from different suppliers.

This similarity in transport properties points to a significant difference in the substrates from different suppliers. The samples grown on Shinkosha substrates are both conducting, while of the samples grown on SurfaceNet substrates only the LaO//TiO$_2$ sample is conducting. One important difference is that the Shinkosha substrates were pre-annealed *in situ* at $7\cdot10^{-6}$ mbar for 1 hour while the SurfaceNet substrates were pre-annealed *ex situ* in flowing oxygen for 1–2 hours. This difference in oxygen conditions might have great influence on the STO substrate stoichiometry. However, in both cases substrates treated at deposition conditions were insulating, indicating that the pre-anneal procedure itself does not create the conducting state. In addition, other LAO//STO samples with *in situ* pre-annealing did show the termination dependence[3, 20].

XPS and far-infrared spectroscopy were performed on substrates from both companies[2]. In total, about 6 samples from each supplier were investigated. Two observations were made. First, the Shinkosha substrates contain more carbon and silicon compared to the SurfaceNet substrates. The silicon is likely a contamination from the STO crystal growth. Second, far-infrared spectroscopy showed that the Shinkosha STO has a higher Drude contribution. This indicates that a larger amount of free carriers is present in those substrates. Figure 5.8 shows the optical conductivity down to 8 meV (63 cm^{-1}) and at 10 K for substrates from both companies. Taking the integrated intensity between 63 and 165 cm^{-1} (just below the soft phonon peak at 170 cm^{-1}) as representative for the spectral weight of the Drude contribution, the Shinkosha substrate contains about 1.5 times as many carriers as the SurfaceNet substrate.
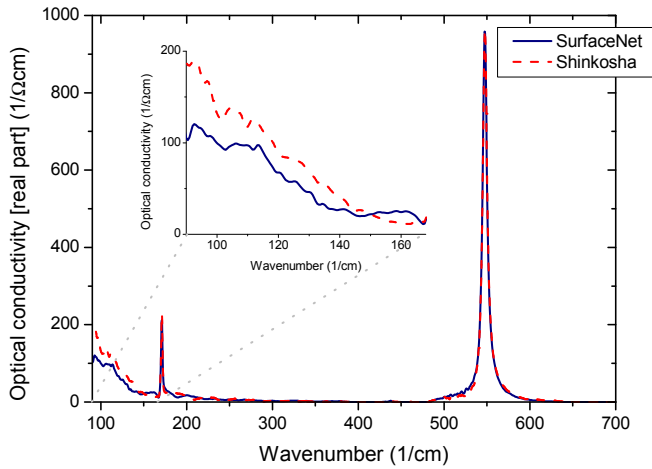
Figure 5.8: Real part of the optical conductivity at 10 K for STO substrates from different suppliers.

Though post-annealing recovers the insulating state of the AlO$_2$//SrO interface (as can be seen in Figure 4.10) it is an extra complication that should preferably be avoided. *In situ* cool-down at higher pressures is one procedure to obtain oxygen-stoichiometric samples[29, 39]. Choosing a different substrate supplier is another.

5.7   Influence of the PLD process

It was already briefly touched upon how the PLD process itself influences the sample: STO substrates treated under the same temperature and pressure conditions as a grown sample are insulating, while the deposition of just 5 monolayers of LAO

---

[2]Both XPS and far-infrared spectroscopy were performed by Prof. dr. C. Bernhard, University of Fribourg, Fribourg, Switzerland.

- a procedure of about 1 minute - makes the sample conducting. For high-pressure grown samples this can readily be attributed to the interface reconstruction inherent to the LAO//STO interface. But for low-pressure grown samples which are dominated by oxygen vacancies there must be some process that kick-starts the oxygen vacancy creation. Oxygen scavenging by LAO or sputtering by the PLD plasma are two of the candidate processes that are investigated here.

5.7.1   Film thickness

For samples grown at Hwang lab Figure 5.9 shows the thickness dependence of the sheet resistance. Two series are shown, grown at either $1.3 \cdot 10^{-6}$ or $1.3 \cdot 10^{-5}$ mbar O_2. Both show an decreasing trend with increasing thickness or, equivalently, deposition time. The first series grown at lower pressure has a sheet resistance similar to that of $SrTiO_{3-\delta}$ thins film and the $1 \cdot 10^{-6}$ mbar O_2 sample from the pressure series grown by Brinkman[8].
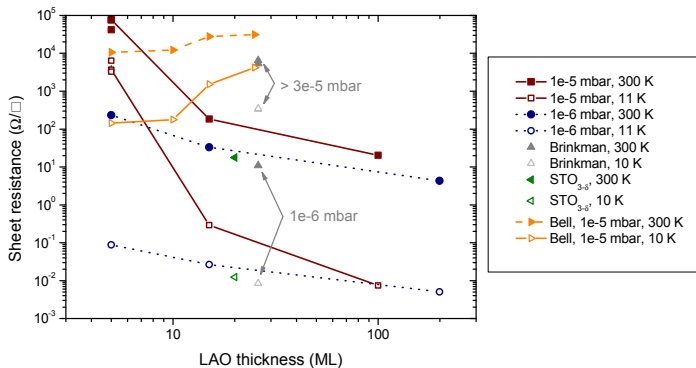
Figure 5.9: Sheet resistance vs. LAO thickness for several series. The two pressure series are new work, the Bell[29] and Brinkman[8] series are from literature, the $STO_{3-\delta}$ series is from private communication.

The sheet resistance of these samples has an inverse relation with the deposition time. This may point to a simple process of out-diffusion of oxygen as the source of the doping. Oxygen gettering by the LAO may be another source, but in that case the sheet resistance drop off should be more pronounced for the low-pressure grown samples as in that case the LAO is more deficient. Thus chemical out-diffusion of oxygen is the main source of carriers in this system, though plasma sputtering plays a role in activating the oxygen diffusion, as substrates treated to the same conditions but without actual deposition taking place do not show conductivity.

The samples fabricated at $1.3 \cdot 10^{-5}$ mbar have higher sheet resistances for thin LAO layers, but rapidly drop off to values close to the oxygen-deficient samples. A possible explanation for the increase in sheet resistance for thinner films is that re-oxidation takes place during the cool-down. For example, ultraviolet photoelectron

spectroscopy (UPS) carried out on LAO//STO interfaces showed that *in situ* post-annealing also reduces the electron density at the interface[6]. For the samples grown at low pressure the oxygen chemical equilibrium between substrate and environment is such that no re-oxidation can take place during the entire cool-down. Referring back to the Ellingham phase diagram of Figure 5.2 it can be seen that the boundary between oxygenated and reduced STO can either be crossed by increasing the pressure or by lowering the temperature. For thin samples, oxygen ions can migrate through the LAO layer and re-oxidate the interfacial STO. Thus the carrier density is decreased and the sheet resistance is increased. For thicker samples the LAO is too thick and no re-oxidation takes place. Thus the thick samples are comparable to the low-pressure grown samples.

The influence of the cool-down conditions is very pronounced. Figure 5.9 also shows the thickness series fabricated by Bell[29]. These samples were cooled down at 400 mbar, similar to other high-pressure cool-down procedures indicated in Figure 5.2. These samples actually show an increase in sheet resistance with increasing thickness, opposite to the two series cooled down at deposition pressure. Both the Bell series and the high-pressure series were grown at $1.3 \cdot 10^{-5}$ mbar, showing the influence of the cool-down recipe. This difference between these two series shows the importance of the temperature during re-oxidation, as the diffusion speed of oxygen vacancies rapidly decreases with temperature[69]. Assuming the diffusion coefficient vs. temperature relation holds down to 400 °C (a typical post-anneal temperature) the diffusion speed is a factor 60 lower. Thus the $1.3 \cdot 10^{-5}$ mbar series undergoes only limited re-oxidation as the process takes place around 300 °C. The Bell series is put into high pressure at deposition pressure and re-oxidation can take place at a high rate. Figure 5.10 shows a suggested phase diagram similar to Figure 5.2. It clearly shows how the Bell series are taken to a high pressure at high temperature, where the oxygen diffusion is high. Thus these samples can be more fully re-oxidized compared to the $1.3 \cdot 10^{-5}$ / $1.3 \cdot 10^{-6}$ mbar grown series.

Though electron density and mobility data were not obtained for all samples in the pressure series, the general trend is that both electron density and mobility increase with increasing LAO thickness. The increase in electron density can easily be explained by the increase in oxygen vacancy density for thicker samples. The increase in electron mobility might be due to the increase of the dielectric constant of STO[44] which increases the screening of defects and causes the electrons to migrate away from the interface. As most scattering defects are located close to the interface, the total average mobility probed by Hall measurements increases. The Bell series shows the opposite behaviour with decreasing electron density and mobility with increasing thickness, but as has already been discussed at the end of Section 5.2, the higher local electric field due to the larger electron density confines the electrons close to the interface, thus reducing the electron density and mobility.
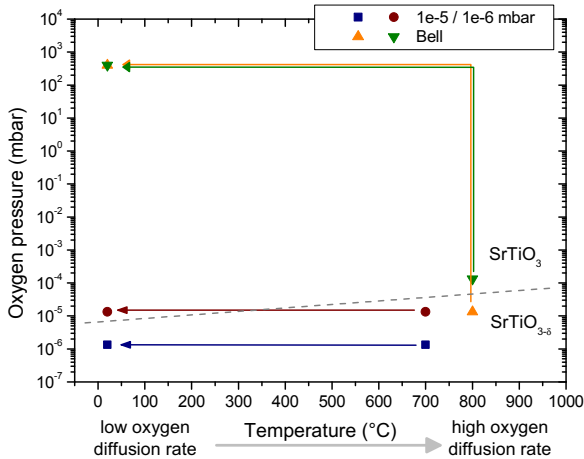
Figure 5.10: Suggested phase diagram for the cool-down of LAO//STO interfaces. The deposition takes place at high temperature, after which the cool-down traces the paths shown. The Bell samples are from literature[29]. The grey dashed line is the proposed boundary between stoichiometric and deficient STO.

5.7.2 Gas pressure & composition

The dependence of the LAO//STO interface properties on the deposition gas has already been noted throughout this thesis. It not only directly influences the oxygen vacancy density but also indirectly the electron mobility. But aside from the pressure, or equivalently the density, of the gas, the composition of the gas may also play a role. Using a mixture of gases the kinetic energy of the plasma can be tuned independently of the partial oxygen pressure.

Given the precision with which such interfaces need to be fabricated (the necessity to control of the substrate termination is an example), any residual gas contaminations might influence the interface properties. Figure 5.11(a) & (b) compare the electron densities and mobilities for two 15 monolayer thick LAO//STO interface samples, both fabricated at $7 \cdot 10^{-5}$ mbar O_2 but one with a base pressure of $5 \cdot 10^{-7}$ mbar and one with a base pressure of $4 \cdot 10^{-8}$ mbar.

Both electron density and electron mobility are almost the same for both samples. The average deviation is 4 resp. 5 %. The electron density at low temperature should be the most sensitive to defects induced by the inclusion of gas contaminations. At 2 K the deviation in the electron density is 6 %, far below the order of magnitude difference in the base pressure which should be proportional to the contamination density.
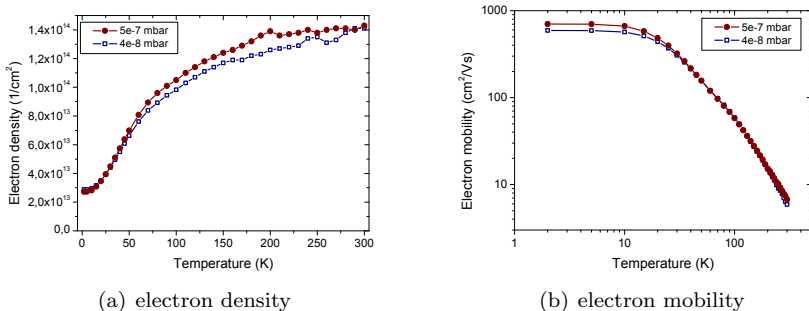
(a) electron density

(b) electron mobility

Figure 5.11: Electron density (a) & mobility (b) for two LAO//STO interface samples fabricated at the same deposition pressure, but with two different base pressures.

Though contaminations of the deposition gas do not seem to play a role, the gas composition during deposition still may. The previous subsection showed how the oxygen gas pressure can control the oxidation state of the STO (for example, see the phase diagram in Figure 5.2). The deposition gas affects the growth process primarily by providing a reservoir of oxygen for incorporation into the oxide thin film. For the pressure range discussed here the target-to-substrate distance is smaller than the plasma thermalization length, indicating that the plasma is not moderated by the surrounding gas[70]. To study the effect of the gas mixture on the LAO//STO sample growth, two series of LAO//STO inter-block interfaces with a 20 ML LAO layer were grown. For both series the deposition pressures were varied, but one series was grown in pure oxygen while the other was grown in an oxygen/argon mixture where the oxygen partial pressure was kept constant at $3 \cdot 10^{-5}$ mbar.
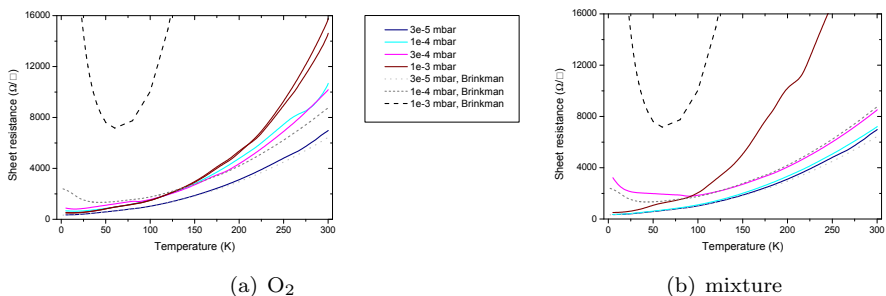

(a) O_2

(b) mixture

Figure 5.12: Sheet resistance vs. temperature plots for both series, grown in pure O_2 (a) and in an O_2/Ar mixture (b). The grey lines included are the comparable plots from literature[8].

Figure 5.12 compares sheet resistances vs. temperature plots of the O_2 and mixture series. All samples show the typical $1/T^2$ electron mobility dependence charac-

113

teristic of Fermi-liquid behaviour and have a thermally-activated electron density with activation energies on the order of 6 meV[22]. The graphs for the mix series shows some kinks, but these varied between measurements and samples, indicating they are due to extrinsic effects such as contact resistance or measurements disturbances. Comparing the two series both to each other and to a pressure series from literature[8] shows that the pure O_2 series is very different from the series from literature. Remarkably, the O_2/Ar mixture series shows more similarity to the literature pressure series though here the Kondo-like upturn is not recovered either.

Looking more closely to the transport properties, it is clear from the graphs in Figure 5.13 that the sample grown at $3 \cdot 10^{-5}$ mbar (which is the same sample for both series) is very similar to the comparable sample from the Brinkman series. The global trends with increasing pressure are basically the same for both gas composition series. The electron density varies only about 10 % compared to the Brinkman data which almost doubles. For the electron mobilities both gas composition series show a decrease with increasing pressure. The Brinkman shows a similar decrease, but again much more pronounced.

Comparing these results to the overview in Figure 5.1 shows that these data fit well into the reported results. The spread in electron density is large enough for the results in Figure 5.13(a) to accommodate both the gas composition series and the Brinkman data. The decreasing trend for the mobility is again reproduced and has already been discussed.

Despite the fact that the transport data in Figure 5.13 is has some similarities to earlier reported data the difference with the Brinkman data, especially for the electron density, is intriguing. Almost all samples from all three series were fabricated on the same PLD set-up and comparison between the deposition parameters for the new pressure series and the Brinkman series shows that the settings were nearly the same, from fluency down to spotsize and target-to-substrate distance. The similarity in deposition rates of ∼20 pulses/u.c. confirms this once more. Two possible sources for this discrepancy can be suggested. One is a difference in actual substrate temperature due to differences in the heater element and thermal connection with the sample by the silver glue. Another is the difference in substrate fabrication or preparation, an example of which was discussed in the previous section.

Focussing solely on the two new gas composition series there is very little difference between the two. This indicates that the relative oxygen content of the deposition gas has little influence on the transport properties. This is consistent with the flat dependence of the electron density above the critical pressure shown in Figure 5.1(b). The observation that the electron mobility develops the same for both gas compositions shows that the mobility is not only driven by the dielectric constant as a function of the oxygen vacancy density, but probably also by the crystallinity of the LAO top layer. The higher pressures influence the adatom diffusion over the substrate, lowering their energy which can result in more crystalline films[71]. In both the electron-transfer and the structural-polarization model this would confine
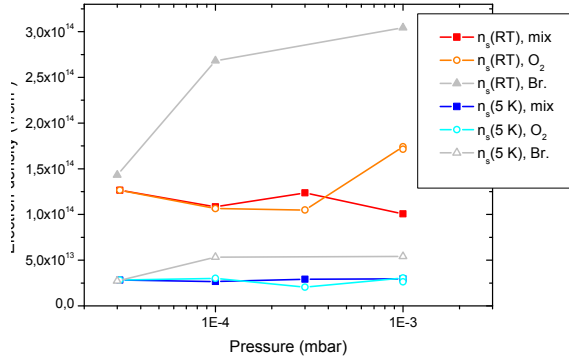
(a) electron density
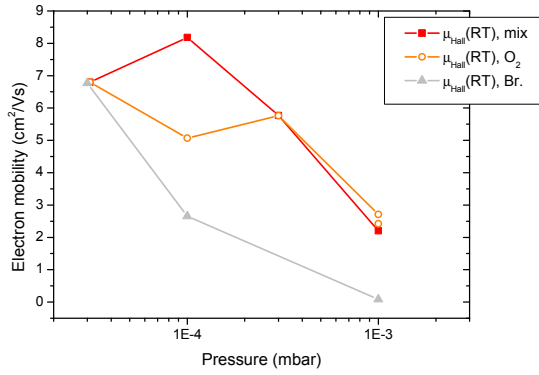
(b) electron mobility, 300 K
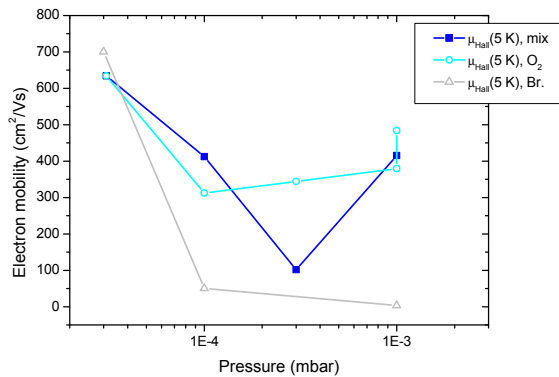
(c) electron mobility, 5 K

Figure 5.13: Electron density (a) and electron mobility (b) & (c) at 300 and 5 K for both gas composition series. The grey values are from Brinkman[8].

the electrons closer to the interface because of a deeper potential well. This has the same effect as the change in dielectric constant discussed in Section 5.2, so it is unclear which of the two mechanism is prevalent.

5.8 LaO//TiO$_2$ interfaces within LaTiO$_3$

In Section 5.3 strain engineering was discussed as a method to investigate which model for the interface conduction was the most appropriate. This can be realised by growing inter-block interfaces on different substrates to obtain strained heterostructures. Table 5.3 lists a variety of LAO//STO interface structures with the corresponding in-plane strain $(a_{\mathrm{strained}} - a_0)/a_0$ and conducting state. Here the strain is defined as the strain on the STO at the LaO//TiO$_2$ interface.

interface structure	in-plane strain (%)	conducting state
LAO//STO//NdGaO$_3$[72]	-1.2	insulating
LAO//STO//LSAT	-0.9	conducting
LAO//STO	*-0.2*	metallic
KTO//STO[64]	*+0.2*	metallic
LAO//STO//DyScO$_3$[72]	+0.9	insulating

Table 5.3: Overview of strained LaO//TiO$_2$ heterostructures. The strain values are based on the bulk lattice parameters of the substrates and STO, except for LAO//STO[73] and KTO//STO which are estimates. The distinction between 'conducting' and 'metallic' is that for the latter $\partial R_{\mathrm{s}}/\partial T > 0$, while the former has $\partial R_{\mathrm{s}}/\partial T < 0$ even though the sheet resistance is measurable down to 10 K.

From Table 5.3 it seems clear that only small amounts of strain result in conducting interfaces, mostly for compressive strain. This is as expected from the structural-polarization model. Compressive strain, either from the substrate or from the LAO layer, will induced a polarization in the STO perpendicular to the interface[55]. Too much compressive strain will polarize the entire STO layer and thus lift the polarization discontinuity. Tensile strain will counteract the compressive strain required to form the polarization band bending. Only a small amount of tensile stress can be accommodated by the interfacial strain induced by LAO.

The electron-transfer model would expect interface conduction for all these samples, except for KTO//STO which should be insulating. For the interface structures on NdGaO$_3$ and DyScO$_3$ there is a little uncertainty about the surface termination. However, even a small amount of mixed termination should result in a conducting interface[20]. No conduction is observed at all, which is contrary the electron-transfer model.

To more directly compare the LAO//STO inter-block and LTO intra-block interface both have been grown on STO substrates. The LTO intra-block interface had the structure shown in Figure 5.4(b) where one-and-a-half monolayer of strontium

ruthenate (SRO) is included to perform the termination switch from chemically TiO$_2$ to deposited SrO. The SRO growth was checked with a thick SRO film which had a RRR of 2.3 and a ferromagnetic T_C of 120 K. Both values are lower than those of bulk SRO, probably due to ruthenium deficiency which is estimated at 9 % for the SRO test sample[74]. A heterostructure of 1.5 monolayer SRO capped with 10 monolayers of STO was insulating, proving that the termination-switch SRO layer does not contribute to the transport.

Several inter- and intra-block interfaces were fabricated. Samples with the STO interlayer grown at $1 \cdot 10^{-3}$ mbar were all insulating, whether the interface was inter-block or intra-block. In the structural-polarization model this can be explained if deposited STO has less defect states than substrate STO. In that case there are no defect states which could provide electrons to the interface conduction band. For STO grown at high pressures, where the mean free path of the plasma is smaller than the target-to-substrate distance, more defect states may be created. With the electrons more freely available, the interface conduction band can be populated. Table 5.4 shows the structure and deposition conditions of three conducting LaO//TiO$_2$ heterostructures.

material	LAO	LTO	STO	SRO
pressure (mbar)	$1 \cdot 10^{-3}$	$1 \cdot 10^{-3}$	$1.3 \cdot 10^{-1}$	$1.3 \cdot 10^{-1}$
temperature (°C)	850	850	700	700
LTO_20	20	1	10	1.5
LTO_05	5	1	10	1.5
LAO//STO_05	5		10	

Table 5.4: Sample descriptions for the inter/intra-block interface comparison. The numbers give the thickness of the respective layer in monolayers.

All three heterostructures are conducting at room temperature, but behave very differently upon cooling to lower temperatures. Figure 5.14 shows the sheet resistance vs. temperature graphs of these samples. The LTO_20 heterostructure has an insulating temperature dependence ($\partial R_s / \partial T < 0$), becoming unmeasurable below 200 K. The sharp dip at 270 K has been attributed to ice formation inside the measurement chamber. The LTO_05 heterostructure also has an insulating dependence, but with a sheet resistance an order of magnitude smaller and with only a very small increase for lower temperatures. Such a decrease of the sheet resistance compared to the LTO_20 sample has also been observed in LAO//STO inter-block interfaces cooled down at high pressure[29]. The decreasing tail below 50 K is due to the detection limits of the measurement system. The LAO//STO_05 heterostructure shows metallic behaviour ($\partial R_s / \partial T > 0$), though at first glance it looks different from the LAO//STO inter-block interfaces (compare for example with Figure 5.7(a)). The difference between the LTO_05 and LAO//STO_05 heterostructures is especially interesting as XPS measurements have shown that both interfaces show the presence of Ti^{3+}. This can be explained by the fact that XPS probes all electrons, both mobile and stationary. If the electrons in the LTO_05 sample are somehow localized they would not contribute to the transport.
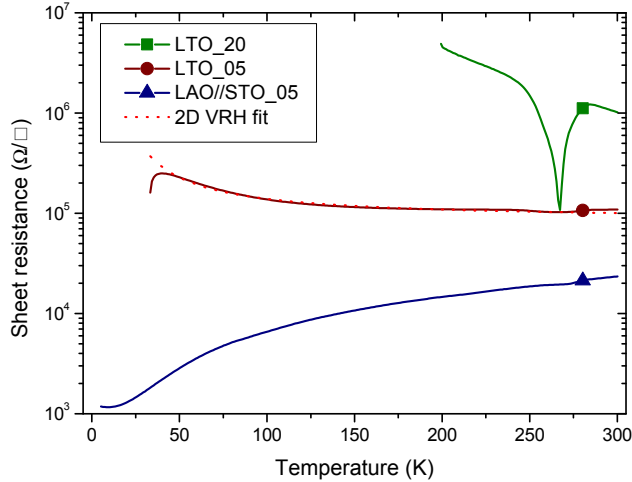
Figure 5.14: Sheet resistance vs. temperature graphs for a comparison of inter- and intra-block interface heterostructures.

To analyse the transport behaviour of the LTO_05 and LAO//STO_05 heterostructures literature can give clues about what mechanisms are at work. As has been seen for the solid solution of STO and LAO, the bulk $Sr_{1-x}La_xTi_{1-x}Al_xO_3$ system can be described with 3D variable-range hopping (VRH) for $x < 0.6$[75]. In this case the aluminium ions form randomly distributed binding sites for the electrons. The sheet resistance can then be described by:

$$R_s(T) = R_{s,0} exp\left(\left(\frac{E_a}{k_B T}\right)^\alpha\right) \tag{5.1}$$

Here $R_s(T)$ is the sheet resistance, $R_{s,0}$ is a pre-exponential factor, E_a is the activation energy and α is an exponent describing the dimensionality of the conducting state: $\alpha = 1/(D+1)$ where D is the dimensionality. This equation can be fit to the insulating LTO_05 heterostructure, with the two-dimensional exponent $\alpha = 1/3$ giving the best results. This reflects the two-dimensional nature of the conducting state at the interface.

Though the sheet resistance appears to be different compared to the LAO//STO inter-block interfaces fabricated directly on STO substrates, the LAO//STO_05 heterostructure can be analysed in the same way. Figure 5.15 shows the electron density and electron mobility vs. temperature. It is immediately clear that the same thermally-activated, $1/T^2$ behaviour is present that has already been observed for such interfaces[22]. The main difference is the activation energy E_a which is 12.9 meV compared to the 6 meV for the substrate-grown LAO//STO inter-block interfaces.

Figure 5.15(b) shows that the electron mobility of the LTO_05 heterostructure could be measured down to 85 K, but did not depend on the temperature over
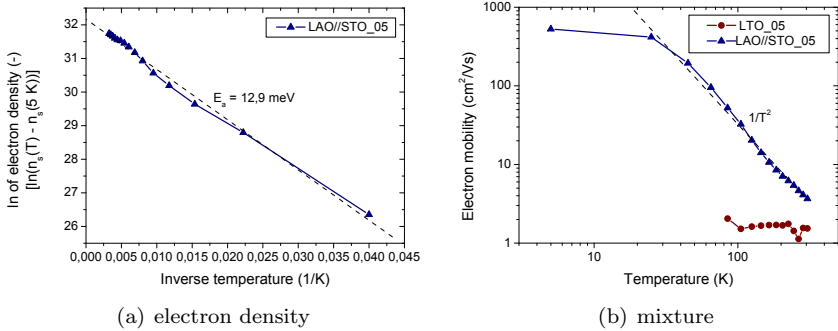
Figure 5.15: Transport properties of a LAO//STO_05 heterostructure. (a) electron density, (b) electron mobility.

that range: $\langle\mu\rangle = 1.6\pm0.2$ cm^2/Vs. The electron density is almost constant over that temperature range as well: $\langle n_{2D}\rangle = 3.5\pm0.6\cdot10^{13}$ cm^{-2}. Table 5.5 compares the results from the two models, VRH for LTO_05 and thermal-activation for LAO//STO_05.

parameter	2D VRH ($\alpha = 1/3$)	thermal-activation
$R_{s,0}$ ($\Omega/\square$)	$8.54\pm0.03\cdot10^4$	
N (cm^{-2})		$9.4\pm0.4\cdot10^{13}$
E_a (meV)	12.65 ± 0.07	12.9 ± 0.3
R^2 (-)	0.991	0.997

Table 5.5: Parameters for the transport models describing inter- and intra-block interfaces.

What is remarkable is the similarity in the activation energy for both heterostructures. This may indicate that the binding sites for both mechanisms, the hopping sites for VRH and the donor states for thermal-activation, are the same. The difference in transport properties would then be due to the fact that for the LTO intra-block interface the discontinuity is resolved differently compared to the LAO//STO inter-block interface. In the structural-polarization model this can easily be explained by the difference in structural relaxation. LTO has a larger lattice constant compared to both STO and LAO. As such the layer will put tensile strain on the STO interlayer. This will partly offset the compressive strain of the LAO top layer and as discussed above this will reduce the polarization and thus the band bending. Without a potential well, the electrons stay with their donors and can only hop from site to site instead of flow through the titanium lattice. An explanation in terms of the electron-transfer model is more difficult, as it would require the absence of a potential well at the LaO//TiO$_2$ interface. This would indicate that the polar discontinuity is resolved within the LTO monolayer, so there would be no LAO band shift and thus no electron transfer. This could

only be achieved if the LaO layer would have an ionic charge of $+1/2$ (see Figure 2.14), which would require an off-stoichiometry of 5/6: $(\mathrm{La}_{5/6}^{3+}\mathrm{O}_1^{2-})^{+1/2}$. TEM images of heterostructures incorporating LTO monolayers show no such defects in the crystal lattice.

To estimate the density of hopping sites the localization length ξ, the average spatial extent of a hopping site, needs to be calculated. This length is related to the activation energy by[76]:

$$E_{\mathrm{a}} = \frac{27/\pi}{\rho(E_{\mathrm{F}})\xi^2} \tag{5.2}$$

Assuming that the density of states at the Fermi level equals the electron density and taking E_{a} from Table 5.5 yields a localization length of $\xi = 44\pm8$ Å. In a two-dimensional closest packing this yields a hopping site density of $1\cdot10^{13}$ cm^{-2}. This is the same order of magnitude (for LAO//STO_05 even the same value: $n_{2\mathrm{D}}(5$ K$) = 1\cdot10^{13}$ cm^{-2}) as the zero Kelvin convergence value for the LAO//STO inter-block interfaces.

Together these observation seem to indicate that the electron transport in the inter- and intra-block interfaces on deposited STO has a common origin. The defect states in STO either form donors from which the electron can be thermally excited to the interface potential well or act as hopping sites when no potential well is present. This shows that though both interfaces are nominally the same LaO//TiO$_2$ interface, their actual behaviour is much different. The structural-polarization model explains this in the difference in local polarization due to the different materials and deposition sequence.

5.9   Conclusions

From analysis of results published in literature two important trends are observed for LAO//STO interfaces. First, there is a critical deposition pressure of about $1\cdot10^{-5}$ mbar below which the transport properties are vacancy dominated and above which the transport is dominated by the interface. Second, the mobility decreases with increasing deposition pressure. This is opposite to bulk STO crystals where the mobility decreases upon reduction at lower pressure.

The first observation can likely be attributed to a thermodynamic threshold. During the deposition the sample-plasma interaction activates oxygen diffusion, which can be substrate-dependent. The difference in deposition pressure then shifts the oxygen equilibrium towards out-diffusion for low pressures or no net diffusion for higher pressures. The cool-down pressure is as important as the deposition pressure, as for high cool-down pressure the interface-dominated properties are recovered even for samples grown at pressures below the critical pressure. Plotting the p vs. T phase diagram shows that there is indeed a clear boundary between the vacancy-dominated and interface-dominated samples.

This recovery of low-pressure grown samples is driven by re-oxidation of the sample after deposition. Here the difference in oxygen diffusion speed at high and low temperature becomes important. At high temperatures the full oxygenation of the sample can be recovered, while samples cooled down at low pressures only partial re-oxidized or not at all. The thickness of the LAO layer can also block the re-oxidation, showing the dependence on oxygen diffusion. The combination of these three parameters, pressure, temperature and thickness, traces different paths through the phase diagram.

A question still remains what process activates the oxygen diffusion, especially in low-pressure depositions. The (partial) oxygen pressure does not seem to play an important role. This is clearly shown by the fact that substrates treated at the deposition conditions do not become conducting. Gettering of oxygen from the STO by the LAO layer should result in a sharp drop of the sheet resistance due to the increase in oxygen vacancies followed by a more gradual decrease as the oxygen transport through the LAO layer becomes impossible. This effect should be more pronounced at lower pressures, as the LAO scavenges more oxygen from the STO substrate. A sharp drop-off is observed for higher pressures, so LAO gettering is not the likely source. The similarities between the transport properties for both pure O_2 and O_2/Ar mixed deposition gasses indicates that it is the plasma sputtering process that starts the oxygen diffusion.

The second observation of the decreasing mobility is the result of a very subtle interplay at the interface. The samples grown at higher pressures have less oxygen vacancies, but also a lower dielectric constant. This decreases the spatial extent of the electron layer, confining them closer to the interface. There the interaction with the defects at the interface, further enhanced by the reduced screening, lowers the electron mobility. Here the interplay between 3D electron density, dielectric constant and electric field can result in a tightly bound electron layer.

For the mobility a comparison between samples grown in pure O_2 and in an O_2/Ar mixture show that in both cases the mobility decreases with increasing total pressure. This indicates that it is not only the oxygen content of the STO layer that controls the electron distribution; the crystallinity of the LAO layer has an influence as well, either through induced strain or through an increased dipole response. Which of the two sources, substrate oxygen content or LAO layer quality, is the main driver for the changes in mobility depends on all deposition parameters, not just the pressure.

The theoretical view of LAO//STO interfaces starts from the polar discontinuity at the interface that drives a band shift in the LAO. When the LAO valence band crosses the Fermi level, electrons can be transferred from the LAO valence band into the STO conduction band. However, this LAO band shift has so far not been observed by, for example, photoelectron spectroscopy. An alternative model has been developed where the local structural reconstruction driven by both strain and electrostatic charge results in band bending towards the Fermi level. Defect states in the STO can then provide conduction electrons. Of course, a combination of these two mechanisms may occur.

Comparing different LAO//STO interfaces fabricated on different substrates, it appears that only small compressive strain on the STO can create conducting interfaces. This, combined with the lack of conducting interfaces for large or tensile strains, may be arguments for this structural-polarization model. The reduced electron density for LAO//STO interfaces with a STO interlayer compared to interfaces without such an interlayer also favours the structural-polarization model. As the LAO layer is equal for both structures, the electron-transfer model predicts similar results. The deposited STO, however, has less defect states, so the structural-polarization model predicts the lower electron density observed.

So far all experimental interfaces discussed in literature are LAO//STO inter-block interfaces. By fabricating LTO intra-block interfaces the strain and charge state can be different. Comparing the two interfaces show that the LTO intra-block interface confines electrons to its interface, but the conduction is by variable-range hopping. This is different from the $\sim T^2$ behaviour of the LAO//STO inter-block interface. Both transport mechanisms exhibit the same activation energy, suggesting that the binding sites in both systems are similar. The difference between the two systems may be due to the presence of a potential well at the LAO//STO interface, while it is absent at the LTO interface due to the different strain and electrostatic forces. The density of these binding sites is close to the convergent zero-Kelvin electron density, hinting that these sites may be the source of this residual electron density.

5.10 References

[1] A. Ohtomo, D. A. Muller, J. L. Grazul, and H. Y. Hwang, "Artificial charge-modulation in atomic-scale perovskite titanate superlattices," *Nature*, vol. 419, pp. 378–380, 2002.

[2] N. Nakagawa, H. Y. Hwang, and D. A. Muller, "Why some interfaces cannot be sharp," *Nature Materials*, vol. 5, pp. 204–209, 2006.

[3] A. Ohtomo and H. Y. Hwang, "A high-mobility electron gas at the $LaAlO_3/SrTiO_3$ heterointerface," *Nature*, vol. 427, pp. 423–426, 2004.

[4] J. Mannhart, D. H. A. Blank, H. Y. Hwang, A. J. Millis, and J. M. Triscone, "Two-dimensional electron gases at oxide interfaces," *MRS Bulletin*, vol. 33, pp. 1027–1034, 2008.

[5] M. Huijben, A. Brinkman, G. Koster, G. Rijnders, H. Hilgenkamp, and D. H. A. Blank, "Structure-property relation of $SrTiO_3$-$LaAlO_3$ interfaces," *Advanced Materials*, vol. 21, pp. 1665–1677, 2009.

[6] W. Siemons, G. Koster, H. Yamamoto, T. H. Geballe, D. H. A. Blank, and M. R. Beasley, "Experimental investigation of electronic properties of buried heterointerfaces of $LaAlO_3$ on $SrTiO_3$," *Physical Review B*, vol. 76, p. 155111, 2007.

[7] A. Kalabukhov, R. Gunnarsson, J. Börjesson, E. Olsson, T. Claeson, and D. Winkler, "Effect of oxygen vacancies in the $SrTiO_3$ substrate on the electrical properties of the $LaAlO_3/SrTiO_3$ interface," *Physical Review B*, vol. 75, p. 121404, 2007.

[8] A. Brinkman, M. Huijben, M. van Zalk, J. Huijben, U. Zeitler, J. C. Maan, W. G. van der Wiel, G. Rijnders, D. H. A. Blank, and H. Hilgenkamp, "Magnetic effects at the interface between nonmagnetic oxides," *Nature Materials*, vol. 6, pp. 493–496, 2007.

[9] Y. Li and J. Yu, "Polarization screening and induced carrier density at the interface of $LaAIO_3$ overlayer on $SrTiO_3(001)$." cond-mat/0904.1636, 2009.

[10] W.-J. Son, E. Cho, B. Lee, J. Lee, and S. Han, "Density and spatial distribution of charge carriers in the intrinsic n-type $LaAlO_3$-$SrTiO_3$ interface," *Physical Review B*, vol. 79, p. 245411, 2009.

[11] H. Chen, A. M. Kolpak, and S. Ismail Beigi, "Fundamental asymmetry in interfacial electronic reconstruction between insulating oxides: An ab initio study," *Physical Review B*, vol. 79, p. 161402, 2009.

[12] N. C. Bristowe, E. Artacho, and P. B. Littlewood, "Oxide superlattices with alternating p and n interfaces," *Physical Review B*, vol. 80, p. 045425, 2009.

[13] N. Reyren, S. Thiel, A. D. Caviglia, L. Fitting Kourkoutis, G. Hammerl, C. Richter, C. W. Schneider, T. Kopp, A. S. Rüetschim, D. Jaccard, M. Gabay, D. A. Muller, J. M. Triscone, and J. Mannhart, "Superconducting interfaces between insulating oxides," *Science*, vol. 317, pp. 1196–1199, 2007.

[14] A. D. Caviglia, S. Gariglio, N. Reyren, D. Jaccard, T. Schneider, M. Gabay, S. Thiel, G. Hammerl, J. Mannhart, and J. M. Triscone, "Electric field control of the $LaAlO_3/SrTiO_3$ interface ground state," *Nature*, vol. 456, pp. 624–627, 2008.

[15] T. Schneider, A. D. Caviglia, S. Gariglio, N. Reyren, and J. M. Triscone, "Electrostatically-tuned superconductor-metal-insulator quantum transition at the LaAlO$_3$/SrTiO$_3$ interface," *Physical Review B*, vol. 79, p. 184502, 2009.

[16] M. van Zalk, J. Huijben, A. J. M. Giesbers, M. Huijben, U. Zeitler, J. C. Maan, W. G. van der Wiel, Rijnders G., D. H. A. Blank, H. Hilgenkamp, and A. Brinkman, "Magnetoresistance oscillations and relaxation effects at the SrTiO$_3$-LaAlO$_3$ interface." cond-mat/0806.4450, 2008.

[17] S. Thiel, C. W. Schneider, L. Fitting Kourkoutis, D. A. Muller, N. Reyren, A. D. Caviglia, S. Gariglio, J. M. Triscone, and J. Mannhart, "Electron scattering at dislocations in LaAlO$_3$/SrTiO$_3$ interfaces," *Physical Review Letters*, vol. 102, p. 046809, 2009.

[18] G. Herranz, M. Basletić, M. Bibes, C. Carrétéro, E. Tafra, E. Jacquet, K. Bouzehouane, C. Deranlot, A. Hamzić, J. M. Broto, A. Barthélémy, and A. Fert, "High mobility in LaAlO$_3$/SrTiO$_3$ heterostructures: Origin, dimensionality, and perspectives," *Physical Review Letters*, vol. 98, p. 216803, 2007.

[19] M. Strikovski and J. H. Miller Jr., "Pulsed laser deposition of oxides: why the optimum rate is about 1 Å per pulse," *Applied Physics Letters*, vol. 73, pp. 1733–1735, 1998.

[20] J. Nishimura, A. Ohtomo, A. Ohkubo, Y. Murakami, and M. Kawasaki, "Controlled carrier generation at a polarity-discontinued perovskite heterointerface," *Japanese Journal of Applied Physics*, vol. 43, pp. L1032–L1034, 2004.

[21] A. S. Kalabukhov, R. Gunnarsson, J. Börjesson, E. Olsson, T. Claeson, and D. Winkler, "The role of oxygen vacancies in SrTiO$_3$ at the LaAlO$_3$/SrTiO$_3$ interface." cond-mat/0603501, 2006.

[22] M. Huijben, G. Rijnders, D. H. A. Blank, S. Bals, S. van Aert, J. Verbeeck, G. van Tendeloo, A. Brinkman, and H. Hilgenkamp, "Electronically coupled complementary interfaces between perovskite band insulators," *Nature Materials*, vol. 5, pp. 556–560, 2006.

[23] G. Herranz, M. Basletic, M. Bibes, C. Carretero, E. Tafra, E. Jacquet, K. Bouzehouane, C. Deranlot, J. L. Maurice, A. Hamzic, J. P. Contour, A. Barthélémy, and A. Fert, "Origin and perspectives of high mobility in LaAlO$_3$/SrTiO$_3$ structures." cond-mat/0606182, 2006.

[24] C. W. Schneider, S. Thiel, G. Hammerl, C. Richter, and J. Mannhart, "Microlithography of electron gases formed at interfaces in oxide heterostructures," *Applied Physics Letters*, vol. 89, p. 122101, 2006.

[25] S. Thiel, G. Hammerl, A. Schmehl, C. W. Schneider, and J. Mannhart, "Tunable quasi-two-dimensional electron gases in oxide heterostructures," *Science*, vol. 313, pp. 1942–1945, 2006.

[26] W. Siemons, G. Koster, H. Yamamoto, W. A. Harrison, G. Lucovsky, T. H. Geballe, D. H. A. Blank, and M. R. Beasley, "Origin of charge density at LaAlO$_3$ on SrTiO$_3$ heterointerfaces: possibility of intrinsic doping," *Physical Review Letters*, vol. 98, p. 196802, 2007.

[27] A. Kalabukhov, R. Gunnarsson, J. Börjesson, E. Olsson, D. Winkler, and T. Claeson, "Effect of various deposition conditions on the electrical properties of LAO/STO hetero interfaces," *Journal of Physics: Conference Series*, vol. 100, p. 082039, 2008.

[28] F. J. Wong, M. Chi, R. V. Chopdekar, B. B. Nelson Cheeseman, N. D. Browning, and Y. Suzuki, "Potential barrier lowering and electrical transport at the LaAlO$_3$/SrTiO$_3$ heterointerface." cond-mat/0809.0926, 2008.

[29] C. Bell, S. Harashima, Y. Hikita, and H. Y. Hwang, "Thickness dependence of the mobility at the LaAlO$_3$/SrTiO$_3$ interface," *Applied Physics Letters*, vol. 94, p. 222111, 2009.

[30] M. Basletic, J. L. Maurice, C. Carrétéro, G. Herranz, O. Copie, M. Bibes, E. Jacquet, K. Bouzehouane, S. Fusil, and A. Barthélémy, "Mapping the spatial distribution of charge carriers in LaAlO$_3$/SrTiO$_3$ heterostructures," *Nature Materials*, vol. 7, pp. 621–625, 2008.

[31] C. Cen, S. Thiel, G. Hammerl, C. W. Schneider, K. E. Andersen, C. S. Hellberg, J. Mannhart, and J. Levy, "Nanoscale control of an interfacial metal-insulator transition at room temperature," *Nature Materials*, vol. 7, pp. 298–302, 2008.

[32] L. Liborio and N. Harrison, "Thermodynamics of oxygen defective Magnéli phases in rutile: A first-principles study," *Physical Review B*, vol. 77, p. 104104, 2008.

[33] A. Hirata, A. Ando, K. Saiki, and A. Koma, "Characterization of surface defects formation in strontium titanate(100)," *Surface Science*, vol. 310, pp. 89–94, 1994.

[34] R. Moos, W. Menesklou, and K. H. Härdtl, "Hall mobility of undoped n-type conducting strontium titanate single crystals between 19 K and 1373 K," *Applied Physics A: Materials Science & Processing*, vol. 61, pp. 389–395, 1995.

[35] H. Yamada and G. R. Miller, "Point defects in reduced strontium titanate," *Journal of Solid State Chemistry*, vol. 6, pp. 169 – 177, 1973.

[36] H. P. R. Frederikse and W. R. Hosler, "Hall mobility in SrTiO$_3$," *Physical Review*, vol. 161, pp. 822–827, 1967.

[37] O. N. Tufte and P. W. Chapman, "Electron mobility in semiconducting strontium titanate," *Physical Review*, vol. 155, pp. 796–802, 1967.

[38] K. Ueno, S. Nakamura, H. Shimotani, A. Ohtomo, N. Kimura, T. Nojima, H. Aoki, Y. Iwasa, and M. Kawasaki, "Electric-field-induced superconductivity in an insulator," *Nature Materials*, vol. 7, pp. 855–858, 2008.

[39] O. Copie, V. Garcia, C. Bödefeld, C. Carrétéro, M. Bibes, G. Herranz, E. Jacquet, J. L. Maurice, B. Vinter, S. Fusil, K. Bouzehouane, H. Jaffrès, and A. Barthélémy, "Towards two-dimensional metallic behavior at LaAlO$_3$/SrTiO$_3$ interfaces," *Physical Review Letters*, vol. 102, p. 216804, 2009.

[40] C. Bell, S. Harashima, Y. Kozuka, M. Kim, B. G. Kim, Y. Hikita, and H. Y. Hwang, "Dominant mobility modulation by the electric field effect at the LaAlO$_3$/SrTiO$_3$ interface." cond-mat/0906.5310, 2009.

[41] Z. S. Popović, S. Satpathy, and R. M. Martin, "Origin of the two-dimensional electron gas carrier density at the LaAlO$_3$ on SrTiO$_3$ interface," *Physical Review Letters*, vol. 101, p. 256801, 2008.

[42] M. Lippmaa, N. Nakagawa, M. Kawasaki, S. Ohashi, and H. Koinuma, "Dielectric properties of homoepitaxial SrTiO$_3$ thin films grown in the step-flow mode," *Journal of Electroceramics*, vol. 4, pp. 365–368, 2000.

[43] X. Cai, C. D. Frisbie, and C. Leighton, "Optimized dielectric properties of SrTiO$_3$:Nb/SrTiO$_3$ (001) films for high field effect charge densities," *Applied Physics Letters*, vol. 89, p. 242915, 2006.

[44] X. Z. Liu, B. W. Tao, and Y. R. Li, "Effect of oxygen vacancies on nonlinear dielectric properties of SrTiO$_3$ thin films," *Journal of Materials Science*, vol. 42, pp. 389–392, 2007.

[45] H. Föll, "2.4.2 Debye Length." http://www.tf.uni-kiel.de/matwis/amat/elmat_en/kap_2/backbone/r2_4_2.html (12-03-2009), 2007.

[46] C. S. Koonce, M. L. Cohen, J. F. Schooley, W. R. Hosler, and E. R. Pfeiffer, "Superconducting transition temperatures of semiconducting SrTiO$_3$," *Physical Review*, vol. 163, pp. 380–390, 1967.

[47] M. Minohara, Y. Furukawa, R. Yasuhara, H. Kumigashira, and M. Oshima, "Orientation dependence of the Schottky barrier height for $La_{0.6}Sr_{0.4}MnO_3/SrTiO_3$ heterojunctions," *Applied Physics Letters*, vol. 94, p. 242106, 2009.

[48] S. Gemming and G. Seifert, "$SrTiO_3(001)|LaAlO_3(001)$ multilayers: a density-functional investigation," *Acta Materialia*, vol. 54, pp. 4299–4306, 2006.

[49] R. Pentcheva and W. E. Pickett, "Ionic relaxation contribution to the electronic reconstruction at the n-type $LaAlO_3/SrTiO_3$ interface," *Physical Review B*, vol. 78, p. 205106, 2008.

[50] U. Schwingenschlögl and C. Schuster, "Surface effects on oxide heterostructures," *Europhysics Letters*, vol. 81, p. 17007, 2008.

[51] R. Pentcheva and W. E. Pickett, "Avoiding the polarization catastrophe in $LaAlO_3$ overlayers on $SrTiO_3(001)$ through a polar distortion," *Physical Review Letters*, vol. 102, p. 107602, 2009.

[52] C. L. Jia, S. B. Mi, M. Faley, U. Poppe, J. Schubert, and K. Urban, "Oxygen octahedron reconstruction in the $SrTiO_3/LaAlO_3$ heterointerfaces investigated using aberration-corrected ultrahigh-resolution transmission electron microscopy," *Physical Review B*, vol. 79, p. 081405, 2009.

[53] J. L. Maurice, C. Carrétéro, M. J. Casanove, K. Bouzahouane, S. Guyard, E. Larquet, and J. P. Contour, "Electronic conductivity and structural distortion at the interface between insulators $SrTiO_3$ and $LaAlO_3$," *Physica Status Solidi A*, vol. 203, pp. 2209–2214, 2006.

[54] V. Vonk, M. Huijben, K. J. I. Driessen, P. Tinnemans, A. Brinkman, S. Harkema, and H. Graafsma, "Interface structure of $SrTiO_3/LaAlO_3$ at elevated temperatures studied in situ by synchrotron X-rays," *Physical Review B*, vol. 75, p. 235417, 2007.

[55] J. H. Haeni, P. Irvin, W. Chang, R. Uecker, P. Reiche, Y. L. Li, S. Choudhury, W. Tian, M. E. Hawley, B. Craigo, A. K. Tagantsev, X. Q. Pan, S. K. Streiffer, L. Q. Chen, S. W. Kirchoefer, J. Levy, and D. G. Schlom, "Room-temperature ferroelectricity in strained $SrTiO_3$," *Nature*, vol. 430, pp. 758–761, 2004.

[56] J. Seidel, L. W. Martin, Q. He, Q. Zhan, Y. H. Chu, A. Rother, M. E. Hawkridge, P. Maksymovych, P. Yu, M. Gajek, N. Balke, S. V. Kalinin, S. Gemming, F. Wang, G. Catalan, J. F. Scott, N. A. Spaldin, J. Orenstein, and R. Ramesh, "Conduction at domain walls in oxide multiferroics," *Nature Materials*, vol. 8, pp. 229–234, 2009.

[57] P. Maksymovych, S. Jesse, P. Yu, R. Ramesh, A. P. Baddorf, and S. V. Kalinin, "Polarization control of electron tunneling into ferroelectric surfaces," *Science*, vol. 324, pp. 1421–1425, 2009.

[58] M. K. Niranjan, Y. Wang, S. S. Jaswal, and E. Y. Tsymbal, "Prediction of a switchable two-dimensional electron gas at ferroelectric oxide interfaces," *Physical Review Letters*, vol. 103, p. 016804, 2009.

[59] A. Tsukazaki, A. Ohtomo, T. Kita, Y. Ohno, H. Ohno, and M. Kawasaki, "Quantum Hall effect in polar oxide heterostructures," *Science*, vol. 315, pp. 1388–1391, 2007.

[60] J. Lu, M. V. S. Chandrashekhar, J. J. Parks, D. C. Ralph, and M. G. Spencer, "Quantum confinement and coherence in a two-dimensional electron gas in a carbon-face 3C-SiC/6H-SiC polytype heterostructure," *Applied Physics Letters*, vol. 94, p. 162115, 2009.

[61] W. A. Feil and B. W. Wessels, "Defect structure of strontium titanate thin films," *Journal of Applied Physics*, vol. 74, pp. 3927–3931, 1993.

[62] T. Fix, J. L. MacManus Driscoll, and M. G. Blamire, "Delta-doped $LaAlO_3/SrTiO_3$ interfaces," *Applied Physics Letters*, vol. 94, p. 172101, 2009.

[63] N. Pavlenko and T. Kopp, "Structural relaxation and metal-insulator transition at the interface between $SrTiO_3$ and $LaAlO_3$." cond-mat/0901.4610, 2009.

[64] A. Kalabukhov, R. Gunnarsson, T. Claeson, and D. Winkler, "Electrical transport properties of polar heterointerface between $KTaO_3$ and $SrTiO_3$." cond-mat/0704.1050, 2007.

[65] E. D. Murray and D. Vanderbilt, "Theoretical investigation of polarization-compensated II-IV/I-V perovskite superlattices," *Physical Review B*, vol. 79, p. 100102, 2009.

[66] G. Rijnders, D. H. A. Blank, J. Choi, and C.-B. Eom, "Enhanced surface diffusion through termination conversion during epitaxial $SrRuO_3$ growth," *Applied Physics Letters*, vol. 84, pp. 505–507, 2004.

[67] E. J. Tarsa, E. A. Hachfeld, F. T. Quinlan, J. S. Speck, and M. Eddy, "Growth-related stress and surface morphology in homoepitaxial $SrTiO_3$ films," *Applied Physics Letters*, vol. 68, pp. 490–492, 1996.

[68] P. Bouvier and J. Kreisel, "Pressure-induced phase transition in $LaAlO_3$," *Journal of Physics: Condensed Matter*, vol. 14, pp. 3981–3991, 2002.

[69] P. Pasierb, S. Komornicki, and M. Rekas, "Comparison of the chemical diffusion of undoped and Nb-doped $SrTiO_3$," *Journal of Physics and Chemistry of Solids*, vol. 60, pp. 1835–1844, 1999.

[70] P. te Riele, *Direct patterning of oxides by pulsed laser stencil deposition.* PhD thesis, University of Twente, 2008.

[71] T. Ohnishi, M. Lippmaa, T. Yamamoto, S. Meguro, and H. Koinuma, "Improved stoichiometry and misfit control in perovskite thin film formation at a critical fluence by pulsed laser deposition," *Applied Physics Letters*, vol. 87, p. 241919, 2005.

[72] L. M. van Rees, "Electronic effects at interfaces between complex oxides," Master's thesis, University of Twente, the Netherlands, 2008.

[73] K. Driessen, "X-ray investigations of $SrTiO_3$-$LaAlO_3$ superlattices," Master's thesis, University of Twente, the Netherlands, 2006.

[74] W. Siemons, G. Koster, A. Vailionis, H.i Yamamoto, D. H. A. Blank, and M. R. Beasley, "Dependence of the electronic structure of $SrRuO_3$ and its degree of correlation on cation off-stoichiometry," *Physical Review B*, vol. 76, p. 075126, 2007.

[75] A. Ohtomo, J. Nishimura, Y. Murakami, and M. Kawasaki, "Electronic transport properties in $SrTiO_3$-$LaAlO_3$ solid-solution films," *Applied Physics Letters*, vol. 88, p. 232107, 2006.

[76] V. L. Nguyen and D.-T. Dang, "Variable range hopping in finite one-dimensional and anisotropic two-dimensional systems," *Physica B: Condensed Matter*, vol. 334, pp. 88–97, 2003.

Chapter 6

Interacting interfaces in LaAlO$_3$//SrTiO$_3$ heterostructures

Abstract

Double-interface structures of LaAlO$_3$ and SrTiO$_3$ with two n-type interfaces were investigated. Above 70 K the interfaces behave like a Fermi liquid. The electron density behaves as if thermally-activated and at low temperatures there are signatures for multiple conduction bands. At low temperatures a Coulomb scattering mechanism becomes dominant and the electron density freezes out, while at room temperature the electron density is a function of the interface separation. For double-interface np structures the electron density decreases with smaller separation, but for nn structures it increases. A model including the dipoles inherent to LaAlO$_3$ and those due to electron transfer was developed and fit to the data. The difference in behaviour for the np and nn structures is then ascribed to the difference in energy required to free the electrons from their donors. For np structures it is positive, indicating it costs energy to free the electron from its corresponding trap, while for nn structures it is negative, so the energy of the system is lowered when the electron is moved away from the second n-type interface.

6.1 Introduction

The previous chapter already showed how the electron layer at the LAO//STO interface can be influenced by deposition parameters such as gas pressure or by the

design of the heterostructure. However, it has also been shown that a nearby interface influences the transport properties at the interface. In fact, any LAO/STO sample can be considered a double-interface structure, as the interface with air also influences the properties[1–4]. However, there is a clear difference between the LAO/STO samples that are capped with nothing but air and those capped with another STO layer. While the first turn insulating for thin LAO films[1], the latter stay conducting though with a reduced electron density[5].

In this chapter double-interface LAO/STO heterostructures with two n-type interfaces are studied. The results are compared with those for double-interface heterostructures with both a n- and a p-type interface. It is of great interest to study the effect of the interface separation on the ground state of the electron layer. As already discussed in Chapter 2, there is some debate about the ground state of the single-interface LAO/STO system. Both a superconducting and a magnetic state have been observed as a function of the total electron doping, which includes contributions from the interface, from oxygen vacancies and from external field effects[6]. But as the previous chapter showed, a careful choice of the deposition pressure makes it possible to avoid most of the problems associated with vacancies.

The double-interface heterostructures offer a different way to probe the polar catastrophe. The air//film surface is found to be very susceptible to the processing conditions such as post-annealing[7] or indeed to the local environment at all[8]. Thus, growing a series of single-interface samples does not automatically yield a systematic trend in, for example, the electron density[2]. This is illustrated by the overview in Figure 5.1(b). Comparing the electron fraction ($n_{2D}a^2$) for thin (5 monolayer) LAO//STO interfaces grown in different groups, and with different parameters, a wide range of values is observed: 0.03-0.30[1, 2, 7, 9]. Growing another layer on top of the LAO, however, stabilizes the environment of the second STO//LAO interface and separates this interface from any surface effect[5]. Figure 6.1 compare the electron density vs. interface separation data for both types of samples, taken from their respective literature.
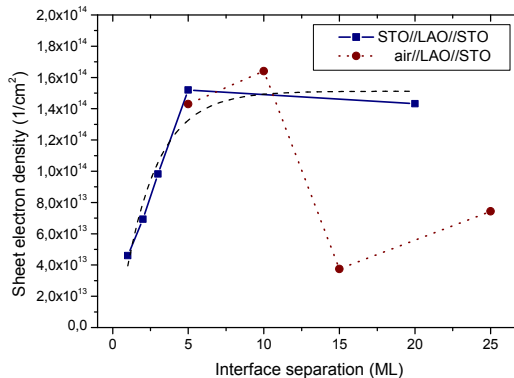

Figure 6.1: Electron density as a function of interface separation for a STO//LAO//STO[5] and an air//LAO//STO sample[2]. The dashed line is an exponential decay fit to the STO//LAO//STO data.

Thus the double-interface structure offers a more stable way to investigate both the ground state of the interface electrons (probed at large interface separation) and allows for the study of the separation dependence which can give clues about the polar catastrophe mechanism.

6.2 Sample fabrication

Two series of samples were fabricated, both nominally containing two n-type interfaces. The first LaO//TiO$_2$ interface is obtained as a standard LAO//STO inter-block interface. The thickness of the LAO layer then determines the interface separation. In layer-by-layer growth mode the surface termination is preserved, so the LAO layer is AlO$_2$-terminated. The monolayer of LTO then constitutes the second n-type intra-block interface. The interface separation is thus a fractional number of unit cell monolayers, i.e. the number of monolayers of LAO plus the half monolayer of the LTO unit cell. Note that in the rest of this chapter, the number of monolayers of LAO is taken as a parameter, without stating the extra 0.5 monolayer involved. Finally 20 monolayers of STO are deposited, both to provide the necessary material on the STO side of the second interface and to separate the interface from the air//film surface. Figure 6.2 compares the np and nn double-interface structures.
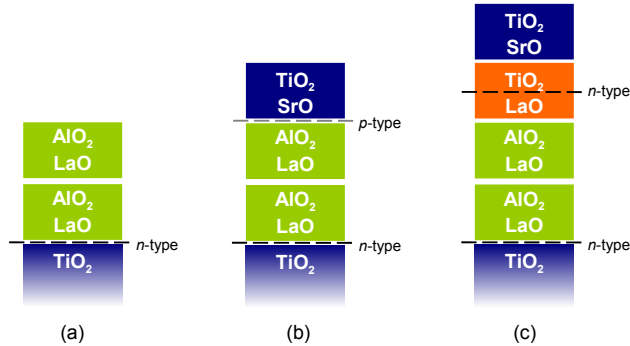
Figure 6.2: Designed structures for the single- and double-interface LAO/STO structures. (a) a single-interface, (b) a np double-interface and (c) a nn double-interface structure. In this case the interface separation is 2, 2 and 2.5 monolayer, respectively.

The settings for the growth of LAO and STO were the same as for Huijben[5]. The settings for LTO are those stated in the previous Chapter optimized for the PLD set-up at the MESA+ Institute for Nanotechnology. Figure 6.3 shows the RHEED oscillations for the growth of thick films of LTO and LAO, respectively. For all samples oscillations in the RHEED intensity, main peak FWHM and in-plane d-spacing were readily obtained.

Figure 6.3: RHEED oscillations during the growth of thick films of LTO and LAO. The arrows indicate where the electron beam intensity is increased.

Typical deposition parameters are a fluency of 1.3 or 1.6 J/cm^2 for LAO / STO and LTO, respectively. The pulse frequency was 1 or 2 Hz with a spotsize area of 0.9-1.7 mm^2. The target-to-substrate distance was 55 mm. Etched-and-anne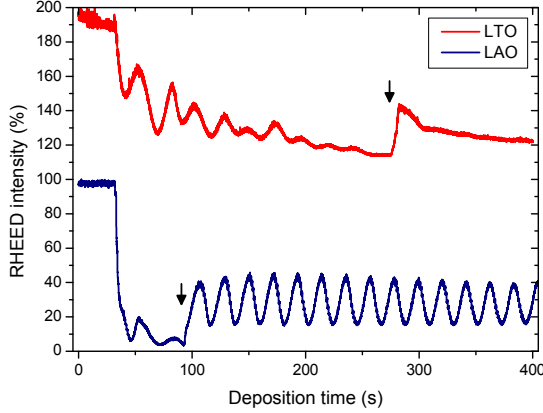aled TiO$_2$-terminated STO(001) substrates were used. The deposition temperature was 850 °C and the samples were cooled down in deposition pressure. The average heating rate was 50 °C/min, while the cool-down was uncontrolled and limited by thermal exchange. Typical cool-down time between switching off the heater and taking the sample out of the deposition chamber is 4 hours. These settings resulted in deposition rates of about ∼20, ∼20 and ∼25 pulses per monolayer for LAO, LTO and STO respectively.

For each of the two series, the interface separation was varied by controlling the number of monolayers of LAO in the central layer. One series was fabricated at a deposition pressure of 3·10^{-5} mbar O$_2$ for comparison with the np series from literature[5]. The other series was fabricated at a deposition pressure of 1·10^{-3} mbar O$_2$ following the discussion in Section 2.5.2 as to exclude the effect of oxygen vacancies as much as possible. Both series are referred to as 'NNx_p' where x is the number of LAO monolayers and p is either 'LP' for 3·10^{-5} mbar or 'HP' for 1·10^{-3} mbar O$_2$ deposition pressure. A 'NN∞_p' sample would signify a sample with an infinite separation between the interfaces grown at either pressure. In effect it is a single-interface sample with only 20 monolayers of LAO grown.

6.3   Structural characterization

AFM scans of the surfaces of the double-interface samples reproduce the step-and-terrace structure of the etched-and-annealed substrates. Figure 6.4 shows a 5×5

μm scan for a substrate (a) and a single-layer sample (b) for comparison. RMS values are of the order of 2 Å over the same area, which is a common value for all double-interface samples. The friction force scan in Figure 6.4(c) shows there is no difference in the chemical composition of the surface and so it is probably singly-terminated. As the stacking is preserved in layer-by-layer growth the top surface is expected to be TiO_2.

(a) substrate   (b) topography map   (c) friction map
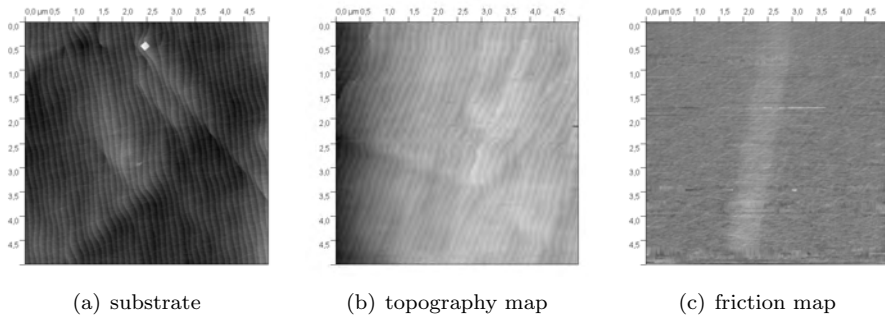
Figure 6.4: Comparison of top surface AFM scans for (a) substrate topography and a NN09_HP sample (b) topography and (c) friction map. The horizontal stripes are artefacts of the AFM scanning.

For thin LAO layers (<10 monolayers) the film peaks were not resolved from the substrate peaks in the θ-2θ scans. This is probably due to the small volume probed. For thicker LAO layers a c-axis parameter $c_{film} = 3.73$ Å is found, which is identical to that of thick LAO films $c_{LAO} = 3.73$ Å. Figure 6.5 shows a θ-2θ scan for a NN10_HP sample.
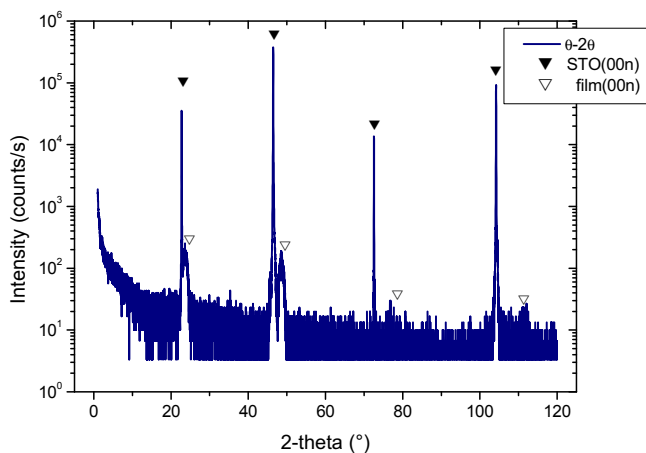
Figure 6.5: θ-2θ scan of a NN20_HP sample. c-axis parameters extracted from this scan were $c_{STO} = 3.904$ Å and $c_{film} = 3.728$ Å.

Figure 6.6: hkl reciprocal space map around (112) of a NN10_HP sample. c_{film} from this scan is 3.74 Å.

Rocking curves from the (002) peaks of the substrate and the film had a FWHM of 0.03° and 0.05°, respectively. ϕ-scans show that the heterostructure is grown cube-on-cube without twinning. These small values show that there is little spread in the in-plane orientation. The reciprocal space map shown in Figure 6.6 shows that the film is coherently grown on the STO substrate.
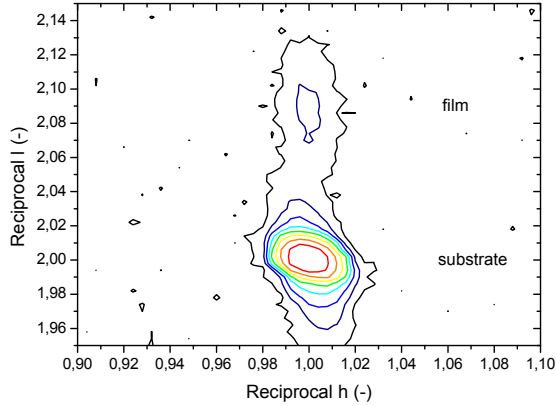
TEM imaging confirmed the coherent growth. From TEM it can also be seen that the thickness of the LAO layer is as designed. From either XRD or TEM it is difficult to estimate any chemical intermixing at the interfaces. But light intermixing would lead to a conducting $La_xSr_{1-x}Al_yTi_{1-y}O_3$ compound, even for small x[10–13]. As shown in the previous Chapter the LTO intra-block interface is insulating, so the LAO/STO structures have little to no intermixing.

6.4 Transport in double-interface heterostructures

Transport measurements are one of the main tools to study these interfaces, either single or double. For one, the conducting state is a unique property of the LaO//TiO$_2$ interface. For another, they are relatively easy to do though the interpretation can be more difficult. Van-der-Pauw and Hall measurements were carried out on all samples to determine the sheet resistances, electron densities and electron mobilities. These values are compared with the results from similar measurements on np double-interface samples obtained from literature[5] or private communication.

6.4.1 Inclusion of a LaTiO$_3$ intra-block interface

In the previous chapter the difference between the LaO//TiO$_2$ interface in LTO and in LAO//STO has already been discussed. It was found that the conductivity at the LTO intra-block interface was greatly reduced compared to that of the LAO//STO inter-block interface. In the double-interface structures this effect is again observed. If both interfaces were identical it would be naively expected that for well-separated interfaces the sheet resistance is half that of a single-interface sample because there are now two conduction channels. However, as Figure 6.7(a) shows this is certainly not the case. The transport properties of NN∞_p and NN20_p grown under the same settings are compared.

(a) sheet resistance

(b) electron density

(c) electron mobility

(d) Arrhenius plot
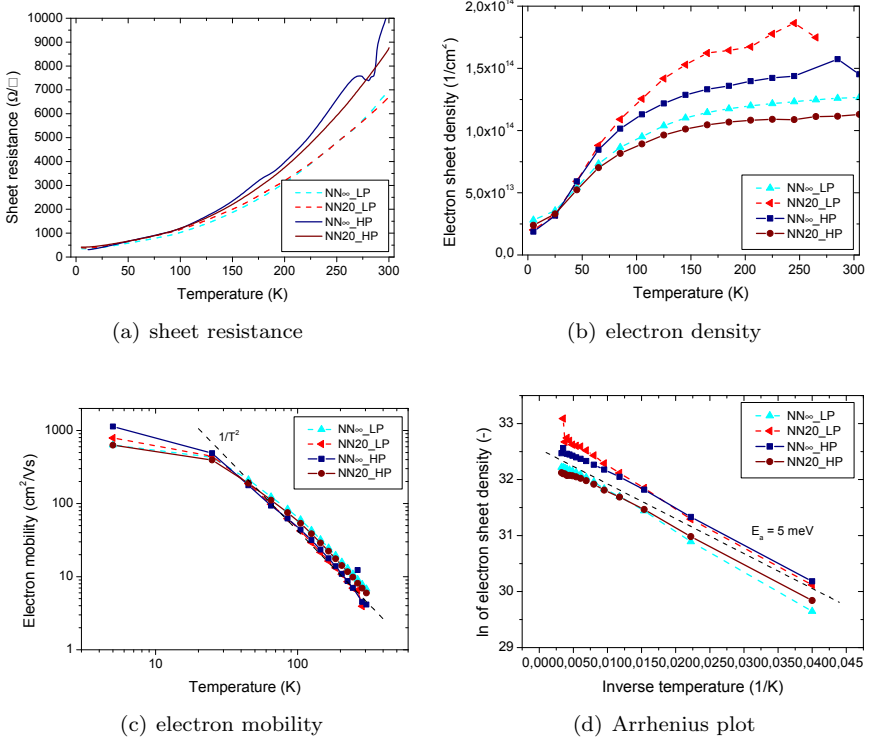
Figure 6.7: Transport properties of single- and double-interface samples. The interfaces in the NN20_p samples are thought to be independent of one another[5]. The dip in the NN∞_HP curve around 275 K in (a) is due to ice formation.

Figures 6.7(c) and 6.7(d) show that both single- and double-interface structures behave very similar. The electron mobility is Fermi liquid-like with a $1/T^2$ temperature dependence above 50 K, while the electron sheet density is thermally-activated with an activation energy E_a of about 5 meV. This is very similar to the results for np structures[5].

The observation that the electrons behave like a Fermi liquid up to room temperature is surprising. Typically, electron-phonon interactions dominate at higher temperatures[14]. But the poor heat conduction indicates that the electron-phonon interaction may be be weak in STO so Fermi liquid electron-electron interactions dominate at room temperature. In addition, electron-phonon scattering would give a T^5 temperature dependence which is not observed[5]. Other scattering mechanisms such as disorder or polaron[15] scattering are also unlikely. The former should result in a larger spread of mobilities as the degree of disorder would be different for each sample, the latter yields phonon frequencies for the double-interface structures that show no systematic trends or tend to zero.

The difference in transport behaviour is mostly due to the changes in electron density. But in no case does the electron density double for the structure with two n-type interfaces compared to the single n-type interface structure. Indeed, in some cases the double-interface sample has a *lower* electron density compared to the corresponding single-interface sample. So, despite the fact that Ti^{3+} is present at the intra-block LTO interface as determined by XPS those electrons do not directly contribute to the conduction in double-interface structures (see discussion in Section 5.8). The variation shown in Figure 6.7(b) is most likely due to sample-to-sample variation.

6.4.2   Overview of the transport properties

For smaller interface separations it is expected that the two interfaces do interact[5]. In the np structures the p-type interface does not conduct either, similar to the n-type LTO intra-block interface, but it still influences the electron density at the LAO//STO inter-block interface. Comparing the results for nn structures with those for np structures can yield interesting information on the formation of the conducting layer at the interface.

Figure 6.8 shows the sheet resistance, electron density and electron mobility of both nn series and the np series from literature for an interface separation s of 1, 5, 10 and 20 monolayers.

From Figure 6.8(a) it can be seen that though the absolute magnitude of the sheet resistance varies with interface separation, the temperature relation is similar for all samples. Figure 6.8(c) emphasizes this, as the electron mobility for all samples basically collapse onto another. The black dashed line shows that above 60 K the electrons can be described as a Fermi liquid with a $1/T^2$ dependence. Towards lower temperatures the mobility seems to reach a constant value of about 800 cm^2/Vs. The comparison with the np data already shows that the nn structures behave very similar to earlier interfaces.

Just as for the comparison between single- and double-interfaces in the previous subsection the main difference between samples is in the absolute magnitude of the electron density. Figure 6.8(d) shows an Arrhenius plot from which an activation energy of 5-6 meV is derived. This shows that the electrons behave as if thermally-

(a) sheet resistance

(b) electron density

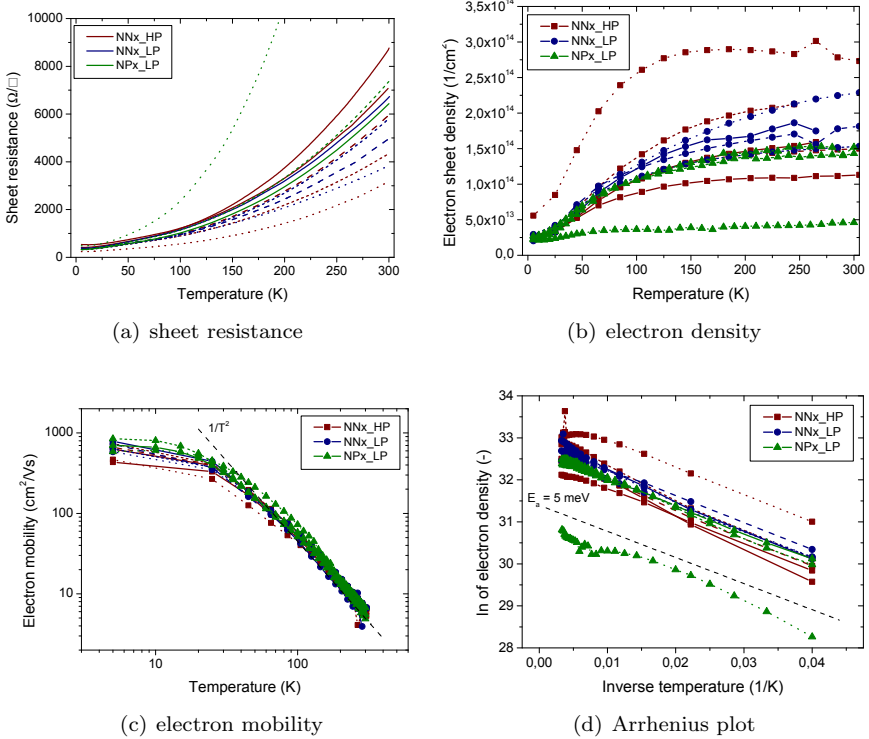(c) electron mobility

(d) Arrhenius plot

Figure 6.8: Transport properties of double-interface samples with different interface separations. The different line styles represent the interface separation: solid for $x = 20$, dashed for $x = 10$-9, short-dashed for $x = 6$-5 and dotted for $x = 1$.

activated from donors and freeze out below a temperature of 60 K. Interestingly enough the electron density at 5 K converges for all samples to about $2 \cdot 10^{13}$ cm^{-2}. This is valid not only for the samples discussed here, but also for other LAO//STO interface samples reported in literature[1, 7, 16, 17]. This value is close the critical electron density above which strong confinement of the electrons to the interface can occur[18]. Whether there is an actual causal relation is unclear as of yet.

Even further down in temperature there is the possibility for a superconducting transition at about 250-300 mK[17]. It was shown that the critical temperature could be changed by field-effect doping of the interface[19]. The maximum T_c was about 300 mK at 5–$6 \cdot 10^{13}$ cm^{-2}. Using a ^{3}He cryostat samples from each pressure series, one of which had an electron density of $6.1 \cdot 10^{13}$ cm^{-2} at 5 K, were cooled down to 254 mK in hope of observing the superconducting transition. Current-voltage plots show Ohmic behaviour all the way down to the base temperature and no superconducting transition was observed. Lowering the measurement current to drop below any possible critical current did also not result in a superconducting

state. Most likely the spatial distribution of the electrons in the STO was different from the reported samples so the 3D electron distribution did not exceed the required minimum density of about $5 \cdot 10^{19}$ cm^{-3}[20].

From these observations it seems clear that the scattering mechanism in double-interface structures is the same as for the single-interface structures. The scattering behaviour is very similar to that of doped or reduced STO[21], something which has been noted before[22]. In a way this is not surprising, as the conduction is *along* the interface, mostly through the first few monolayers of STO next to the interface. Any influence on the scattering mechanism due to sputtering during the PLD process or chemical intermixing will not be much different for 1 or 20 monolayers of LAO. The first deposited LAO monolayer will prevent any further arriving species from reaching the STO. The one aspect that LAO//STO interfaces are different to doped STO is the dependence of the electron density on the LAO layer. This was shown experimentally for the LAO/STO[5] and LAO/LVO[23] systems.

Figure 6.9 shows the sheet resistance at room temperature as a function of LAO layer thickness in monolayers. The actual interface separation would be s unit cells for the np samples from Huijben and $s + 1/2$ unit cells for the nn samples investigated here. A similar plot for 5 K shows that the ground state resistance is around 400 $\Omega/\square$ for all systems and series. This is unsurprising considering the freeze-out behaviour discussed before.
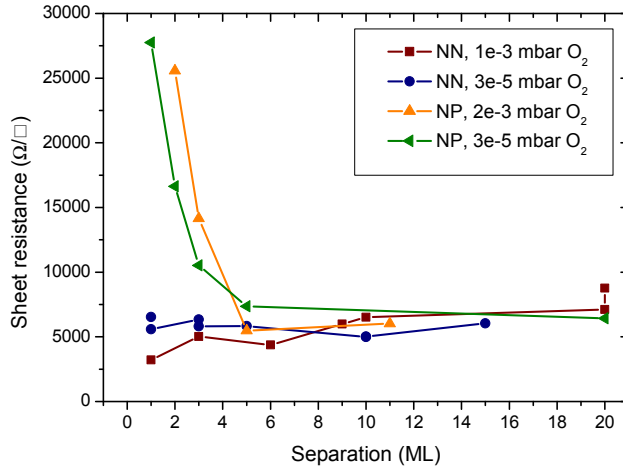
Figure 6.9: Sheet resistance at 300 K as a function of interface separation for LAO/STO double-interface samples. NPx_LP, $3 \cdot 10^{-5}$ mbar O$_2$ values are from Huijben[5], while the NPx_HP, $2 \cdot 10^{-3}$ mbar O$_2$ values are from private communication. Other values are original work.

Clearly the two systems, nn and np, behave differently. For one, the np system shows an increasing sheet resistance with decreasing interface separation. The nn system shows constant or even opposite behaviour, a decreasing sheet resistance

with decreasing separation. For another, the difference between the series grown at different pressures for the *np* system is negligible, while the *nn* system shows a more pronounced difference. Reconciling these differences requires a model that takes into account both separation and pressure.

6.4.3   Modelling the interface interaction

To understand the physics of the interaction between two interfaces a detailed look at the sheet electron density and mobility is needed. Figures 6.10(a) & (b) plot these values as a function of the interface separation, showing that the differences are mainly due to changes in the electron density.

The electron mobility is rather constant around 6.1 cm^2/Vs with a standard deviation of 0.3 cm^2/Vs. This is averaged over all four sample series (see also Table 6.3). Given the near-constant value of the electron mobility, most of the observations on the sheet resistance transfer directly to the electron density. These observations can be summarized as follows:

1. At large separation, all samples and series converge to a single value, similar to a single-interface sample.

2. The *np* system is similar for both pressures; a decreasing electron density for smaller separations.

3. The *nn* system is dissimilar for both pressures; for the low-pressure ($3 \cdot 10^{-5}$ mbar O_2) samples the density is nearly constant, while for the high-pressure ($1 \cdot 10^{-3}$ mbar O_2) samples the electron density increases for smaller separations.

A simple source/sink model can explain some of the behaviour. EELS measurements showed that the *n*-type interface is electron-doped, while the *p*-type interface is hole-doped though compensated through oxygen vacancies[24, 25]. However, if two complementary interfaces come close together electrons from the *n*-type interface, the source, can transfer to the *p*-type interface, the sink, thus reducing the electron density. In the case of a double *n*-type interface sample electrons from the LTO intra-block interface might transfer to the LAO//STO inter-block interface. As discussed in the previous section, the LTO intra-block interface does not contribute directly to the conduction, but does form a reservoir of (trapped) electrons. Once transferred to the LAO//STO inter-block interface, they do contribute to the conduction.

Recent DFT calculations argue that the driving mechanism behind the electron doping at the LAO//STO interface is a band bending of the LAO valence band that lifts it above the STO conduction band after a certain critical thickness[4, 26–28]. The calculations show that electrons from the LAO valence band at the sample surface are transferred to the STO conductance band at the interface. This model assumes that each LAO layer creates a band bending of about 1 eV: the band gap
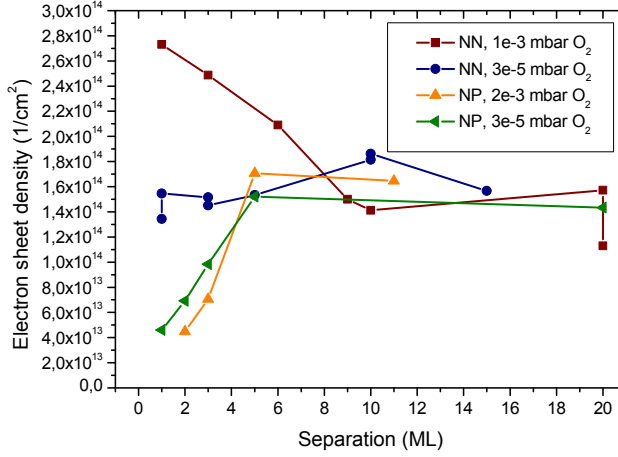
(a) electron density
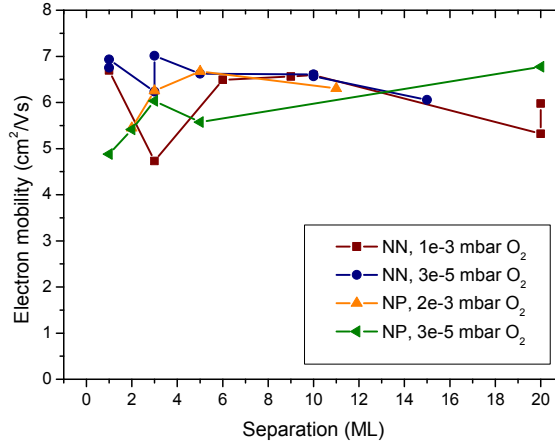
(b) electron mobility

Figure 6.10: Transport properties at 300 K for LAO/STO double interface samples. Sources are the same as Figure 6.9.

of STO divided by the critical number of monolayers required for a conducting interface. The fact that both the np and nn systems are already conducting for a single monolayer of LAO indicates that the potential that needs to be overcome is smaller than 1 eV in these systems. Interestingly, for the high-pressure grown nn system it appears as if it lowers the energy of the system if electrons are transferred for thin layers. Where for single interfaces or np systems it costs a certain amount of energy U_{bind} to delocalize electrons, for the nn system it frees energy.

These transferred electrons may not all contribute to the conducting state. It has been suggested that the lowest-lying orbitals are actually insulating due to

Anderson localization or effective high masses close to the interface[26, 29]. It was recently postulated that the electron mobility is greatly dependent on the position, with lower values close to the interface[30]. As such, the transferred electron density may be split up in a mobile electron density observed from Hall measurements and a stationary electron density that is not probed by the transport measurements. The Ti^{3+} observed by XPS in the LTO intra-block interface in the previous chapter may be an example of this. XPS probes the total electron density, so the presence of electrons at the LTO intra-block interface but the lack of conduction indicates that these electrons are stationary.

Looking into more detail at the np system, the electrons can be thought to be captured at the p-type interface, where they compensate the holes. In this qualitative discussion the stationary electrons can be neglected for this moment. Before such electrons can be transferred to the n-type interface it costs energy to either free them from their corresponding holes and/or to create the necessary oxygen vacancies. Thus, electrons are transferred if:

$$\Phi_{pc} > \Phi_{et} + U_{bind}$$

where Φ_{pc} is the energy of the polar catastrophe, i.e. the band bending of LAO, and Φ_{et} is the energy of the electron transfer between the two interfaces. The fact that oxygen vacancies are involved in the transfer process is also the reason that the low- and high-pressure series of np samples behave so similar. The vacancy density at the p-type interface is about $5 \cdot 10^{20}$ cm^{-3} (assuming a deficient layer of 10 monolayers)[25], much higher than typical vacancy densities of 10^{17} cm^{-3} in thick STO films[31]. The EELS scans for a p-type interface as presented in literature clearly show that the vacancies are limited to an area close to the interface[25]. Thus their creation is an effect of the presence of the p-type interface and not of the deposition pressure. Accordingly, the transfer mechanism is independent of the deposition pressure.

In the nn system, the top layer of the LAO is an additional LaO layer. Extra electrons are needed to compensate for the additional $(LaO)^+$. These electrons are mostly concentrated around the LTO intra-block interface, bound by the Coulomb force. This is not an optimal situation, as these electrons fill the LTO conduction band which lies above the Fermi level. However, doping electrons into the LAO//STO inter-block interface above the half electron per unit cell boundary shifts the polar catastrophe in such a way that the LTO conduction band is pulled down towards the Fermi level. Thus, it would lower the energy of the system if these electrons could be transferred: the second interface in the nn system has a negative 'binding energy' for the electrons. For thicker layers this energy gain is reduced by the increasing electron transfer dipole. The condition for transfer becomes:

$$\Phi_{pc} > \Phi_{et} - U_{bind}$$

In the nn system the deposition pressure does have a clear influence. The n-type interface does not inherently create oxygen vacancies like the p-type interface as no vacancies are needed to supply the necessary electrons. Any vacancies in the

top STO layer are then related to the deposition pressure. The low-pressure series has more vacancies compared to the high-pressure series. The extra vacancies in the top STO layer of the low-pressure grown samples can act like extra trapping sites[32, 33], lowering the delocalization energy and forcing the TiO_2 occupancy to its constant value around $1.6 \cdot 10^{14}$ cm^{-2}. In the high-pressure series the electrons are not trapped at the second interface and they can participate in the electron-transfer mechanism described above.

To describe this behaviour a dipole model can be developed, similar to the model used to describe the single-layer LTO/LAO samples in Section 4.4.2. The start is the ionic model of the LAO/STO system where each LaO and AlO_2 layer in LAO has a charge of +e or -e respectively, as shown in Figure 2.14. Theoretically, this gives rise to a dipole per unit cell:

$$D_{uc} = q\Delta z = e\frac{c}{2} \approx 1.9 \ \text{eÅ} \tag{6.1}$$

where c is the LAO c-axis lattice parameter. The total dipole due to the polar catastrophe can then be written as:

$$D_{pc} = sD_{uc} = es\frac{c}{2} \tag{6.2}$$

where s is the number of LAO monolayers. However, at a certain moment this potential build-up exceeds the electron trapping energy and an electronic reconstruction takes place: charge will be transferred to lower the potential build-up as depicted in Figure 6.11.
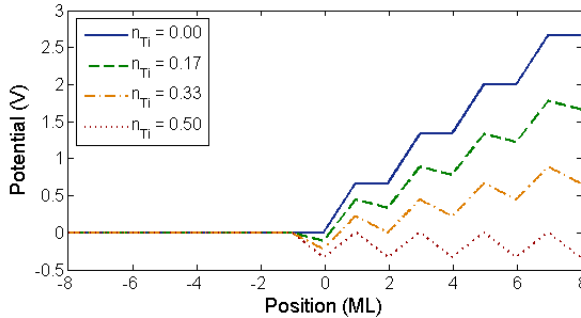
Figure 6.11: Potential build-up according to the purely ionic model for different electron occupations of the interfacial TiO_2 layer. The first LaO layer is at 0, with the neutral STO layers towards the left and the charged LAO layers to the right.

This transferred charge also leads to an additional dipole between the transferred electrons and their donors on the other interface. Similar to Equation 4.3 this can be written as:

$$D_{et} = q\Delta z = xesc \tag{6.3}$$

yielding a total dipole of:

$$D_{\text{total}} = se\frac{c}{2} - xesc \tag{6.4}$$

The minus sign between the two dipoles indicates that they point in opposite directions. Starting with a positive LaO layer, the polar-catastrophe dipole points to the right. While the electron-transfer dipole has its positive layer at the second interface, thus pointing towards the left.

As a repeat of Equation 4.4 & 4.5, a dipole gives rise to a polarization:

$$P = \frac{D}{V}$$

where V is the unit cell volume, here a^2sc with a the in-plane STO lattice parameter. Using the values of $a = 3.905$ Å and $c = 3.74$ Å results in an unscreened dipole per LAO unit cell of 0.03 e/Å^2, a value also found in DFT calculations[4]. The resulting electric field is related to the polarization by $P = \epsilon_0 \chi E$, where $\chi = K - 1$ is the susceptibility and K the dielectric constant. The electric field due to this LAO dipole is 0.26 V/Å, again similar to the results from DFT calculations[26, 34]. The potential resulting from a dipole is thus:

$$\Phi = Esc = \frac{Psc}{\epsilon_0 \chi} = \frac{D}{\epsilon_0 \chi a^2}$$

Using Equation 6.1 and the values for a and c given above yields $\Phi = 1$ eV per unit cell. Assuming that in the case of a single interface the potential build-up has to be larger than the band gap of STO to transfer electrons from the top surface to the bottom interface we find a minimum thickness of ∼3.3 monolayers. This is comparable to the value found experimentally[1].

Applying the above calculation to the total reconstructed dipole the potential becomes:

$$\Phi_{\text{total}} = \frac{se\frac{c}{2} - xesc}{\epsilon_0 \chi a^2} \tag{6.5}$$

Equating the formula to the potential difference U_{bind} and solving for x yields the electron occupancy of the first interface as a function of the number of LAO layers and the energy U_{bind}:

$$x = \frac{1}{2} - \frac{\epsilon_0 \chi a^2 U_{\text{bind}}}{esc} \tag{6.6}$$

Similar equations are derived by Li[4] and Son[26] for single-interfaces, though they work more phenomenological with the assumption that an electric field develops due to the bridging of the band gap of STO. The assumption is that the potential build-up due to the polar catastrophe must be so large that the LAO valence band is lifted above the Fermi level (which is close to the STO conduction band) before electrons from the LAO valence band can be transferred to the STO conduction

band at the interface[3, 27, 28]. For a single-interface structure, the potential to overcome is the band gap of STO, so $U_{\mathrm{bind}} = 3.2$ eV. In this case, $s = 4$ (the minimum thickness for which electrons are transferred) gives an occupancy of $x(4) = 0.09$, $x(5) = 0.17$ and $x(\infty) = 0.50$. The latter value recovers the purely ionic doping of half an electron per unit cell.

The above derivation is based on the electron-transfer model as described in Section 5.3. Within the structural-polarization model a similar equation can be derived. Here there is no dipole in the LAO layer, so the only remaining term is the electron transfer dipole:

$$D_{\mathrm{sp}} = (x_{\infty} - x)esc \tag{6.7}$$

Here x_{∞} is the electron fraction for an infinitely thick LAO film, so the interface interaction is zero. In the structural-polarization model this fraction is due to the doping from defect states. Following through the entire derivation yields an equation similar to Equation 6.6:

$$x = x_{\infty} - \frac{\epsilon_0 \chi a^2 U_{\mathrm{bind}}}{esc} \tag{6.8}$$

The difference between the two systems is captured purely in the infinite layer behaviour: the origin of the electrons at the interface in both models is different. For the electron-transfer model the doping is due to the polar discontinuity resulting in 1/2 electron per unit cell. For the structural-polarization model it is due to defect states in the STO, and the density is not exactly known. This uncertainty is convoluted by the fact that Hall measurements only probe the mobile electron density and not the total electron density. As this makes distinguishing between the two models impossible, the interface separation dependence is the same for both equations so in the rest of the discussion Equation 6.6 is used.

Both the np and nn systems differ from the single-interface case because they have another STO layer on top of the second interface. So, instead of a transition from a polar material to a zero-energy vacuum there is another material with a different band structure. This greatly changes the potential difference U_{bind} that needs to be overcome to achieve electron transfer, as can already be seen from the fact that there is effectively no critical thickness for the double-interface samples. A single monolayer of LAO is enough to overcome the potential difference in those systems.

Continuing the analogy with the dipole model in Section 4.4.2 it seems logical to introduce a thickness-dependent susceptibility. However, DFT calculations show that relaxation in the LAO layer only occurs in single-interface films[35]. Thus a constant susceptibility is used.

An equation of the form of Equation 6.6 can easily be fit to the data from Figure 6.10(a) with a least-squares fit. Figure 6.12 shows both the low-pressure np and the higher-pressure nn occupancy data, as defined by $a^2 n_{\mathrm{2D}}$, and fits to the equation $x = (1/2 - x_{\mathrm{stat}}) - B/s$. All data series were fitted, but Figure 6.12 shows only two for clarity. In this quantitative model, the contribution from the stationary electrons[26, 29] is explicitly taken into account. Here x_{stat} represents a constant

background from the electrons in the lowest bands for the mobile electrons in higher-lying bands.
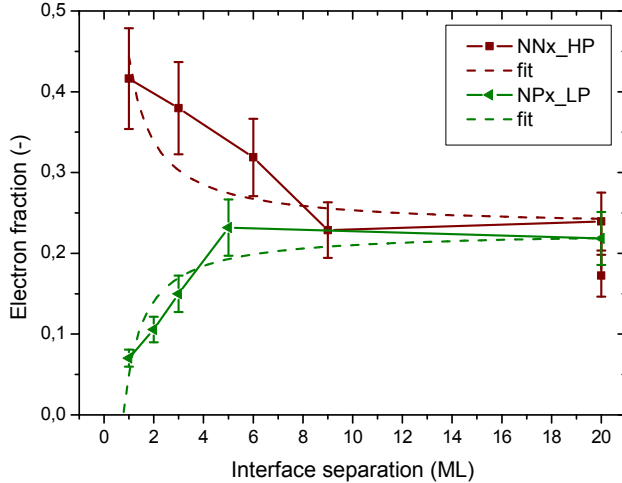

Figure 6.12: Interfacial TiO_2 occupancy data, together with fits to Equation 6.6 for the np, $3 \cdot 10^{-5}$ mbar O_2 and the nn, $1 \cdot 10^{-3}$ mbar O_2 series. The error bars show the sample-to-sample variation of 15 %.

The dipole model can clearly reproduce the general trends observed. Fit parameters and quality factors are given in Table 6.1, where the potential difference U_{bind} is already extracted from the parameter B using the values for a and c mentioned above. Compared to the dipole fit of the LTO/LAO system in Section 4.4.2 the fit for the double-interface structures is rather poor with R^2 values of about 0.7 compared to 0.97 for the LTO/LAO. The probable reason for this is that the Hall measurements only probe the mobile electrons, while XPS probes all electrons. Sample-to-sample variations in the stationary electron density would lead to differences in the probed Hall electron density.

parameter	np, $3 \cdot 10^{-5}$	np, $2 \cdot 10^{-3}$	nn, $3 \cdot 10^{-5}$	nn, $1 \cdot 10^{-3}$
x_{stat} (-)	0.27 ± 0.02	0.25 ± 0.05	0.24 ± 0.01	0.27 ± 0.03
U_{bind} (eV)	0.34 ± 0.09	0.5 ± 0.2	0.08 ± 0.04	-0.4 ± 0.1
R^2 (-)	0.826	0.690	0.368	0.666
X^2 (-)	0.0011	0.0043	0.0005	0.0038

Table 6.1: Fit parameters for fitting Equation 6.6 to the electron density data from Figure 6.12. The pressures in the header are expressed in millibar.

The values for x_{stat} show that occupancy fraction of the lowest electron bands is about 1/4. Single-interface films show a similar value of $x_{stat} = 0.26$[36]. From DFT calculations it is easily shown that if the lowest-lying orbital is immobile, the

Hall electron density can be reduced by a factor $1/2$ as observed here[26]. However, the Hall electron density can also be controlled by the depositions pressure[24] or surface reconstruction[1]. Here all samples were fabricated under the same conditions and with a capping layer that protects the second interface from any surface reconstruction effects. As such, the assumption of a constant stationary electron density is appropriate.

The interesting thing in the fit parameters is the trend in the potential difference U_{bind}. Its absolute value is much smaller compared to the 3.2 eV expected for single-interfaces. This reduction of the energy gap is completely due to the capping of the top interface. For example, double-interface samples with 2 monolayers of LAO capped with even a single monolayer of STO are conducting, as opposed to uncapped 2 monolayer LAO samples which are insulating[1, 37]. This may also explain why the susceptibility is more constant for the double-interface system compared to the single-interface system with LTO/LAO. As the electron transfer is now easier due to the lower energy gap, there is less need for the LAO bands to shift due to internal polarization. In fact, the immediate electron transfer lowers the band shift. This reduction of the structural polarization in the LAO also implies that the susceptibility of the LAO layer does not vary as much as it does for the LTO/LAO system (Section 4.4.2). Note however that this energy gap is not the activation energy obtained from the Arrhenius plot of the electron density. It is almost two orders of magnitude larger than the 5-6 meV obtained from that equation. The electron transfer can thus not be attributed to a thermal process, but has to be electrostatic in origin. This confirms the applicability of the dipole model. Finally, the sign of the energy also confirms the qualitative model sketched above. For the np system U_{bind} is *positive*, indicating an energy that is to be overcome to transfer electrons, while for the nn system at high pressure it is *negative*, indicating that it lowers the total energy when electrons are transferred. For the nn system at low pressure the electron density is nearly independent of the interface separation. As already discussed qualitatively, the additional oxygen vacancies in the top STO layer act as extra trapping sites, binding the electrons at the LTO intra-block interface and reducing the delocalization energy almost to zero.

Figures 6.13 and 6.14 show band schematics that help visualize this model. For the np-system the electron fraction on the interfacial TiO_2-layer is below $1/2$ and as such the polar discontinuity heightens the bands, lifting the trapping states to the Fermi level at the LTO intra-block interface. In Figure 6.13 these states are represented by V^*. Electron transfer from these states at the LTO intra-block interface to the LAO//STO interface lowers the band bending in a process very similar to that for single-interfaces.

In the unreconstructed nn-system the conduction band of the LTO layer is filled with immobile electrons. Due to the polar catastrophe band bending this level is far above the Fermi level. Doping electrons into the LAO//STO inter-block interface increases the electron fraction on the interfacial TiO_2 layer above $1/2$ and as such the polar discontinuity *lowers* the bands at the LTO intra-block interface.
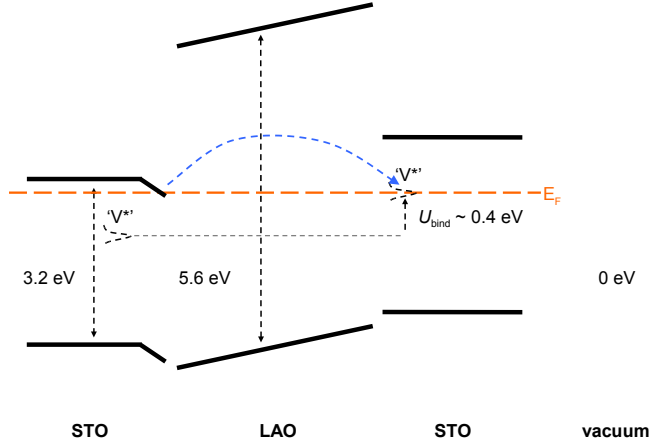
Figure 6.13: Schematic band picture for a *np* double-interface structure. Here the indicated V* are any electron trap sites, either oxygen vacancies or Al ions.
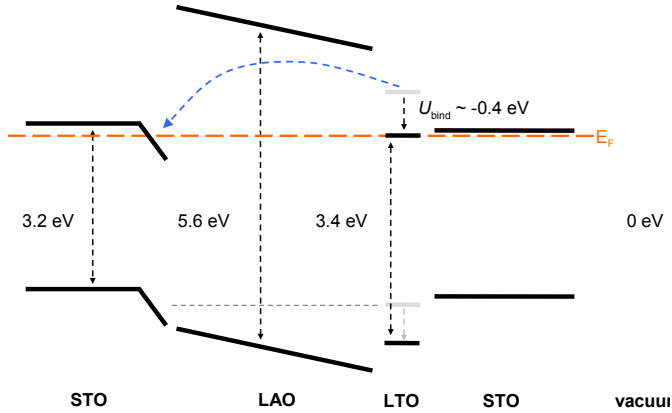
Figure 6.14: Schematic band picture for a *nn* double-interface structure. Here two bands for LTO are drawn. The light grey band is the energy level before electron transfer, while the black band is the reconstructed level.

A similar equation to Equation 6.6 but stated in terms of the critical thickness was derived by Son[26]:

$$x = \frac{1}{2}\left(1 - \frac{s_{\mathrm{c}}}{s}\right)$$

Comparing this with Equation 6.6 makes it possible to relate U_{bind} to s_{c} and vice-versa. Table 6.2 shows the critical thicknesses observed in literature, both

experimental and theoretical and the calculated potential differences. It is clear that for single interfaces the potential difference is about the size of the STO band gap, while for the double-interfaces it is much smaller. Accordingly, the critical thicknesses are below a single unit cell. The negative value for the high-pressure nn system reflects that in that structure the electrons are not trapped, but actually in a higher energy state before electron transfer.

system	s_c (ML)	U_{bind} (eV)	source
single	2.949	*2.8*	Son[26]
single	3.94	*3.8*	Li[4]
single	4	*3.9*	Thiel[1]
single	*3.3*	3.2	theoretical, from band gap
NP	*0.4*	0.4	this thesis, averaged, Table 6.1
NN, HP	*-0.4*	-0.4	this thesis, Table 6.1

Table 6.2: Critical thicknesses and potential differences for single- and double-interfaces structures. The values in *italic* are the calculated values. Values for a, c and K are as in the main text.

6.4.4 Multi-band transport properties at low temperature

So far the discussion has been mostly about the room temperature measurements. That is because only these show any dependence on the interface separation. Just as the mobility at room temperature is independent of the interface separation, so are the electron mobility *and density* at 5 K. Figure 6.15 shows the electron mobility and density at those low temperatures for comparison.

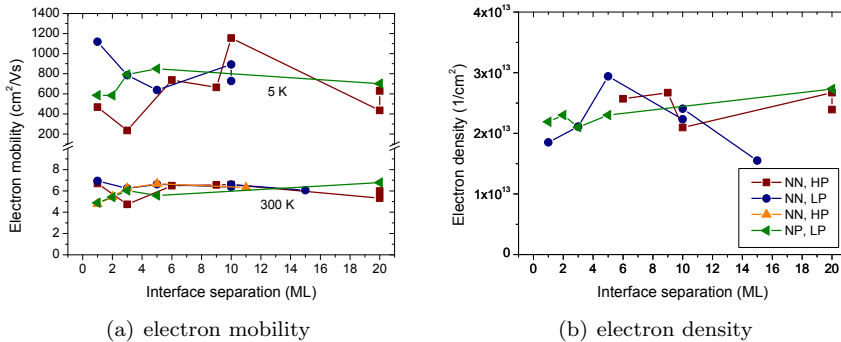(a) electron mobility   (b) electron density

Figure 6.15: Transport properties at 5 K for LAO/STO double interface samples. Sources are the same as Figure 6.9.

In general the electron density at low temperature is independent of the interface separations. Some samples yield higher values, but these results are not reproducible. For example, a second sample with a LAO thickness of 3 ML does give

an electron density $6 \cdot 10^{13}$ cm^{-2}; much higher than the average value $2 \cdot 10^{13}$ cm^{-2} for all samples. As such, these data points are not considered in the discussion.

Table 6.3 shows the average values for the electron mobilities at 300 and 5 K and the electron density at 5 K for all series and an overall average. The $\pm$ values are the standard deviations of the respective averages. It can clearly be seen that the electron mobilities at room temperature are practically the same for all series. The electron mobility fluctuates more at 5 K, something that is hidden by the logarithmic scale in Figure 6.8(c). Part of this may be an extra contribution of the magnetoresistance to the Hall measurement. Another reason may be that the system is sensitive to small differences in the scatterer density at low temperatures.

It is interesting that for these double-interface structures the mobility is independent from the LAO layer thickness. For single-interface structures a decreasing dependence with increasing layer thickness was observed[2]. Most likely it is the higher deposition pressure for the double-interface structures, in combination with the extra STO layer, that makes these samples less sensitive to re-oxidation during cool-down. As the oxygen content of the STO substrate remains the same, the mobility does not change either. Referring to the phase diagram of Figure 5.10 the higher-pressure grown samples from Bell[2] should have a more stable oxygen content as well. The mobility for that series does indeed show a weaker dependence on the LAO layer thickness.

series	μ (300 K) (cm^2/Vs)	μ (5 K) (cm^2/Vs)	n_{2D} (5 K) (cm^{-2})
NNx_HP	6.1 ± 0.7	616 ± 129	$2.5 \pm 0.2 \cdot 10^{13}$
NNx_LP	6.5 ± 0.3	832 ± 185	$2.2 \pm 0.5 \cdot 10^{13}$
NPx_HP	5.9 ± 0.7	-	-
NPx_LP	5.7 ± 0.7	703 ± 120	$2.3 \pm 0.2 \cdot 10^{13}$
overall	6.1 ± 0.3	717 ± 109	$2.3 \pm 0.2 \cdot 10^{13}$

Table 6.3: Average electron mobility and density values for the different series. Error values are the standard deviations.

It is remarkable again how for all these samples the low-temperature electron density is the same $2.3 \cdot 10^{13}$ cm^{-2} or 0.04 electron per unit cell. Its apparent universality in double- and single-interface structures indicates that this is a property of the LAO//STO inter-block interface itself, not influenced by any nearby other interface, either air//film or film//film.

The conduction mechanism of the LAO/STO system can also be probed by measuring the transport properties under applied magnetic field. Negative magnetoresistance has been observed in high-pressure grown LAO/STO samples[36], which has been explained as an effect of surface steps[38]. Positive magnetoresistance has also been observed, but on samples grown under different, low-pressure conditions[2, 39].

The NNx samples studied here all displayed *positive* magnetoresistance with a near-perfect quadratic dependence on the magnetic field. Figure 6.16 shows the

magnetoresistance $(R_s(B) - R_s(0))/R_s(0)$ curves at 5 K with the field applied at different angles to the normal of the interface. The magnetoresistance reduces as the field becomes parallel to the interface. For 90° the magnetoresistance appears negative, but this is most likely due to a miss-alignment of the rotator and is the positive magnetoresistance on the other side of the minimum, but with the current flowing opposite. Using the quadratic dependence on B we can extract the magnetoresistance electron mobility μ_{MR} from the curves, using[40–42]:

$$\Delta R_s(B) = \frac{R_s(B) - R_s(0)}{R_s(0)} = \xi \left(\mu_{MR} B \right)^2 \qquad (6.9)$$

Figure 6.16(b) shows the magnetoresistance mobility as a function of field-normal angle for different temperatures. The mobilities drop to zero for the field parallel to the interface (90°). A similar change between field perpendicular and parallel was seen in the superconducting state of the LAO//STO interface where the critical field changes drastically[43].

(a) magnetoresistance curves

(b) magnetoresistance mobility
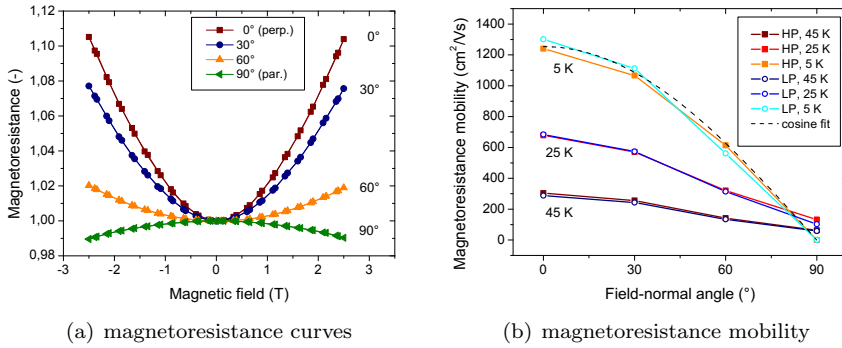
Figure 6.16: Magnetoresistance measurements on NN10_p sample at 5 K with the field at different angles to the interface normal. (a) shows only the results for a NN10_LP sample. (b) shows the μ_{MR} obtained from quadratic fitting assuming $\xi = 1$.

This positive and quadratic magnetoresistance behaviour is very similar to that of doped STO[42, 44]. In solid state theory, such a quadratic magnetoresistance is attributed to a cyclotron process[45]. The reduction of the magnetoresistance effect for the field closer to parallel indicates that perpendicular to the field, the electron layer is not wide enough to sustain full cyclotron motion. The cosine fit in Figure 6.16(b) follows exactly the relation $r_{c,\text{in-plane}} = r_c \cos(\theta)$, indicating that only the part of the cyclotron motion parallel to the electron layer contributes to the magnetoresistance. This allows for an estimation of the upper limit to the electron layer thickness. With the field parallel to the interface, the electron layer must be thinner than the cyclotron radius[46]:

$$r_c = \frac{m^* v_F}{eB} = \frac{\hbar k_F}{eB}$$

Assuming an average thickness of the electron layer of 20 nm[18] and an electron sheet density of $n_{2D} = 2.5 \cdot 10^{13}$ cm^{-2} the Fermi wave vector can be calculated from $k_F = \sqrt[3]{3\pi^2 n_{2D}/L}$. Taking the maximum applied field for which the quadratic behaviour still holds to be 3 T, the cyclotron radius is about 160 nm. This is much larger than the electron layer thickness, indicating two-dimensional behaviour of the electron liquid.

Plotting the Hall and MR mobility vs. temperature or interface separation shows that both follow the same trends.The magnetoresistance in a way is a local probe, as it depends on the ability to perform cyclotron motion which requires continuous conducting areas of only 300 nm in diameter. Hall measurements, though, probe the entire sample at the same time. If there was a difference in behaviour for both mobilities, it would point to a different conduction mechanism on long and short length scales. However, the similarity observed here shows that the conducting state is continuous.

This is exemplified by the nearly constant μ_{MR}/μ_{Hall} ratio. Averaged over both high- and low-pressure grown samples, the μ_{MR}/μ_{Hall} ratio is 1.3 with a standard deviation 0.2. This actually gives us information about the scattering mechanism at low temperatures. As mentioned above the Hall and MR mobilities are different entities, related to the drift mobility with different pre-factors: $\mu_i = f_i \mu_{drift}$[41, 47]. The magnitude of the mobilities, and more importantly their ratio, depends on the scattering process involved. Vice-versa, by comparing the obtained μ_{MR}/μ_{Hall} ratio to the calculated values it might be possible to identify the scattering process involved at the LAO//STO interface at low temperature. Table 6.4 shows the calculated values for the mobility factors of different scattering mechanisms based on a power-law dependence of the relaxation time. Comparing the observed μ_{MR}/μ_{Hall} ratio of 1.3 with the calculated values from Table 6.4 shows that the most likely scattering mechanism at low temperature is Coulomb scattering.

scattering mechanism	exponent	Hall factor	MR factor	μ_{MR}/μ_{Hall} ratio
acoustic phonon	-1/2	1.18	1.32	1.13
neutral impurity	0	1.00	1.00	1.00
piezoelectric	+1/2	1.10	1.15	1.04
Coulomb scattering	+3/2	1.93	2.43	1.26

Table 6.4: Scattering mechanisms, power-law exponents and mobility factors calculated from a power-law relaxation time approximation[40, 47].

For single-interface samples it was shown that the mobility, both Hall and magnetoresistance, decreases with LAO layer thickness[2]. μ_{Hall} can decrease almost two orders of magnitude, while the change in μ_{MR} are much smaller. This also indicates that the μ_{MR}/μ_{Hall} ratio changes with the LAO layer thickness for the single-interface samples. For the double-interface samples it was shown that the mobilities are independent of the interface separation. Most likely this is once again an indication that a covered LAO surface is more stable compare to a LAO surface that is exposed to air, especially when grown at low pressure.

Most of the magnetoresistance results were obtained for low magnetic field, up to 2.5 T. For higher fields deviations from the simple Drude picture are observed. Figure 6.17 shows the sheet and Hall resistance vs. magnetic field, as well as a quadratic and linear fit to each respectively. From the low-field fits, the sheet resistance and Hall coefficient at zero field are $537.50\pm0.07\ \Omega/\square$ and -23.15 ± 0.08 Ω/T, respectively. Assuming a single-band model these values translate into an electron mobility and density of 431 ± 2 cm^2/Vs and $2.696 \pm 0.009 \cdot 10^{13}$ cm^{-2}, respectively. The deviations at higher fields have been attributed to an anomalous Hall effect[48] or, more recently, a two-band model.
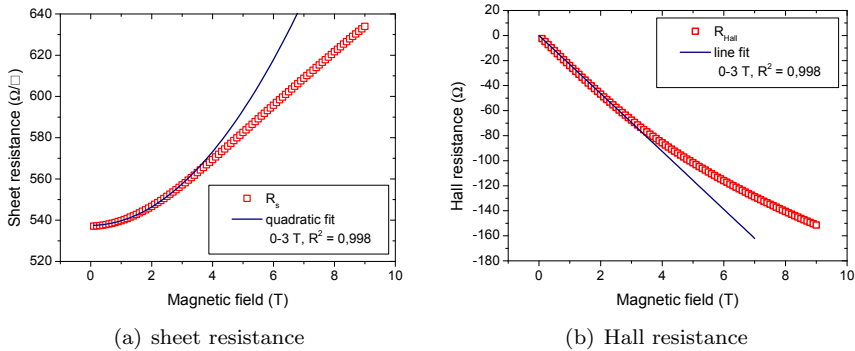

(a) sheet resistance

(b) Hall resistance

Figure 6.17: Hall measurement data for a NN20_HP sample at 5 K up to an applied magnetic field of 9 T. Here the data for positive and negative field has been averaged.

There has been some discussion, both for and against, whether a multi-band model with two electron populations is needed to describe the transport at the LAO//STO interfaces[26, 29, 36, 49, 50]. Recently a two-band model where the sheet resistance R_s and Hall coefficient R_H depend on the magnetic field was proposed[37, supplementary information]:

$$R_s(B) = \frac{R_{s,0} + R_{s,\infty} \langle \mu \rangle^2 B^2}{1 + \langle \mu \rangle^2 B^2} \tag{6.10}$$

$$R_H(B) = \frac{R_{H,0} + R_{H,\infty} \langle \mu \rangle^2 B^2}{1 + \langle \mu \rangle^2 B^2} \tag{6.11}$$

Here $R_{s,0}$ and $R_{H,0}$ are the values at zero field and $R_{s,\infty}$ and $R_{H,\infty}$ are the values at high field. $\langle \mu \rangle$ is a weighted-average mobility. All five parameters are functions of n_i and μ_i, the electron densities and mobilities for band $i = 1, 2$. Fitting Equations 6.10 and 6.11 to the data shown in Figure 6.17 yields the results as shown in Table 6.5. At very low temperatures the fitting is actually complicated by scattering from impurities, resulting in least-square deviations on the order of 10^{-3} compared to 10^{-5} for fits around 25 K. The data and graphs shown here

parameter	single-band	two-band
μ_1 (cm^2/Vs)	431 ± 2	70.3
n_1 (cm^{-2})	$2.696 \pm 0.009 \cdot 10^{13}$	$1.14 \cdot 10^{14}$
μ_2 (cm^2/Vs)	-	1297
n_2 (cm^{-2})	-	$2.66 \cdot 10^{12}$
R^2 (-)	0.998	0.983
	(0-3 T)	(0-9 T)

Table 6.5: Comparison of the results for single- and two-band model fitting to Hall data of a NN20_HP sample at 5 K.

are for a double-interface sample, but similar results have been obtained for single interfaces as well.

There is a large difference between the results for the two models. For example, the total electron density expressed in electrons per unit cell area (e/a^2) is 0.04 and 0.18, respectively. At room temperature, though, the two-band behaviour has disappeared as a near-constant sheet resistance (change at 9 T is about 0.1 % compared to 18 % for the 5 K data) and a linear Hall resistance are observed up to 9 T. Either the high-mobility band is drowned out by the thermally-activated electrons or it disappears for higher temperatures, allowing the low-mobility band to become prominent. Given the fact that the electron density at room temperature $n_{\mathrm{RT}} = 1.59 \cdot 10^{14}$ cm^{-2} is close to the density of the low-mobility band it is likely that the latter explanation is applicable.

This shows that at higher temperature the single-band model is sufficient to describe the transport data. At low temperature there is more of a discrepancy. Even in the low-field limit, the single-band picture is not recovered. For example, if Equation 6.10 is taken in the low field limit, a simple quadratic dependence on the magnetic field similar to Equation 6.9 emerges:

$$R_{\mathrm{s}}(B) = R_{\mathrm{s},0} + R_{\mathrm{s},\infty} \langle \mu \rangle^2 B^2$$

Comparing the values of μ_{MR} and $\langle \mu \rangle$ resulting from these equations shows that they differ by a factor 1.5: 644 and 928 cm^2/Vs[1], respectively. This is of course unsurprising given the $R_{\mathrm{s},\infty}$ prefactor, but it gives an indication to the difference between Equation 6.9 for a single band model[47] and Equation 6.10 which is explicitly derived for a two-band model. Until this difference is resolved, the discussion of the $\mu_{\mathrm{MR}}/\mu_{\mathrm{Hall}}$ ratio is at least suggestive of the scattering process that is dominant at low temperature.

Not only the high-field mangetoresistance data gives hints of a two-band model. Figure 6.18 shows an Arrhenius plot for a NN10_HP sample. It is clear that the graph is curved, likely indicating two independent thermally-activated electron bands[51]. This is not a feature that is unique to the double-interface structures, as single-interface samples show this behaviour as well. Figure 6.7(d) does not

---

[1] $\langle \mu \rangle$ is calculated as a weighted average of μ_1 and μ_2 as described in [37].

show this behaviour because the lowest temperature value in those plots is 25 K, above the curvature point shown in Figure 6.18.
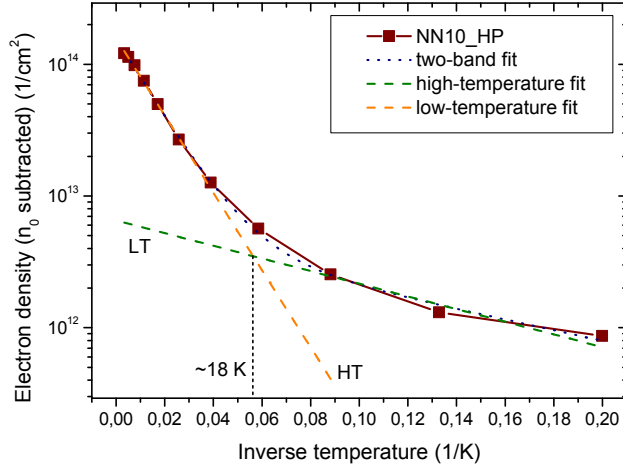

Figure 6.18: Arrhenius plot of a NN10_HP sample with fine spacing at low temperature. Single-exponential fits at high and low temperature are also included. The factor n_0 has been subtracted for clarity.

Fitting the data shown in Figure 6.18 to a double-exponential equation $n = n_0 + n_{\mathrm{HT}} \exp(-E_{\mathrm{a,HT}}/k_{\mathrm{B}}T) + n_{\mathrm{LT}} \exp(-E_{\mathrm{a,LT}}/k_{\mathrm{B}}T)$ allows for the extraction of the activation energies and pre-exponential factors. These are shown in Table 6.6. Here the values are compared with single-exponential fits at high and low temperature. The single-exponential fit at high temperature compares well to the equivalent term in the double-exponential fit. The high temperature fit also corresponds well to the similar data and fits shown in Figure 6.7(d).

parameter	double-exponential	single-exponential, high-temperature	single-exponential, low-temperature
n_0 (cm^{-2})	$2.0\cdot10^{13}$	$2.0\cdot10^{13}$	$2.0\cdot10^{13}$
n_{HT} (cm^{-2})	$1.6\cdot10^{14}$	$1.6\cdot10^{14}$	-
$E_{\mathrm{a,HT}}$ (meV)	6.2	5.8	-
n_{LT} (cm^{-2})	$5.1\cdot10^{12}$	-	$6.5\cdot10^{12}$
$E_{\mathrm{a,LT}}$ (meV)	0.8	-	0.9
R^2 (-)	0.999	0.997	0.953
X^2 (-)	$7.5\cdot10^{-4}$	$7.2\cdot10^{-4}$	$1.5\cdot10^{-4}$

Table 6.6: Double- and single-exponential fits to the Arrhenius plot in Figure 6.18. Here the n_0 values for the single-exponential fits are fixed to that from the double-exponential fit, as indicated by italic type.

Table 6.6 shows that there is more discrepancy between the low-temperature fits. In part this is due to the small amount of data points, in part this is due to the small magnitude of the signal. The low-temperature population is about a factor 100 smaller than the high-temperature population. What is interesting is the correspondence in magnitudes between the results for the high-field magnetoresistance measurements and the Arrhenius fit here. Both have one population of the order of 10^{14} cm^{-2} and another of 10^{12} cm^{-2}. For the magnetoresistance measurement, it seems as if the low-density population disappears at higher-temperature, which is seemingly incompatible with the co-existence of the two populations assumed in the double-exponential fit of the Arrhenius data. However, above the activation temperature E_a/k_B for the high-density population, the contribution of the low-density population is negligible. If the low-density population disappears at some point above the activation temperature of 72 K, it is unlikely to significantly influence the fit. This seems to coincide with the structural phase transition of STO at 105 K. Above that temperature the cubic structure does not allow multiple sub-bands, while the tetragonal structure below that transition temperature would allow for multiple bands.

6.4.5 Robustness of double-interface heterostructures

Given the dependence of the LAO/STO system on the oxygen pressure during and after deposition[7, 36], it is interesting to study the effect of post-annealing on the transport properties. In these cases the heterostructures were single-interfaces, where the top air//LAO surface is very sensitive to the oxidation state. In fact, the top surface can easily influence the LAO//STO interface[8], so the name 'single interface' is in fact misleading: the LAO/STO system (for small separations) is always a coupled-interface system. A double-interface heterostructure isolates this second interface from the environment, thus making the system more robust with respect to changes in that environment. Figure 6.1 in the Introduction clearly illustrates this. To study the effect of changes in the environment on double-interface heterostructures, several samples grown at low pressure were post-annealed at 400 °C in flowing oxygen for 2 hours in a tube oven. The post-annealing had little influence on the temperature-dependence of both the electron mobility and electron density, retaining the thermally-activated and $1/T^2$ behaviour.

Looking in more detail at the transport properties, it seems clear that even though post-annealing the low-pressure grown sample does induce changes it does not transform fully into the high-pressure behaviour. Figure 6.19 compares the electron density and mobility for the low-pressure, post-annealed and high-pressure samples. For the low-pressure and post-annealed samples the electron density shows little dependence on the interface separation, while the high-pressure samples shows their typical increase for low separation. Here the thick LAO layer samples (>5 ML) show a change of the electron density at room temperature of about 4 %, which is small compared to 30 % for single interfaces[7, 24]. This shows the stability of electron transfer mechanism in the double-interface heterostructure compared to single-interface samples.
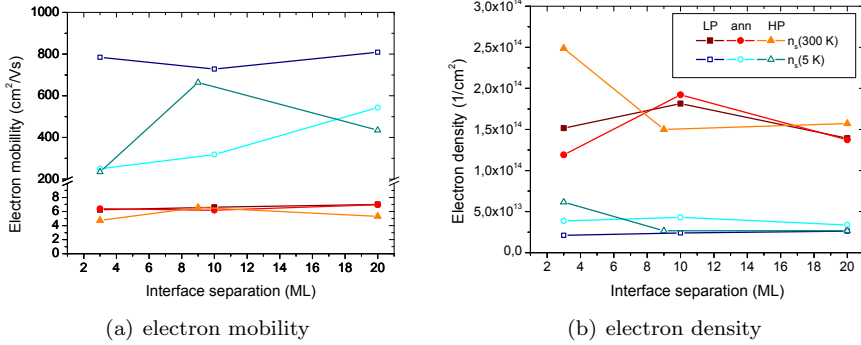
(a) electron mobility (b) electron density

Figure 6.19: Transport properties for low-pressure, post-annealed and high-pressure grown NNx samples.

The electron mobility at room temperature does not vary much between the different samples, even upon post-annealing. At 5 K though, the mobility of the post-annealed sample shifts to much lower values compared to the low-pressure grown samples. The high-pressure grown samples show a lot more variation in their mobilities, but it seems as if the post-annealed and high-pressure mobilities are of the same order of magnitude. Strangely enough, post-annealing appears to decrease the mobility - in other words, increase the electron scattering - which is opposite to what is normally expected[52, 53]. This points to the difference in the scattering process at high and low temperature. At high temperature the $1/T^2$ dependence points to an electron-electron process and as the electron density for the post-annealed samples is not much changed from the low-pressure grown samples the mobility is equally unchanged. At low temperatures a defect scattering process is dominant, as evidenced by the magnetoresistance measurements above. This defect scattering can be greatly affected by changes in the dielectric constant in a similar process as discussed in Section 5.2. Upon post-annealing, the dielectric constant of STO decreases[54–56] and the electrons are pulled closer to the interface. There the interface defects reduce the overall mobility. These observations show that in any LAO//STO interface structure both interfaces have to be considered together and that capping of the second interface results in a more robust doping mechanism.

6.5 Optical investigations of double-interface heterostructures

The optical response of LAO//STO interfaces has not been investigated intensively, though optical absorption measurements show that superlattices of LAO and STO have interesting properties[57]. One advantage of optical measurements is that the complete electron population is probed instead of just the mobile part

as Hall measurements do. Another is that the band transitions can be probed, which is not possible with resistance measurements. In this Section the dynamics of the photocarriers[58] and the band transition in the LAO/STO system are investigated

6.5.1 Photocarrier dynamics from photoconductivity relaxation

It was already known that the LAO//STO conducting state is sensitive to photocarrier injection[5, 58], not unlike STO itself[42, 59]. Thus, samples were kept inside the darkened measurement chamber for some time before start of the actual measurement. Data obtained during this waiting time yields information on the relaxation time of the photocarriers that were captured in the interface potential well. Figure 6.20 shows the several relaxation curves for samples from both pressure series. Here the sheet resistance values are normalized to one at the start of the measurement.
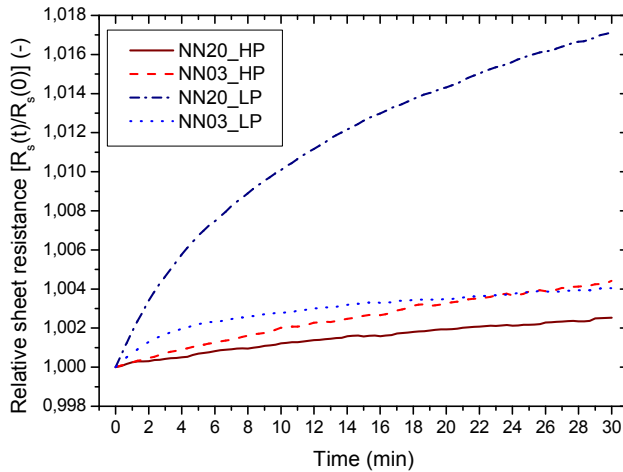
Figure 6.20: Normalized sheet resistance relaxation curves for a NN03 and NN20 sample from both pressure series, obtained at 300 K.

Identical curves were obtained with the magnetic field perpendicular and parallel to the interface. Slight relaxation was still observed after 24 hours, but with important differences in the relaxation times. To study the relaxation in more detail, the curves in Figure 6.20 were fit using a double-exponential decay function. Relaxation times in three ranges were obtained: 2-3 min, 25-40 min and >60 min.

The short relaxation time was present in all measurements, even after prolonged stay in the dark measurement chamber. It showed little to no dependence on sample structure or orientation. Averaged, this relaxation time was 2.5 min with

a standard deviation of 0.3 min. It was attributed to a measurement error, perhaps charging or heating of the sample.

The long relaxation times of over an hour were discarded as fitting artefacts. The relaxation data was only obtained for about 30 minutes to an hour, so relaxation times beyond this limit have only a very small contribution in the measured range. In the cases where very long relaxation times (>150 min) were obtained from double-exponential fitting, the data was equally well fit with a single exponential decay function.

The medium relaxation times show a dependence on the sample structure, as double-interface samples with smaller separation have longer relaxation times. Also this relaxation is only present immediately after insertion into the dark measurement chamber. Thus these relaxation times can give information on the photocarrier process. In the simplest approximation, photoelectrons disappear through recombination with holes. As such, the mobility of electrons should be correlated with the relaxation times, as higher mobilities allow electrons and holes to find each other faster. Figure 6.21 does indeed show that for longer relaxation times, the electron mobilities are lower.
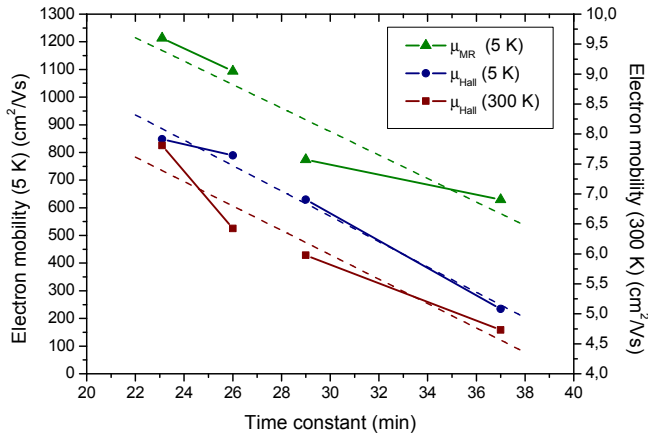
Figure 6.21: Electron mobilities, both Hall and magnetoresistance, vs. the photocarrier relaxation times at 300 K in nn double-interface samples. The data points on the left (short τ) are low-pressure grown, the samples on the right (long τ) are high-pressure grown. Lines are guides to the eye. No data for np series was available.

This direct relation between the electron mobility and the relaxation time indicates that at room temperature the recombination is not limited by trapping of either electrons or holes. This is interesting, as the magnetoresistance measurements indicate that the main scattering mechanism at low temperature is Coulomb scattering. It is unlikely that charged impurities would not trap holes and/or electrons, so a different scattering mechanism should play a role at room temperature. Electron-electron scattering is a likely candidate, given the large increase in elec-

tron density upon warming. Applying the Drude model equation for the mobility $\mu = \frac{e}{m^*}\tau$ a mean free path l of 6 Å can be derived for the $\mu_{\text{Hall}} = 6$ cm^2/Vs at room temperature. For the calculation of the Fermi wave vector $\sqrt[3]{3\pi^2 n_{\text{2D}}/L}$ the electron layer thickness and sheet density were taken to be 10 nm[18, 60] and $1.6 \cdot 10^{14}$ cm^{-2}, respectively. This is very close to the electron-electron separation distance $1/\sqrt{n_{\text{2D}}} = 8$ Å, indicating that electron-electron scattering plays an important role in the transport properties of LAO//STO interfaces at room temperature. This supports the idea that the transport mechanism follows Fermi liquid behaviour above 70 K as suggested from the $1/T^2$ temperature-dependence of the electron mobility.

6.5.2 Photoreflectance investigation of band transitions

Similarly to the LTO/LAO system, photoreflectance measurements of the double-interface samples was carried out to investigate the possibility of band bending. Figure 6.22 shows the results for the high-pressure nn series. As can be seen from the Figure, and as was confirmed by fitting with Lorentz oscillators, the transition energies did not change with the interface separation. The difference for the NN∞_HP sample can be explained by the difference in the actual surface which is AlO$_2$ compared to TiO$_2$ for the other samples.
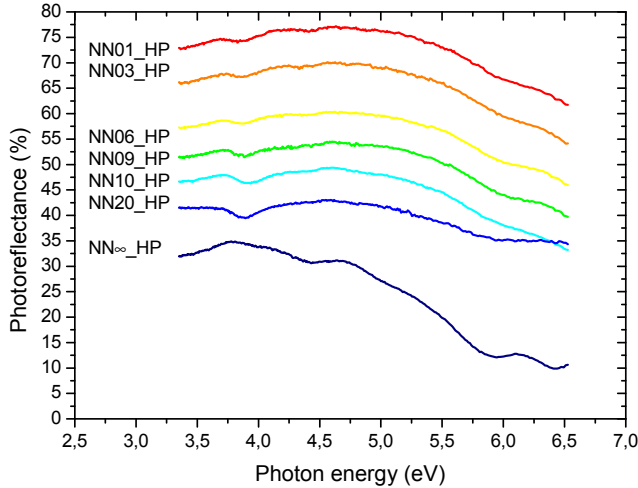
Figure 6.22: Photoreflectance data for the NNx_HP series. The graphs are offset for clarity.

Table 6.7 shows the obtained transition energies for three series: the np series grown at low pressure and both nn series. All values are averaged over all separations, with a standard deviation of about 0.1 eV for all values. STO has slightly higher transition energies, but all are the same within error margins. This
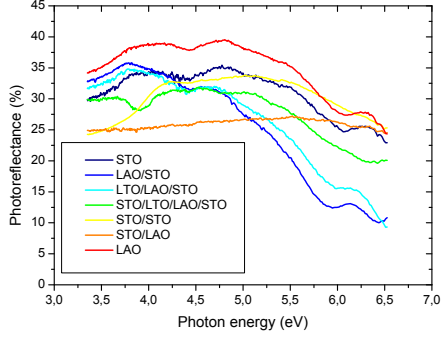
(a) different structures
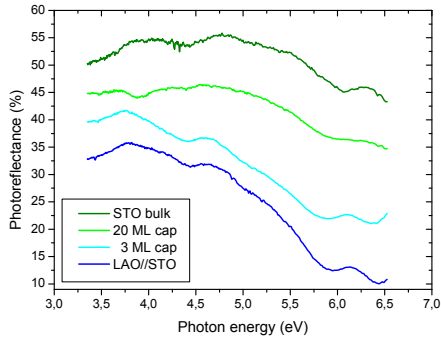
(b) STO capping thickness

Figure 6.23: Photoreflectance data for different LAO-LTO-STO structures grown at low-pressure. For (a), the rightmost material in each entry in the legend is the substrate. For (b) the m ML cap samples are NN20_LP samples with a STO cap of m monolayer.
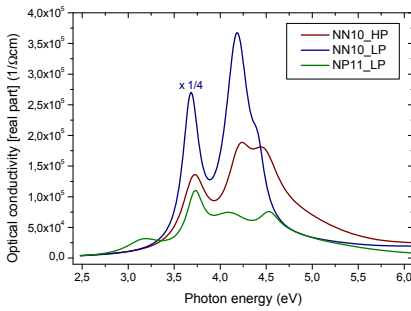
(a) double-interface samples
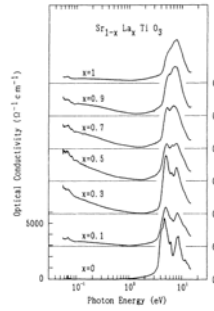
(b) $Sr_{1-x}La_xTiO_3$

Figure 6.24: Optical conductivities for (a) double-interface 10 ML LAO layer samples and (b) $Sr_{1-x}La_xTiO_3$, taken from Ref. [61]. The NN10_LP curve has been scaled down. The peak at 3.2 eV in the NP11_LP curve is due to one of the discarded transitions, as discussed in Section 4.4.3.

160

shows that opposite to the LTO/LAO system no band bending is observed in the LAO/STO double interfaces.

transition	NPx_LP	NNx_LP	NNx_HP	LAO//STO	bare STO
E_2 (eV)	3.73	3.73	3.74	3.67	3.82
E_3 (eV)	4.04	4.10	4.10	4.03	4.05
E_4 (eV)	4.50	4.40	4.48	4.52	4.60
E_5 (eV)	5.16	5.20	5.12	5.16	5.21

Table 6.7: Eigenenergies obtained from Lorentz fitting to the reflectance data for the LAO/STO double-interface and reference samples.

Figure 6.23(a) compares the photoreflectance spectra for different structures. It is clear that the dip around 3.9 eV (318 nm) is unique to the double-interface system. It appears in all double-interface series, both np and nn. Comparing Figures 6.22 and 6.23(a) shows that for thinner LAO layers the double-interface sample closer resembles STO. The depth of the dip at 3.9 eV increases with increasing LAO thickness. Given the very similar eigenenergies for all structures, any changes in the spectra must be due to redistribution of spectral weight. Figure 6.23(b) shows the evolution of the photoreflectance spectra for different thicknesses of the STO capping layer. The dip around 3.9 eV is a feature that develops for thicker capping layers, but is not purely due either to STO film or bulk.

As discussed in Section 4.4.3 the optical conductivity obtained from the Lorentz fitting has no absolute value due to the lack of calibration in the reflectance measurement. However, the general shape can already tell us something about the system under investigation. Figure 6.24(a) shows the obtained optical conductivities for the 10 ML LAO layer samples from the low-pressure np and both nn series. From this Figure it can be seen that the distribution of spectral weight is different.

The nn series seem to have more weight at higher energies, while the np series has more weight at lower energy. The latter compares well to the optical conductivity data for $Sr_{1-x}La_xTiO_3$, especially the data for $x = 0.3$[61]. For the $Sr_{1-x}La_xTiO_3$ system the La fraction corresponds directly to the electron fraction[10]. This fits remarkable well to the mobile electron fraction in these samples of $x = 0.25$.

In summary, though there are no changes in the transition energies reminiscent of band bending, the optical weight is re-distributed giving rise to new features in the reflectivity spectrum. The optical conductivity spectrum of these LAO//STO interfaces is qualitatively similar to that obtained for doped STO, again showing that the transport mechanism is the same for both systems.

6.6 Conclusions

Though the LAO/STO system is often investigated as being a single interface, in reality it is always a coupled-interface structure with either the air//LAO surface or another LAO//STO interface. Not only is it always necessary to investigate the system as a function of two interfaces, the chemical nature of both interfaces is also of utmost importance. Whether the simple LAO layer on STO is topped with either AlO_2 or LaO, with the same LAO//STO interface, already influences the properties of the heterostructure[35]. Post-annealing shows that indeed the electron density is protected by a capping layer. However, the electron mobility can still change due to changes in the effective dielectric constant[18, 30].

In this chapter the transport behaviour of double-interface structures with two n-type interfaces was investigated. To achieve the second LaO//TiO$_2$ interface a monolayer of LTO was included in the LAO/STO stack. Though in the ideal case the two interfaces are supposed to be identical, it was found that the LTO intra-block interface is non-conducting, though still a reservoir of electrons as discussed in Section 5.8. These electrons can then be doped to the LAO//STO inter-block interface, similar to the doping of holes from a p-type interface[5].

Above a carrier freeze-out temperature of 70 K the transport at the LAO//STO inter-block interface behaves as a Fermi liquid. The electron mobility is limited by the electron-electron scattering and has a $1/T^2$ temperature dependence with a value of 6 cm^2/Vs at room temperature. At low temperature there is a transition to a Coulomb impurity scattering mechanism and the mobility reaches a more constant value of about 700 cm^2/Vs. The electron density at low temperature seems to be independent of deposition conditions (above a minimum pressure of about $1 \cdot 10^{-5}$ mbar O$_2$) and sample structure. All samples described in this thesis, as well as a wide collection of samples from literature, all exhibit a low-temperature electron density of $2.5 \cdot 10^{13}$ cm^{-2}. Upon going to higher temperature, the carrier freeze-out is reversed and the electron density behaves as if thermally-activated with an activation energy E_a of 5-6 meV with values on the order of 10^{14} cm^{-2} at room temperature.

Measurements at 5 K show that the LAO//STO system is actually a two-band system at low temperatures. Both high-field magnetoresistance and temperature-dependent electron density measurements show the existence of two populations of electrons. One with a high density but low mobility and one with a low density but high mobility. The latter dominates in the Hall mobility at low temperature, while the former determines the electron density at higher temperatures. The temperature crossover between the two regimes seems to be about 70 K. As in a cubic crystal it is impossible for sub-bands to occur, it would be interesting to investigate whether this phenomenon is related to the cubic-to-tetragonal phase transition around 105 K.

Though the mobility is independent of the interface separation for both system with two n-type interfaces or with both a n- and a p-type interface, the electron density at room temperature systematically depends on the separation. In total,

the mobile electron density can be tuned by about a factor of 7 by varying the separation and interface. For np structures the electron density always decreases for smaller separation, while for nn structures it either stays constant or increases for smaller separations depending on the oxygen vacancy density. This behaviour can be modelled with the second interface acting as a sink (for np) or source (for nn) of electrons for the first interface. More precisely, the driving mechanism behind the electron transfer is a competition between the potential build-up inherent in the polar discontinuity in LAO and the potential due to electron transfer from one interface to the other. This is an electrostatic process, as the thermal energy of the system is too low to overcome the energy barrier which is on the order of 0.1-1 eV. This yields a $1/s$ dependence of the electron density. The sign of the change, either negative (np) or positive (nn) depends on the energy required to free the electrons at the donor interface. For np structures the energy is positive, as it costs energy to free the electrons from the trapped oxygen vacancies. For nn structures the energy is negative, as the local over-abundance of electrons at the second LTO intra-block interface raises their energy and redistribution of those electron lowers the total energy.

The model indicates that for thick films the electron fraction at the interface should approach 1/2 electron per unit cell area as predicted from the simple ionic model. However, the data leads to a value close to 1/4 electron per unit cell area, a value not unfamiliar from literature[36, 62]. Again, a multi-band model may be applied here, as Hall measurements only probe the mobile electrons and not the localized electrons[26, 29]. In this case the other 1/4 electron per unit cell is attributed to stationary electrons.

6.7   References

[1] S. Thiel, G. Hammerl, A. Schmehl, C. W. Schneider, and J. Mannhart, "Tunable quasi-two-dimensional electron gases in oxide heterostructures," *Science*, vol. 313, pp. 1942–1945, 2006.

[2] C. Bell, S. Harashima, Y. Hikita, and H. Y. Hwang, "Thickness dependence of the mobility at the $LaAlO_3/SrTiO_3$ interface," *Applied Physics Letters*, vol. 94, p. 222111, 2009.

[3] R. Pentcheva and W. E. Pickett, "Avoiding the polarization catastrophe in $LaAlO_3$ overlayers on $SrTiO_3(001)$ through a polar distortion," *Physical Review Letters*, vol. 102, p. 107602, 2009.

[4] Y. Li and J. Yu, "Polarization screening and induced carrier density at the interface of $LaAIO_3$ overlayer on $SrTiO_3(001)$." cond-mat/0904.1636, 2009.

[5] M. Huijben, G. Rijnders, D. H. A. Blank, S. Bals, S. van Aert, J. Verbeeck, G. van Tendeloo, A. Brinkman, and H. Hilgenkamp, "Electronically coupled complementary interfaces between perovskite band insulators," *Nature Materials*, vol. 5, pp. 556–560, 2006.

[6] M. Huijben, A. Brinkman, G. Koster, G. Rijnders, H. Hilgenkamp, and D. H. A. Blank, "Structure-property relation of $SrTiO_3$-$LaAlO_3$ interfaces," *Advanced Materials*, vol. 21, pp. 1665–1677, 2009.

[7] W. Siemons, G. Koster, H. Yamamoto, W. A. Harrison, G. Lucovsky, T. H. Geballe, D. H. A. Blank, and M. R. Beasley, "Origin of charge density at $LaAlO_3$ on $SrTiO_3$ heterointerfaces: possibility of intrinsic doping," *Physical Review Letters*, vol. 98, p. 196802, 2007.

[8] C. Cen, S. Thiel, G. Hammerl, C. W. Schneider, K. E. Andersen, C. S. Hellberg, J. Mannhart, and J. Levy, "Nanoscale control of an interfacial metal-insulator transition at room temperature," *Nature Materials*, vol. 7, pp. 298–302, 2008.

[9] M. Sing, G. Berner, K. Goß, A. Müller, A. Ruff, A. Wetscherek, S. Thiel, J. Mannhart, S. A. Pauli, C. W. Schneider, P. R. Willmott, M. Gorgoi, F. Schäfers, and R. Claessen, "Profiling the interface electron gas of $LaAlO_3/SrTiO_3$ heterostructures with hard X-ray photoelectron spectroscopy," *Physical Review Letters*, vol. 102, p. 176805, 2009.

[10] Y. Tokura, Y. Taguchi, Y. Okada, Y. Fujishima, and T. Arima, "Filling dependence of electronic properties on the verge of metal-Mott-insulator transitions in $Sr_{1-x}La_xTiO_3$," *Physical Review Letters*, vol. 70, pp. 2126–2129, 1993.

[11] A. Ohtomo, J. Nishimura, Y. Murakami, and M. Kawasaki, "Electronic transport properties in $SrTiO_3$-$LaAlO_3$ solid-solution films," *Applied Physics Letters*, vol. 88, p. 232107, 2006.

[12] P. R. Willmott, S. A. Pauli, R. Herger, C. M. Schlepütz, D. Martoccia, B. D. Patterson, B. Delley, R. Clarke, D. Kumah, C. Cionca, and Y. Yacoby, "Structural basis for the conducting interface between $LaAlO_3$ and $SrTiO_3$," *Physical Review Letters*, vol. 99, p. 155502, 2007.

[13] S. Okazaki, N. Okazaki, Y. Hirose, J. Nishimura, K. Ueno, A. Ohtomo, M. Kawasaki, H. Koinuma, and T. Hasegawa, "Quantitative conductivity mapping of $SrTiO_3$-$LaAlO_3$-$LaTiO_3$ ternary composition-spread thin film by scanning microwave microscope," *Applied Physics Express*, vol. 1, p. 055003, 2008.

[14] C. Kittel, *Introduction to solid state physics*. Hoboken, NJ: Wiley, 8th ed., 2005.

[15] S. Liang, D. J. Wang, J. R. Sun, and B. G. Shen, "Effect of oxygen content on the transport properties of La-doped $SrTiO_3$ thin films," *Solid State Communications*, vol. 148, pp. 386–389, 2008.

[16] A. Kalabukhov, R. Gunnarsson, J. Börjesson, E. Olsson, D. Winkler, and T. Claeson, "Effect of various deposition conditions on the electrical properties of LAO/STO hetero interfaces," *Journal of Physics: Conference Series*, vol. 100, p. 082039, 2008.

[17] N. Reyren, S. Thiel, A. D. Caviglia, L. Fitting Kourkoutis, G. Hammerl, C. Richter, C. W. Schneider, T. Kopp, A. S. Rüetschim, D. Jaccard, M. Gabay, D. A. Muller, J. M. Triscone, and J. Mannhart, "Superconducting interfaces between insulating oxides," *Science*, vol. 317, pp. 1196–1199, 2007.

[18] O. Copie, V. Garcia, C. Bödefeld, C. Carrétéro, M. Bibes, G. Herranz, E. Jacquet, J. L. Maurice, B. Vinter, S. Fusil, K. Bouzehouane, H. Jaffrès, and A. Barthélémy, "Towards two-dimensional metallic behavior at $LaAlO_3/SrTiO_3$ interfaces," *Physical Review Letters*, vol. 102, p. 216804, 2009.

[19] A. D. Caviglia, S. Gariglio, N. Reyren, D. Jaccard, T. Schneider, M. Gabay, S. Thiel, G. Hammerl, J. Mannhart, and J. M. Triscone, "Electric field control of the $LaAlO_3/SrTiO_3$ interface ground state," *Nature*, vol. 456, pp. 624–627, 2008.

[20] C. S. Koonce, M. L. Cohen, J. F. Schooley, W. R. Hosler, and E. R. Pfeiffer, "Superconducting transition temperatures of semiconducting $SrTiO_3$," *Physical Review*, vol. 163, pp. 380–390, 1967.

[21] O. N. Tufte and P. W. Chapman, "Electron mobility in semiconducting strontium titanate," *Physical Review*, vol. 155, pp. 796–802, 1967.

[22] G. Herranz, M. Basletić, M. Bibes, C. Carrétéro, E. Tafra, E. Jacquet, K. Bouzehouane, C. Deranlot, A. Hamzić, J. M. Broto, A. Barthélémy, and A. Fert, "High mobility in $LaAlO_3/SrTiO_3$ heterostructures: Origin, dimensionality, and perspectives," *Physical Review Letters*, vol. 98, p. 216803, 2007.

[23] M. Takizawa, Y. Hotta, T. Susaki, Y. Ishida, H. Wadati, Y. Takata, K. Horiba, M. Matsunami, S. Shin, M. Yabashi, K. Tamasaku, N. Nishino, T. Ishikawa, A. Fujimori, and H. Y. Hwang, "Spectroscopic evidence for competing reconstructions in polar multilayers $LaAlO_3/LaVO_3/LaAlO_3$," *Physical Review Letters*, vol. 102, p. 236401, 2009.

[24] A. Ohtomo and H. Y. Hwang, "A high-mobility electron gas at the $LaAlO_3/SrTiO_3$ heterointerface," *Nature*, vol. 427, pp. 423–426, 2004.

[25] N. Nakagawa, H. Y. Hwang, and D. A. Muller, "Why some interfaces cannot be sharp," *Nature Materials*, vol. 5, pp. 204–209, 2006.

[26] W.-J. Son, E. Cho, B. Lee, J. Lee, and S. Han, "Density and spatial distribution of charge carriers in the intrinsic n-type $LaAlO_3$-$SrTiO_3$ interface," *Physical Review B*, vol. 79, p. 245411, 2009.

[27] H. Chen, A. M. Kolpak, and S. Ismail Beigi, "Fundamental asymmetry in interfacial electronic reconstruction between insulating oxides: An ab initio study," *Physical Review B*, vol. 79, p. 161402, 2009.

[28] N. C. Bristowe, E. Artacho, and P. B. Littlewood, "Oxide superlattices with alternating p and n interfaces," *Physical Review B*, vol. 80, p. 045425, 2009.

[29] Z. S. Popović, S. Satpathy, and R. M. Martin, "Origin of the two-dimensional electron gas carrier density at the $LaAlO_3$ on $SrTiO_3$ interface," *Physical Review Letters*, vol. 101, p. 256801, 2008.

[30] C. Bell, S. Harashima, Y. Kozuka, M. Kim, B. G. Kim, Y. Hikita, and H. Y. Hwang, "Dominant mobility modulation by the electric field effect at the $LaAlO_3/SrTiO_3$ interface." cond-mat/0906.5310, 2009.

[31] A. A. Sirenko, I. A. Akimov, J. R. Fox, A. M. Clark, H.-C. Li, W. Si, and X. X. Xi, "Observation of the first-order Raman scattering in $SrTiO_3$ thin films," *Physical Review Letters*, vol. 82, pp. 4500–4503, 1999.

[32] N. Shanthi and D. D. Sarma, "Electronic structure of electron doped $SrTiO_3$: $SrTiO_{3-d}$ and $Sr_{1-x}La_xTiO_3$," *Physical Review B*, vol. 57, pp. 2153–2158, 1998.

[33] D. D. Cuong, B. Lee, K. M. Choi, H.-S. Ahn, S. Han, and J. Lee, "Oxygen vacancy clustering and electron localization in oxygen-deficient $SrTiO_3$: LDA+U Study," *Physical Review Letters*, vol. 98, p. 115503, 2007.

[34] J. Lee and A. A. Demkov, "Charge origin and localization at the n-type $SrTiO_3/LaAlO_3$ interface," *Physical Review B*, vol. 78, p. 193104, 2008.

[35] N. Pavlenko and T. Kopp, "Structural relaxation and metal-insulator transition at the interface between $SrTiO_3$ and $LaAlO_3$." cond-mat/0901.4610, 2009.

[36] A. Brinkman, M. Huijben, M. van Zalk, J. Huijben, U. Zeitler, J. C. Maan, W. G. van der Wiel, G. Rijnders, D. H. A. Blank, and H. Hilgenkamp, "Magnetic effects at the interface between nonmagnetic oxides," *Nature Materials*, vol. 6, pp. 493–496, 2007.

[37] R. Pentcheva, M. Huijben, K. Otte, W. E. Pickett, J. E. Kleibeuker, J. Huijben, H. Boschker, D. Kockmann, W. Siemons, G. Koster, H. J. W. Zandvliet, G. Rijnders, D. H. A. Blank, H. Hilgenkamp, and A. Brinkman, "Parallel electron-hole bilayer conductivity from electronic interface reconstruction," *Nature Physics*, p. *submitted*, 2009.

[38] M. van Zalk, J. Huijben, A. J. M. Giesbers, M. Huijben, U. Zeitler, J. C. Maan, W. G. van der Wiel, Rijnders G., D. H. A. Blank, H. Hilgenkamp, and A. Brinkman, "Magnetoresistance oscillations and relaxation effects at the $SrTiO_3$-$LaAlO_3$ interface." cond-mat/0806.4450, 2008.

[39] M. Ben Shalom, C. W. Tai, Y. Lereah, M. Sachs, E. Levy, D. Rakhmilevitch, A. Palevski, and Y. Dagan, "Anisotropic magnetotransport at the $SrTiO_3\backslash LaAlO_3$ interface," *Physical Review B*, vol. 80, p. 140403, 2009.

[40] M. Lundstrom, *Fundamentals of carrier transport*. Cambridge: Cambridge University Press, 2 ed., 2000.

[41] K. Seeger, *Semiconductor physics: an introduction*. Berlin: Springer, 9 ed., 2004.

[42] Y. Kozuka, Y. Hikita, and T. Susaki, "Optically tuned dimensionality crossover in photocarrier-doped $SrTiO_3$: Onset of weak localization," *Physical Review B*, vol. 76, p. 085129, 2007.

[43] N. Reyren, S. Gariglio, A. D. Caviglia, D. Jaccard, T. Schneider, and J. M. Triscone, "Anisotropy of the superconducting transport properties of the $LaAlO_3/SrTiO_3$ interface," *Applied Physics Letters*, vol. 94, p. 112506, 2009.

[44] H. P. R. Frederikse, W. R. Hosler, and W. R. Thurber, "Magnetoresistance of semiconducting $SrTiO_3$," *Physical Review*, vol. 143, pp. 648–651, 1966.

[45] N. W. Ashcroft and N. D. Mermin, *Solid state physics*. Philadelphia: Saunders College Publishing, 1976.

[46] H. Nakamura, H. Tomita, H. Akimoto, R. Matsumura, I. H. Inoue, T. Hasegawa, K. Kono, Y. Tokura, and H. Takagi, "Tuning of metal-insulator transition of quasi-two-dimensional electrons at parylene/$SrTiO_3$ interface by electric field," *Journal of the Physical Society of Japan*, vol. 78, p. 083713, 2009.

[47] L. Donetti, F. Gamiz, and S. Cristoloveanu, "Monte Carlo simulation of Hall and magnetoresistance mobility in SOI devices," *Solid-State Electronics*, vol. 51, pp. 1216–1220, 2007.

[48] T. Fix, J. L. MacManus Driscoll, and M. G. Blamire, "Delta-doped $LaAlO_3$/$SrTiO_3$ interfaces," *Applied Physics Letters*, vol. 94, p. 172101, 2009.

[49] Y. Kozuka, T. Susaki, and H. Y. Hwang, "Vanishing Hall coefficient in the extreme quantum limit in photocarrier-doped $SrTiO_3$," *Physical Review Letters*, vol. 101, p. 096601, 2008.

[50] S. S. A. Seo, Z. Marton, W. S. Choi, G. W. J. Hassink, D. H. A. Blank, H. Y. Hwang, T. W. Noh, T. Egami, and H. N. Lee, "Multiple conducting carriers generated in $LaAlO_3$/$SrTiO_3$ heterostructures," *Applied Physics Letters*, vol. 95, p. 082107, 2009.

[51] J. P. Poirier, *Creep of crystals: high-temperature deformation processes in metals, ceramics, and minerals.* Cambridge University Press, 1985.

[52] R. Moos, W. Menesklou, and K. H. Härdtl, "Hall mobility of undoped n-type conducting strontium titanate single crystals between 19 K and 1373 K," *Applied Physics A: Materials Science & Processing*, vol. 61, pp. 389–395, 1995.

[53] H. Yamada and G. R. Miller, "Point defects in reduced strontium titanate," *Journal of Solid State Chemistry*, vol. 6, pp. 169 – 177, 1973.

[54] M. Lippmaa, N. Nakagawa, M. Kawasaki, S. Ohashi, and H. Koinuma, "Dielectric properties of homoepitaxial $SrTiO_3$ thin films grown in the step-flow mode," *Journal of Electroceramics*, vol. 4, pp. 365–368, 2000.

[55] X. Cai, C. D. Frisbie, and C. Leighton, "Optimized dielectric properties of $SrTiO_3$:Nb/$SrTiO_3$ (001) films for high field effect charge densities," *Applied Physics Letters*, vol. 89, p. 242915, 2006.

[56] X. Z. Liu, B. W. Tao, and Y. R. Li, "Effect of oxygen vacancies on nonlinear dielectric properties of $SrTiO_3$ thin films," *Journal of Materials Science*, vol. 42, pp. 389–392, 2007.

[57] A. Ohkubo, A. Ohtomo, J. Nishimura, T. Makino, Y. Segawa, and M. Kawasaki, "Combinatorial synthesis and optical characterization of alloy and superlattice films based on $SrTiO_3$ and $LaAlO_3$," *Applied Surface Science*, vol. 252, pp. 2488–2492, 2006.

[58] M. Huijben, *Interface engineering for oxide electronics*. PhD thesis, University of Twente, 2006.

[59] K. Shibuya, T. Ohnishi, T. Uozumi, H. Koinuma, and M. Lippmaa, "An in situ transport measurement of interfaces between $SrTiO_3$(100) surface and an amorphous wide-gap insulator," *Applied Surface Science*, vol. 252, pp. 8147–8150, 2006.

[60] M. Basletic, J. L. Maurice, C. Carrétéro, G. Herranz, O. Copie, M. Bibes, E. Jacquet, K. Bouzehouane, S. Fusil, and A. Barthélémy, "Mapping the spatial distribution of charge carriers in $LaAlO_3$/$SrTiO_3$ heterostructures," *Nature Materials*, vol. 7, pp. 621–625, 2008.

[61] Y. Fujishima, Y. Tokura, T. Arima, and S. Uchida, "Optical-conductivity spectra of $Sr_{1-x}La_xTiO_3$: filling-dependent effect of the electron correlation," *Physical Review B*, vol. 46, pp. 11167–11170, 1992.

[62] A. Kalabukhov, R. Gunnarsson, J. Börjesson, E. Olsson, T. Claeson, and D. Winkler, "Effect of oxygen vacancies in the $SrTiO_3$ substrate on the electrical properties of the $LaAlO_3$/$SrTiO_3$ interface," *Physical Review B*, vol. 75, p. 121404, 2007.

Chapter 7

Epilogue

Correlated electron materials, such as the transition metal perovskites, show many interesting and useful properties like superconductivity or ferromagnetism. And these properties can be combined in heterostructures due to the similarity in crystal structures. Such properties are already applied, for example in hard disk read heads, but in most cases fundamental research is necessary. Two-dimensional structures are especially suited, as they offer the possibility of field-effect doping and are conceptually simpler compared to bulk systems.

Quasi-two-dimensional electron layers have been the subject of my thesis. Relatively simple heterostructures fabricated by pulsed laser deposition allow for the study of such layers in different ways, most importantly by resistance and optical measurements. Though the properties of two-dimensional layers can be very different, it is interesting that sometimes models describing bulk properties can be used to describe observations for layers with a thickness of only 10 nm. Examples of both two-dimensional and bulk behaviour have been shown in my thesis.

An example of the latter is the LTO/LAO system. LTO in bulk form is a Mott insulator, but thin layers of LTO embedded in STO are not. Increasing the electron confinement perpendicular to the layer by embedding the LTO in LAO makes it possible to recover this Mott insulating behaviour. Such layers could form the active layer in FET's with in the ideal case a perfect metal-to-insulator transition. Even if this goal is not reached, an on/off ratio of 2000 should theoretically be possible. In $La_xSr_{1-x}TiO_3$ a change of x from 1 to 0.95 yields such a resistance ratio at room temperature.

Another example is the conduction at the LAO//STO interface. The transport can be described by a combination of thermal activation of the electron density and a Fermi-liquid-like electron-electron scattering process where the electron mobility has a $1/T^2$ dependence up to at least 400 K. Field-effect doping for these interfaces has also been reported in litreature. For applications such interfaces may be interesting as interconnects between different perovskite functional blocks or for

transparent devices. The patterning of 2D devices has already been demonstrated, both by local oxidation with AFM or by optical lithography.

The two-dimensional nature of the heterostructures becomes obvious in the doping of the electron layers from another nearby interface, either with air or with another material. Both the LTO/LAO system and the LAO//STO interfaces have a doping mechanism where the distance between donor and receiver interfaces controls the amount of doping. In the LAO/STO system the electron density can be varied by a factor of 7 without changing the electron mobility.

Focussing on the LAO//STO interfaces it is found that the in-plane strain on the STO influences the conducting state at the interface. Calculations do indeed show that the screening of the polar discontinuity at the interface is a combination of both structural and electronic screening. In fact, changing the in-plane strain can lead to the complete disappearance of the conducting state. Such a strain dependence may be useful in for example pressure sensors. This implies that engineering the strain will require careful attention when designing devices, especially when combinations with silicon are required.

Both systems were found to depend strongly on the oxygen stoichiometry in the sample. Oxygen vacancies dominate the electron doping below a critical deposition pressure of 10^{-5} mbar, while the electron mobility is also dependent on the oxygen content. But the pressure not only influences the interface doping through the creation of oxygen vacancies in the STO, but also through surface oxidation of the LAO layer. The latter process is very sensitive to small changes in the environment and difficult to control. Capping the LAO layer with a second STO layer protects this interface and insulates it from the environment. This greatly improves the stability of the doping of the interface without affecting the electron mobilities. This enhances the chemical robustness of the perovskite structures. The control over the oxygen content offers possibilities to tune the electrical properties.

One could think of several subjects for follow-up research. For example, it would be very interesting to study actual FET structures based on LTO/LAO Mott layers. Already modulation of the LTO layer filling could provide useful information about the behaviour of 2D Mott-Hubbard systems. Such systems should have a very thin LAO capping layer, as to facilitate the doping from surface to interface. For the interface systems, the spatial distribution of both electrons and their mobility are important factors determining the transport properties of LAO//STO interfaces. Heterostructures in which the STO interlayer of variable thickness is sandwiched between a LAO layer and another high band gap insulator could be a way to investigate the effects of this distribution. The Montgomery method may be another way to probe the mobility in the out-of-plane direction. STO interlayers with different defect densities could help to investigate the validity of the structural-polarization model. Especially substrate bending experiments could yield useful information on the influence of strain on the transport properties.

<div align="right">Gerwin Hassink</div>

Summary

Correlated-electron materials are currently at the forefront of fundamental condensed matter physics. In one part this is because these materials exhibit many useful properties such as ferromagnetism and superconductivity. Another part is that the study of these materials is a natural extension of the research done on metals and semiconductors in the last century. The free-electron model which describes the metals and semiconductors is the basis for much of our current advanced technology, but breaks down for the correlated-electron materials where electron-electron interactions cannot be neglected. Indeed, these very interactions drive most of the interesting properties.

Today fabrication techniques for the correlated-electron materials, in particular the perovskite oxides, are reaching the same levels of sophistication as they did for the semiconductors in the early days of the electronic revolution. Pulsed laser deposition can fabricate coherently strained heterostructures with flat surfaces. *In situ* monitoring of the film growth by reflective high-energy electron diffraction allows for the fabrication of near-perfect superlattices and interfaces. With these structures more precise and deliberate investigations into the fundamental physics are being made. Similar to semiconductors the combination of two materials is not always the sum of their properties. Proximity effects at metal/superconductor interfaces which turn part of the metal superconducting is one example, the control of polarization in one material by the strain induced at the interface with a second material is another.

The two main systems discussed in this thesis are the $LaTiO_3/LaAlO_3$ (LTO/LAO) system and the $LaAlO_3/SrTiO_3$ (LAO/STO) system. All three materials are perovskites with varying properties. LTO is a Mott insulator, indicating that despite the single $3d^1$ electron the material is insulating due to Coulomb interaction between the electrons. Both LAO and STO are band insulators, but STO can easily be doped by oxygen vacancies or other elements. Such doped STO can even become superconducting below 300 mK.

The research on the LTO/LAO system is based on the observation that LTO/STO superlattices become conducting. This is because the $3d^1$ electron of the LTO spreads out into the STO due to the repulsive Coulomb force. Once doped into the STO the electron behaves as if free and the system becomes conducting. This suggests that if the electrons can be confined to the LTO layer, a two-dimensional

Mott insulator would result: something unknown in natural occurring materials. Such confinement could result from replacing the STO buffer material with a material that has a higher band gap, similar to the band engineering approach in semiconductors.

The LAO/STO system is equally interesting, as here two band insulators with no unpaired electrons combine to yield a conducting interface. The charge difference at the interface between $(LaO)^+//(TiO_2)^0$ gives rise to a band shift in the LAO layer that can be (partially) compensated by doping electrons from the LAO valence band into the STO conduction band at the interface. The transport can be described by a thermally-activated (E_a = 5-6 meV) electron density and a $1/T^2$ dependence of the electron mobility. These properties are greatly influenced by the oxygen pressure during deposition and cool-down, as evidenced by the fact that samples have been found which are superconducting while other samples have a magnetic signature.

Superlattices of LTO and LAO are investigated with scanning transmission electron microscopy in combination with electron energy loss spectroscopy to determine the electron distribution around the LTO layers. These measurements show that the Ti^{3+} fraction inside the LTO layer increases from 0.25 for the LTO/STO system to 0.85 for the LTO/LAO system. This increase in the electron confinement is enough to turn the superlattices insulating. Calculations show that the increase in electron density combined with the concomitant increase in the effective electron mass is enough make the LTO/LAO superlattices fulfil the Mott criterion. Ellipsometry measurements on these superlattices in combination with density functional theory calculations confirm the existence of a Mott insulating state for the superlattices with a single monolayer of LTO. The orbital order in these LTO monolayers is xz/yz, minimizing the interaction in-plane. For thicker layers xy orbitals become involved, as interactions out-of-plane become more likely.

These embedded LTO layers can also be hole-doped by a nearby air//LAO surface. This process is driven by the surface oxidation and requires a balance between the creation of oxygen vacancies on the surface and electron transfer from the LTO layer. For thick LAO capping the surface oxidation is completely resolved by oxygen vacancies. As the capping becomes thinner electrons can transfer from the LTO layer to the surface, but this induces an extra dipole that costs energy. As the capping becomes even thinner, the dipole energy cost decreases and more electrons are transferred up to the maximum of 1/2 electron per unit cell. X-ray photoemission spectroscopy shows this thickness dependence clearly in the Ti^{3+} fraction and fitting with the above model yields a band-shift energy of $\Sigma = 2.2$ eV. One remaining question is why the observed Ti^{3+} fraction does not recover full occupation of 1 for thick capping, as neither oxygen nor cation off-stoichiometry can explain this observation.

Such dipole fields can also result in changes in the band structure. Optical measurements are a good way to probe such changes. Photoreflectance spectroscopy shows that indeed the transition from the LTO valence band to the LAO conduction band at the LAO//LTO interface changes with the capping thickness.

However, the change in band energy are only about 0.03 eV per monolayer, much smaller than the band-shift energy of about $\Sigma = 2.2$ eV. In addition, the band bending energy is independent of the electron density, so it is a feature of the LAO capping layer only. The strain on the LAO capping creates internal dipoles due to relative shifts of the cations and anions within. From the band bending energy the average dipole per LAO layer is calculated to be 0.06 eÅ, which corresponds to a relative shift of 1.5 %. This is very close to the lattice mismatch in the c-direction of 1.1 %, indicating that this band bending is probably a strain effect independent of the electron transfer.

While in the LTO/LAO system the confinement is in part due to the band gap engineering with LTO and LAO, in the LAO/STO system it is purely the electrostatic force that keeps the electrons bound to the two-dimensional layer. Careful examination of published results for the LAO//STO interfaces show two important observations. First, there is a critical deposition pressure of $1 \cdot 10^{-5}$ mbar O_2 below which the conduction is vacancy dominated and above which the conduction is interface-dominated. Second, the electron mobility decreases with increasing deposition pressure. This is linked to the concomitant decrease in the dielectric constant of the STO. The lower dielectric screening pulls the electrons closer to the interface where interface defects increase the average scattering rate.

The critical deposition pressure and cool-down pressures sketch a pressure-temperature phase diagram where above the critical pressure or at low temperature re-oxidation of the STO occurs. The reduction of the STO occurs due to oxygen out-diffusion during the deposition and is activated by the initial plasma sputtering. The stoichiometric and crystalline quality of the STO substrate influences the diffusion process, resulting in different transport properties for STO from different manufacturers.

The developing model for the conduction at LAO//STO interfaces involves shifting LAO bands, which so far have not been observed in experiments. The structural-polarization model is proposed where the strain and electrostatic forces at the interface induce a local polarization in the STO. This polarization lowers the STO bands locally and electrons from defect states in the STO can then be trapped in the potential well at the interface and give rise to a conducting state. The results from LAO/STO heterostructures fabricated on different substrates, producing different strain states, seem to agree with this model.

Including the LaO//TiO$_2$ interface in heterostructures allows for the fabrication of such interfaces by either depositing LAO on TiO$_2$-terminated STO or by depositing a monolayer of LTO on SrO-terminated STO. Though these two interfaces are nominally equivalent, their actual properties are different. LAO//STO interfaces display the typical $1/T^2$ mobility-dependence, while LTO interfaces behave as variable-range hopping insulators. X-ray photoelectron spectroscopy confirms that both interfaces have electrons on the titanium ions. Both transport mechanisms have the same activation energy, indicating that the binding sites are similar. The difference between the two interfaces can be explained by a difference in strain and polarization at the interface due to the deposition of the LTO interlayer.

Using this LTO layer heterostructures with nominally two LaO//TiO$_2$ n-type interfaces can be fabricated. In this STO//LTO//LAO//STO sandwich the LTO layer acts not as a second conduction channel, but as a reservoir of electrons. An advantage of this heterostructure is that that second interface is protected from the environment by the top STO layer. This reduces the influence of sample treatment and handling after the deposition and expands the possibility for the investigation of systematic trends.

The transport properties of such heterostructures resembles that of single interfaces with a thermally-activated electron density and a Fermi-liquid-like $1/T^2$ electron mobility dependence. Similar to the heterostructures with both a LaO//TiO$_2$ n-type and an AlO$_2$//SrO p-type interface, the double n-type interface structures show that the electron density depends on the interface separation. Interestingly, the behaviour is reversed for the two heterostructures. The np heterostructure shows an increase with increasing interface separation, the nn heterostructure shows a decrease with increasing separation.

This difference in behaviour can be explained by a model where the second interface acts as a sink (p-type) or source (LTO n-type) of electrons. For small interface separation, the electron transfer has only a small electrostatic energy cost. As the interface separation increases, the energy cost increases and the electron transfer decreases. For the np heterostructure less electrons are transferred *away* from the conducting interface, so the electron density increases to approach the limit of half electron per unit cell. For the nn heterostructure less electrons are transferred *to* the conducting interface, so the electron density decreases towards this same limit. In both cases the energy associated with binding the electron to the second interface is 0.4 eV.

At low temperature both the magnetoresistance and the electron density vs. temperature show indications for the existence of two carrier populations. One has a high mobility, but a low electron density. The other has a low mobility, but has an electron density that is two orders of magnitude larger. The low-density population has a small activation energy of about 1 meV, while the high-density population is the one generally observed with E_a = 5-6 meV. The appearance of these two populations may be related to the cubic-to-tetragonal phase transition of STO at 105 K, as in the cubic phase no multi-band structure is allowed.

Samenvatting
(Summary in Dutch)

Vanuit de vastestoffysica is er veel belangstelling voor elektronen-gecorreleerde materialen. Dit is gedeeltelijk vanwege de vele bruikbare eigenschappen van deze materialen zoals ferromagnetisme en supergeleiding. Een andere reden is dat de studie van dit soort materialen een logische voorzetting is van het onderzoek aan metalen en halfgeleiders dat de afgelopen eeuw verricht is. Het vrije-elektronen model dat de eigenschappen van deze metalen en halfgeleiders beschrijft, is het fundament voor veel van onze moderne technologie. Maar voor elektronen-gecorreleerde materialen is deze theorie niet meer toepasbaar, aangezien de interactie tussen elektronen onderling niet meer verwaarloosbaar is. Het is juist deze interactie die de meeste van de eerdergenoemde nuttige eigenschappen veroorzaakt.

Vandaag de dag bereiken de technieken om elektronen-gecorreleerde materialen te maken dezelfde nauwkeurigheid als die voor halfgeleiders aan het begin van hun opmars. Gepulste laser depositie is nu in staat om coherente heterostructuren met atomair vlakke oppervlaktes te maken. Met reflectieve hoge-energie elektronen diffractie kan de groei tijdens het proces zelf gevolgd worden. Dit stelt ons in staat om bijna perfecte grensvlakken en multilagen te maken. Deze structuren maken het mogelijk om nauwkeuriger en gerichter metingen te doen om de fundamentele fysica van deze materialen te achterhalen. Want net als bij halfgeleiders zijn de eigenschappen van een combinatie van materialen niet altijd de som van de afzonderlijke eigenschappen. Een voorbeeld is het supergeleidend worden van een dunne grenslaag aan een metaal/supergeleider grensvlak. Een ander voorbeeld is beïnvloeding van de polarisatie in een materiaal door de compressie van de eenheidscel ten gevolge van het grensvlak met het substraat.

De twee materiaalsystemen die in dit proefschrift behandeld worden zijn het $LaTiO_3/LaAlO_3$ (LTO/LAO) systeem en het $LaAlO_3/SrTiO_3$ (LAO/STO) systeem. Alle drie de genoemde materialen zijn perovskieten, maar met verschillende fysische eigenschappen. LTO is een Mott-isolator waar, ondanks het ene enkele elektron in de 3d band, een isolerende toestand ontstaat door de Coulomb afstoting tussen de elektronen. LAO en STO zijn beide eenvoudige isolatoren, maar STO kan geleidend gemaakt worden door doping met zuurstofvacatures of andere elementen. Gedoopt STO kan zelfs supergeleidend worden beneden de 300 mK.

Het onderzoek met het LTO/LAO systeem werd gestart naar aanleiding van de observatie dat multilagen van LTO/STO geleidend worden. Dit komt omdat het $3d^1$ elektron van LTO gedeeltelijk het STO binnendringt om zo de Coulomb energie te verlagen. Eenmaal in het STO kunnen de elektron zich als vrije elektronen gedragen en ontstaat er een geleidende toestand. Dit suggereert dat als de elektronen beter opgesloten kunnen worden in de LTO laag, er een twee-dimensionale Mott isolator kan ontstaan: iets wat ongekend is in natuurlijk voorkomende materialen. Een mogelijke manier om een dergelijke opsluiting te verkrijgen is door de STO buffer te vervangen door een materiaal met een grotere band gap, net als in de halfgeleiderfysica.

Het LAO/STO systeem is net zo interessant. Hier ontstaat aan het grensvlak tussen de twee isolatoren een geleidende laag. Het ladingsverschil tussen beide materialen, $(LaO)^+//(TiO_2)^0$, zorgt er voor dat de elektronenbanden in LAO verschuiven. Deze verschuiving kan (gedeeltelijk) gecompenseerd worden door elektronen vanuit het LAO in het STO te dopen. De geleiding langs het n-type grensvlak kan beschreven worden door een thermisch-geactiveerde elektronendichtheid ($E_a = 6$ meV) en een $1/T^2$ temperatuursafhankelijkheid van de elektronenmobiliteit. Deze eigenschappen zijn erg afhankelijk van de zuurstofdruk tijdens de fabricatie en afkoeling. Daardoor is het mogelijk dat in vergelijkbare samples totaal verschillende eigenschappen zoals supergeleiding en magnetisme worden waargenomen.

Multilagen van LTO en LAO zijn met behulp van scanning transmissie elektronenmicroscopie en elektronen energie-verlies spectroscopie onderzocht. Met deze metingen is het mogelijk om de verdeling van elektronen rond de LTO lagen te bepalen. Deze metingen tonen aan dat de Ti^{3+} fractie in de LTO laag toeneemt van 0,25 voor het LTO/LAO systeem naar 0,85 voor het LTO/LAO systeem. Deze toename in opsluiting van de elektronen is voldoende om van de gehele multilaag een isolator te maken. Berekeningen tonen aan dat de toegenomen elektronendichtheid, samen met de daaraan gerelateerde toename in de effectieve massa van de elektronen, voldoende is om het LTO/LAO systeem te laten voldoen aan het Mott criterium. Ellipsometrie-metingen aan deze multilagen gecombineerd met berekeningen binnen de dichtheidsfunctionaaltheorie tonen aan dat multilagen met monolagen LTO inderdaad zich in een Mott-isolerende toestand bevinden. De ordening van de bezette orbitalen in deze LTO monolagen is xz/yz, zodat de interactie in het vlak geminimaliseerd wordt. Voor dikkere LTO lagen worden er ook xy orbitalen bijgemengd, omdat er interacties tussen de verschillende monolagen kunnen optreden.

LTO lagen omgeven door LAO kunnen ook gedoopt worden met gaten van een vacuüm//LAO grensvlak in de buurt. De drijvende kracht is de oxidatie van het LAO oppervlak. Dit vereist een balans tussen het creëren van zuurstofvacatures aan het oppervlak en het verplaatsen van elektronen van de LTO laag naar het oppervlak. In de limiet voor dikke LAO toplagen wordt deze oppervlakte-oxidatie geheel verzorgd door zuurstofvacatures. Voor dunnere LAO toplagen kunnen elektronen van de LTO laag naar het oppervlak worden verplaatst. Echter, deze elektronen vormen een dipool die de energie van het systeem verhoogt. Als de LAO toplaag nog dunner wordt, neemt deze dipoolenergie af en worden er meer elektronen naar het

oppervlak verplaatst tot een maximum van een 1/2 elektron per eenheidscel. Met röntgen fotoelektron spectroscopie kan dit dikte-afhankelijke dipoolmodel getest worden door de Ti^{3+} fractie van de LTO laag te bepalen. Een fit van het bovenstaande model aan deze data geeft een waarde voor de bandenverschuiving van Σ = 2,2 eV. Een open vraag is waarom de Ti^{3+} fractie niet de waarde van 1 aanneemt voor dikke LAO lagen zonder verplaatsing van elektronen. Afwijkingen in de chemische samenstelling, zowel van zuurstof-anionen als van kationen, kunnen dit verschijnsel niet verklaren.

Het elektrische veld van de beschreven dipool kan ook invloed hebben op de bandstructuur. Optische metingen zijn een goede manier om veranderingen in de bandtransities te meten. Fotoreflectie-spectroscopie metingen tonen aan dat de transitie van de LTO valentieband naar de LAO geleidingsband aan het LAO//LTO grensvlak inderdaad afhankelijk is van de dikte van de LAO toplaag. Echter, de verandering is slechts 0,03 eV per monolaag, veel lager dan de bandverschuiving van Σ = 2,2 eV. Bovendien is deze verandering onafhankelijk van de doping, in tegenstelling tot de Ti^{3+} fractie. Deze optische bandverschuiving is dus puur een eigenschap van de LAO toplaag. De krachten op de LAO toplaag zorgen voor een verschuiving van de kationen en anionen, die vervolgens interne dipolen vormen. Uit de optische bandverschuiving is af te leiden dat de gemiddelde dipool per monolaag LAO 0,06 eÅ moet zijn. Dit komt overeen met een verschuiving van de ionen van 1,5 %, vergelijkbaar met de verschuiving van 1,1 % in de c-richting ten gevolge van het verschil in roosterconstantes tussen LAO in bulk en dunne-film vorm. Deze overeenkomst lijkt te bevestigen dat de bandverschuiving een gevolg is van de structurele vervorming en niet van de verplaatste elektronen.

Hoewel in het LTO/LAO systeem de opsluiting van de elektronen vooral te danken is aan het verschil in bandkloven, voor het LAO/STO systeem zijn het puur de elektrostatische krachten die de elektronen aan het grensvlak binden. Een zorgvuldige analyse van reeds gepubliceerde literatuur geeft twee belangrijke resultaten. Ten eerste is er een kritieke depositiedruk van $1\cdot10^{-6}$ mbar. Bij lagere drukken wordt de geleiding gedomineerd door zuurstofvacatures, bij hogere drukken door doping van het grensvlak. Ten tweede, de elektronenmobiliteit neemt af voor hogere depositiedrukken. Deze afname wordt veroorzaakt door de gelijktijdige afname van de diëlektrische constante van STO. Een lagere diëlektrische constante betekent dat de elektronen dichter bij het grensvlak komen te zitten waar de grotere dichtheid aan defecten de mobiliteit onderdrukken.

De kritieke depositiedruk en de druk tijdens het afkoelen geven een schets van een druk-temperatuur fasediagram. Bij hoge temperatuur en lage depositiedruk zorgen de eerste plasmapulsen ervoor dat de reductie van het STO wordt geactiveerd. Boven de kritieke druk of bij lagere temperaturen vindt later in het groeiproces re-oxidatie van het STO plaats. Gecombineerd zorgen de reductie en oxidatie voor de verschillende eigenschappen bij verschillende drukken. De chemische en structurele kwaliteit van het substraat beïnvloedt deze processen ook, oftewel substraten van verschillende leveranciers kunnen verschillende resultaten geven.

Het model voor de doping in het LAO/STO systeem dat op het moment in de literatuur besproken wordt, vereist een bandverschuiving in het LAO die tot op heden niet is waargenomen. Een alternatief structurele-polarisatie model heeft geen bandverschuiving nodig aangezien structurele en elektrostatische krachten aan het grensvlak een lokale polarisatie in het STO creëren. Deze polarisatie zorgt voor een lokale verlaging van de bandstructuur in het STO, waarna elektronen van donor-defecten in het STO in deze potentiaalput gevangen worden en een geleidende toestand vormen. De resultaten van LAO//STO heterostructuren gefabriceerd op verschillende types substraten, en daaraan gekoppeld verschillende polarisatietoestanden, lijken dit model te bevestigen.

Complexere multilaag-structuren maken het mogelijk om LaO//TiO$_2$ grensvlakken te fabriceren zowel door het deponeren van LAO op TiO$_2$-getermineerd STO als door het deponeren van een monolaag LTO op SrO-getermineerd STO. Hoewel deze twee methoden theoretisch een identiek grensvlak zouden moeten creëren, in werkelijkheid hebben ze andere eigenschappen. LAO//STO grensvlakken hebben een weerstand met een $\sim T^2$ afhankelijkheid, terwijl LTO grensvlakken zich als variable-afstand hopping isolatoren gedragen. Röntgen fotoelektron spectroscopie metingen tonen aan dat beide grensvlakken elektronen op de titanium ionen gedoopt hebben. Dat de beide elektrische transportmechanismen dezelfde activatie-energie hebben, geeft aan dat de elektronen aan hetzelfde type donoren gebonden zijn. Het verschil in geleiding kan in het structurele-polarisatie model verklaard worden door het verschil in polarisatie aan het grensvlak vanwege de extra LTO laag.

Met behulp van een monolaag LTO kunnen multilaag-structuren met twee LaO//TiO$_2$ n-type grensvlakken gemaakt worden. Het LTO grensvlak in deze STO//LTO//LAO//STO multilaag vormt geen tweede geleidingspad, maar is alleen een reservoir van extra elektronen. Eén voordeel van deze structuur is dat het tweede grensvlak afgeschermd wordt van de omgeving, waardoor de eigenschappen van de grensvlakken onafhankelijker worden van de behandeling van het sample na de fabricatie. Dit vergroot de mogelijkheden voor systematisch onderzoek aan dit systeem.

De transporteigenschappen van deze dubbele-grensvlak multilagen lijken erg op die van heterostructuren met maar één LAO//STO grensvlak. De elektronendichtheid is thermisch geactiveerd en de elektronenmobiliteit heeft een $1/T^2$ temperatuursafhankelijkheid vergelijkbaar met een Fermi-vloeistof. Net als de multilaag-structuren met zowel een n-type (LaO//TiO$_2$) en een p-type (AlO$_2$//SrO) grensvlak is de elektronendichtheid afhankelijk van de afstand tussen de twee grensvlakken. Interessant genoeg is deze afhankelijkheid tegenovergesteld voor deze beide structuren: voor de np multilaag neemt de elektronendichtheid toe met de afstand, voor de nn multilaag neemt de elektronendichtheid juist af.

Een model waar het tweede grensvlak respectievelijk elektronen invangt (p-type) of afgeeft (n-type) kan dit verschil verklaren. Wanneer de grensvlakken dicht bij elkaar zijn, kost het verplaatsen van elektronen van het ene naar het andere grensvlak weinig energie. Als de afstand tussen de grensvlakken toeneemt, neemt ook de energie toe en zal er minder verplaatsing van elektronen plaatsvinden. Voor

een *np* multilaag betekent dit dat minder elektronen *van* het geleidende grensvlak naar het *p*-type grensvlak verplaatst worden, dus de elektronendichtheid neemt toe naar de limiet van een half elektron per eenheidscel. Voor een *nn* multilaag worden er minder elektronen *naar* het geleidende grensvlak verplaatst worden waardoor de elektronendichtheid afneemt naar dezelfde limiet. In beide gevallen is de energie van de binding aan het tweede grensvlak ongeveer 0,4 eV.

Metingen van de magnetoweerstand en elektronendichtheid vs. temperatuur bij lage temperaturen lijkt te laten zien dat er twee groepen ladingsdragers zijn. Eén groep heeft een hoge mobiliteit maar een lage elektronendichtheid. De andere groep heeft een lage mobiliteit, maar de elektronendichtheid is twee ordes groter. De ladingsdragers met een lage dichtheid hebben een hele lage activatie-energie van ongeveer 1 meV, terwijl de ladingsdragers met een hoge dichtheid de gebruikelijke activatie-energie van ongeveer $E_\mathrm{a} = 6$ meV hebben. Deze dubbele populatie is waarschijnlijk gerelateerd aan de kubisch-naar-tetragonale fase-overgang van STO rond 105 K, aangezien in een kubisch kristal meerdere geleidingsbanden niet mogelijk zijn.

Dankwoord

Met deze pagina's komen we aan het einde van dit boekwerk. Het is ook het einde van een veelbewogen periode. Vijf jaren van hoogtepunten, maar ook moeilijkere tijden. Maar wel een periode waar ik met veel genoegen op terugkijk. Ik heb veel geleerd, zowel over de wetenschap als over mijzelf. Ik heb ook veel (nieuwe) mensen leren kennen. Veel van hen hebben op hun manier een bijdrage geleverd aan dit proefschrift, hetzij direct, hetzij indirect.

Ten eerste natuurlijk mijn promotor en begeleiders. Zonder hun ondersteuning had ik vijf jaar geleden niet aan dit avontuur kunnen beginnen. Dave, Harold, I want to thank you for the opportunity you both gave me to do my Ph.D. research with your groups. It has been interesting (and fun) to live with both your lab groups and see how science is made. Both of you offered opportunities to follow my own interests, but also made me part of the work done in both your groups. Guus, jouw ondersteuning de laatste twee jaar was geweldig. Ik heb alle gesprekken die we gehad hebben erg gewaardeerd. In die tijd heb ik veel geleerd, niet alleen over mijzelf, maar ook over de wetenschap van het doen van onderzoek.

Er zijn een aantal mensen die ik speciaal moet vermelden, omdat ze een belangrijke bijdrage hebben geleverd aan dit onderzoek. Vaak in de vorm van metingen, maar altijd in de vorm van discussie. Sung Seok Seo, Lena Fitting-Kourkoutis, Masaru Takizawa, Hans Boschker, Josée Kleibeuker, thanks for all the experiments and discussions we had together. It made this thesis all the better for it. It was great to work with you all and I hope to do so again in the future. So: kamsamnida, thank you very much, domo arigato gozaimasu & dank je wel!

Een andere groep mensen is eveneens onmisbaar geweest de afgelopen jaren. Frank, Henk, Gerrit en Harry, bedankt voor alle technische hulp binnen en buiten het lab. Voor vragen was altijd tijd en als er iets stuk was, duurde dat gewoonlijk niet lang. Marion, José en Tanaka-san, thank you for all the help with the more administrative parts of my Ph.D. Thank you for saving me all that paperwork!

Jeroen, Oktay, I enjoyed sharing our office with you, though at times it seemed as if each of us had an office elsewhere. Jeroen at the CoMat system, Oktay in Langezijds and me either at the PLD-RHEED system or the PPMS. Still, the whiteboard has been filled with discussions and the desks filled with paper. I wish you both the best with completing your own Ph.D.!

Er zijn een hele hoop collega's, hier op de Universiteit Twente, op de Universiteit van Tokyo en op sommige andere plekken die ik wil bedanken. Met hen heb ik de afgelopen jaren die ups en downs van het leven op de universiteit gedeeld. Er zijn discussies geweest over de metingen, over de (wetenschaps)politiek maar ook over voetbal, koffie en waar je het afgelopen weekend geweest bent. We zijn samen naar conferenties geweest, hebben studiereizen gemaakt en colloquia gevolgd. Daarom in willekeurige volgorde: Mark, Gertjan (bedankt voor de tip!), Professor Hilgenkamp, Alexander, Bernard (jammer dat EIS op electronische materialen zo'n hoge frequentie vereiste), André (bedankt voor die artikelencursus), Professor Noh, Susaki-san, Hikita-san, Nakagawa-san, Kozuka-san, Hotta-san, Stefan, Willem, Anthony, Nicolas, Arjen, Suresh, Michiel, Tomasz, Ruud, Peter, Frank, Xin, Matthijn, Ole, Evert, Mercy, Hajo, Andreas, Paul, Wolter, Joska, Vittorio, Koray (from my first PLD to my defence), Ashima, May, Zhicheng, Tian, Maarten, Jeroen H. Thank you all!

Maar ook buiten de vakgroep moet ik een hoop mensen bedanken voor de afgelopen jaren. Allereerst mijn huisgenoten: Aafke, Femke & Robert, bedankt voor jullie steun de afgelopen jaren. Het ging niet altijd gemakkelijk, maar ik denk dat het een geweldige tijd is geweest. Ook bij de Navigators moet ik de nodige mensen bedanken. De bijbelstudies waren altijd weer een rustmoment. Peter, Rick, Stefan, Henk, Tjitze, Jan-Willem, Linda & Matthias. Bedankt voor wat ik heb mogen leren het afgelopen jaren! I should also not forget the people from the Matsudo House Church! Thank you for all the good times! En ik mag de mensen bij Scouting niet vergeten. Die hebben ook alles eigenlijk wel meegemaakt. Daarom, Welpen & leiding, hij was KNAL!

Tenslotte wil ik nog al mijn familie bedanken. Pa, wat mooi dat ma en jij mij nog konden opzoeken in Japan. Ik hoop dat zij ook een beetje van dit resultaat zal genieten. André, Judith, bedankt voor alle interesse die er altijd was. Verdere ooms & tantes, neefjes & nichtjes, het zal wat moeilijker worden om contact te houden vanuit de VS, maar we gaan het gewoon doen. (Al ben ik ook al gevraagd of ik een logeerplekje kon regelen..)

Nu zijn we toch echt aan het einde van dit avontuur gekomen.

Maar het volgende avontuur wacht al weer..

Gerwin